Functional Polyoxometalates for Clean Environment and Energy Applications

हैदराबाद विश्वविद्यालय
University of Hyderabad

प्रतिष्ठित संस्थान
INSTITUTION OF EMINENCE
राष्ट्रीय अपेक्षाएँ, वैश्विक मानक
National Needs, Global Standards

A Thesis Submitted for the Degree of
DOCTOR OF PHILOSOPHY
By

Sateesh Mulkapuri

September 2020

School of Chemistry, University of Hyderabad (IoE), Hyderabad-500 046, India

Functional Polyoxometalates for Clean Environment and Energy Applications

A Thesis Submitted for the Degree of

DOCTOR OF PHILOSOPHY

By

Sateesh Mulkapuri

September 2020

School of Chemistry, University of Hyderabad (IoE), Hyderabad-500 046, India

Dedicated to

My Father (Late Rajaiah)

And

My Beloved Supervisor (Prof. Samar K. Das)

CONTENTS

Chapter 2. W^{VI}–OH Functionality on Polyoxometalates for Hydrogen Evolution Reaction

DECLARATION

I, **Sateesh Mulkapuri** hereby declare that the matter embodied in the thesis "***Functional Polyoxometalates for Clean Environment and Energy Applications***" is the result of my investigation carried out in School of Chemistry, University of Hyderabad, Hyderabad, India, under the supervision of **Professor Samar K. Das**.

In keeping with the general practice of reporting scientific observations, due acknowledgements have been made wherever the work described is based on the findings of other investigators. Any omission, which might have occurred by oversight or error, is regretted. This research work is free from plagiarism. I hereby agree that my thesis can be deposited in Shodhganga/INFLIBNET. A report on plagiarism statistics from the University Library is enclosed.

22/09/20

Sateesh Mulkapuri

(13CHPH12)

S. K. Das

Professor Samar K. Das

(Supervisor) 22/09/2020

Prof. Samar K. Das
School of Chemistry
University of Hyderabad
Hyderabad-500 046., INDIA.
skdas@uohyd.ac.in

हैदराबाद विश्वविद्यालय
University of Hyderabad

प्रतिष्ठित संस्थान
INSTITUTION OF EMINENCE
राष्ट्रीय अपेक्षाएँ, वैश्विक मानक
National Needs, Global Standards

CERTIFICATE

This is to certify that the thesis entitled ***"Functional Polyoxometalates for Clean Environment and Energy Applications"*** submitted by **Mr Sateesh Mulkapuri** bearing registration number **13CHPH12** in partial fulfilment of the requirements for the award of Doctor of Philosophy in the School of Chemistry is a bonafide work carried out by him under my supervision and guidance. This thesis is free from plagiarism and has not been submitted previously in part or in full to this or any other University or Institution for the award of any degree or diploma.

Parts of this thesis have been published in the following publications:

1. S. Mulkapuri, S. K. Kurapati, S. Mukhopadhyay and S. K. Das. ***New J. Chem.*,2019**, *43*, 17670-17679(Chapter 4).

2. S. Mulkapuri, S. K. Kurapati and S. K. Das. ***Dalton Trans.*, 2019**, *48*, 8773–8781 (Chapter 5).

He has also participated in oral/poster presentations in the following conferences:

1. Poster presentation in **MTIC–XVII(2017)**, CSIR-NCL-and IISER-Pune, India.
2. Poster presentation in **ICCCS-8 (2017)**, SoC, UoH, Hyderabad, India.
3. Poster presentation in **CHEMFEST (2018)**, SoC, UoH, Hyderabad, India.
4. Oral and poster presentation in**CHEMFEST (2019)**, SoC, UoH, Hyderabad, India.

Further, the student has passed the following courses towards the fulfilment of the coursework requirement for Ph. D.:

	Course	Title	Credits	Pass/Fail
1.	CY-801	Research Proposal	3	Pass
2.	CY-805	Instrumental Methods A	3	Pass
3.	CY-401	Basic Concepts in Coordination Chemistry	3	Pass
4.	CY-451	Main group and inner transition elements	3	Pass

S. K. Das

ProfessorSamar K. Das
(Research Supervisor)

22/09/2020

Prof. Samar K. Das
School of Chemistry
University of Hyderabad
Hyderabad-500 046., INDIA.
skdas@uohyd.ac.in

Dean
(School of Chemistry)

Dean
SCHOOL OF CHEMISTRY
University of Hyderabad
Hyderabad-500 046

SYNOPSIS

Of the Thesis Entitled

Functional Polyoxometalates for Clean Environment and Energy Applications

To be submitted to the

University of Hyderabad

For the Degree of

DOCTOR OF PHILOSOPHY

By

Sateesh Mulkapuri

(13CHPH12)

हैदराबाद विश्वविद्यालय
University of Hyderabad

प्रतिष्ठित संस्थान
INSTITUTION OF EMINENCE
राष्ट्रीय अपेक्षाएँ, वैश्विक मानक
National Needs, Global Standards

School of Chemistry, University of Hyderabad (IoE), Hyderabad-500 046, India.

September 2020

Synopsis

Functional Polyoxometalates for Clean Environment and Energy Applications

The doctoral thesis titled **"Functional Polyoxometalates for Clean Environment and Energy Applications"** consists of four working chapters followed by concluding remarks and future scope of the thesis, in addition to a chapter dedicated to general introduction. The chapters are titled as (**1**) An Introduction to Recent Advances in POM Based Functional Materials and Their Applications, (**2**) W^{VI}–OH Functionality on Polyoxometalates for Hydrogen Evolution Reaction, (**3**) Barrel-shaped Polyoxometalates Exhibiting Electrocatalytic Hydrogen Evolution at Neutral pH, **(4)** A Fully Reduced $\{V_{18}{}^{IV}O_{42}\}$ Host and VO_4^{3-}, Cl^- as Guest Anions: Synthesis, Characterization and Proton Conductivity and **(5)** Carbonate Encapsulation from Dissolved Atmospheric CO_2 into a Polyoxovanadate Capsule.

All the working chapters (Chapter 2-5) consist of (i) a brief overview of the work, (ii) introduction, which includes the relevant literature survey and importance of the work, (iii) experimental methods, (iv) results and discussion, and (v) conclusion. All the compounds, synthesized in this thesis, are characterized by routine analytical methods such as single-crystal X-ray diffraction (SCXRD) studies, powder X-ray diffraction (PXRD) studies, Fourier-transform infrared (FTIR)–, electronic–, Raman–spectral studies including inductively coupled plasma optical emission spectroscopy (ICP-OES), Field emission scanning electron microscopy (FESEM), Thermogravimetric (TG) analysis, and X-ray photoelectron spectroscopy (XPS). In addition, variable temperature magnetic measurement studies, TGA-FTIR–, TGA-mass– and HR-MS–analyses have been performed whenever they are needed. Electrochemical hydrogen evolution reactions (HERs) were conducted in an aqueous as well as in non-aqueous medium (using both heterogeneous and homogeneous materials). Proton conductivity studies were performed on solid pelletized samples using a home-made setup. The gas-solid interface reaction was conducted using a home-made setup.

Chapter 1

An Introduction to Recent Advances in POM Based Functional Materials and Their Applications

Polyoxometalates (POMs) are biocompatible systems prepared from earth-abundant resources. POM compounds are considered as the most emerging class of inorganic materials. The history of the POMs begins 200 years ago and contains thousands of diverse molecules. The materials, based on POMs, are capable to hold and exchange multiple-number of electrons and/or protons (H^+) with small or no structural changes. The faster multi-electron redox properties of POMs enable researchers to employ these materials in a broad range of applications, including magnetism, energy storage, and catalysis (e.g. organic and electrochemical catalysis, *etc.*). Simple and easy synthetic protocols of these materials are added advantages that are vital for bulk production. All these fundamental features of POMs motivated us to explore them in clean energy applications. Thus, this introductory note (chapter 1) contains a general introduction about the importance and development of abundant and electrochemically active POM

materials including their hydrogen evolution reactions (HERs) and proton conductivity studies. More specifically, this chapter discusses a short overview of the development of electrocatalysts for water reduction (WR) or hydrogen evolution reaction (HER) and materials for proton-conduction. It also provides a brief discussion on interactions of POMs with CO_2. This chapter ends with the motivation of the present thesis work for clean energy applications.

Chapter 2

W^{VI}–OH Functionality on Polyoxometalates for Hydrogen Evolution Reaction

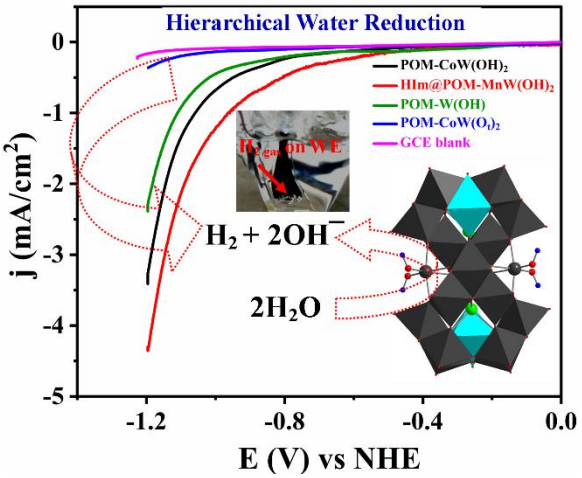

Figure 1. Schematic representation of POM-$CoW(OH)_2$ and HIm@POM-$MnW(OH)_2$ modified electrodes exhibited electrocatalytic hydrogen evolution reaction.

Grafting a W^{VI}–$(OH)_2$ functionality on a polyoxometalate (POM) surface makes the concerned POM compounds, $[\{Na_6(H_2O)_2\}][\{Co^{II}(H_2O)_3\}_2\{W^{VI}(OH)_2\}_2\{Bi^{III}W^{VI}_9O_{33})_2\}]\cdot 14H_2O$ (**POM-CoW(OH)$_2$**) and $[(W^{VI}(OH)_2)_2(Mn^{II}(H_2O)_3)_2(Na_4(H_2O)_{14}(BiW_9O_{33})_2](Him)_2\cdot 16H_2O$ (**HIm@POM-MnW(OH)$_2$**) prominent heterogeneous electrocatalysts for direct water reduction to molecular hydrogen ($2H_2O + 2e^- \rightarrow H_2 + 2OH^-$) at the neutral pH. We have identified that the W^{VI}–$(OH)_2$ functionality acts as the active site for hydrogen evolution reaction (HER) in the cathodic window. Controlled experiments exclude the chances of formation and participation of metal particles in this electrocatalytic water reduction. We could demonstrate that the electrocatalysts (**POM-CoW(OH)$_2$** and **HIm@POM-MnW(OH)$_2$**) are stable enough towards HER up to 1000 cycles. The concerned (HER) Faradaic efficiencies for **POM-CoW(OH)$_2$** and **HIm@POM-MnW(OH)$_2$** are 79% and 86% at pH 7, and 93 % and 96% at pH 3, respectively. The respective turn over frequencies (TOFs) are 0.318 s^{-1} and 0.402 s^{-1} (at pH 7) and 1.154 s^{-1} and 1.289 s^{-1} (at pH 3). The W–OH group, grafted on a POM surface, is known for a while; however, the evidence that this can be a well-defined functionality for water reduction (at the neutral pH) has never been demonstrated until this work. **Figure 1** shows the

schematic representation of the hydrogen evolution reaction by **POM-CoW(OH)$_2$** and **HIm@POM-MnW(OH)$_2$**.

Chapter 3

Barrel-shaped Polyoxometalates Exhibiting Electrocatalytic Hydrogen Evolution at Neutral pH

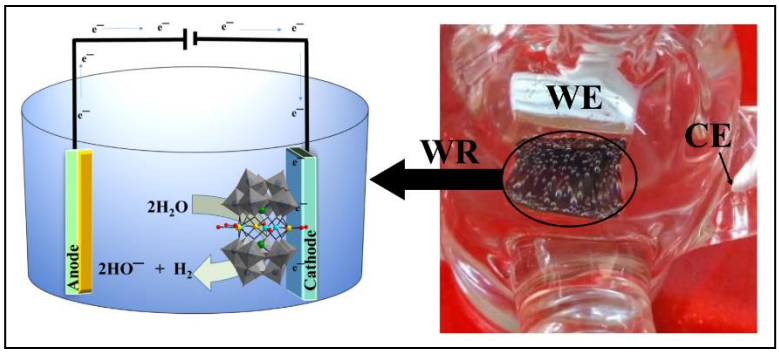

Figure 2. Schematic representation of the electrocatalytic hydrogen evolution reaction exhibited by electrodes modified with **NaCu-POM** and **LiCu-POM** at neutral pH.

Two copper-based barrel-shaped POMs, namely $[\{H_3O\}_4\{Na_6(H_2O)_{22}\}][\{(Cu^{I}_{0.25}Cu^{I}_{0.75})(H_2O)_3\}_2\{Cu^{II}(H_2O)\}_3\{B\text{-}\alpha\text{-}Bi^{III}W^{VI}_9O_{33}\}_2]\cdot 7H_2O$ (**NaCu-POM**) and $Li_4[\{NH_4\}_2\{H_3O\}_3\{Li(H_2O)_5\}][\{Cu^{II}(SH)\}\{(Cu^{II}Cu^{I}_{1.5})(B\text{-}\alpha\text{-}Bi^{III}W^{VI}_9O_{33})\}_2]\cdot 9H_2O$ (**LiCu-POM**) were synthesized and characterized. The molecular structures of **NaCu-POM** and **LiCu-POM** are obtained from their single-crystal diffraction studies that reveal a hexa-nuclear copper $\{Cu_6\}$-wheel, sandwiched between two lacunary $\{B\text{-}\alpha\text{-}Bi^{III}W^{VI}_9O_{33}\}^{9-}$ POM units to form barrel-shaped title POM molecules. In both the compounds (**LiCu-POM** and **NaCu-POM**), the mixed-valent nature of copper centers in the hexa- and penta-nuclear copper wheels were confirmed by bond valence sum (BVS) calculations and XPS analysis. The core structures of **NaCu-POM** and **LiCu-POM** are quite similar, but the **LiCu-POM** additionally shows a sulfide ligand (SH^-) that is coordinated to one of the copper centers of $\{Cu_6\}$-wheel. The sulfide in **LiCu-POM** was expected to be generated from the *in situ* reduction of sulfate anion since it was the only source of sulfur in the reaction (reducing agent is expected to be ammonia). The presence of redox-active mixed-valent copper centers and their synergetic interactions with tungsten are probably driving the electrocatalytic activity of these compounds in water reduction at neutral pH. **Figure 2** shows a schematic representation of the electrocatalytic hydrogen evolution reaction at neutral pH exhibited by electrodes modified with **NaCu-POM** and **LiCu-POM**. The Tafel slope values of 267 and 352 mV dec^{-1} are found for **NaCu-POM** and **LiCu-POM**, respectively. The respective turn over frequencies (TOFs) are 1.598 mol H_2 s^{-1} and 1.117 mol H_2 s^{-1} at pH 7. The Faradic efficiencies are 89% for **NaCu-POM** and 92% for **LiCu-POM** at pH 7. The catalysts are stable during 4 hours of chronoamperometric experiment

and 100 cycles of cyclic voltammetric (CV) experiments. The controlled experiments exclude the chances of the decomposition of molecular catalysts to other electrochemically active species (such as, Cu or W metal nano-particles) during the course of the reaction which establish the true catalytic nature of concerned barrel-shaped POMs.

Chapter 4

A Fully Reduced $\{V_{18}^{IV}O_{42}\}$ Host and VO_4^{3-}, Cl^- as Guest Anions: Synthesis, Characterization, and Proton Conductivity

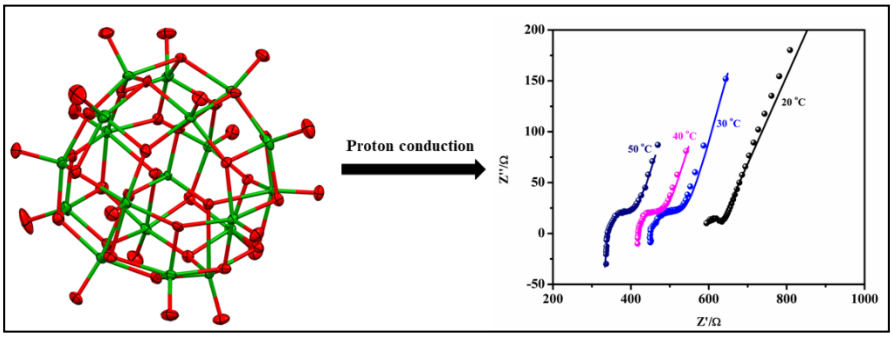

Figure 3. Schematic representation of the fully reduced proton-rich polyoxovanadate based solid-state proton conductivity.

Fully reduced polyoxometalates (POMs), generally, have a high negative charge that can be compensated by diverse cations including protons. The POMs with a larger number of acidic protons often exhibit solid-state proton conduction. We synthesized two polyoxovanadate (POV)-based compounds $[Na_7(H_2O)_{14}][H_8V^{IV}_{18}O_{42}(V^VO_4)]\cdot N_2H_4\cdot 7H_2O$ (**1**) and $[Na_5(H_2O)_{16}][H_8V^{IV}_{18}O_{42}(Cl)]\cdot 4N_2H_4\cdot 6H_2O$ (**2**), each of which accommodates eight acidic protons (per formula unit) acting as the cations. Compounds **1** and **2** were characterized by routine analytical techniques, such as IR, Raman, XPS, PXRD, TGA, elemental analysis and unambiguously by single-crystal X-ray diffraction. As expected, compounds **1** and **2** having eight protons per formula unit exhibit proton conductivity in the solid-state. Proton conductivity (σ) measurements of compounds **1** and **2** were performed (a) at variable temperature (20–50 °C), with constant humidity (70% RH) and (b) variable relative humidity (relative humidity from 40 % to 70%) under constant temperature (30 °C). The proton conductivity was observed to increase with the increase in temperature and relative humidity. The good conductivity values were obtained at 50 °C under 70% RH and found to be 3.62×10^{-3} S cm^{-1} for compound **1** and 2.16×10^{-4} S cm^{-1} for compound **2**. Reproducibility of proton conductivity was verified by repetitive data recording over a long period and determining the mean value of conductivity of compounds **1** and **2** at 50 °C. The activation energies (23.34 kJ mol^{-1} for **1** and 18.40 kJ mol^{-1} for **2**), calculated using Arrhenius plots ($\ln(\sigma T)$ vs. $1000/T$) of compounds **1** and **2**, suggest a Grotthuss proton hoping mechanism for solid-state proton conduction. Controlled experiments have shown that the synthesized compounds **1** and **2** are stable and robust under operational

conditions. **Figure 3** shows a schematic representation of the fully reduced proton-rich polyoxovanadate based solid-state proton conductivity.

Chapter 5

Carbonate Encapsulation from Dissolved Atmospheric CO_2 into a Polyoxovanadate Capsule

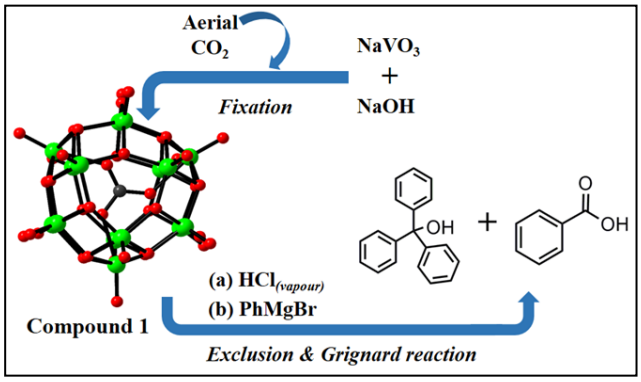

Figure 4. Schematic representation of the aerial CO_2 absorption and its encapsulation into the cavity of the fully reduced polyoxovanadate capsule followed by its exclusion in a gas-solid interface reaction for the formation of organic products.

An aqueous synthesis, involving the reduction of VO_3^- anion in a mild alkaline pH in the presence of α-Bi_2O_3, leads to the formation of a fully reduced polyoxovanadate (POV) capsule, with CO_3^{2-} anion encapsulation in its internal cavity, in the compound $[Na_6(H_2O)_{24}][H_8V^{IV}_{15}O_{36}(CO_3)]\cdot 3N_2H_4\cdot 10H_2O$ (**1**). This CO_3^{2-} anion encapsulation, the source of which is absorbed aerial CO_2 in the pertinent aqueous alkaline reaction mixture, occurs only in the presence of α-Bi_2O_3. Compound **1** crystals, upon exposure to HCl acid vapor, exclude CO_2 gas that can be reacted to the Grignard reagent (PhMgBr) to form triphenyl carbinol and benzoic acid; during this solid-vapor interface reaction, compound **1** itself is transformed into an amorphous material that includes Cl^- anion, but could not be characterized unambiguously. Thus, we have synthesized a chloride ion (Cl^-) encapsulated compound $[Na_{10}(H_2O)_{24}][H_3V^{IV}_{15}O_{36}(Cl)]\cdot 6H_2O$ (**2**) in a direct synthesis protocol, which has been characterized by crystallography as well as by other spectroscopic methods. Compounds **1** and **2**, each having fifteen vanadium (IV) centers, exhibit interesting magnetism in their solid-state. The temperature-dependent magnetic susceptibilities for compounds 1 and 2 have solid states. The temperature-dependent magnetic susceptibilities for compounds **1** and **2** have been recorded at 0.1 T in the temperature range of 3–300 K. **Figure 4** shows a schematic representation of the aerial CO_2 capture and its encapsulation into the cavity of fully reduced polyoxovanadate capsule followed by its exclusion in a gas-solid interface reaction for the formation of organic products.

CHAPTER 1

An Introduction to Recent Advances in Polyoxometalate Based Functional Materials and Their Applications

Overview:

Polyoxometalates (POMs) are biocompatible systems prepared from earth-abundant resources. POM compounds are considered as the most emerging class of inorganic materials. The history of the POMs begins 200 years ago and contains thousands of diverse molecules. The materials, based on POMs, are capable to hold and exchange multiple-number of electrons and/or protons (H^+) with a little or no structural changes. The faster multi-electron redox properties of POMs enable researchers to employ these materials in a broad range of applications, including magnetism, energy storage, and catalysis (e.g., organic and electrochemical catalysis, *etc.*). Simple and easy synthetic protocols of these materials are added advantages that are vital for bulk production. All these fundamental features of POMs motivated us to explore them in clean energy applications. Thus, this introductory note (chapter 1) contains a general introduction about the importance and development of abundant and electrochemically active POM materials including their hydrogen evolution reactions (HERs) and proton conductivity studies. More specifically, this chapter discusses a short overview of the development of electrocatalysts for water reduction (WR) or hydrogen evolution reaction (HER) and materials for proton-conduction. It also provides a brief discussion on interactions of POMs with CO_2. This chapter ends with the motivation of the present thesis work for clean energy applications.

1.1. Introduction

Over past fifty years, with rapid industrialization and technological growth along with sudden explosion in population, urge for high-density energy sources and production of clean enery has been increasing rapidly. According to the recent statistics, global energy demand is expected to reach 27.6 (almost ~30) Terawatt (TW) in the year 2050.[1-6] Currently, we mainly

dependent on fossil fuels for energy production. But, excess use of fossil fuels is not only the concern of our inability to preserve available natural energy resources for future generations, but also is alarming in terms of irreversibly changing environmental factors. In recent times, to substitute fossil fuels, significant progress has been made in the production of energy from various unconventional energy resources including geothermal, nuclear, solar and tidal energy. However, from total energy consumption, energy harnessing techniques, renewable energy sources are contributing to only 20.5%, even after our best efforts based on available resources; the remaining major share (79.5%) of energy is mainly being obtained by burning fossil

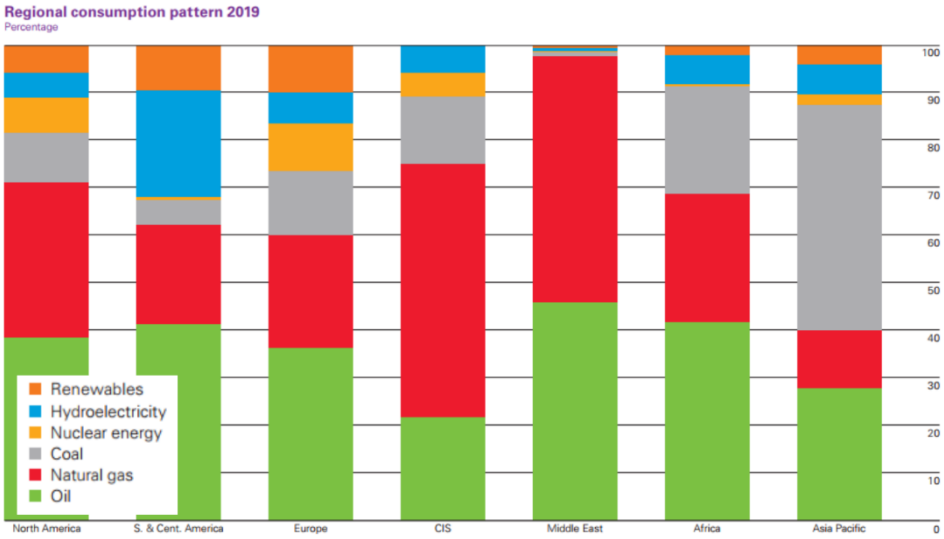

Figure 1.1. Rate of all forms of fuel consumption (%) in the main regions of the world in the year 2019.[4]

fuels. Notably, economic growth of India, China and other developing Asia Pacific countries has primarily been associated with a high rate of fossil fuel consumption such as coal, oil, and natural gas (**Figure 1.1**). These findings collectively conclude that human development is still over-reliant on the carbon energy economy. Therefore, it is a need of the moment to build a clean, renewable, and carbon-free energy economy for the sustainable growth (**Figure 1.2**).[1-12]

Among a plethora renewbale enrgy sources, hydrogen (H_2) is holding significant position, owing not only to its relatively high gravimetric energy density (146 kJ g^{-1}) but also to production of harmless carbon-free end product (*i.e.*, H_2O), on burning.[2,8,9] These benefits are keeping it as an emergent green fuel for present and future generations. There are plenty of hydrogen production technologies, that have been developed in recent times, starting from chemical methods to photocatlytic and electrocatalytic water splitting for storing (electric) energy in chemical energy form *i.e.*, H–H bond formation.[3,7-18] Though, photocatalytic water splitting (direct conversion of solar energy into chemical energy) has been of a great importance, it is still in the conceptualization stage and requires even more attention to develop it to industrial scale.[19-21] Besides, the electrocatalytic hydrogen production, storing electric

energy (from other renewable sources like solar, hydal *etc.*) in the form of chemical bonds, has been growing parallelly to tackle with the exponentially growing thirst for renewable energy. During the course of electrocatlytic water splitting, hydrogen evolution takes place at the cathode (a cathodic reaction). The reduction catalyst electrochemically reduces the water into molecular hydrogen (HER: $2H_2O + 2e^- \rightarrow H_2 + 2OH^-$; at neutral or alkaline pH) in the cathodic potential window. On the other hand, its counter-response electrochemically produced $2OH^-$ ions which could be later oxidized to the molecular oxygen (OER: $2OH^- \rightarrow 1/2O_{2(g)} + 2e^- + H_2O_{(aq)}$) at the anode.[2,7,8]

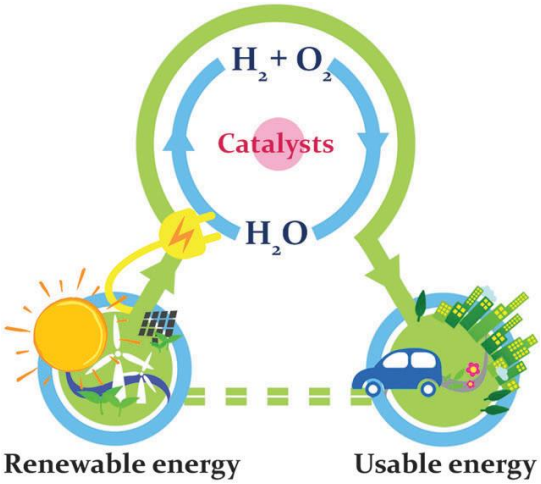

Figure 1.2. The future hydrogen energy cycle.[8]

For rapid hydrogen fuel production, highly active and robust HER and OER electrocatalysts are required.

On the other hand, it is not only important to search for methods to produce clean, easily accessable and highest gravimetric energy density fuel materials, it is also essential to develop a technology for efficient harvesting of usable form energy using those materials. Fuel Cell (FC) is one such technology, developed to safely convert chemical energy into usable electric energy (as far as hydrogen as a energy source is concerned). The FC has the highest chemical energy to an electrical energy conversion factor and its end products are essentially water and electric energy.[22,23] The working principle of FC is almost opposite to that of cell using for electrocatalytic hydrogen production. Here, at the anode oxidation of hydrogen molecules takes place and at the cathode oxygen (O_2) is reduced.

For a fuel to harvest electric energy, besides hydrogen fuel there are other components like polyelectrolyte membrane (PEM), that also plays vital role in its efficiency. As it was hinted above, the catalytic hydrogen oxidation at the anodic chamber is accompanied by (i) flow of electrons through the external circuit (the usable electrical energy) and (ii) catalytically generated protons in the anodic chamber that essentially transports to the cathodic chamber

through a PEM separator. Here comes the role of PEM which directly influences the output of FC. Higher the proton transportation ability of PEM higher is the efficiency of FC.[23]

Considering these facts, it could be conveniently stated that, efficient water reduction/hydrogen evolution and effective proton conduction process are vital for clean energy generation (**Figure 1.2**). In the present thesis, we mainly focused on the developing of polyoxometalate based electrocatalyst for hydrogen production and proton conductivity materials for their viable electrochemical application. Besides these, there is also a high demand for materials for sustainable fixing/incorporation of major air pollutants like CO_2 in to usable substances. In this thesis, we have also presented a carbonate ion (derived from *in-situ* absorbed aerial CO_2) encapsulated polyoxovanadate (POV) cluster and its exclusion (as CO_2 by a gas-solid interface reaction) for organic synthesis.

To work on POM based materials for sustainable energy processing applications, it will be handy to have at least concise knowledge of all stake holders (molecular properties of POMs, and factors involving in electrocatalysis *etc.*) involving in this field of science. Hence, elements associated with these system and relevant studies will be briefly introduced in following sections.

Keeping the above facts in mind and for convenience of readers, the present chapter will be discussed in five parts: (1) brief introduction and general synthetic procedure of POMs, (2) basic requirements to design and development of a water reduction (WR)/hydrogen evolution reaction (HER) catalyst, (3) proton-rich POMs as proton-conducting polyelectrolytes, (4) aerial CO_2 sequestration by POMs and finally (5) the motivation behind the work presented in following chapters.

1.2. Brief introduction and general synthetic procedure of POMs

POMs are commonly known as, metal-oxide cages of early transition metal ions (e.g., V, Mo, W, Nb, Ta, Ti) which can be formed in their highest oxidation state. POMs have a very long history (almost ~200 years) when Jöns Jacob Berzelius in 1826 first reported a metal-oxide cluster of ammonium phosphomolybdate (*i.e.*, $[NH_4]_3[PMo_{12}O_{40}]$).[24] Later on, James Fargher Keggin, in 1933, experimentally determined the structure of phosphomolybdic acid ($[H_3PW_{12}O_{40}]\cdot 6H_2O$) by X-ray diffraction studies.[25] POM like metal-oxides are also naturally present in the earth-crusts. These POMs have completely constructed a three dimensional (3D) molecular structure by metal-oxide backbone and can form unmatched molecular structures (for example, Keggin, Lindqvist, Wells-Dawson, Anderson, Strandberg, Waugh, *etc.*).[24-30] It is commonly known that, POMs can hold multi-electrons/protons without structural change and can have excellent physicochemical stabilities. Due to these features, POMs are considered as solid-state Brønsted acids. POMs are superior redox-active materials for various types of

catalysis (such as organic transformations, photo-/electro-chemical catalysis for sustainable energy harvesting), magnetism, bio-medical, *etc*. applications.[31-35]

Further, POMs could be prepared in a straightforward synthesis. Most of the POMs are isolated in a one-pot wet synthesis and the formation of POMs is mainly proceeded by proton-induced condensation-/dehydration reactions in an aqueous solution. On the other hand, the formation mechanism of POMs is still ambiguous and is generally expected that it involves self-assembly reaction process. Few factors play a crucial role in the formation of POMs, such as (i) stoichiometric ratios of reactants, (ii) reaction mixture pH, (iii) temperature, (iv) solvent effect, (v) addition of reducing agents, and (vi) presence of additional ligands. It is always challenging to synthesize a novel POM using sequential multi-step reactions, but careful functionalization of *in-situ* generated or presynthesized lacunary POM clusters makes possible in isolating the targeted POMs. This functionalization strategy can lead to form discrete molecule to multi-dimensional structures, such as, complete inorganic or organic-inorganic network structures.[34-38]

1.3. Basic requirements to design and develop the HER catalyst

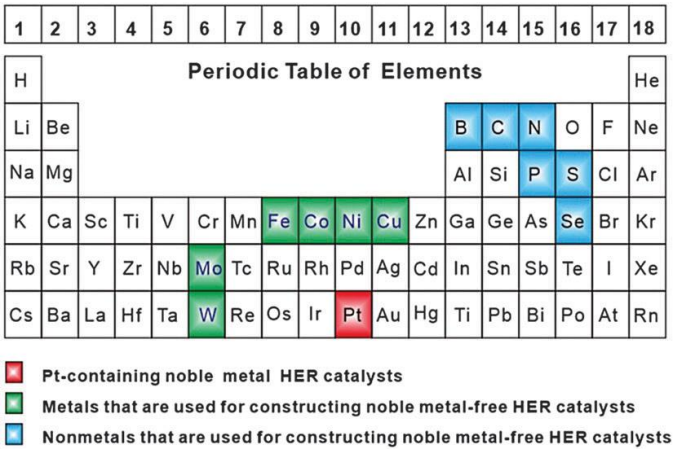

Figure 1.3. Three different groups of elements for designing hydrogen evolution reaction catalysts.[8]

To develop an efficient HER electrocatalyst for sustainable energy production in the cost-effective path, two things needs to be considered. Firstly, the abundance of catalyst or catalyst precursor elements and secondly, their electrochemical redox activity. Based on these parameters, the HER catalysts are mainly divided into three groups (i) noble metal(s)- (platinum and metals in its group), (ii) transition metal(s)- and (iii) non-metal- based electrocatalysts [7-11, 39-42] (**Figure 1.3**).

On the other hand, as mentioned before, it essential to have basic knowledge of parameters, that include (1) HER activity of electrode, (2) stability, (3) overpotential, (4) Tafel plot, (5) HER mechanism, (6) Faradic efficiency, and (7) turnover frequency (TOF).[2,7-11]

1.3.1. HER activity of the electrode

Generally, the HER activity of a developed catalyst can be tested by the cyclic voltammogram (CV) or linear sweep voltammogram (LSV). To understand better the preliminary behaviour of the HER electrocatalyst, at least five consecutive CV- or LSV-scans have to be recorded. While comparing the activity of analogous catalytic systems, the HER onset potential (where the hydrogen evolution reaction starts) of that particular catalyst becomes significant. Based on the response obtained from any one of these techniques, the catalyst material would be assessed further to estimate its stability and efficiency under operational conditions.

1.3.2. Stability of the catalyst

The stability of the developed catalyst under electrochemical conditions is highly essential for its practical application. There are two basic methods, that have been commonly in use to estimate the extent of stability of a given catalyst; these are (i) electrochemical analyses (chronoamperometric analysis (>10 h; *I-t* curve) and continuous CV/LSV scanning (>1000 scans)), and (ii) spectroscopic techniques to characterize the electrode material before and after the experiment (or by *in-situ* methods during the electrochemical reaction). These two methods are useful in evaluating the stability of a catalyst. A good catalyst retains its electrochemical and spectroscopic identity even after prolonged electrochemical tests.

1.3.3. Overpotential

To get clear insights into this interesting parameter, having brief understanding of electrochemical cell and its associated processes, is advisable. Hence, they are summerised in the following paragraph.

An electrochemical cell consists of three necessary components: anode, cathode, and an electrolyte (*i.e.*, H_2O in this case). The OER and HER catalysts can be coated on the anode and cathode, respectively, to accelerate the overall water splitting reaction. When an external potential applied to the electrochemical cell, the reactant water molecules would be decomposed into hydrogen and oxygen at cathode and anode chambers, respectively (**Figure 1.4**). The evolved H_2 and O_2 will be collected in separate containers and stored for later use. This water splitting (WS: $H_2O_{(l)} \rightarrow H_{2(g)} + 1/2\ O_{2(g)}$) reaction phenomenon was first reported in 1789 and presented in two half-cell reactions: (i) HER at the cathode and (ii) OER at the anode.[2,44]

Depending on the reaction medium in which WS takes place, it proceeds in two different pathways.

<u>Electrocatalytic water splitting in an acidic media</u>:

Anode: $2H_2O \rightleftharpoons O_2 + 4H^+ + 4e^-$ $\quad E^\circ_{ox} = +1.23$ V (eqn. 1)

Cathode:	$4H^+ + 4e^- \rightleftharpoons 2H_2$	E°_{red} = 0.00 V	(eqn. 2)
Net reaction:	$2H_2O \rightarrow 2H_2 + O_2$	ΔE° = +1.23 V	

The OER requires high energy in an acidic aqueous electrolyte, and it practically takes place at higher than thermodynamic potential (>1.23V vs NHE). In contrast, the HER is carried out at 0.00 V vs NHE in the presence of noble metal as the cathode (*e.g.*, Pt).

Electrocatalytic water splitting in an alkaline/neutral media:

Anode:	$4OH^- \rightleftharpoons O_2 + 2H_2O + 4e^-$	E°_{ox} = –0.40 V	(Eqn. 3)
Cathode:	$4H_2O + 4e^- \rightleftharpoons 2H_2 + 4OH^-$	E°_{red} = +0.83 V	(Eqn. 4)
Net reaction:	$2H_2O \rightarrow 2H_2 + O_2$	ΔE° = +1.23 V	

Acidic to alkaline aqueous electrolytes the OER becomes feasible but HER demands more energy for cleavage of O–H bond in water molecule and for the formation of H–H bond. In this process, several reaction intermediate steps (Volmer, Heyrowsky and Tafel) are involved and follows the sluggish reaction kinetics.[7-11]

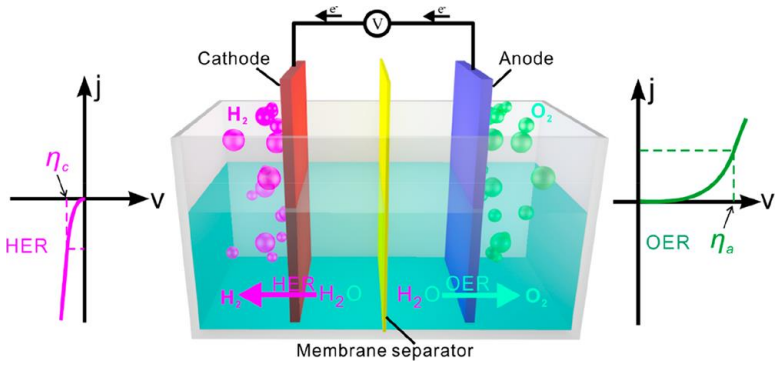

Figure 1.4. The water-splitting reaction in the electrochemical cell: HER (left side) and OER (right side).[2]

But, irrespective of the reaction medium, the overall WS reaction is carried out to complete at the thermodynamic potential E° = +1.23 V (*vs* NHE at 25 °C and 1atm). However, in the real-reaction conditions, due to the sluggish reaction kinetics (such as electron and ion transportation from the electrode along with other contact resistances), it consumes more than 1.23 V *vs* NHE to complete the electrochemical WS at 25 °C and 1 atm. This additional potential needed above 1.23 V called overpotential (η) which is basically needed to cross the intrinsic energy barriers for HO–H bond breaking and making of H–H as well as O–O bond at the cathode (η_c) and anode (η_a), respectively. In addition to those mentioned earlier, there are some other resistances (η_{iR}) such as electrolyte resistance, electrode and wire contact resistance, electrode surface blockage due to the H_2 gas generated on the electrode surface, that also would be present. Thus,

the practically consumed potential (E_{cp}) could be the combination of all, and it can be represented as E_{cp} = 1.23 V + η_c + η_a + η_{iR}. It is visible from this equation that, suitable modulations would play a vital role to lower down the required overpotential to achieve an efficient water-splitting reaction. In other words, η_{iR} can be minimized by designing an efficient electrochemical cell.[2,7,8,44,45] But, η_c and η_a can be lowered only through the development of highly active electrode materials. In this scenario, design and fabrication of highly active electrocatalysts using earth-abundant metal ions are essential for the efficient WS reaction in a more cost-effective way. Deliberately two striking overpotentials (η), corresponding to the current densities of 1 (η_1) and 10 (η_{10}) mA/cm^2, are considered to represent the efficiency of a catalyst. And this can be used to make a comparison between different catalysts (**Figure 1.5(a)**). The overpotential (η_1) can commonly be known as HER or OER onset overpotential. On the other hand, the specific current density of 10 mA/cm^2 is equivalent to the efficiency of a solar-water splitting device (12.3 %). Hence, the overpotential needed to this specific current density provides a means of comparison of a developed catalyst with a solar-water splitting device.[2,8]

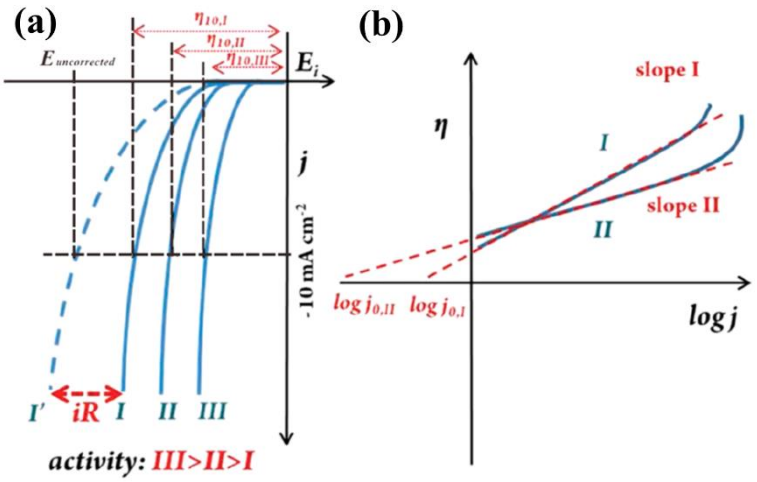

Figure 1.5. (**a**) Schematic illustration of HER polarization curves for different electrocatalysts with *iR*-corrected overpotentials at 10 mA/cm^2; (**b**) schematic representation of Tafel plots for different electrocatalysts with the Tafel slopes and exchange current densities.[42]

Therefore, an efficient HER catalyst should have low overpotential with minimal Tafel slope value (discussed in follwing section). Another important issue is that the direct comparison of the developed catalyst with different HER catalysts could not make the real-time catalytic activity comparison because the loading level of catalytically active material on the particular geometric area of the electrode may vary for different cases. Thus, to make a more precise comparison of catalytic activity of various catalysts, the standard quantity (*e.g.*, 0.1 mg) or the same amount of catalyst loading on a standard geometric area of the electrode (*e.g.*, GCE area of 0.0706 cm^2) is highly recommended.[2]

1.3.4. Tafel plot

Tafel plot helps in understanding the dependence of the rate of hydrogen evolution reaction in terms of overpotentials at various current density values. The Tafel plot is constructed under study-state mass flow following the chronopotentiometry electrolysis.[46-48] The obtained overpotential (η) can be plotted as a function of log |j| ($\eta = b\log|j/j_o|$) (**Figure 1.5(b)**), where b is the slope of Tafel plot acquired by the linear fit of data points, and j and j_o are the current density and exchange-current density, respectively. Exchange-current density (j_o) and Tafel slope (b) values are crucial factors, and these depict the intrinsic catalytic activity of the electrocatalyst. The j_o value is obtained by the extrapolation of the linear fit on the X-axis. That particular point current density value, where the linear fit line touching to the X-axis, is considered to be the exchange-current density (j_o) and assumed to be the zero overpotential (η_o) under equilibrium reaction condition. The small b and low η along with high j_o value, are required to deliver the particular current density, indicating the fast electron-transfer rate or reaction kinetics. An excellent electrocatalyst must possess these parameters.[2]

1.3.5. HER mechanism

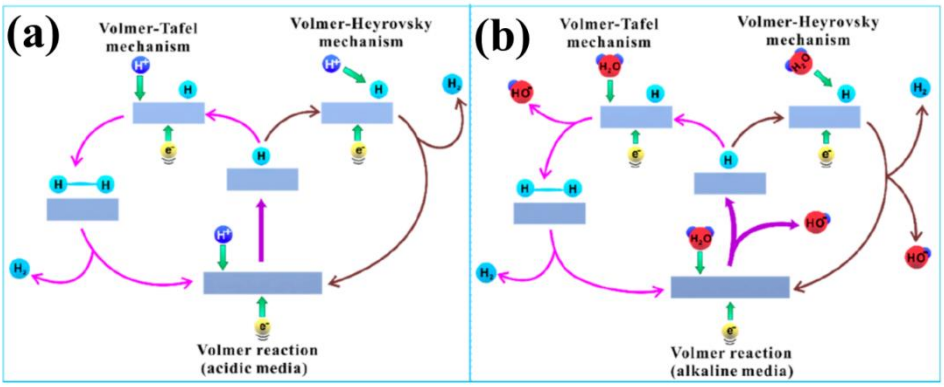

Figure 1.6. Schematic representation of the hydrogen evolution reaction mechanism on the electrode surface (**a**) in acidic and (**b**) alkaline or neutral solutions.[2]

The HER mechanism takes place by three necessary steps in an acidic medium (**Figure 1.6(a)** and **Table 1.1**), whereas in the alkaline or neutral medium it is still ambiguous. Researchers have explained the plausible HER mechanism using the acidic reaction path steps (**Figure 1.6(b)** and **Table 1.1**). However, the detailed investigation of HER mechanism in alkaline and neutral pH condition is essential for its fundamental understanding.[7,8]

Table 1.1. Plausible HER reaction pathways

Condition	Overall reaction	Reaction path	
In acidic medium:	$2H^+ + 2e^- \rightarrow H_2$	Volmer: Heyrovsky: Tafel:	$H_3O^+ + Cat + e^- \rightleftharpoons Cat–H^* + H_2O$ $H^+ + e^- + Cat–H^* \rightleftharpoons H_2 + Cat$ $2Cat –H^* \rightleftharpoons H_2 + 2\ Cat$
In alkaline and neutral medium:	$2H_2O + 2e^- \rightleftharpoons H_2 + 2OH^-$	Volmer: Heyrovsky:	$H_2O + Cat + e^- \rightleftharpoons Cat–H^* + OH^-$ $H_2O + e^- + Cat–H^* \rightleftharpoons H_2 + OH^- + Cat$

Tafel:	$2Cat–H^* \rightleftharpoons H_2 + 2Cat$

Note: Cat: catalyst; Cat–H*: adsorbed hydrogen atom or hydrogen adduct on the active electrocatalyst surface.

In all the HER reaction conditions Volmer step takes place first, where the proton and electron react together to form adsorbed hydrogen atom (H*) on the active electrocatalyst surface (Cat). The source of proton for the adsorbed hydrogen atom (H*) is acidic water (H_3O^+) in acidic medium and the source is water molecule (H_2O) in alkaline or neutral medium. After the Volmer step (Cat–H*), molecular hydrogen (H_2) would be formed through the Heyrovsky step or Tafel step or the result of both (Heyrovsky-Tafel) steps. The Tafel slope (*b*) value determines the hydrogen evolution reaction path. According to the theoretical calculations, when the Tafel slope (*b*) values are 30, 40, and 118 mV dec^{-1} then the Tafel, Heyrovsky, and Volmer steps are the rate-determining step in the HER process, respectively.[7-11,49]

1.3.6. Faradic efficiency of the catalyst

Faradic efficiency is another important parameter to estimate the efficiency of HER catalyst. Generally, the Faradic efficiency can be measured chronopotentiometrically by bulk electrolysis using a standard procedure.[12,46-48] The Faradic efficiency is defined as the ratio of the experimental to the theoretically evolved hydrogen gas in an electrochemical hydrogen evolution reaction utilizing the externally supplied energy in the form of electrons. A suitable catalyst produces higher catalytic Faradic efficiency.

$$\text{Faradic efficiency} = \frac{\text{Experimentally evolved hydrogen}}{\text{Ideally evolved hydrogen}} \times 100$$

1.3.7. Turn over frequency (TOF)

The turnover frequency (TOF) is an another important feature of the catalyst to express the efficiency of a catalyst. It is expressed as the number of reactant molecules getting converted into the products per active site per second.[50,51] Researchers use several methods to predict the TOF of a catalyst. [12,46-48] Still, it is quite challenging to determine the precise TOF value because all the active sites in the coated material may not be accessible or equally reactive, particularly in heterogeneous or solid-state catalytic reaction condition. However, in our present investigations, the recently reported method is used to determine the TOF value of the hydrogen evolution reaction catalyst.[12,52] A high-end active catalyst should always exhibit high turnover frequency. The turnover frequency of the catalyst can be determined using this equation TOF $= \frac{I}{2mF}$, where I = steady-state current (A) value obtained from chronoamperometry electrolysis, F = Faraday constant (C mol^{-1}), m = number of active sites (mol), 2 = number of electrons required to form one mole of hydrogen.

1.3.8. POMs as HER catalysts

A large number of POM molecules have been isolated and characterized, but their efficient employment as electrode materials remains unexplored. As mentioned elsewhere, POMs possess very high redox activity, and they can accommodate as many electrons as possible without changing their respective structures. Recently, considerable interest has been given to develop the POMs as the new-generation electrode materials for HER and OER, solid-state batteries, redox flow batteries and fuel cells.[31-33,53-55] Cronin group has published plenty of research articles on POM based electrode materials such as HER and OER catalysts, solid-state batteries, redox flow batteries (**Figure 1.7**), and supercapacitors.[56-62] Kortz[63-64] and Hill[65,66] and other groups[67-71] contributed significantly to this field.

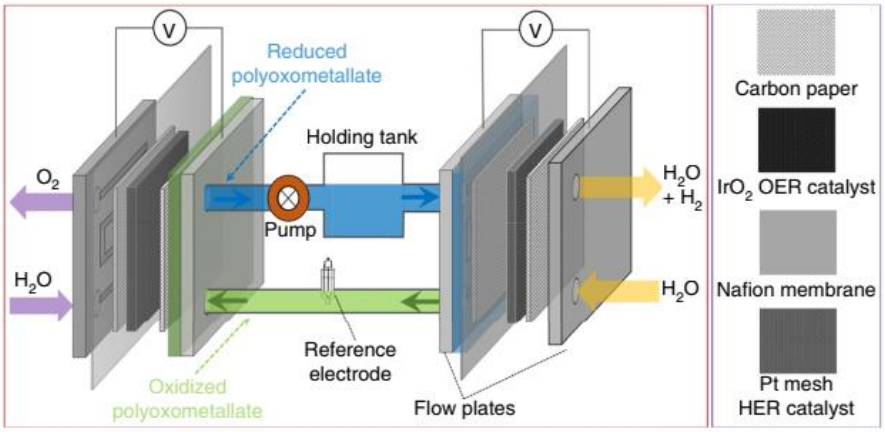

Figure 1.7. $[P_2W_{18}O_{62}]^{6-}$ based reversible multi-electron redox flow cell device used for the hydrogen evolution reaction (at the cathode) and oxygen evolution reaction (at the anode).[56]

1.4. Proton conductivity

Being associated with majority of fundamental biological energy-transportation processes (*e.g.*, photosynthesis) and artificial energy related technologies, like fuel cells for sustainable energy conversion, proton conductivity phenomenon is found to be essential part of fundamental and applied sciences.[72,73] The FCs consist of two compartments, *i.e.*, cathodic and anodic chambers separated by polyelectrolyte membrane. In the FC, the molecular H_2 is oxidized in the anodic chamber and generate protons and electrons. In the cathodic chamber, oxygen is reduced to water using the protons and electrons circulated from the anodic chamber. The uninterupted electron flow in external circuit provides the usable electrical energy. At the end of the process, FC emits H_2O as a by-product at the cathodic chamber. For the sustainable fuel cell operation, efficient and continuous proton transportation from the anodic chamber to the cathodic chamber is essential. Otherwise, increasing concentration of protons (H^+) in the anodic chamber can result in the stoppage of the fuel cell in its functioning. Hence, designing and fabrication of high proton-conducting membrane is vital in the construction of FCs for sustainable energy management. It is remarkable to mention that the efficiency of a FC is highly reliant not only on the ability of hydrogen oxidation and oxygen reduction at the anode and cathode but also on

the efficient proton transportation by PEM. Thus, the scientists across the globe are putting their best efforts in preparing a highly efficient and robust proton conductor that can perform continuous proton transportation in the fuel cell under operational conditions.[72-99]

1.4.1. Proton conductivity mechanism

Water is the universal solvent for the versatile class of studies, including proton conductivity in the viable FC operations. As we know, it is an excellent proton conductor by establishing an extensive hydrogen bonding. Thus, the initial proton conductivity and its mechanism studies are mainly conducted in the water and protic acids solvents (source of labile protons). It was well established that, the water-assisted proton transportation follows the Grotthuss proton mechanism (**Figure 1.8**) and it takes place at ambient temperature (< 100 °C) with high efficiency. Proton transportation by Grotthuss mechanism occurs through the flipping of water molecules *via* O–H bonds, which requires very less activation energy (< 0.4 eV) for proton transportation. At he temperature above 100 °C, the operation of the Grotthuss mechanism is unusual to happen. Generally at elevated temperatures, the proton transportation takes place through the vehicular mechanism instead of the Grotthuss pathway. In the vehicular mechanism, the proton-conducting channels or Brønsted acidic molecules play a crucial role in proton transportation.[100-102]

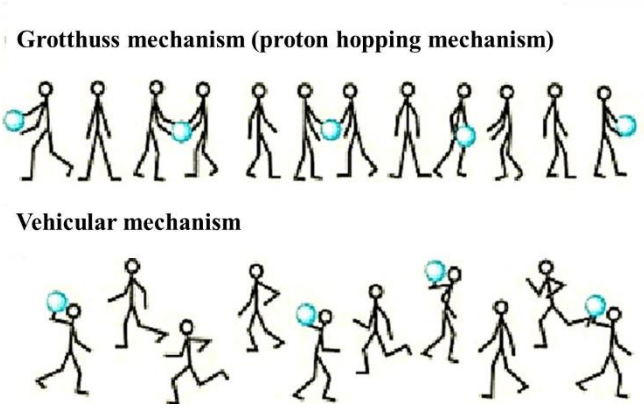

Figure 1.8. Represention of Grotthuss and Vehicular proton conduction mechanisms.

1.4.2. POM based proton conductivity

POMs have immense importance in various fields including solid-state electrolytes (proton conductivity electrolytes). In general, the charge of anionic POVs/POMs was mainly compensated by 1A group cations (*e.g.*, Li^+, Na^+, K^+ and Cs^+), ammonium ions, organic cations, and transition metal ions/complex cations (mostly 3*d* metals)[103-110] as well as the required number of protons. Due to the ascribed acidity by these protons, the concerned POMs are considered as heteropolyacids. Solid-state electrolytes like POMs with acidic protons are of great importance as the high concentration of acidic protons and rich H-bonding on the POM

surface play an important role in the proton conductivity. The proton exchange membrane fuel cells (PEMFCs) efficiency is highly depended on the efficiency of polyelectrolyte material.[111-113] So far, Nafion has been used as polyelectrolyte material in PEMFCs. It shows lareger proton conductivity (10^{-1} S cm^{-1}) among the reported proton conductive materials.[75] However, its high manufacturing cost and low water-holding capability still motivate us to search for suitable alternative materials.[78,79] In this regard, several materials including metal-organic frameworks (MOFs),[73,74] covalent organic frameworks (COFs),[80,81] and functionalized zeolites[49-53] have been employed for proton conductivity studies, but they often showed poor proton conductivity values due to their hydrophobicity and internal resistances due to the organic backbone.[82,83] Hence, POMs have been opted as one of the potential proton conductive materials. For the first time in 1979, Nakamura *et al.* employed a novel Keggin-POM {$H_3PM_{12}O_{40}\cdot 29H_2O$; M = Mo, W} as solid electrolyte material in the fuel cell ($H_2||O_2$) and it was shown as superior proton conductor (0.18 S cm^{-1}) among all POMs, till date.[114] Very recently, Lin *et al.* reported a mixed-valent Mo_{240} [$Mo^{V}_{180}Mo^{VI}_{60}$] hollow sphere POM with second highest proton conductivity value of 0.103 S cm^{-1} (at 80 °C and 98% RH).[115] Recently, Liu *et al.*[118] and Li *et al.*[117] have reported a stable mixed-valent Mo_{132} spherical cluster containing- and reduced vanadium (IV) containing- POM based-proton conductivity materials, respectively. In general, fully reduced POVs are relatively more negatively charged compounds compared to their mixed-valent and oxidized analogues. This feature may result in a high probability of having more number of protons on the relevant POV cluster surface, thereby bringing them as a potential proton conductivity materials.[118,119] Cronin group has described a thiometalate associated POM based wheel type material $(CH_3)_4N]_{1.5}K_{5.5}Na_2[I_3\subset(Mo^{V}_2O_2S_2)_8(Se^{IV}O_3)_8(OH)_8]\cdot 25H_2O$ with a proton conductivity value of 1.2×10^{-2} S cm^{-1} (at 55 °C and 97% RH).[120] In 2010, Ohkoshi *et al.* reported proton conductivity of 2.6×10^{-3} S cm^{-1} based on reduced vanadium compound ($V^{II}[Cr^{III}(CN)_6]_{2/3}\cdot zH_2O$).[121] Inspite of their potential applicability in this area, vanadium-based POMs are less explored as solid-state proton conductivity materials compared to the other POMs. In this context, we are more interested in studying proton conductivity, based on reduced POVs.[122]

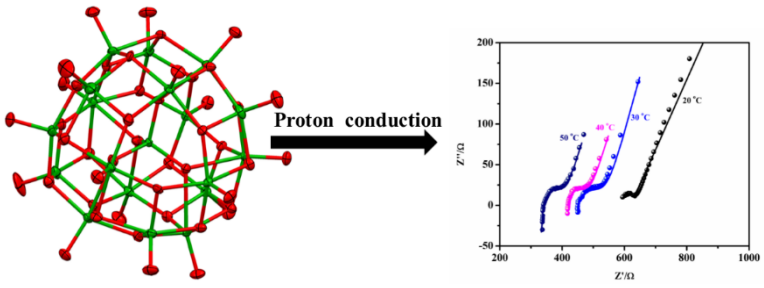

Figure 1.9. Illustrating the highly protonated POV turns into the proton conduction material.[122]

1.5. Aerial CO_2 sequestration

As it was discussed earlier, the CO_2 concentration is enormously increasing in the environment due to fossil fuel burning. Besides the developments in sustainable fuel production techniques, it is essential to sequester the excess amount of pre-existed CO_2 gas from the atmosphere for sustainable life on the earth surface. In Nature, photosynthesis is a well-known reaction, that converts the aerial CO_2 gas into the useful feedstocks. Across the globe, reserchers have been continuously working in this direction, and numerous research articles have been published.[123-128] These mainly include the CO_2 absorption by porous materials (*e.g.*, MOFs, COFs etc. which are mostly used as storage materials), electro/photocatalytic CO_2 reduction by various catalysts. Despite the enormous contribution in this area of CO_2 management, its adsorption and conversion into the useful feedstocks is still growing with very slow pace. Especially, POMs are less explored in this area. Recently, we have demonstrated the CO_3^{2-} ion encapsulation into a POV capsule from the absorbed atmospheric CO_2.[129] The encapsulated CO_2 as CO_3^{2-} ion can further be removed by a gas-solid interface reaction. In the gas-solid interface reaction, the crystals of isolated host-guest compound (POV capsule) were treated with the HCl vapours in a mild reaction condition and the excluded CO_3^{2-} as CO_2 gas, without capsule braking, was then treated with Grignard (PhMgBr) reagent for its organic transformation. In the Grignard reaction, triphenylmethanol and benzoic acid products were the main products. This work is part of the working chapter of this thesis and will be discussed in detail in **Chapter 5**.

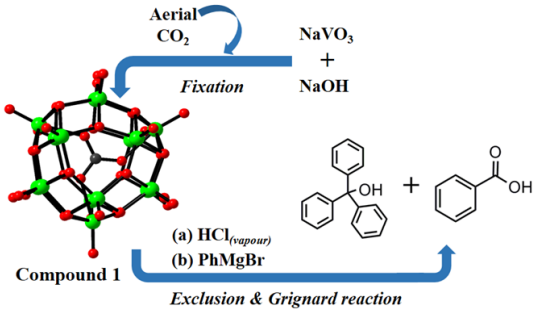

Figure 1.10. Depiction of carbonate encapsulation into the POV capsule from absorbed aerial CO_2, and its exclusion by gas-solid interface reaction for organic formation.[129]

1.6. The motivation behind the work presented in following chapters

The increasing energy demand along with a growing population, has largely motivated us to search for high-density energy materials. In this context, presently, most of the energy is being produced by combustion of all forms of fossil fuels. The rapid burning of fossil fuels is not only leading to exhaust of the natural resources but also depositing the hazardous by-products (*e.g.*, CO_2) into the environment, which are damaging the eco-system. Producing high-density sustainable energy sources, like molecular hydrogen using renewable resources is most important to reach the world energy demand. It is already discussed that among all possible energy-producing technologies, the electrochemical hydrogen production is the most promising

way at the moment. For the efficient electrochemical hydrogen evolution, we need to develop an electrocatalyst using bio-compatible materials; this is highly desirable because of its safe disposal into the environment. In this regard, earth-abundant metal-oxides or POMs are the best option for sustainable energy production. POMs can be easily isolated through simple and one-pot wet synthesis.

The present thesis work is mainly divided into three major parts: (1) electrocatalytic hydrogen evolution, (2) POMs based solid-state proton conductivity, and (3) CO_3^{2-} ion encapsulation into a polyoxovanadate (POV) shell from absorbed atmospheric CO_2 and its exclusion for value-added conversion to organic products. The first part of the thesis work, *i.e.*, **Chapters 2** and **3**, we have discussed the POMs based electrocatalytic hydrogen evolution at neutral pH condition. More specifically, in **Chapter 2**, we have demonstrated that the POM surface grafted W–OH functional site catalyzes electrocatalytic hydrogen evolution in both neutral and acidic pH medium. **Chapter 3** describes hexa-nuclear and penta-nuclear copper wheel sandwiched barrel-shaped POMs that exhibit electrocatalytic hydrogen evolution at neutral pH. The second part of the thesis, *i.e.*, **Chapter 4**, depicts the POVs based solid-state proton conductivity. And in the third part of the thesis, *i.e.*, **Chapter 5**, we have demonstrated that the CO_3^{2-} ion encapsulation into a POV shell from the absorbed atmospheric CO_2 and its exclusion by gas-solid interface reaction for value-added organic products.

1.7. References

(1). Gray, H. B., Powering the Planet with Solar Fuel. *Nat. Chem.* **2009**, *1*, 7.
(2). Zhu, J.; Hu, L.; Zhao, P.; Lee, L. Y. S.; Wong, K.-Y., Recent Advances in Electrocatalytic Hydrogen Evolution Using Nanoparticles. *Chem. Rev*. **2020**, *120*, 851-918.
(3). Lewis, N. S.; Nocera, D. G., Powering the Planet: Chemical Challenges in Solar Energy Utilization. *Proc. Natl. Acad. Sci. U. S. A.* **2006**, *103*, 15729.
(4). The Statistical Review of World Energy Analyses Data on World Energy Markets from the Prior Year. https://www.bp.com/content/dam/bp/business-sites/en/global/corporate/pdfs/energy-economics/ statistical -review/bp -stats-review-**2020**-full-report.
(5). REN21; Renewables **2018** Global Status Report, http://www. ren21.net/about-ren21/about-us/,2018.
(6). United States Department of Energy. A National Vision of America's Transition to a Hydrogen Economy-To 2030 and Beyond; Washington, DC, **2003**.
(7). Bae, S.-Y.; Mahmood, J.; Jeon, I.-Y.; Baek, J.-B., Recent Advances in Ruthenium-based Electrocatalysts for the Hydrogen Evolution Reaction. *Nanoscale Horiz.* **2020**, *5*, 43-56.
(8). Zou, X.; Zhang, Y., Noble Metal-free Hydrogen Evolution Catalysts for Water Splitting. *Chem. Soc. Rev.* **2015**, *44*, 5148-5180
(9). Morales-Guio, C. G.; Stern, L.-A.; Hu, X., Nanostructured Hydrotreating Catalysts for Electrochemical Hydrogen Evolution. *Chem. Soc. Rev.* **2014**, *43*, 6555−6569.
(10). Jiao, Y.; Zheng, Y.; Jaroniec, M.; Qiao, S. Z., Design of Electrocatalysts for Oxygen- and Hydrogen-Involving Energy Conversion Reactions. *Chem. Soc. Rev*. **2015**, *44*, 2060−2086.
(11). Wang, J.; Xu, F.; Jin, H.; Chen, Y.; Wang, Y., Non-Noble Metal based Carbon Composites in Hydrogen Evolution Reaction: Fundamentals to Applications. *Adv. Mater*. **2017**, *29*, 1605838.
(12). Ghosh, S.; Srivastava, A. K.; Govu, R.; Pal, U.; Pal, S., A Diuranyl(VI) Complex and Its Application in Electrocatalytic and Photocatalytic Hydrogen Evolution from Neutral Aqueous Medium. *Inorg. Chem.* **2019**, *58*, 14410-14419.
(13). Frey, M., Hydrogenases: Hydrogen-Activating Enzymes. *ChemBioChem* **2002**, *3*, 153-160.
(14). Dresselhaus, M. S.; Thomas, I. L., Alternative Energy Technologies. *Nature* **2001**, 414, 332–337.

(15). Steele, B. C. H.; Heinzel, A., Materials for Fuel-Cell Technologies. *Nature* **2001**, *414*, 345–352.
(16). Nicholsa, E. M.; Gallagherc, J. J.; Liua, C.; Sua, Y.; Resascoe, J.; Yua, Y.; Sunf, Y.; Yanga, P.; Changa, M. C. Y.; Chang, C. J., Hybrid Bioinorganic Approach to Solar-to-Chemical Conversion. *Proc. Natl. Acad. Sci. U.S.A.* **2015**, *112*, 11461-11466.
(17). Torellaa, J. P.; Gagliardib, C. J.; Chena, J. S.; Bediakob, D. K.; Colóna, B.; Way, J. C.; Silver, P. A.; Nocera, D. G., Efficient Solar-to-Fuels Production from a Hybrid Microbial–Water-Splitting Catalyst System. *Proc. Natl. Acad. Sci. U.S.A.* **2015**, *112*, 2337-2342.
(18). Liu, C.; Colón, B. C.; Ziesack, M.; Silver, P. A.; Nocera, D. G., Water Splitting–Biosynthetic System with CO_2 Reduction Efficiencies Exceeding Photosynthesis. *Science* **2016**, *352*, 1210-1213.
(19). Hunter, B. M.; Gray, H. B.; Müller, A. M. Earth-Abundant Heterogeneous Water Oxidation Catalysts. *Chem. Rev.* **2016**, *116*, 14120–14136.
(20). Ruttinger, W.; Dismukes, G. C., Synthetic Water-Oxidation Catalysts for Artificial Photosynthetic Water Oxidation. *Chem. Rev.* **1997**, *97*, 1–24.
(21). Downes, C. A.; Marinescu, S. C., Electrocatalytic Metal–Organic Frameworks for Energy Applications. *ChemSusChem* **2017**, *10*, 4374–4392.
(22). Zhang, J. ed., **2008**. PEM Fuel Cell Electrocatalysts and Catalyst Layers. Available at: http://dx.doi.org/10.1007/978-1-84800-936-3.
(23). Laberty-Robert, C.; Vallé, K.; Pereira, F.; Sanchez, C., Design and Properties of Functional Hybrid Organic–Inorganic Membranes for Fuel Cells. *Chem. Soc. Rev.* **2011**, *400*, 961–1005.
(24). Berzelius, J. J., Contribution to a Closer Knowledge of Molybdenum. *Ann. Phys.* **1826**, *82*, 369-392. doi:10.1002/andp.18260820402.
(25). Keggin, J. F., Structure of the Molecule of 12-Phosphotungstic Acid. *Nature* **1933**, *131*, 908–909.
(26). Anderson, J. S., Constitution of the Poly-acids. *Nature* **1937**, *140*, 850.
(27). Evans, H. T., Jr., The Crystal Structures of Ammonium and Potassium Molybdotellurates *J. Am. Chem. Soc*. **1948**, *70*, 1291.
(28). Lindqvist, I., Crystal-Structure Investigation of the Paramolybdate ion. *Arkiv Kemi*. **1950**, 2, 325.
(29). Strandberg, R., Multicomponent Polyanions. *Acta Chem. Scand.* **1973**, *27*, 1004.
(30). Evans, H. T., Jr., Perspect. *Struct. Chem.* **1971**, *4*, 1-4.
(31). Katsoulis, D. E., A Survey of Applications of Polyoxometalates. *Chem. Rev.* **1998**, *98*, 359-388.
(32). Roger, I.; Shipman, M. A.; Symes, M. D., Earth-Abundant Catalysts for Electrochemical and Photoelectrochemical Water Splitting. *Nat. Rev. Chem.* **2017**, *1*, 0003.
(33). Ueda, T., Electrochemistry of Polyoxometalates: From Fundamental Aspects to Applications. *ChemElectroChem* **2018**, *5*, 823-838.
(34). Fang, W.-H.; Zhang, L.; Zhang, J., Synthetic Strategies, Diverse Structures and Tuneable Properties of Polyoxo-Titanium Clusters. *Chem. Soc. Rev.* **2018**, *47*, 404-421.
(35). Izarova, N, V.; Michael, T. P.; Kortz, U., Noble Metals in Polyoxometalates. *Angew. Chem. Int. Ed.* **2012**, *51*, 9492-9510.
(36). Ginsberg, A. P., *Inorganic Syntheses, Vol.* 27, **1990**, *Online* ISBN:9780470132586, *DOI:10.1002/9780470132586*.
(37). Pope, M. T., Heteropoly and Isopoly Oxometalates; Springer-Verlag: Berlin, **1983**, https://doi.org/10.1002/ange.19840960939.
(38). Hutin, M.; Rosnes, M. H.; Long, D.–L.; Cronin, L., Polyoxometalates: Synthesis and Structure–from Building Blocks to Emergent Materials; Glasgow, UK, **2013**, http://dx.doi.org/10.1016/B978-0-08-097774-4.00210-2.
(39). Zheng, Y.; Jiao, Y.; Vasileff, A.; Qiao, S.-Z. The Hydrogen Evolution Reaction in Alkaline Solution: From Theory, Single Crystal Models, to Practical Electrocatalysts. *Angew. Chem., Int. Ed.* **2018**, *57*, 7568−7579.
(40). Jin, H. Y.; Guo, C. X.; Liu, X.; Liu, J. L.; Vasileff, A.; Jiao, Y.; Zheng, Y.; Qiao, S. Z. Emerging Two-Dimensional Nanomaterials for Electrocatalysis. *Chem. Rev.* **2018**, *118*, 6337−6408.
(41). Hou, J.; Wu, Y.; Zhang, B.; Cao, S.; Li, Z.; Sun, L. Rational Design of Nanoarray Architectures for Electrocatalytic Water Splitting. *Adv. Funct. Mater.* **2019**, *29*, 1808367.
(42). Gao, Q. S.; Zhang, W. B.; Shi, Z. P.; Yang, L. C.; Tang, Y. Structural Design and Electronic Modulation of Transition-Metal Carbide Electrocatalysts toward Efficient Hydrogen Evolution. *Adv. Mater*. **2019**, *31*, 1802880.

(43). van Troostwijk, A. P.; Deiman, J. Sur Une Maniere De` Decopoer L´ 'eau en Air Inflammable et en Air Vital. *Obs. Phys.* **1789**.
(44). Gileadi, E., *Physical Electrochemistry: Fundamentals, Techniques and Applications*; Wiley-VCH Verlag GmbH & Co.: Weinheim, **2011**.
(45). Shinagawa, T.; Takanabe, K., Towards Versatile and Sustainable Hydrogen Production Through Electrocatalytic Water Splitting: Electrolyte Engineering. *ChemSusChem* **2017**, *10*, 1318-1336.
(46). Mukhopadhyay, S.; Debgupta, J.; Singh, C.; Kar, A.; Das, S. K., A Keggin Polyoxometalate Shows Water Oxidation Activity at Neutral pH: POM@ZIF-8, an Efficient and Robust Electrocatalyst. *Angew. Chem. Int. Ed.* **2018**, *57*, 1918-1923.
(47). Singh, C.; Das, S. K., Anderson Polyoxometalate Supported Cu(H_2O)(phen) Complex as an Electrocatalyst for Hydrogen Evolution Reaction in Neutral Medium. *Polyhedron* **2019,** *172*, 80-86.
(48). Singh, C.; Mukhopadhyay, S.; Das, S. K., Polyoxometalate-Supported Bis(2,2′-Bipyridine)Mono(Aqua)Nickel(II) Coordination Complex: an Efficient Electrocatalyst for Water Oxidation. *Inorg. Chem.* **2018**, *57*, 6479-6490.
(49). Shinagawa, T.; Garcia-Esparza, A. T.; Takanabe, K., Insight on Tafel Slopes from a Microkinetic Analysis of Aqueous Electrocatalysis for Energy Conversion. *Sci. Rep.* **2015**, *5*, 13801.
(50). Boudart, M., Turnover Rates in Heterogeneous Catalysis. *Chem. Rev.* **1995**, *95*, 661-666.
(51). Kozuch, S.;. Martin, J. M. L., Turning Over Definitions in Catalytic Cycles. *ACS Catal.* **2012**, *2*, 2787–2794.
(52). Mahmood, J.; Li, F.; Jung, S.-M.; Okyay, M. S.; Ahmad, I.; Kim, S.-J.; Park, N.; Jeong, H. Y.; Baek, J.-B., An Efficient and pH-Universal Ruthenium-Based Catalyst for the Hydrogen Evolution Reaction. *Nat. Nanotechnol.* **2017**, *12*, 441-446.
(53). Glezos, N.; Velessiotis, D.; Chaidogiannos, G.; Argitis, P.; Tsamakis, D.; Zianni, X., Transport Properties of Polyoxometalate Containing Polymeric Materials. *Synth. Met.* **2003**, *138*, 267-269.
(54). Chaidogiannos, G; Velessiotis, D.; Argitis P.; Koutsolelos, P.; Diakoumakos, C. D.; Tsamakis, D.; Glezos, N., Tunneling and Negative Resistance Effects for Composite Materials Containing Polyoxometalate Molecules. *Microelectron. Eng.* **2004**, *73*, 746-751.
(55). Glezos, N.; Argitis, P.; Velessiotis, D.; Diakoumakos, C. D., Tunneling Transport in Polyoxometalate Based Composite Materials. *Appl. Phys. Lett.* **2003**, *83*, 488.
(56). Chen, J.-J.; Symes, M. D.; Cronin, L., Highly Reduced and Protonated Aqueous Solutions of $[P_2W_{18}O_{62}]^{6-}$ for On-Demand Hydrogen Generation and Energy Storage. *Nat. Chem.* **2018**, *10*, 1042-1047.
(57). Martin-Sabi, M.; Soriano-López, J.; Winter, R. S.; Chen, J.-J.; Vilà-Nadal, L.; Long, D.-L.; Galán-Mascarós, J. R.; Cronin, L., Redox tuning the Weakley-type Polyoxometalate Archetype for the Oxygen Evolution Reaction. *Nat. Catal.* **2018**, *1*, 208-213.
(58). Long, D.-L.; Burkholder, E.; Cronin, L., Polyoxometalate Clusters, Nanostructures and Materials: From Self-Assembly to Designer Materials and Devices. *Chem. Soc. Rev.* **2007**, *36*, 105-121.
(59). Miras, H. N.; Yan, J.; Long, D.-L.; Cronin, L., Engineering Polyoxometalates with Emergent Properties. *Chem. Soc. Rev.* **2012**, *41*, 7403-7430.
(60). Chen, J. J.; Symes, M. D.; Fan, S. C.; Zheng, M. S.; Miras, H. N.; Dong, Q. F.; Cronin, L., High-Performance Polyoxometalate-Based Cathode Materials for Rechargeable Lithium-Ion Batteries. *Adv. Mater.* **2015**, *27*, 4649-4654.
(61). Chen, J. J.; Ye, J. C.; Zhang, X. G.; Symes, M. D.; Fan, S. C.; Long, D.-L.; Zheng, M. S.; Wu, D. Y.; Cronin, L.; Dong, Q. F., Design and Performance of Rechargeable Sodium Ion Batteries, and Symmetrical Li-Ion Batteries with Supercapacitor-Like Power Density Based upon Polyoxovanadates. *Adv. Energy Mater.* **2017**, *8*, 1701021.
(62). Chisholm, G.; Cronin, L.; Symes, M. D., Decoupled Electrolysis using a Silicotungstic Acid Electron-Coupled-Proton Buffer in a Proton Exchange Membrane Cell. *Electrochim. Acta* **2020**, *331*, 135255.
(63). Fernandes, D. M.; Araújo, M. P.; Haider, A.; Mougharbel, A. S.; Fernandes, A. J. S.; Kortz, U.; Freire, C., Polyoxometalate-Graphene Electrocatalysts for the Hydrogen Evolution Reaction. *ChemElectroChem* **2018**, *5*, 273-283.
(64). Bassil, B. S.; Haider, A.; Ibrahim, M.; Mougharbel, A. S.; Bhattacharya, S.; Christian, J. H.; Bindra, J. K.; Dalal, N. S.; Wang, M.; Zhang, G.; Keita, B.; Rutkowska, I. A.; Kulesza, P. J.; Kortz, U., 15-Copper(II)-Containing 36-Tungsto-4-Silicates(IV) $[Cu_{15}O_2(OH)_{10}X(A\text{-}\alpha\text{-}SiW_9O_{34})_4]^{25-}$ (X = Cl, Br):

Synthesis, Structure, Magnetic Properties, and Electrocatalytic CO_2 Reduction. *Dalton Trans.* **2018**, *47*, 12439-12448.

(65). Jabbour, D.; Keita, B.; Nadjo, L.; Kortz, U.; Mal, S. S., The Wheel-Shaped Cu_{20}–Tungstophosphate $[Cu_{20}Cl(OH)_{24}(H_2O)_{12}(P_8W_{48}O_{184})]^{25-}$, Redox and Electrocatalytic Properties. *Electrochem. commun*. **2005**, *7*, 841-847.

(66). Lv, H.; Gao, Y.; Guo, W.; Lauinger, S. M.; Chi, Y.; Bacsa, J.; Sullivan, K. P.; Wieliczko, M.; Musaev, D. G.; Hill, C. L., Cu-based Polyoxometalate Catalyst for Efficient Catalytic Hydrogen Evolution. *Inorg. Chem*. **2016**, *55*, 6750-6758.

(67). Qin, J.-S.; Du, D.-Y.; Guan, W.; Bo, X.-J.; Li, Y.-F.; Guo, L.-P.; Su, Z.-M.; Wang, Y.-Y.; Lan, Y.-Q.; Zhou, H.-C., Ultrastable Polymolybdate-Based Metal–Organic Frameworks as Highly Active Electrocatalysts for Hydrogen Generation from Water. *J. Am. Chem. Soc*. **2015**, *137*, 7169-7177.

(68). Tourneur, J.; Fabre, B.; Loget, G.; Vacher, A.; Mériadec, C.; Ababou-Girard, S.; Gouttefangeas, F.; Joanny, L.; Cadot, E.; Haouas, M.; Leclerc-Laronze, N.; Falaise, C.; Guillon, E., Molecular and Material Engineering of Photocathodes Derivatized with Polyoxometalate-Supported $\{Mo_3S_4\}$ HER Catalysts. *J. Am. Chem. Soc.* **2019**, *141*, 11954-11962.

(69). Nohra, B.; El Moll, H.; Rodriguez Albelo, L. M.; Mialane, P.; Marrot, J.; Mellot-Draznieks, C.; O'Keeffe, M.; Ngo Biboum, R.; Lemaire, J.; Keita, B.; Nadjo, L.; Dolbecq, A., Polyoxometalate-Based Metal Organic Frameworks (POMOFs): Structural Trends, Energetics, and High Electrocatalytic Efficiency for Hydrogen Evolution Reaction. *J. Am. Chem. Soc.* **2011**, *133*, 13363-13374.

(70). Song, Y.-F.; Tsunashima, R., Recent Advances on Polyoxometalate-based Molecular and Composite Materials. *Chem. Soc. Rev.* **2012**, *41*, 7384-7402.

(71). Miao, J.; Lang, Z.; Zhang, X.; Kong, W.; Peng, O.; Yang, Y.; Wang, S.; Cheng, J.; He, T.; Amini, A.; Wu, Q.; Zheng, Z.; Tang, Z.; Cheng, C., Polyoxometalate-Derived Hexagonal Molybdenum Nitrides (MXenes) Supported by Boron, Nitrogen Codoped Carbon Nanotubes for Efficient Electrochemical Hydrogen Evolution from Seawater. *Adv. Funct. Mater.* **2019**, *29*, 1805893.

(72). Scofield, M. E.; Liu, H.; Wong, S. S., A Concise Guide to Sustainable PEMFCs: Recent Advances in Improving Both Oxygen Reduction Catalysts and Proton Exchange Membranes. *Chem. Soc. Rev.* **2015**, *44*, 5836–5860.

(73). Ramaswamy, P.; Wong, N. E.; Shimizu, G. K. H., MOFs as Proton Conductors–Challenges and Opportunities. *Chem. Soc. Rev*. **2014**, *43*, 5913–5932.

(74). Mukhopadhyay, S.; Debgupta, J.; Singh, C.; Sarkar, R.; Basu, O.; Das, S. K., Designing UiO-66-Based Superprotonic Conductor with the Highest Metal–Organic Framework Based Proton Conductivity. *ACS Applied Mater. Interfaces* **2019,** *11*, 13423-13432.

(75). Ochi, S.; Kamishima, O.; Mizusaki, J.; Kawamura, J., Investigation of Proton Diffusion in Nafion®117 Membrane by Electrical Conductivity and NMR. *Solid State Ionics* **2009**, *180*, 580-584.

(76). Schmidt-Rohr, K.; and Chen, Q.; Parallel Cylindrical Water Nanochannels in Nafion Fuel-Cell Membranes. *Nat. Mater*., **2008**, *7*, 75–83.

(77). Kim, Y.; Ketpang, K.; Jaritphun, S.; Park, J. S.; Shanmugam, S., A Polyoxometalate Coupled Graphene Oxide–Nafion Composite Membrane for Fuel Cells Operating at Low Relative Humidity. *J. Mater. Chem. A* **2015,** *3*, 8148-8155.

(78). Lu, S.; Wang, D.; Jiang, S. P.; Xiang, Y.; Lu J.; and Zeng, J.; HPW/MCM-41 Phosphotungstic Acid/Mesoporous Silica Composites as Novel Proton-Exchange Membranes for Elevated-Temperature Fuel Cells. *Adv. Mater*., **2010**, *22*, 971–976.

(79). Kreuer, K.-D.; Paddison, S. J.; Spohr, E.; Schuster, M., Transport in Proton Conductors for Fuel-Cell Applications: Simulations, Elementary Reactions, and Phenomenology. *Chem. Rev.*, **2004**, *104*, 4637-4678.

(80). Chandra, S.; Kundu, T.; Kandambeth, S.; BabaRao, R.; Marathe, Y.; Kunjir, S. M.; Banerjee, R., Phosphoric Acid Loaded Azo (−N═N−) Based Covalent Organic Framework for Proton Conduction. *J. Am. Chem. Soc.* **2014,** *136*, 6570-6573.

(81). Han, W.; Kwan S.; and Yeung, K., Zeolite Applications in Fuel Cells: Water Management and Proton Conductivity. *Chem. Eng. J.*, **2012**, *187*, 367-371.

(82). Han, W.; Kwan, S.; and Yeung, K., Zeolite Proton Conducting Membrane for Micro Fuel Cell Applications. *Top. Catal.*, **2010**, *53*, 1394-1400.
(83). McKeen, J. C.; Yan, Y. S.; Davis, M. E., Proton Conductivity in Sulfonic Acid-Functionalized Zeolite Beta: Effect of Hydroxyl Group. *Chem. Mater.* **2008**, *20*, 3791-3793.
(84). Zhou, Y.; Yang, J.; Su, H.; Zeng, J.; Jiang, S. P.; Goddard, W. A., Insight into Proton Transfer in Phosphotungstic Acid Functionalized Mesoporous Silica-Based Proton Exchange Membrane Fuel Cells. *J. Am. Chem. Soc.* **2014**, *136*, 4954-4964.
(85). Wu, G.; Zhang, H.; Zhou, J.; Huang, A.; Wan, Q., Proton Conducting Zeolite Films for Low-voltage Oxide-based Electric-double-layer Thin-film Transistors and Logic Gates. *J. Mater. Chem. C* **2013**, *1*, 5669-5674.
(86). Meng, X.; Wang, H.-N.; Song, S.-Y.; Zhang, H.-J., Proton-conducting Crystalline Porous Materials. *Chem. Soc. Rev.* **2017**, *46*, 464-480.
(87). Yang, P.; Alsufyani, M.; Emwas, A.-H.; Chen, C.; Khashab, N. M., Lewis Acid Guests in a $\{P_8W_{48}\}$ Archetypal Polyoxotungstate Host: Enhanced Proton Conductivity via Metal-Oxo Cluster within Cluster Assemblies. *Angew. Chem. Inter. Ed.* **2018**, *57*, 13046-13051.
(88). Zhou, Y.; Yang, J.; Su, H.; Zeng, J.; Jiang S. P.; and Goddard, W. A., Insight into Proton Transfer in Phosphotungstic Acid Functionalized Mesoporous Silica-Based Proton Exchange Membrane Fuel Cells. *J. Am. Chem. Soc.*, **2014**, *136*, 4954-4964.
(89). Yang, L.; Ma, P.; Zhou, Z.; Wang, J.; Niu, J., A Crown-Shaped 24-Molybdate Cluster Constructed by Organotriphosphonate Ligand. *Inorg. Chem.* **2013**, *52*, 8285-8287.
(90). Zang, H.-Y.; Chen, J.-J.; Long, D.-L.; Cronin, L.; Miras, H. N., Assembly of Thiometalate-Based $\{Mo_{16}\}$ and $\{Mo_{36}\}$ Composite Clusters Combining $[Mo_2O_2S_2]^{2+}$ Cations and Selenite Anions. *Adv. Mater.* **2013**, *25*, 6245-6249.
(91). Gao, Q.; Wang, X.-L.; Xu, J.; Bu, X.-H., The First Demonstration of the Gyroid in a Polyoxometalate-based Open Framework with High Proton Conductivity. *Chem. Eur. J.* **2016**, *22*, 9082-9086.
(92). Wu, X.; Cai, H.; Wu, Q.; Yan, W., Synthesis and High Proton Conductive Performance of Vanadium-Substituted Dawson Structure Heteropoly Acid $H_8P_2W_{16}V_2O_{62}\cdot 20H_2O$. *Mater. Lett.* **2016**, *181*, 1-3.
(93). Tian, N.; Zhu, M.; Wu, Q.; Yan, W.; Yaroslavtsev, A. B., Preparation and Conductivity of the Keggin-type Trivanadium-substituted Tungstosilicic Acid $H_7SiW_9V_3O_{40}\cdot 9H_2O$. *Mater. Lett.* **2014**, *115*, 165-167.
(94). Dong, B.-X.; Wu, Y.-C.; Tian, H.; Liu, C.-B.; Liu, W.-L.; Teng, Y.-L., Synthesis, Crystal Structure and Electrochemical Properties of A New 2D Network Containing Linear $\{\varepsilon\text{-}H_2PMo_8{}^{V}Mo_4{}^{VI}O_{40}Zn_4\}\infty$ Inorganic Chain. *J. Clust. Sci.* **2016**, *27*, 361-371.
(95). Liu, J.-C.; Han, Q.; Chen, L.-J.; Zhao, J.-W.; Streb, C.; Song, Y.-F., Aggregation of Giant Cerium–Bismuth Tungstate Clusters into a 3D Porous Framework with High Proton Conductivity. *Angew. Chem. Int. Ed.* **2018**, *57*, 8416-8420.
(96). Wang, Y.-D.; Wang, J.-X.; Wei, M.-J.; Liu, B.-L.; Zang, H.-Y.; Tan, H.-Q.; Wang, Y.-H.; Li, Y.-G., Niobium Oxyhydroxide-Polyoxometalate Composite as an Efficient Proton-Conducting Solid Electrolyte. *ChemElectroChem* **2018**, *5*, 1125-1129.
(97). Wang, J.-X.; Wang, Y.-D.; Wei, M.-J.; Tan, H.-Q.; Wang, Y.-H.; Zang, H.-Y.; Li, Y.-G., Inorganic Open Framework based on Lanthanide Ions and Polyoxometalates with High Proton Conductivity. *Inorg. Chem. Front.* **2018**, *5*, 1213-1217.
(98). Tong, X.; Tian, N.; Wu, W.; Zhu, W.; Wu, Q.; Cao, F.; Yan, W.; Yaroslavtsev, A. B., Preparation and Electrochemical Performance of Tungstovanadophosphoric Heteropoly Acid and Its Hybrid Materials. *J. Phys. Chem. C* **2013**, *117*, 3258-3263.
(99). Cai, H.; Wu, X.; Wu, Q.; Yan, W., Synthesis and High Proton Conductive Performance of a Quaternary Vanadomolybdotungstosilicic Heteropoly Acid. *Dalton Trans.* **2016**, *45*, 14238-14242.
(100). Kreuer, K.-D. Proton Conductivity: Materials and Applications. *Chem. Mater.* **1996**, *8*, 610–641.

(101). Grancha, T.; Ferrando-Soria, J.; Cano, J.; Amorós, P.; Seoane, B.; Gascon, J.; Bazaga-García, M.; Losilla, E. R.; Cabeza, A.; Armentano, D., Insights into the Dynamics of Grotthuss Mechanism in a Proton-Conducting Chiral BioMOF. *Chem. Mater.* **2016**, 28, 4608–4615.
(102). Belousov, V. V. Next-Generation Electrochemical Energy Materials for Intermediate Temperature Molten Oxide Fuel Cells and Ion Transport Molten Oxide Membranes. *Acc. Chem. Res.* **2017**, *50*, 273–280.
(103). Wang, S.-S.; Yang, G.-Y., Recent Advances in Polyoxometalate-Catalyzed Reactions. *Chem. Rev.* **2015**, *115*, 4893-4962.
(104). Lv, H.; Geletii, Y. V.; Zhao, C.; Vickers, J. W.; Zhu, G.; Luo, Z.; Song, J.; Lian, T.; Musaev, D. G.; Hill, C. L., Polyoxometalate Water Oxidation Catalysts and the Production of Green Fuel. *Chem. Soc. Rev.* **2012**, *41*, 7572-7589.
(105). Fernando, A.; Weerawardene, K. L. D. M.; Karimova, N. V.; Aikens, C. M., Quantum Mechanical Studies of Large Metal, Metal Oxide, and Metal Chalcogenide Nanoparticles and Clusters. *Chem. Rev.* **2015**, *115*, 6112-6216.
(106). Miras, H. N.; Yan, J.; Long, D.-L.; Cronin, L., Engineering Polyoxometalates with Emergent Properties. *Chem. Soc. Rev.* **2012**, *41*, 7403-7430.
(107). Chen, J. J.; Symes M. D.; Fan, S. C.; Zheng, M. S.; Miras H. N.; Dong, Q. F.; Cronin, L., High-Performance Polyoxometalate-Based Cathode Materials for Rechargeable Lithium-Ion Batteries. *Adv. Mater.* **2015**, *27*, 4649-4654.
(108). Chen, J. J.; Ye, J. C.; Zhang, X. G.; Symes M. D.; Fan, S. C.; Long, D.-L.; Zheng, M. S.; Wu, D. Y.; Cronin, L.; Dong, Q. F., Design and Performance of Rechargeable Sodium Ion Batteries, and Symmetrical Li-Ion Batteries with Supercapacitor-Like Power Density Based upon Polyoxovanadates. *Adv. Energy Mater.* **2017**, *8*, 1701021.
(109). Müller, A.; Peters, F.; Pope, M. T.; Gatteschi, D., Polyoxometalates: Very Large Clusters Nanoscale Magnets. *Chem. Rev.* **1998**, *98*, 239-272.
(110). Calzado, C. J.; Clemente-Juan, J. M.; Coronado, E.; Gaita-Arino, A.; Suaud, N., Role of the Electron Transfer and Magnetic Exchange Interactions in the Magnetic Properties of Mixed-Valence Polyoxovanadate Complexes. *Inorg. Chem.* **2008**, *47*, 5889-5901.
(111). West, A. R., *Basic Solid State Chemistry*, Wiley, **1999**.
(112). Kreuer, K.-D., Proton Conductivity: Materials and Applications. *Chem. Mater.*, **1996**, *8*, 610–641.
(113). Barboiu, M.; Gilles, A., From Natural to Bioassisted and Biomimetic Artificial Water Channel Systems. *Acc. Chem. Res.*, **2013**, *46*, 2814–2823.
(114). Nakamura, O.; Kodama, T.; Ogino, I.; Miyake, Y., High-Conductivity Solid Proton Conductors: Dodecamolybdophosphoric Acid Anddodecatungst Ophosphoric Acid Crystals. *Chem. Lett.* **1979**, *8*, 17-18.
(115). Lin, J.; Li, N.; Yang, S.; Jia, M.; Liu, J.; Li, X-M.; An, L.; Tian, Q.; Dong, L-Z.; Lan Y-Q., Self-Assembly of Giant Mo_{240} Hollow Opening Dodecahedra. *J. Am. Chem. Soc.* **2020**, *142*, 13982–13988.
(116). Liu, W.-J.; Dong, L.-Z.; Li, R.-H.; Chen, Y.-J.; Sun, S.-N.; Li, S.-L.; Lan, Y.-Q., Different Protonic Species Affecting Proton Conductivity in Hollow Spherelike Polyoxometalates. *ACS Applied Mater. Interfaces* **2019**, *11*, 7030-7036.
(117). Li, J.; Cao, X.-L.; Wang, Y.-Y.; Zhang, S.-R.; Du, D.-Y.; Qin, J.-S.; Li, S.-L.; Su, Z.-M.; Lan, Y.-Q., The Enhancement on Proton Conductivity of Stable Polyoxometalate-Based Coordination Polymers by the Synergistic Effect of MultiProton Units. *Chem. Eur. J.* **2016**, *22*, 9299-9304.
(118). Johnson, G. K.; Schlemper, E. O., Existence and Structure of the Molecular ion 18-Vanadate(IV). *J. Am. Chem. Soc.* **1978**, *100*, 3645-3646.
(119). Wutkowski, A.; Niefind, F.; Näther, C.; Bensch, W., A New Mixed-Valent High Nuclearity Polyoxovanadate Cluster Based on the $\{V_{18}O_{42}\}$ Archetype. *Z. anorg. allg. Chem.* **2011,** *637*, 2198-2204.
(120). Zang, H.-Y.; Chen, J.-J.; Long, D.-L.; Cronin, L.; Miras, H. N., Assembly of Thiometalate-Based $\{Mo_{16}\}$ and $\{Mo_{36}\}$ Composite Clusters Combining $[Mo_2O_2S_2]^{2+}$ Cations and Selenite Anions. *Adv. Mater.* **2013**, *25*, 6245-6249.

(121). Ohkoshi, S-I.; Nakagawa, K.; Tomono, K.; Imoto, K.; Tsunobuchi, Y.; Tokoro H., High Proton Conductivity in Prussian Blue Analogues and the Interference Effect by Magnetic Ordering. *J. Am. Chem. Soc*. **2010**, *132*, 6620–6621.
(122). Mulkapuri, S.; Kurapati, S. K.; Mukhopadhyay, S.; Das, S. K., A Fully Reduced $\{V^{IV}_{18}O_{42}\}$ Host and VO_4^{3-}, Cl^- as Guest Anions: Synthesis, Characterization and Proton Conductivity. *New J. Chem.* **2019**, *43*, 17670-17679.
(123). Yua, B.; Zoua, B.; Hu, C-W., Recent Applications of Polyoxometalates in CO_2 Capture and Transformation. *J. CO_2 Utilization* **2018**, *26*, 314–322.
(124). Khenkin, A. M.; Efremenko, I.; Weiner, L.; Martin, J. M. L.; Neumann, R., Photochemical Reduction of Carbon Dioxide Catalyzed by a RutheniumSubstituted Polyoxometalate. *Chem. Eur. J*. **2010**, *16*, 1356 – 1364.
(125). Garai, S.;. Haupt, E. T. K.; Bçgge, H.; Merca, A.; Mller, A., Picking up 30 CO_2 Molecules by a Porous Metal Oxide Capsule Based on the Same Number of Receptors. *Angew. Chem. Int. Ed.* **2012**, *51*, 10528 –10531.
(126). Liu, J.; Thallapally, P. K.; McGrail, B. P.; Brown, D. R.; Liu, J., Progress in Adsorption-Based CO_2 Capture by Metal–Organic Frameworks. *Chem. Soc. Rev.*, **2012**, *41*, 2308-2322.
(127). Sabouni, R.; Kazemian, H.; Rohani, S., Carbon Dioxide Capturing Technologies: A Review Focusing On Metal Organic Framework Materials (Mofs). *Environ. Sci. Pollut. Res.* **2014**, *21*, 5427–5449.
(128). Dutche, B.; Fan, M; Russell, A. G., Amine-Based CO_2 Capture Technology Development from the Beginning of **2013**—A Review. *ACS Appl. Mater. Interfaces* **2015**, *7*, 2137–2148.
(129). Mulkapuri, S.; Kurapati, S. K.; Das, S. K., Carbonate Encapsulation from Dissolved Atmospheric CO_2 into A Polyoxovanadate Capsule. *Dalton Trans.*, **2019**, *48*, 8773–8781.

CHAPTER 2

W^{VI}–OH Functionality on Polyoxometalates for Hydrogen Evolution Reaction

Overview:

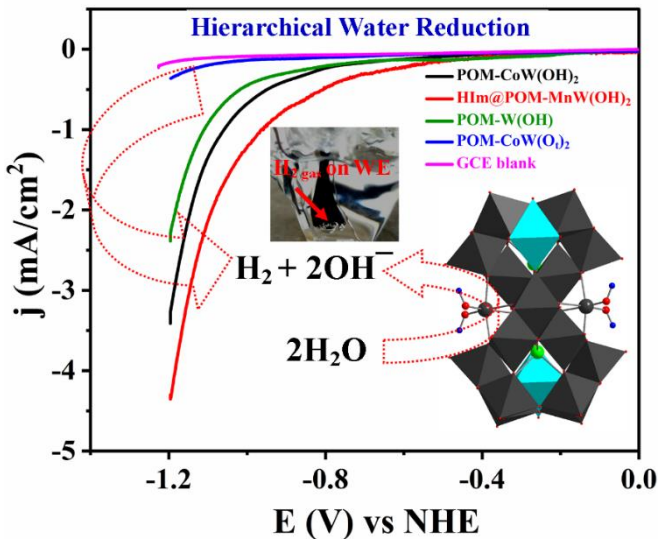

Grafting a W^{VI}–$(OH)_2$ functionality on a polyoxometalate (POM) surface makes the concerned POM compounds, $[\{Na_6(H_2O)_2\}][\{Co^{II}(H_2O)_3\}_2\{W^{VI}(OH)_2\}_2\{Bi^{III}W^{VI}_9O_{33})_2\}]\cdot 14H_2O$ (**POM-CoW(OH)$_2$**) and $[(W^{VI}(OH)_2)_2(Mn^{II}(H_2O)_3)_2(Na_4(H_2O)_{14}(BiW_9O_{33})_2](Him)_2\cdot 16H_2O$ (**HIm@POM-MnW(OH)$_2$**) prominent heterogeneous electrocatalysts for direct water reduction to molecular hydrogen ($2H_2O + 2e^- \rightarrow H_2 + 2OH^-$) at the neutral pH. We have identified that the W^{VI}–$(OH)_2$ functionality acts as the active site for hydrogen evolution reaction (HER) in the cathodic window. Controlled experiments exclude the chances of formation and participation of metal particles in this electrocatalytic water reduction. We could demonstrate that the electrocatalysts **(POM-CoW(OH)$_2$** and **HIm@POM-MnW(OH)$_2$)** are stable enough towards HER up to 1000 cycles. The concerned (HER) Faradaic efficiencies for **POM-CoW(OH)$_2$** and **HIm@POM-MnW(OH)$_2$** are 79% and 86% at pH 7.0, and 93 % and 96% at pH 3.0, respectively. The respective turn over frequencies (TOFs) are 0.318 s^{-1} and 0.402 s^{-1} (at pH 7.0) and 1.154 s^{-1} and 1.289 s^{-1} (at pH 3.0). The W–OH group, grafted on a POM surface, is known for a while; however, the evidence that this can be a well-defined functionality for water reduction (at the neutral pH) has never been demonstrated until this work.

2.1. Introduction

We are still dependent on fossil fuels as far as 'energy needed on the earth surface' is concerned. But the utmost truth is that fossil fuels are getting depleted. Scientists, worldwide, have realized that hydrogen energy can be considered as the next-generation energy source, because this not only has huge energy density (146 kJ g^{-1}), but also it is a carbon free energy carrier (usage of fossil fuels adds air pollution, thereby global warming!).[1-15] Among the three industrial hydrogen production routes (steam reforming of natural gas, coal gasification and water electrolysis), the **electrochemical water splitting**, a carbon zero hydrogen production process, has been thought to be the best one because it produces hydrogen in a sustainable manner using the most abundant substance on the earth surface, water as the raw material.[15] The overall electrochemical water splitting consists of the oxygen evolution reaction (OER) and hydrogen evolution reaction (HER) as the most crucial half-reactions.[1-22]

For example, in an acidic aqueous solution, the water oxidation to molecular oxygen (eqn. 1)

Acidic media

Anode: $2H^+ + O_2 + 4e^- \rightleftharpoons 2H_2O$ $E_0 = +1.23$ V (eqn. 1)

Cathode: $2H^+ + 2e^- \rightleftharpoons H_2$ $E_0 = 0.00$ V (eqn. 2)

followed by proton reduction to molecular hydrogen (eqn. 2) gives rise to overall water splitting reactions (eqns. 1 and 2). Besides these water splitting reactions (eqns. 1 and 2), there are two more important half-reactions (eqns. 3 and 4) giving rise to overall water splitting in neutral as well as in an alkaline medium.

Alkaline media

Anode: $O_2 + 2H_2O + 4e^- \rightleftharpoons 4OH^-$ $E_0 = +0.40$ V (eqn. 3)

Cathode: $4H_2O + 4e^- \rightleftharpoons 2H_2 + 4OH^-$ $E_0 = -0.83$ V (eqn. 4)

Regardless of the reaction media (acidic or alkaline), in which water splitting occurs, the overall thermodynamic potential of water splitting is 1.23 V at 25 ℃ and at 1 atm pressure. The water splitting reactions demonstrate that equations (2) and (4) are hydrogen evolution reactions (HERs), occurred at the cathode and reactions (1) and (3) are oxygen evolution reactions (OERs), taken place at the anode. The bottleneck problem of water oxidation at the anode (eqn.1) is high thermodynamic potential and large kinetic barrier. The resulting H^+ can be converted into molecular hydrogen at the cathode (eqn.2), but in the presence of an expensive catalyst (e.g., platinum metal). Therefore, a lot of efforts have been made in the development of noble metal-free electrocatalysts for the hydrogen evolution reaction (HER). Zou and Zhang[15] have written recently a landmark review article mentioning several noble-metal-free

metal electrocatalysts, that work in a heterogeneous manner, e.g., metal sulphides,[23-29] metal selenides,[30,31] metal carbides,[32-35] metal nitrides,[36-42] metal phosphides,[43-46] heteroatom-doped nanocarbons,[47-49] *etc*.[12,15,23-55] The reported catalytic studies on HER are mainly performed in acidic conditions because, in an acidic condition,[10-12,22,54,55] it follows a simple reaction pathway: $2H^+ + 2e^- \rightleftharpoons H_2$, for which the mechanism [the Volmer step, $H^+ + e^- \rightarrow H_{ads}$ (adsorbed hydrogen atom on the electrode surface), followed by the Tafel step ($2H_{ads} \rightarrow H_2$) or the Heyrovsky step ($H_{ads} + H^+ + e^- \rightarrow H_2$) or both result in hydrogen evolution] is well established. On the other hand, the HER mechanism in alkaline or in neutral media (eqn. 4: $2H_2O + 2e^- \rightleftharpoons H_2 + 2OH^-$) is still unclear,[15,56-59] despite the fact that, in the photoelectrochemical water splitting technology for hydrogen production,[50,60] the electrocatalysts for OER (eqn. 3: $O_2 + 2H_2O + 4e^- \rightleftharpoons 4OH^-$) work very well in the basic or neutral media.[61-66] Thus the development of HER catalysts, suitable for alkaline as well as neutral solutions (eqn. 4: $2H_2O + 2e^- \rightleftharpoons H_2 + 2OH^-$) is vital. Catalysing this reaction, because of its mechanistic ambiguity, has not much been explored as far as neutral pH is concerned. This half-reaction (eqn. 4: $2H_2O + 2e^- \rightleftharpoons H_2 + 2OH^-$) has drawn our immense attention and interest because it represents the direct hydrogen production from neutral water.[3,5,67-72] In this direction, we were very keen to develop polyoxometalate (POM) based catalysts, that can be coupled with direct water reduction half reaction (eqn. 4). This is because, POMs, not only show enormous applications in diverse areas including medicinal science, magnetism, photo-/electro-chemical water splitting, *etc*. but also are earth-abundant metal-oxides (inexpensive materials) and most of them are able to hold more number of electrons reversibly, exhibiting rich redox chemistry with structural integrity.[10-12,22,73-95]

We have synthesized and structurally characterized a polyoxometalate (POM)-based compound $[\{Na_6(H_2O)_2\}][\{Co^{II}(H_2O)_3\}_2\{W^{VI}(OH)_2\}_2\{Bi^{III}W^{VI}_9O_{33})_2\}]\cdot 14H_2O$ (**POM-CoW(OH)$_2$**) having $\{W^{VI}(OH)_2\}$ functionality ([POM–$\{W^{VI}(OH)_2\}_2$]), which responds to this half-reaction (eqn. 4) and produces H_2 molecule electrochemically as shown below (eqns. 4,5 and 6)).

$$2H_2O + 2e^- \rightarrow H_2 + 2OH^- \qquad \text{(eqn. 4)}$$

$$[POM–\{W^{VI}(OH)_2\}_2] + 2e^- \rightarrow [POM–\{W^{V}(OH)_2\}_2] \qquad \text{(eqn. 5)}$$

$$[POM–\{W^{V}(OH)_2\}_2]+2H_2O \rightarrow H_2(g)+2OH^-+[POM–\{W^{VI}(OH)_2\}_2] \qquad \text{(eqn. 6)}$$

We could identify that $\{W^{VI}(OH)_2\}$ moiety on the POM cluster surface (POM-CoW(OH)$_2$) is the active site for this electrochemical water reduction. We then dug into the literature of POM chemistry[96-104] to learn the availability of any other report of the POM compound that is associated with $\{W^{VI}(OH)_2\}$ moiety. We indeed found out two compounds $[(W^{VI}(OH)_2)_2(Mn^{II}(H_2O)_3)_2(Na_4(H_2O)_{14}(BiW_9O_{33})_2](Him)_2\cdot 16H_2O$ (**HIm@POM-MnW(OH)$_2$**) and $(Him)_2[Bi_2W_{20}O_{66}(OH)_4Co_2(H_2O)_6Na_4(H_2O)_{14}]\cdot 17H_2O$ (**BWCN**), each

having two $\{W^{VI}(OH)_2\}$ functionality, reported by Zhou–Liu–Yang groups and Zhou–Liu groups respectively, besides the classic Krebs compound $Na_{12}[(WO_2(OH))_2(WO_2)_2(BiW_9O_{33})_2]\cdot 44H_2O$ having two W-OH moieties.[96,98] **HIm@POM-MnW(OH)$_2$** can act as an antitumor agent in prevention and treatment of gastric adenocarcinoma.[99] And **BWCN** can inhibit the cell viability of human cancer cells.[100] We found that, both these compounds having $\{W^{VI}(OH)_2\}$ functionality, as expected, respond to the half-reaction of water reduction (neutral or alkaline pH, eqn. 4) and generates molecular hydrogen. The main goal of this work is to establish a 'new insight' of polyoxometalate (POM) chemistry that a $\{W^{VI}–OH\}$ functionality on a POM cluster surface can be an well-defined functional site for water reduction. We have described a detailed account of electrocatalytic water reduction to molecular hydrogen at the neutral pH value as well as at an acidic pH (=3), catalyzed by the polyoxometalate (POM) compounds $[\{Na_6(H_2O)_2\}][\{Co^{II}(H_2O)_3\}_2\{W^{VI}(OH)_2\}_2\{Bi^{III}W^{VI}_9O_{33})_2\}]\cdot 14H_2O$ (**POM-CoW(OH)$_2$**) and $[(W^{VI}(OH)_2)_2(Mn^{II}(H_2O)_3)_2(Na_4(H_2O)_{14}(BiW_9O_{33})_2](Him)_2\cdot 16H_2O$ (**HIm@POM-MnW(OH)$_2$**). Since the cluster (anionic) part of **BWCN** and that of our compound **POM-CoW(OH)$_2$** are essentially identical, we have not explored further the electrocatalytic properties of **BWCN** in this work.

2.2. Experimental section

2.2.1. Materials and methods

All the experiments were conducted with deionized water under ambient atmospheric conditions and chemicals used as received of A.R grade without any further purification. The $[Na_6(H_2O)_2][\{Co(H_2O)_3\}_2\{W(OH)_2\}_2\{BiW_9O_{33}\}_2]\cdot 14H_2O$ (**POM-CoW(OH)$_2$**) was isolated in a one-pot wet synthesis. And the $[(W(OH)_2)_2(Mn(H_2O)_3)_2(Na_3(H_2O)_{14})(BiW_9O_{33})_2](Him)_2\cdot 16H_2O$ (HIm = protonated imidazole) (**HIm@POM-MnW(OH)$_2$**), $Na_{12}[Bi_2W_{22}O_{74}(OH)_2]\cdot 44H_2O$ (**POM-W(OH)**), $Na_{10}[Bi_2W_{20}Co_2O_{70}(H_2O)_6]\cdot 41H_2O$ (**POM-CoW(O$_t$)$_2$**) were prepared according to the literature.[98,99]

2.2.1.1. Synthesis of $[Na_6(H_2O)_2][\{Co(H_2O)_3\}_2\{W(OH)_2\}_2\{BiW_9O_{33}\}_2]\cdot 14H_2O$ (POM-CoW(OH)$_2$)

0.5 mL of 6 M nitric acid (HNO_3) was added dropwise to the aqueous solution of sodium tungstate (9 mmol (3.0 g) of $Na_2WO_4\cdot 2H_2O$ present in 25 mL of water) and subjected to heat at 90 °C for 15 min with continuous stirring. Then, the reaction mixture was taken from the hot plate and allowed to cool to the room temperature and then filtered off to remove the trace of insoluble material. The cobalt nitrate solution (2 mmol (0.58 g) of $Co(NO_3)_2\cdot 6H_2O$ dissolved in a 2 mL of water) was added dropwise to the above colourless reaction mixture at room temperature under stirring, and immediately it turned to be a purple colour reaction mixture. Successively, a bismuth nitrate solution (1 mmol (0.48 g) of $Bi(NO_3)_3\cdot 5H_2O$ present in 1 mL of 6 M nitric acid) was added dropwise with vigorous stirring. After that, the pH of the reaction

mixture was adjusted to 6.82, using a 15% aqueous ammonia solution. Then again, the reaction mixture was subjected to heat at 90 °C for 1 hour with continuous stirring, while stirring the Erlenmeyer flask mouth was closed with a watch glass. The reaction mixture was offered a cobalt blue colour solution along with purple colour slurry. The hot reaction mixture was filtered off twice. Again, after four hours, the purple colour slurry formed in the filtrate was removed by filtration and the clear filtrate left for crystallization at room temperature. The block type pink colour crystals were formed after ten days. The crystals were isolated by washing twice with a minimal amount of ice-cold water and kept for drying at room temperature. Yield: 1.65 g (61.84 % based on tungsten). Elemental analysis: (%) calc. Bi: 7.12, Co: 2.01, Na: 2.35, W: 62.63 and H_2O: 6.74 and (%) Found. Bi: 7.25, Co: 1.96, Na: 2.17, W: 62.89 and H_2O: 6.59 (TGA). FT-IR (4000-400 cm^{-1}): 3730, 3314, 1625, 941, 874, 831, 782, 730, 640, 579, 475.

2.2.2. Physical measurements

Single-crystal X-ray diffraction data was collected on Bruker D8 Quest CCD diffractometer with Mo–Kα (λ = 0.71073 Å) source. Powder X-ray diffraction (PXRD) data were recorded on Bruker D8-Advance diffractometer using graphite mono chromated Cu Kα1 (1.5406 Å) and Kα2 (1.54439 Å) radiation. Elemental analyses performed on ICP-OES Varian 720ES. Bruker Tensor II equipped with Platinum ATR (Attenuated Total Reflectance) accessory used to collect IR spectra. Thermogravimetric analyses (TGA) carried out on Perkin Elmer – STA 6000 analyzer. Raman spectra obtained with the help of Wi-Tec alpha 300 AR laser confocal optical microscope (T-LCM) facility equipped with a Peltier cooled CCD detector using 633 nm Argon ion laser. Electronic absorption spectra were obtained on the UV-2600 Shimadzu UV−Visible spectrophotometer at room temperature. Field-Emission Scanning Electron Microscopy (FE-SEM) was carried out with a Carl Zeiss model Ultra 55 microscope equipped with Oxford Instruments X-MaxN SDD (50 mm^2) system functioned with INCA analysis software. All the electrochemical studies performed on Zahner Zanium electrochemical workstation operated with Thales software.

2.2.2.1. X-ray crystallography

A suitable single-crystal of **POM-CoW(OH)$_2$** was selected from the mother liquor and mounted on glass fibre-tip, using Araldite resin mask, for X-ray diffraction data collection (at 293 K). The Bruker D8 Quest CCD diffractometer is equipped with a Mo–Kα (λ = 0.71073 Å) graphite monochromatic X-ray beam source used to determine the structure of **POM-CoW(OH)$_2$**. A 40 mm crystal-to-detector distance was maintained during the data collection. The ω scans were recorded with a width of 0.3°. Data reduction was performed by SAINT PLUS,[105] and empirical absorption corrections were done using equivalent reflections performed by the SADABS.[106] Structure solutions were carried out using SHELXT-2015,[107] and full-matrix least-squares refinement was completed with SHELXL-2015.[108] All the non-hydrogen atoms refined anisotropically. Only the O_1 (oxygen) has adopted the disorder of an atomic displacement

parameter (ADP) due to the μ_4–oxo coordination mode with the heavy metal ions such as bismuth and tungsten. Attempts were made successful for the hydrogen atom location on terminal oxo-groups of the tungsten {-$W(OH)_2$} centers through the Fourier electron density map. The crystallographic details such as structure refinement parameters and bond lengths of the **POM-CoW(OH)$_2$** was shortlisted in the **Table 2.1** and *Appendix 2(i)*. The **CSD–2033177** contains the supplementary crystallographic data for **POM-CoW(OH)$_2$**. The crystal data can be obtained free of charge via http://www.ccdc.cam.ac.uk/conts/retrieving.html, or from the Cambridge Crystallographic Data Centre, 12 Union Road, Cambridge CB2 1EZ, UK; fax: (+44) 1223-336-033; or e-mail: deposit@ccdc.cam.ac.uk.

Table 2.1 shows a single crystal data structure refinement parameters for **POM-Co{W(OH)}$_2$**.

Parameter	**POM-Co{W(OH)}$_2$**
Empirical formula	$H_{48}Bi_2Co_2Na_6O_{92}W_{20}$
Formula weight	5858.79
T(K)/ λ (Å)	293(2) K/0.71073
Crystal system	Monoclinic
Space group	*C2/m*
a Å	17.7208(7)
b Å	18.7141(7)
c Å	14.1533(6)
α (°)	90
β (°)	112.74
γ (°)	90
Volume (Å^3)	4328(3)
Z	2
P calcd (Mg m^{-3})	4.438
μ (mm^{-1}), *F*(000)	30.712, 4978
Goodness-of-fit on F^2	1.242
R_1/wR_2 [$I > 2\sigma(I)$]	0.0461/0.0995
R_1/wR_2 (all data)	0.0472/0.1000
Largest diff. peak/hole (e Å^{-3})	3.391/-3.421

2.2.2.2. Electrochemical methods

All the electrochemical experiments were performed using a home-made three-electrode electrochemical cell employing the **POM-CoW(OH)$_2$**, **HIm@POM-MnW(OH)$_2$** modified glassy carbon as working (WE), a home-made Ag/AgCl (3M) as a reference (RE), and Pt wire as counter (CE) electrodes. The preparation of **POM-CoW(OH)$_2$**, **HIm@POM-MnW(OH)$_2$** modified electrode carried out as 4 mg of sample and 1 mg of acetylene carbon black was taken into a 1 mL of the ethanol-water mixture (3:2 ratio). And a 20 µL of 5 wt% aqueous Nafion binder was added and subjected to the ultra-sonication at room temperature for 30 min to make

it as a homogenous suspension. 10 µL of this homogeneous ink was coated on the glassy carbon working electrode (GCWE) having a 3 mm diameter (0.0706 cm^2 geometrical area), resulting in the ~40 µg of the sample on the working electrode. Separately, the diluted Nafion solution was prepared by adding the 40 µL (5 wt %) Nafion solution into a 60 µL of ethanol (in the ratio of 4:6 Nafion-ethanol mixture) and a drop of it was coated over the sample loaded electrode. The same amount of sample loading was maintained for all the electrochemical experiments unless otherwise notified. The drop-cast sample was dried under the IR-lamp (temp~70 ℃), and before using it, the sample coated electrode left at room temperature (for 5 min) to get the ambient atmosphere condition. All the electrochemical experiments were run under the nitrogen atmosphere. The experimentally observed potentials were converted into the NHE (Normal Hydrogen Electrode) scale following the relation $E_{(NHE)} = E_{(Ag/AgCl)} + 0.204$ V, when the Ag/AgCl electrode was used as a standard reference electrode. The cyclic voltammogram (CV) scan was initiated at the open circuit potential (OCP) and first scanned to the cathodic side. All the electrochemical studies were performed in a 0.1 M potassium phosphate buffer (KPi) of neutral pH as well as in acidic pH 3 (acidic electrolyte was prepared by adjusting the pH 7 of 0.1 M KPi using 0.1 M H_3PO_4 solution) used as a supporting electrolyte. The Fluorinated Tin Oxide (FTO) and a large surface area Pt net were used as working and counter electrodes in chronoamperometry/chronopotentiometry bulk electrolysis. The preparation of the FTO working electrode for bulk electrolysis was carried out as 1 mg/cm^2 area catalyst loading. Possible *in-situ* generated species or catalyst degraded metal (M) particles were prepared following the reported procedure (but here we were carried out in our interested cathodic window instead of the anodic window).[62] The generation of metal particles on the working electrode was done in a three-electrode cell (using 1 mM solution of respective metal salt present in 0.1 M potassium phosphate buffer (neutral pH) and the FTO was the working electrode (WE). After the deposition of metal particles on the FTO-WE (M-FTO) at a cathodic potential -1.1 V (vs NHE) for 30 min. The electrode was washed thoroughly with flowing water and dried under IR-lamp before performing the following experiments such as cyclic voltammogram and FE-SEM analysis. The bulk electrolysis of water reduction reaction was carried out to understand the changes in electrolyte pH during the electrolysis. For this, we have employed a neutral pH (0.1 M) KCl solution used as the supporting electrolyte instead of neutral pH (0.1 M) phosphate buffer, to eliminate the buffer action on bulk electrolysis. The electrochemical impedance spectroscopy was done under similar experimental conditions, as mentioned above for CV experiments. The Nyquist plots of impedance spectra were obtained by the employment of 1 Hz to 1 MHz frequency using -0.062 V of sinusoidal potential in both the mediums. And the internal cell resistance was manually calibrated. The Tafel data was collected in a galvanostatic mode under steady-state mass flow by stirring the electrolyte solution at 480 rpm throughout the experiment. Differential Pulsed Voltammogram (DPV) for **POM-CoW(OH)$_2$**, and **HIm@POM-MnW(OH)$_2$** was performed in neutral pH (0.1 M) KPi solution, 15 mV pulse for 10 ms time and 10 mV step height for 100 ms step width used. The integration time was 10 ms.

2.3. Results and Discussion

2.3.1. Detailed discussion on synthesis

The cobalt incorporated anti-Lipscomb (Krebs type) compound $[\{Na_6(H_2O)_2\}][\{Co^{II}(H_2O)_3\}_2\{W^{VI}(OH)_2\}_2\{Bi^{III}W^{VI}_9O_{33})_2\}]\cdot 14H_2O$ (**POM-CoW(OH)$_2$**) has been obtained in a one-pot aqueous wet synthesis involving $Na_2WO_4\cdot 2H_2O$, $Bi(NO_3)_3\cdot 5H_2O$, HNO_3 and $Co(NO_3)_2\cdot 6H_2O$ (at 90 °C for 1 h; pH= 6.82, adjusted with 15% aqueous ammonia solution). The heterpolytungstate, **POM-CoW(OH)$_2$** is isolated as water-insoluble pink coloured crystals. The molecular formula of **POM-CoW(OH)$_2$** is derived from the single-crystal X-ray structure analysis, elemental as well as thermogravimetric analyses and formulated as $[\{Na_6(H_2O)_2\}][\{Co^{II}(H_2O)_3\}_2\{W^{VI}(OH)_2\}_2\{Bi^{III}W^{VI}_9O_{33})_2\}]\cdot 14H_2O$. The manganese analogue, compound $[(W^{VI}(OH)_2)_2(Mn^{II}(H_2O)_3)_2(Na_4(H_2O)_{14}(BiW_9O_{33})_2](Him)_2\cdot 16H_2O$ (**HIm@POM- MnW(OH)$_2$**) has been synthesized according to a similar but reported procedure.[99] These two compounds have a common anionic component except the fact that Co(II) and Mn(II) ions are present in compounds **POM-CoW(OH)$_2$** and **HIm@POM-MnW(OH)$_2$**, respectively. The discussion of this common cluster anion, $[\{M^{II}(H_2O)_3\}_2\{W^{VI}(OH)_2\}_2\{Bi^{III}W^{VI}_9O_{33})_2\}]^{6-}$ (M^{II} = Co and Mn) in compounds **POM-CoW(OH)$_2$** and **HIm@POM-MnW(OH)$_2$**, can not appropriately be justified, unless, we talk about following two systems of heteropolyanions: $[Bi_2W_{22}O_{74}(OH)_2]^{12-}$ and $[X_2W_{20}M_2O_{70}(H_2O)_6]^{(14-2n)-}$ (X = Sb^{3+}, Bi^{3+}; M^{n+} = Fe^{3+}, Co^{2+}, Zn^{2+}), reported by Krebs and co-workers.[96,98] In both of these systems, two $\{\beta\text{-}XW_9O_{33}\}^{9-}$ tri-lacunary Keggin units are connected by two $\{WO_2\}^{2+}$ groups resulting in the hypothetical species, $[X_2W_{20}O_{70}]^{14-}$. When this bis-decatungsto ion is capped by two *facial* $\{WO_2(OH)\}^{+}$ units, it results in the formation of $[(WO_2(OH))_2(WO_2)_2(BiW_9O_{33})_2]^{12-} \equiv [Bi_2W_{22}O_{74}(OH)_2]^{12-}$, isolated as $Na_{12}[(WO_2(OH))_2(WO_2)_2(BiW_9O_{33})_2]\cdot 44H_2O$. And when the hypothetical anion $[X_2W_{20}O_{70}]^{14-}$ adds two $M^{n+}(H_2O)_3$ groups (M^{n+} = Fe^{3+}, Co^{2+}, Zn^{2+}), transition-metal-substituted heteropolyanion clusters $[X_2W_{20}M_2O_{70}(H_2O)_6]^{(14-2n)-}$ arise. The heteropolyanion cluster, in the present work, $[\{M^{II}(H_2O)_3\}_2\{W^{VI}(OH)_2\}_2\{Bi^{III}W^{VI}_9O_{33})_2\}]^{6-}$ is neither of these two systems, but can be argued as a hybrid one of these two systems, as described below. In the present study, two identical tri-lacunary bowls, $\{BiW_9O_{33}\}^{9-}$ are joined together by two units of $\{W^{VI}(OH)_2\}^{4+}$ moieties resulting in a hypothetical entity of bis-dodecatungstate, $[\{W(OH)_2\}_2(BiW_9O_{33})_2]^{10-}$. This is further coordinated to two units of $\{M^{II}(H_2O)_3\}^{2+}$ (M = Co, Mn) to result in M^{II}-incorporated heteropoly cluster anion $[\{M^{II}(H_2O)_3\}_2\{W(OH)_2\}_2(BiW_9O_{33})_2]^{6-}$ (M = Co, Mn) of the title compounds, **POM-CoW(OH)$_2$** and **HIm@POM-MnW(OH)$_2$**. Thus, the present heteropoly tungstate anion, $[\{M^{II}(H_2O)_3\}_2\{W(OH)_2\}_2(BiW_9O_{33})_2]^{6-}$ (M = Co, Mn), having two $W^{VI}(OH)_2$ moieties (instead two $W^{VI}(OH)$ moieties, found in the system $[Bi_2W_{22}O_{74}(OH)_2]^{12-}$) and two $\{M^{II}(H_2O)_3\}$ entities, found in $[Bi_2W_{20}M_2O_{70}(H_2O)_6]^{(14-2n)-}$ (M^{n+} = Fe^{3+}, Co^{2+}, Zn^{2+}), can be described as a kind of mixed-system of $[Bi_2W_{22}O_{74}(OH)_2]^{12-}$ and $[Bi_2W_{20}M_2O_{70}(H_2O)_6]^{(14-2n)-}$.[96,98] The presence of $-W^{VI}(OH)$ group in $[Bi_2W_{22}O_{74}(OH)_2]^{12-}$ and

$–W^{VI}(OH)_2$ functionality in $[\{M^{II}(H_2O)_3\}_2\{W(OH)_2\}_2(BiW_9O_{33})_2]^{6–}$ (M = Co, Mn) can be understood from the synthetic point of view: the relevant former compound $Na_{12}[(WO_2(OH))_2(WO_2)_2(BiW_9O_{33})_2]\cdot 44H_2O$ was isolated from an aqueous synthesis, where acetate buffer was used (pH cannot me more than 5.0); on the other hand, in case of compounds **POM-CoW(OH)$_2$** and **HIm@POM-MnW(OH)$_2$** containing the common heteropolytungstate anion $[\{M^{II}(H_2O)_3\}_2\{W(OH)_2\}_2(BiW_9O_{33})_2]^{6–}$, the pH of the aqueous synthesis mixture was maintained to 6.8 (almost the neutral pH). There are a number of POM compounds, that have bridging hydroxyl (OH) groups;[109,110] but there are only a few POM compounds having terminal M–OH, as found in the compound $Na_{12}[(WO_2(OH))_2\ (WO_2)_2(BiW_9O_{33})_2]\cdot 44H_2O$.[96,98] And there are only two reported structurally characterized POM compounds, $[(W^{VI}(OH)_2)_2(Mn^{II}(H_2O)_3)_2(Na_4(H_2O)_{14}(BiW_9O_{33})_2](Him)_2\cdot 16H_2O$ (**HIm@POM-MnW(OH)$_2$**)[99] and $(Him)_2[Bi_2W_{20}O_{66}(OH)_4Co_2(H_2O)_6Na_4(H_2O)_{14}]\cdot 17H_2O$ (**BWCN**),[100] to our knowledge, that has two terminal hydroxyl (OH) groups, i.e., $–W(OH)_2$ moiety. Compound $[\{Na_6(H_2O)_2\}][\{Co^{II}(H_2O)_3\}_2\{W^{VI}(OH)_2\}_2\{Bi^{III}W^{VI}_9O_{33})_2\}]\cdot 14H_2O$ **POM-CoW(OH)$_2$**) is the third example of structurally characterized POM compound (present work) having $–W(OH)_2$ functionality. This article has been coined to establish the importance of $\{W^{VI}(OH)_2\}$ moiety on the POM cluster surface, that can act as the catalyst for direct water reduction to molecular hydrogen.

2.3.2. Physical characterizations

2.3.2.1. Single-crystal X-ray crystallographic analysis

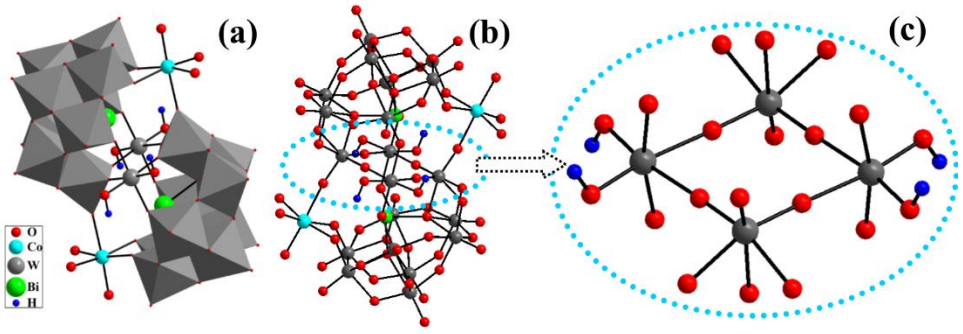

Figure 2.1. Single-crystal X-ray structure: (**a** and **b**) polyhedral and ball-stick representation, respectively, of the molecular structure of the **POM-CoW(OH)$_2$**; (**c**) magnified view of $–W^{VI}(OH)_2$ core of **POM-CoW(OH)$_2$** (W, blue; O, red; H, blue).

Single-crystal X-ray diffraction (SCXRD) analysis reveals that the **POM-CoW(OH)$_2$** crystallizes in a monoclinic *C2/m* space group, but the compound **HIm@POM-MnW(OH)$_2$** crystallized in triclinic *P-1* space group.[99] The presence of protonated imidazole molecule in the crystal structure of **HIm@POM-MnW(OH)$_2$**, probably, makes this difference. The six negative charges of the common heteropoly tungstate anion, $[\{M^{II}(H_2O)_3\}_2\{W(OH)_2\}_2(BiW_9O_{33})_2]^{6–}$, is counter-balanced by six sodium cations in the case

of **POM-CoW(OH)$_2$**, whereas, in the case of **HIm@POM-MnW(OH)$_2$**, it is counter-balanced by four sodium cations and two imidazolium cations.[99]

The molecular structure of the cobalt incorporated cluster anion $[\{Co(H_2O)_3\}_2\{W(OH)_2\}_2(BiW_9O_{33})_2]^{6-}$ in the crystal structure of **POM-CoW(OH)$_2$** is shown in **Figure 2.1**(**a** and **b**). The Bi–O and O–W bond distances in Bi–O–W and W–O–W fragments within this POM cluster unit fall in the range of 2.1 to 2.2 Å, that are consistent with those of reported analogues.[96-100] The complete details of bond distances and bond angles are given in the crystallographic **Table 2.1** and *Appendix 2(i)*. It is important to note that, two units of the tungsten $\{W^{VI}(OH)_2\}$ centers, that are symmetrically related and present at the sandwiched position, are geometrically/environmentally different from the other framework tungsten centers as shown in **Figures 2.1**(**b** and **c**). In each of the $\{W^{VI}(OH)_2\}$ moieties, the tungsten(VI) center is coordinated two hydroxyl groups, that are, in turn, symmetrically related. Thus, there are four W^{VI}–OH groups with an identical W–OH bond distance of 1.839 Å. This W^{VI}–OH functionality plays the title role of this work. The average bond distance of the terminal W=O is 1.71 Å (in the range of 1.70 to 1.72 Å); thus the W^{VI}–OH bond distance in the $\{W^{VI}(OH)_2\}$ moieties is 0.129 Å longer than that of terminal W^{VI}=O groups. This W–OH bond distance of 1.839 Å is consistent with W–OH bond distance of **HIm@POM-MnW(OH)$_2$**,[99] **BWCN**[100] and $Na_{12}[(WO_2(OH))_2(WO_2)_2(BiW_9O_{33})_2] \cdot 44H_2O$.[96,98] The 'H' atom of this W^{VI}–OH functionality is located from differential furrier map during the pertinent structure refinement method. We also performed bond valence sum (BVS) calculations of this hydroxyl oxygen (–OH) in all these systems (*Appendix 2(ii)*). The bond valence sum values of the hydroxyl oxygen (–OH)

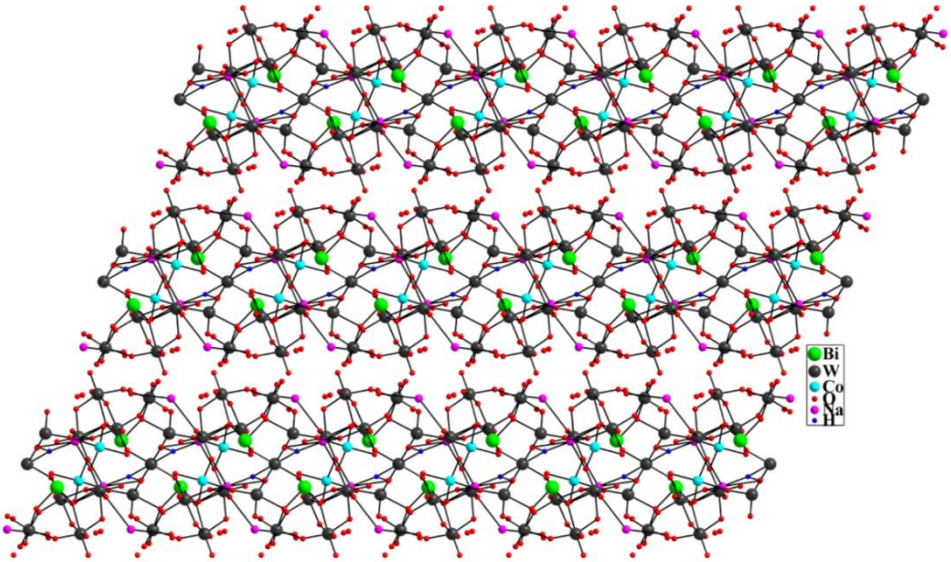

Figure 2.2. Single-crystal X-ray structure of **POM-CoW(OH)$_2$**: **POM-CoW(OH)$_2$** clusters are interconnected through POM-$\{Na(H_2O)\}$-POM linkage and formed as a 2D network.

atoms in **POM-CoW(OH)$_2$**, **BWCN** and **HIm@POM-MnW(OH)$_2$**, respectively are 1.29,1.26, 1.30. This ensures the monoprotonation on this oxygen. There are sixteen lattice water molecules per formula unit of **POM-CoW(OH)$_2$**; out of these sixteen water molecules, two water molecules are coordinated to two sodium cations out of six sodium cations per formula unit. A two-dimensional coordination polymer is observed in the crystal structure of **POM-CoW(OH)$_2$**, formation of which involves the coordinations of bridging type oxygen atoms of the cluster anion and cobalt-coordinated water oxygen atoms toward the sodium cation (**Figure 2.2**). On the other hand, a chain-like coordination polymer was reported to be formed in the crystal structure of **HIm@POM-MnW(OH)$_2$** involving terminal oxygen atoms of the cluster anion and water coordinated sodium cation.[99] The strong coordinate covalent interactions between bridging and terminal oxygen atoms of the POM cluster anion and sodium cation result in the formation of a two-dimensional coordination polymer, thereby making the compound **POM-CoW(OH)$_2$** a water insoluble material (thereby a heterogeneous HER catayst).

2.3.2.2. FT-IR spectra

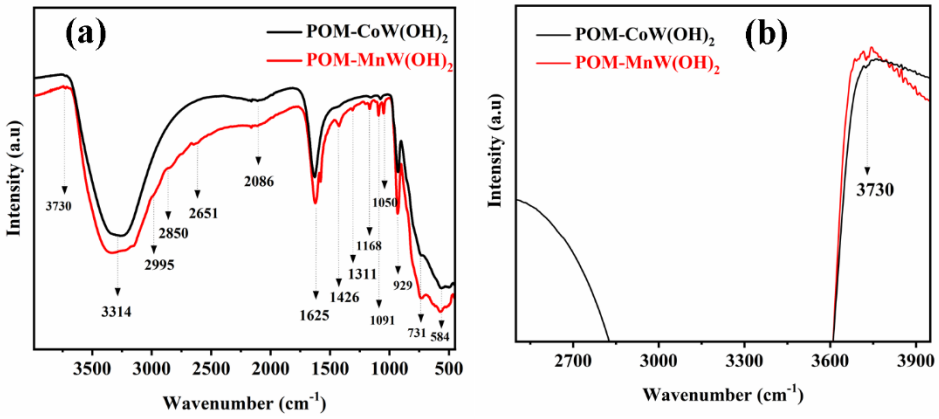

Figure 2.3. FT-IR spectra: (**a**) FT-IR spectra of the **POM-CoW(OH)$_2$** and **HIm@POM-MnW(OH)$_2$**; (**b**) magnified view of FTIR spectra.

The IR spectra of **POM-CoW(OH)$_2$** and **HIm@POM-MnW(OH)$_2$**, as expected, have shown POM characteristic IR peaks in the region of 950 to 450 cm^{-1} for W=O, W–O–W, and Bi–O–W stretching and bending vibrations for **POM-CoW(OH)$_2$** and for **HIm@POM-MnW(OH)$_2$** (**Figure 2.3**(**a** and **b**)). The distinctive small IR features, visible in the region of 1400 and 1100 cm^{-1} in the IR spectrum of **HIm@POM-MnW(OH)$_2$** but not visible in the IR spectrum of **POM-CoW(OH)$_2$**, are due to the presence of imidazolinium cation in **HIm@POM-MnW(OH)$_2$**. The strong IR bands at 1625 cm^{-1} for both compounds are assigned to the lattice water molecules' bending mode. The broad band around 3300 cm^{-1} in both implies the O–H stretching of lattice water. However, in **HIm@POM-MnW(OH)$_2$** two weak bands at 2995 and

2850 cm^{-1} have resembled the N–H, C–H vibrations of the imidazole. The presence of $W(OH)_2$ functionality in these two compounds can also be supported by the appearance of weak feature at around 3730 cm^{-1} in the IR spectra of **POM-CoW(OH)$_2$** and **HIm@POM-MnW(OH)$_2$** (**Figure 2.3**(**b**)) — transition metal-hydroxyl (M–OH) group is known to appear in this region of IR spectrum.[111,112]

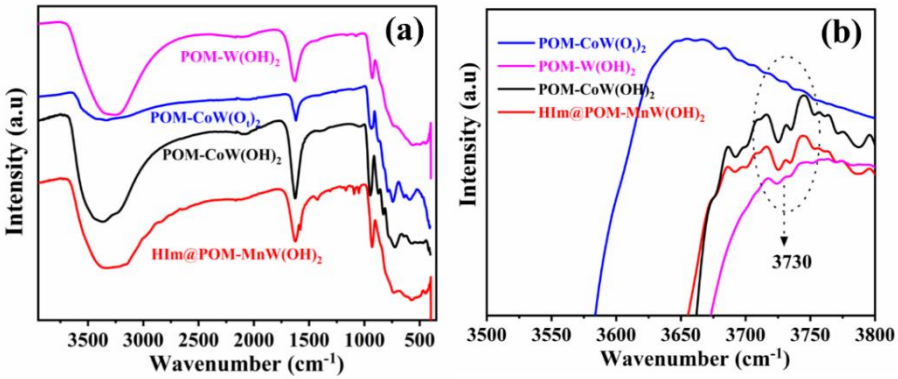

Figure 2.4. FT-IR spectra: (**a**) comparative FT-IR spectra of **POM-CoW(OH)$_2$**, **HIm@POM-MnW(OH)$_2$**, **POM-W(OH)**, and **POM-CoW(O$_t$)$_2$**; (**b**) an enlarged view FT-IR spectra for all the compounds.

In order to validate the appearance of this weak feature at around 3730 cm^{-1} in the IR spectra due to the presence of W–OH group, we synthesized two more known compounds, (i) $Na_{12}[(WO_2(OH))_2(WO_2)_2(BiW_9O_{33})_2]\cdot 44H_2O$ (**POM-W(OH)**) having two W–OH groups and (ii) $Na_{10}[Bi_2W_{20}Co_2O_{70}(H_2O)_6]\cdot 41H_2O$ (**POM-CoW(O$_t$)$_2$**), similar sandwich compound but without W–OH group and performed their IR spectral studies. As expected, compound $Na_{12}[(WO_2(OH))_2(WO_2)_2(BiW_9O_{33})_2]\cdot 44H_2O$ shows the weak IR band around 3730 cm^{-1} in its IR spectrum and compound $Na_{10}[Bi_2W_{20}Co_2O_{70}(H_2O)_6]\cdot 41H_2O$ does not show any IR peak around 3730 cm^{-1} (**Figure 2.4**(**a** and **b**)).

2.3.2.3. Raman spectra

The Raman spectra of **POM-CoW(OH)$_2$** and **HIm@POM-MnW(OH)$_2$** showing a strong peak in the region of 883-950 cm^{-1} for terminal W=O bonds are given in **Figure 2.5**. These Raman spectra are compared with those of two related sandwich compounds, $Na_{12}[(WO_2(OH))_2(WO_2)_2(BiW_9O_{33})_2]\cdot 44H_2O$ **POM-W(OH)** and $Na_{10}[Bi_2W_{20}Co_2O_{70}(H_2O)_6]\cdot 41H_2O$ **POM-CoW(O$_t$)$_2$**. The weak bands in the region of 880–280 cm^{-1} represent to the Raman active modes of POM framework (μ_2–O/μ_4–O oxo-groups). In the case of **HIm@POM-MnW(OH)$_2$**, two weak bands at 1212 and 1430 cm^{-1} are assigned to the Raman active modes of imidazole. At the same time, no response is present in the remaining compounds. Other than these two-week bands, all the compounds have consistent Raman spectral profiles.

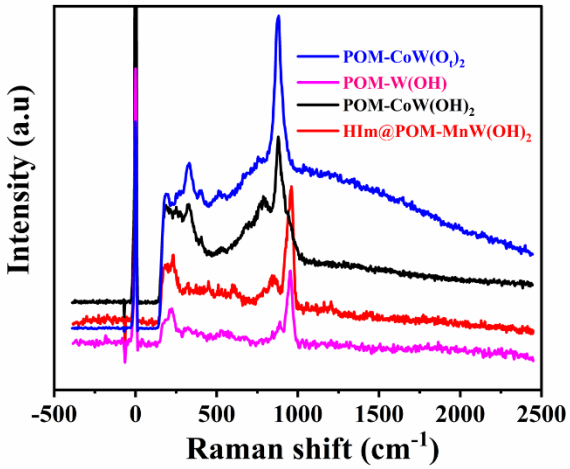

Figure 2.5. Raman spectra of **POM-CoW(OH)$_2$**, **HIm@POM-MnW(OH)$_2$**, **POM-W(OH)**, and **POM-CoW(O$_t$)$_2$** compounds.

2.3.2.4. Electronic spectra

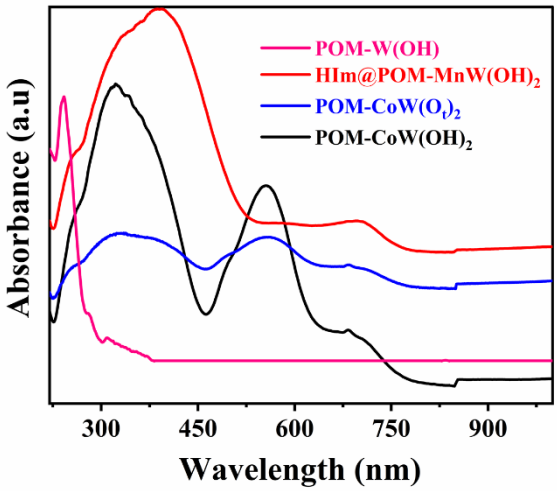

Figure 2.6. Electronic spectra of **POM-CoW(OH)$_2$**, **HIm@POM-MnW(OH)$_2$**, **POM-W(OH)**, and **POM-CoW(O$_t$)$_2$** compounds.

The presence of 3*d* metal ions, such as, Co^{2+}, Mn^{2+} in the **POM-CoW(OH)$_2$** and **HIm@POM-MnW(OH)$_2$**, respectively can be realized from the d-d electronic transitions of cobalt and manganese, respectively. The d–d electronic transitions are in the region of 800 to 540 nm for the **POM-CoW(OH)$_2$** and **HIm@POM-MnW(OH)$_2$** confirm the incorporation of 3*d* metal ion (Co^{2+} and Mn^{2+}) in the respective systems. The diffuse reflectance (electronic) spectra of these two compounds are also compared with those of related two sandwich compounds, as mentioned above for the IR and Raman spectra. As expected, the compound $Na_{12}[(WO_2(OH))_2(WO_2)_2(BiW_9O_{33})_2]\cdot 44H_2O$ does now show any feature for d–d transition and

the compound $Na_{10}[Bi_2W_{20}Co_2O_{70}(H_2O)_6]\cdot 41H_2O$ shows the similar feature in its solid state electronic spectrum as shown by that of **POM-CoW(OH)$_2$** (**Figure 2.6**).

2.3.2.5. Thermogravimetric analysis

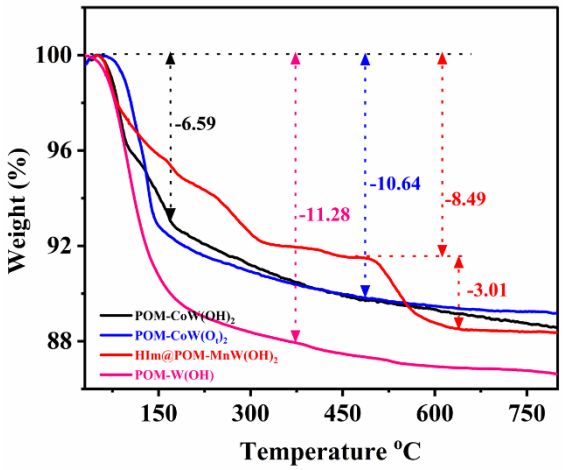

Figure 2.7. Thermogravimetric analysis plots of **POM-CoW(OH)$_2$**, **HIm@POM-MnW(OH)$_2$**, **POM-W(OH)**, and **POM-CoW(O$_t$)$_2$** compounds.

Thermal stability of **POM-CoW(OH)$_2$** and **HIm@POM-MnW(OH)$_2$** along with $Na_{12}[(WO_2(OH))_2(WO_2)_2(BiW_9O_{33})_2]\cdot 44H_2O$ and $Na_{10}[Bi_2W_{20}Co_2O_{70}(H_2O)_6]\cdot 41H_2O$ was carried out from their as-synthesized samples under the He gas atmosphere (**Figure 2.7**). Compounds **POM-CoW(OH)$_2$** and $Na_{10}[Bi_2W_{20}Co_2O_{70}(H_2O)_6]\cdot 41H_2O$ **POM-CoW(O$_t$)$_2$** show similar weight-loss trend in their TGA plots. Compound $Na_{12}[(WO_2(OH))_2(WO_2)_2(BiW_9O_{33})_2]\cdot 44H_2O$ shows steep weight loss in comparison to other three. The gradual weight loss in these cases from the initial temperature to 300 °C indicates the loss of lattice water molecules followed by the loss of coordinated water molecules. But in the case of compound **HIm@POM-MnW(OH)$_2$**,, the additional weight loss of 3.01% in the region of 500 to 630 °C ensures the degradation of the imidazole ring, which is consistent with relevant literature.[99] The presence of the high percentage of residual mass (%) indicates the formation of metal-oxide contents.

2.3.2.6. Powder X-ray diffraction analysis

Powder X-ray diffraction (PXRD) profiles of **POM-CoW(OH)$_2$**, **HIm@POM-MnW(OH)$_2$** **POM-W(OH)**, and **POM-CoW(O$_t$)$_2$** were recorded using respective bulk materials. The experimentally obtained profiles are consistent with simulated patterns, obtained from the crystallographic information file (CIF), hence confirms the bulk purity and homogeneity of the material (**Figure 2.8**).

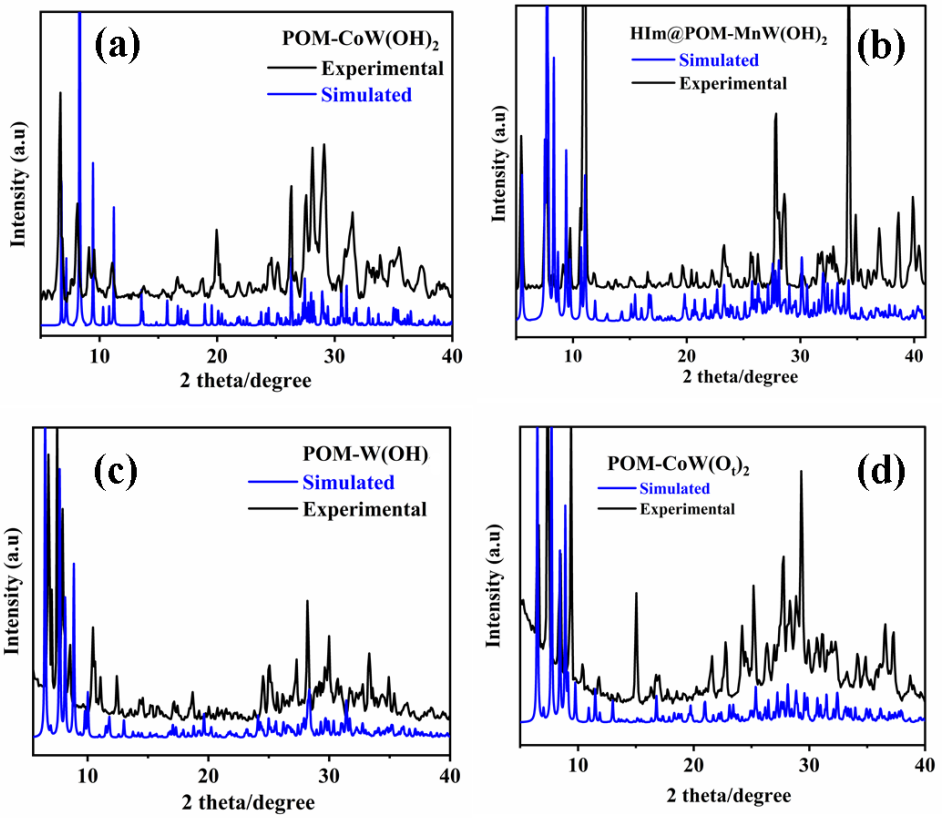

Figure 2.8. (**a-d**) Powder X-ray diffraction patterns of **POM-CoW(OH)$_2$**, **HIm@POM-MnW(OH)$_2$**, **POM-W(OH)**, and **POM-CoW(O$_t$)$_2$** compounds.

2.3.3. Electrochemistry

2.3.3.1. Cyclic voltammograms

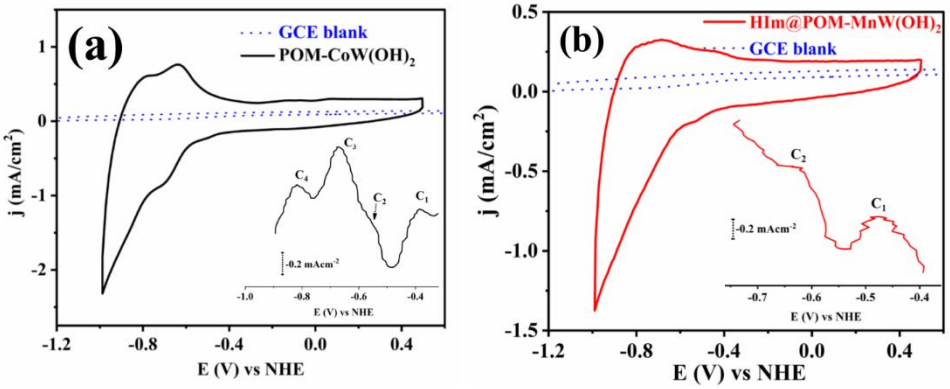

Figure 2.9. Cyclic voltammogram profiles at neutral pH: (**a**) cyclic voltammogram of the **POM-CoW(OH)$_2$** and its differential pulse voltammogram response shown as an inset; (**b**) cyclic voltammogram of the **Him@POM-MnW(OH)$_2$** and its differential pulse voltammogram response shown as an inset. CVs were collected with a scan rate of 100 mVs^{-1}.

The cyclic voltammograms (CVs) of both the compounds of **POM-CoW(OH)$_2$** and **HIm@POM-MnW(OH)$_2$** have been recorded at neutral pH, under nitrogen atmosphere. As shown in **Figure 2.9**(**a**), there is a small feature on reduction wave at around –0.52 V followed by a broad quasi-reversible redox couple at $E_{1/2}$ = –0.655 V (*vs.* NHE; E_{PC} = –0.68 V and E_{PA} = –0.63 V) for **POM-CoW(OH)$_2$** at the neutral pH. Right after this broad cathodic response at around –0.68 V, there is a prominent surge in the current at –0.766 V (*vs.* NHE) indicating electrocatalytic water reduction reaction (WRR), catalyzed by **POM-CoW(OH)$_2$** (blank experiment: the bare glassy carbon electrode, coated with the acetylene-Nafion mixture in the absence of catalyst, was recorded and no considerable response is found as shown in **Figure 2.9**(**a**)). The reduction at –0.52 V (*vs.* NHE) can be assigned to the reduction of $\{W^{VI}(OH)_2\}$ moiety to $\{W^{V}(OH)_2\}$ of the POM cluster as shown in equation 5: $[POM–\{W^{VI}(OH)_2\}_2] + 2e^- \rightarrow [POM–\{W^{V}(OH)_2\}_2]^{2-}$. The reduced species having $\{W^{V}(OH)_2\}$ moieties reduce water to molecular hydrogen according to the equation 6 and this is why we do not see any electrochemical oxidative

$$[POM–\{W^{V}(OH)_2\}_2]^{2-}+2H_2O \rightarrow H_2(g)+2OH^-+[POM–\{W^{VI}(OH)_2\}_2] \quad \text{(eqn. 6)}$$

response (**Figure 2.9**(**a**)), corresponding to the reduction of $[POM–\{W^{VI}(OH)_2\}_2]$ (eqn 5). The broad-like quasi-reversible reductive feature with $E_{1/2}$ = –0.655 V can be attributed to the reduction of the deprotonated form of $[POM–\{W^{VI}(OH)_2\}_2]$ assuming that there is an equilibrium between deprotonated and protonated forms of **POM-CoW(OH)$_2$** at the neutral pH as shown in equation 7.

$$[POM–\{W^{VI}(OH)_2\}_2] \rightleftharpoons [POM–\{W^{VI}(O)_2\}_2]^{2-} + 2H^+ \quad \text{(eqn.7)}$$

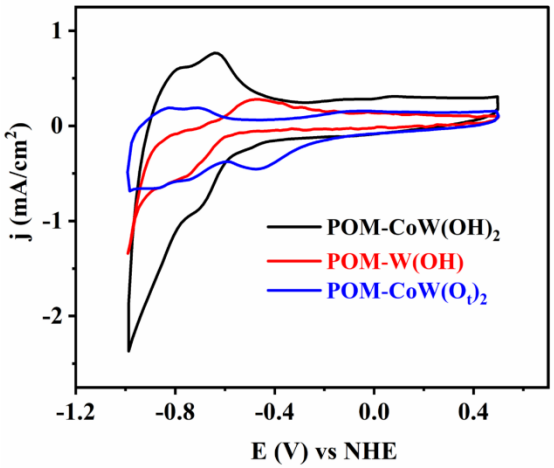

Figure 2.10. Cyclic voltammograms of **POM-CoW(OH)$_2$**, **POM-W(OH)**, and **POM-CoW(O$_t$)$_2$** were recorded at neutral pH (0.1 M potassium phosphate used as a supporting electrolyte) at a scan rate of 100 mV s^{-1}. The CV of **POM-W(OH)** was collected in a homogeneous manner using a 1 mmol of compound **POM-W(OH)** in the 0.1 M potassium phosphate at neutral pH.

This equilibrium is supported by the fact that an aqueous suspension of compound **POM-CoW(OH)$_2$** shows the pH value of 5 (thus the compound behaves like an inorganic acid) and the quasi-reversible response, observed at neutral pH, disappears when the CV experiment is performed at an acidic pH (*vide infra*). Thus the quasi-reversible response in the CV of **POM-CoW(OH)$_2$**, centered at = –0.655 V (*vs.* NHE), is assigned to $\{W^{VI}(O^{-})_2\}$ / $\{W^{V}(O^{-})_2\}$ couple by comparing the relevant response with that of $Na_{12}[(WO_2(OH))_2(WO_2)_2(BiW_9O_{33})_2]\cdot 44H_2O$ and $Na_{10}[Bi_2W_{20}Co_2O_{70}(H_2O)_6]\cdot 41H_2O$ (**Figure 2.10**). It is logical to accept that, this couple (deprotonated form) appears at a more negative potential (–0.655 V) than the reduction potential (–0.52 V) of the protonated form [POM–$\{W^{VI}(OH)_2\}_2$], because it would be easy to reduce $\{W^{VI}(OH)_2\}$ moieties compared to $\{W^{VI}(O^{-})_2\}$ moieties. But only the protonated form, [POM–$\{W^{VI}(OH)_2\}_2$] (not the deprotonated form) responses to the half reaction (eqn 4), HER, occurred at the cathode at neutral pH, despite the fact, it has lower negative potential (–0.52 V) than that (–0.655 V) of deprotonated form. Surprisingly, the manganese analogue **HIm@POM-MnW(OH)$_2$** does not show the reductive response for the deprotonated species at the neutral PH (**Figure 2.9**(**b**)), though its anionic component is identical to that of **POM-CoW(OH)$_2$** [both have two peripheral $\{W^{V}(OH)_2\}$ groups, but the former has Mn(II) and the latter contains Co(II)]. In other words, **HIm@POM-MnW(OH)$_2$** does not behave like an inorganic acid in contrast to its cobalt analogue. The weak broad reductive responses at around –0.52 V in cyclic voltammograms of both compounds, when subjected to DPV experiments, split into two consecutive reductions c1 and c2 corresponding to two $\{W^{V}(OH)_2\}$ groups of the same POM cluster (**Figure 2.9**(**a** and **b**), inset); The consecutive reductions at c3 and c4 after DPV experiments, shown in inset of **Figure 2.9**(**a**) correspond to two deprotonated $\{W^{VI}(O^{-})_2$ groups (see eqn. 7). As expected, because of the presence of protonation-deprotonation equilibrium for the compound **POM-CoW(OH)$_2$**, the HER Faradaic efficiency for **POM-CoW(OH)$_2$** (79%) is less than that (86%) of **HIm@POM-MnW(OH)$_2$** at pH 7.0.

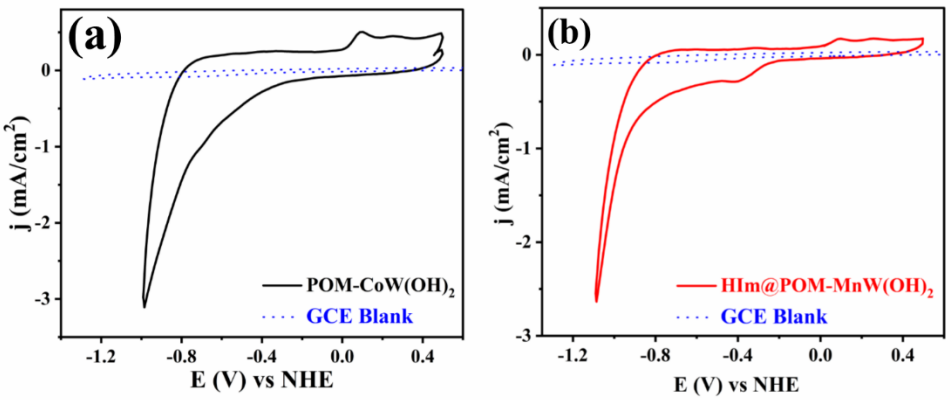

Figure 2.11. Cyclic voltammograms for both catalysts (**POM-CoW(OH)$_2$** and **Him@POM-MnW(OH)$_2$**): (**a**) cyclic voltammogram response of **POM-CoW(OH)$_2$** at acidic pH 3; (**b**) cyclic voltammogram **Him@POM-MnW(OH)$_2$** at pH 3 (CVs were recorded with a scan rate of 100 mVs^{-1}).

Thus, if, at the neutral pH, the compound **POM-CoW(OH)$_2$** has an equilibrium between its protonated and deprotonated forms (eqn. 7), at a lower pH, its protonated form would dominate and we would not observe the redox response/couple for the deprotonated form. Indeed, the CV of **POM-CoW(OH)$_2$** at pH 3 does not show any redox response/couple other than HER current surge. Moreover, the reduction of $\{W^{VI}(OH)_2\}$ moiety to $\{W^{V}(OH)_2\}$ of the POM cluster of compound **POM-CoW(OH)$_2$**, observed at –0.52 V (*vs* NHE) as a weak shoulder response at the neutral pH, is not observed at pH 3. This is not visible clearly at pH 3 due to the large HER onset current as shown in **Figure 2.11**(**a**). It is consistent with the fact that the HER turn over frequency (TOF) at the neutral pH is 0.318 s^{-1} and that at pH 3 is 1.154 s^{-1} for compound **POM-CoW(OH)$_2$**. On the other hand, compound **HIm@POM-MnW(OH)$_2$**, which does not deprotonate at the neutral pH, shows a weak but new response at around –0.40 V (*vs.* NHE) at pH 3 (**Figure 2.11**(**b**)). This can be assigned to the reduction of protonated imidazole, present as the cation in compound **HIm@POM-MnW(OH)$_2$**.[113,114] The CVs of both compounds, **POM-CoW(OH)$_2$** and **HIm@POM-MnW(OH)$_2$** at pH 3 exhibit two weak oxidative responses at around 0.15 V (*vs.* NHE) which could be due to the redox reaction of surface oxygen containing groups, hydroquinone/quinine, inherently formed by oxidation at the edge sites of the glassy carbon working electrode surface.[115]

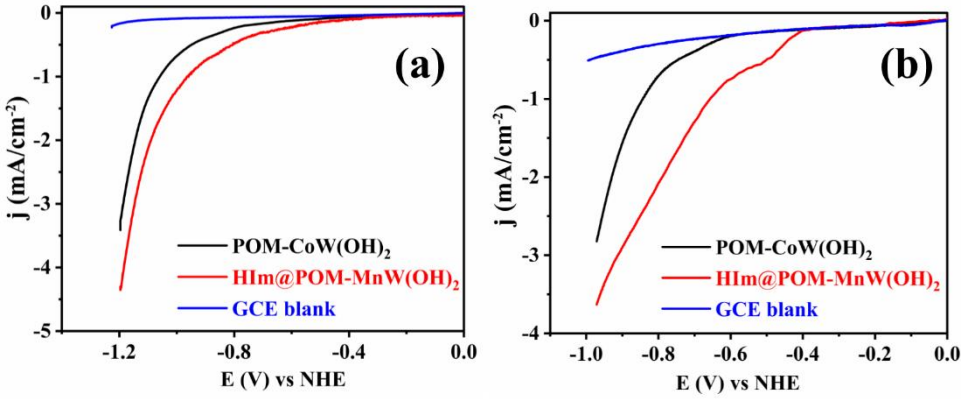

Figure 2.12. Linear sweep voltammograms for both catalysts (**POM-CoW(OH)$_2$** and **Him@POM-MnW(OH)$_2$**): (**a**) linear sweep voltammogram profiles for both catalysts at neutral pH; (**b**) linear sweep voltammogram profiles for both catalysts at acidic pH 3. (LSVs were collected with a sweep rate of 50 mVs^{-1}).

The linear sweep voltammograms (LSVs) were recorded to investigate the HER activity of **POM-CoW(OH)$_2$** and **HIm@POM-MnW(OH)$_2$** at neutral pH (**Figure 2.12**(**a**)) as well as in pH 3 (**Figure 2.12**(**b**)) with sweep rate of 50 mVs^{-1}. The linear sweep voltammetry studies have shown that compound **HIm@POM-MnW(OH)$_2$** exhibits dominant HER activity in terms of less catalytic onset potential with more current density compared to that shown by **POM-CoW(OH)$_2$** at identical experimental conditions. The better HER activity for **HIm@POM-MnW(OH)$_2$** compared to that of **POM-CoW(OH)$_2$** can be understood by the presence of H–bonding network of protonated imidazole (HIm) in the crystal structure of **HIm@POM-**

$MnW(OH)_2$ over its analogous system, the only additional structural deference found among two systems by SCXRD analysis. The protonated/cationic imidazole is supposed to be good charge carrier, which can thus lower the charge-transfer resistance (R_{CT}) in **HIm@POM-$MnW(OH)_2$**, thereby facilitate the electron transfer during its HER activity. This is supported by the electrochemical impedance spectroscopy (EIS) of **HIm@POM-$MnW(OH)_2$** (*vide-infra*). Thus, the catalyst **HIm@POM-$MnW(OH)_2$** has leading HER performance over **POM-$CoW(OH)_2$** (at both pH).

2.3.3.2. W^{VI}–OH Functionality on POM surface for electrocatalytic HER: controlled experiments

It has been known that transition metal-hydroxyl groups (e.g., M^{n+}–OH) are chemically/electrochemically more reactive than the other forms of metal-oxo groups,[3,5,69,72] because metal-hydroxyl groups are Brønsted acid in nature. There are reports of M^{n+}–OH group containing compounds exhibiting hydrogen evolution reaction (HER), but without much emphasis on metal-hydroxyl group that is responsible for HER (a structure–function relationship). The reports, that enlighten on structure-function relation for HER, based on M^{n+}–OH group(s) on a polyoxometalate (POM) cluster surface, are not much known. The main theme of this article is to demonstrate electrochemical water reduction mediated by W^{VI}–OH group of a polyoxometalate. For this, we have chosen the title compounds $[\{Na_6(H_2O)_2\}][\{Co^{II}(H_2O)_3\}_2\{W^{VI}(OH)_2\}_2\{Bi^{III}W^{VI}_9O_{33})_2\}]\cdot 14H_2O$ (**POM-$CoW(OH)_2$**) and $[(W^{VI}(OH)_2)_2(Mn^{II}(H_2O)_3)_2(Na_4(H_2O)_{14}(BiW_9O_{33})_2](Him)_2\cdot 16H_2O$ (**HIm@POM-$MnW(OH)_2$**), each having two symmetrical $–W^{VI}(OH)_2$ functionalities. In order to make this demonstration convincing, we have included two more known structurally relevant compounds, $Na_{12}[(WO_2(OH))_2(WO_2)_2(BiW_9O_{33})_2]\cdot 44H_2O$ (**POM-W(OH)**) having two W–OH groups and $Na_{10}[Bi_2W_{20}Co_2O_{70}(H_2O)_6]\cdot 41H_2O$ (**POM-$CoW(O_t)_2$**), which does not contain any W–OH group. We then performed a series of controlled experiments to reach a conclusion that W–OH functionality on POM surface is responsible for HER. The CV of **POM-$CoW(O_t)_2$** was performed in a heterogeneous manner (as done for **POM-$CoW(OH)_2$** and **HIm@POM-$MnW(OH)_2$**), whereas the CV of **POM-W(OH)** was recorded from its homogeneous solution (using 1 mmol of **POM-W(OH)** in 0.1 M neutral pH potassium phosphate buffer), since it is soluble in water.

As shown in **Figure 2.13**(**a** and **b**), the reductive scans of **POM-W(OH)**, **POM-$CoW(OH)_2$** and **HIm@POM-$MnW(OH)_2$** show the electrocatalytic water reduction but the reductive scan of compound **POM-$CoW(O_t)_2$** does not show any such current surge. This result offers manifold information: (i) –W(OH) functionality containing compounds gives electrocatalytic water reduction, (ii) there is no role of first series transition metal ion, for example, Co(II) and Mn(II) coordination in compounds **POM-$CoW(OH)_2$** and **HIm@POM-$MnW(OH)_2$** respectively, on this electrocatalytic water reduction, because compound **POM-**

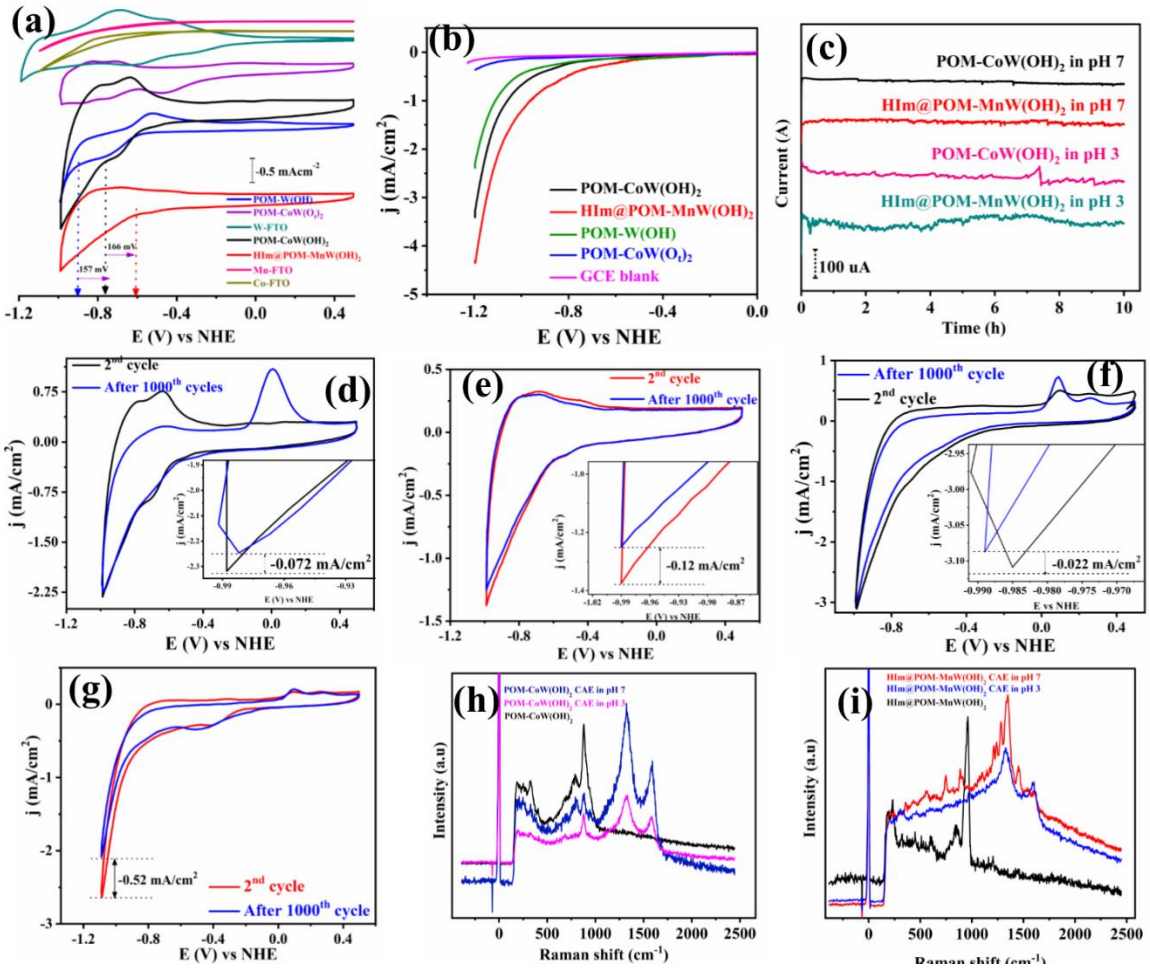

Figure 2.13. (**a**) Cyclic voltammograms for **POM-CoW(OH)$_2$**, **HIm@POM-MnW(OH)$_2$**, **POM-W(OH)$_2$**, **POM-CoW(O$_t$)$_2$**, **W–FTO**, **Co–FTO**, and **Mn–FTO**, that were recorded at neutral pH with a scan rate of 100 mVs^{-1}; (**b**) linear sweep voltammograms of **POM-CoW(OH)$_2$**, **HIm@POM-MnW(OH)$_2$**, **POM-W(OH)$_2$**, **POM-CoW(O$_t$)$_2$**, and GCE blank, recorded at the neutral pH using a sweep rate of 50 mVs^{-1}; (**c**) chronoamperometry electrolysis responses of **POM-CoW(OH)$_2$-**, **HIm@POM-MnW(OH)$_2$-** modified GC electrodes at -1 V (vs NHE) for 10 hours at neutral pH as well as in acidic pH 3; (**d** and **e**) 1000 cycles CVs of **POM-CoW(OH)$_2$-** and **HIm@POM-MnW(OH)$_2$-** modified GC electrodes at neutral pH (scan rate of 100 mVs^{-1}); (**f** and **g**) 1000 cycles CVs of **POM-CoW(OH)$_2$-** and **HIm@POM-MnW(OH)$_2$-** modified GC electrodes at pH 3 (scan rate of 100 mVs^{-1}); (**h** and **i**) the comparison of Raman spectra of **POM-CoW(OH)$_2$-** and **HIm@POM-MnW(OH)$_2$-** modified electrodes after chronoamperometry experiments (at neutral pH and acidic pH 3) with their Raman profiles of partent **POM-CoW(OH)$_2$** and **HIm@POM-MnW(OH)$_2$**.

W(OH) does not contain such first transition series metal ions but contains –W(OH) groups and (iii) structurally similar compound **POM-CoW(O$_t$)$_2$** having –W=O group instead of –W(OH) groups does not show electrocatalytic water reduction. It is noteworthy to mention that, the compound **POM-CoW(O$_t$)$_2$** having –W=O group in place of –W(OH) group show similar CV feature, as shown by the compounds **POM-CoW(OH)$_2$** and **HIm@POM-MnW(OH)$_2$**, but

without a current surge (electrocatalytic hydrogen evolution). This indirectly supports that –W(OH) functionality is responsible for electrocatalytic water reduction. The onset potentials for the electrocatalytic water reduction reactions (WRRs), catalyzed by **POM-W(OH)**, **POM-CoW(OH)$_2$** and **HIm@POM-MnW(OH)$_2$**, respectively are –0.919, –0.766 and –0.600 V (*vs.* NHE), meaning thereby that efficiencies of the catalysts in electrcatalytic WRR are in the order of **HIm@POM-MnW(OH)$_2$** > **POM-CoW(OH)$_2$** > **POM-W(OH)**. The fact that the compound **POM-W(OH)** is less efficient than **HIm@POM-MnW(OH)$_2$** and **POM-CoW(OH)$_2$** in terms of electrocatalytic WRR, is not surprising because the compound **POM-W(OH)** contains two –W(OH) functional groups, whereas the compounds **HIm@POM-MnW(OH)$_2$** and **POM-CoW(OH)$_2$**, each have two –W(OH)$_2$ groups (i.e., there are four hydroxyl groups in the latter two compounds in comparison to two hydroxyl groups present in former compound). Now, why is **HIm@POM-MnW(OH)$_2$** more efficient than **POM-CoW(OH)$_2$**, even though both have identical numbers of –W(OH)$_2$ functionalities? This can be understood by the presence of protonated imidazole cations in compound **HIm@POM-MnW(OH)$_2$** that might contribute to the WRR activity by acting as charge transfer carriers. The less charge transfer resistivity of **HIm@POM-MnW(OH)$_2$** is supported by the EIS studies (*vide infra*).

We also examined the chances of formation and participation of the pre-catalyst that can be formed by the degradation of molecular catalyst under electrochemical operational (reducing) condition. We electrochemically generated the metal nanoparticles of tungsten, cobalt and manganese by reducing aqueous solutions of sodium tungstate, cobalt nitrate and manganese nitrate in the cathodic window in the operational conditions of our interest. The cyclic voltammograms (CVs) of electrochemically generated (a) W–FTO, (b) Co–FTO and (c) Mn–FTO were performed at neutral pH and relevant CV plots are shown in **Figure 2.13**(**a**). These modified–FTO electrodes neither show CVs that are comparable to those of **POM-W(OH)**, **POM-CoW(OH)$_2$** and **HIm@POM-MnW(OH)$_2$** nor show any electrocatalytic HER (not any sudden current surge). All these experiments support that $W^{VI}(OH)_2$ active sites (not any degrated products) of **POM-CoW(OH)$_2$** and **HIm@POM-MnW(OH)$_2$** are responsible for electrocatalytic HER in the present study.

Sustainability or long-term stability of a catalyst is an important factor for its usable applications. For this, we have performed accelerated durability test of the cathodic (modified) electrodes, the working electrodes, on which the title catalysts, **POM-CoW(OH)$_2$** and **HIm@POM-MnW(OH)$_2$** were deposited. The durability tests were carried out by performing (i) chronoamperometry (CA) experiment and (ii) 1000 cycles of CV scan measurements. Chronoamperometric measurements were performed at –1.00 V (*vs* NHE) for 10 hrs at neutral pH as well as at pH 3. As shown in **Figure 2.13**(**c**), both catalysts **POM-CoW(OH)$_2$** and **HIm@POM-MnW(OH)$_2$** have notable long-term stability (minimum 10 hrs) under operational conditions at pH 7 as well as at pH 3. The accelerated durability has also been

Figure 2.14. A photograph of electrochemically generated hydrogen gas on the **POM-CoW(OH)$_2$** catalyst modified working electrode surface at neutral pH.

performed by 1000 cyclic voltammetric scans (from 0.5 to –1.0 V vs NHE) using the catalysts **POM-CoW(OH)$_2$** and **HIm@POM-MnW(OH)$_2$** in neutral pH as well as in acidic solution (pH 3); no significant changes in HER catalytic current have been observed after 1000 scans (**Figures 2.13**(**d** and **e**) and **Figures 2.13**(**f** and **g**)) indicating that compounds **POM-CoW(OH)$_2$** and **HIm@POM-MnW(OH)$_2$** have enormous stability during electrocatalytic HER in a wide pH range (pH 3–7). We must mention that there is a small drop in catalytic current (0.072 and 0.12 mA at neutral pH and 0.022 and 0.53 mA at pH 3 for **POM-CoW(OH)$_2$** and **HIm@POM-MnW(OH)$_2$** respectively), which can be understood by the mechanical loss of the sample from the glassy carbon modified electrode surface during vigorous hydrogen evolution at potential around –1.0 V (vs NHE). It is found that the drop in catalytic current is considerably more for **HIm@POM-MnW(OH)$_2$** compared to that shown by **POM-CoW(OH)$_2$**. This is not surprising because we have seen that **HIm@POM-MnW(OH)$_2$** is more efficient HER catalyst than **POM-CoW(OH)$_2$**, thereby more vigorous hydrogen evolution occurs at the **HIm@POM-MnW(OH)$_2$**-quoted working electrode. And more vigorous the hydrogen evolution more is the loss in catalytic current after 1000 cycles. Another reason of this little loss of catalytic current after 1000 cycles could be due to the considerable amount of resulting hydrogen gas bubbles that block the electrode surface (**Figure 2.14**).

It is necessary to check the structural integrity of a molecular catalyst after its prolonged use to find out its parent identity. We performed Raman spectral analysis, PXRD studies and FESEM analysis of the electrode materials of **POM-CoW(OH)$_2$** and **HIm@POM-MnW(OH)$_2$** after 10 hours of chronoamperometric (CA) measurements. The Raman spectra were recorded after CA electrolysis and compared with their parent compounds' Raman profiles (**Figures 2.13**(**h** and **i**)). In the case of **POM-CoW(OH)$_2$**, the Raman spectral feature of the molecular catalyst **POM-CoW(OH)$_2$** is clearly visible in the Raman spectrum of the electrode material of **POM-CoW(OH)$_2$** after CA measurement (in neutral as well as in acidic pH) along with the Raman active modes of Nafion ($-SO_3^-$, C–C) and acetylene carbon in the region of 1060 to 1650 cm^{-1}, which are not perceived in the parent material profile (**Figure 2.13**(**h**)).[116-119] But in the case

of **HIm@POM-MnW(OH)$_2$** (**Figure 2.13(i)**), the Raman profile of the electrode material after CA experiment is dominated by the Raman spectral features of Nafion ($-SO_3^-$, C–C) and acetylene carbon, but the Raman feature of parent **HIm@POM-MnW(OH)$_2$** is visible as weak peaks in the region of 750-1000 cm^{-1} at neutral pH and is hardly visible in pH 3. This is consistent with vigorous hydrogen evolution at pH 3 with the mechanical loss of the quoting from the working electrode. The PXRD patterns of the coated samples after 10 hrs of CA

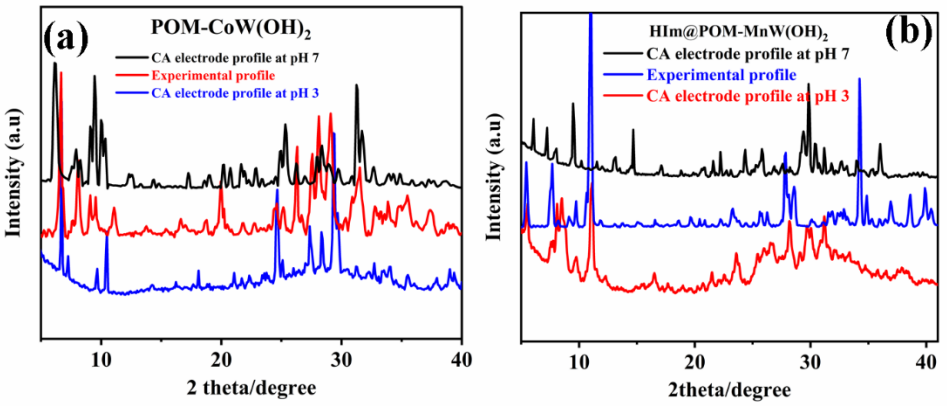

Figure 2.15. Powder X-ray diffraction patterns of catalyst coated FTO electrodes collected after chronoamperometry electrolysis: (**a**) **POM-CoW(OH)$_2$**, and (**b**) **HIm@POM-MnW(OH)$_2$** were performed at neutral pH as well as in pH 3.

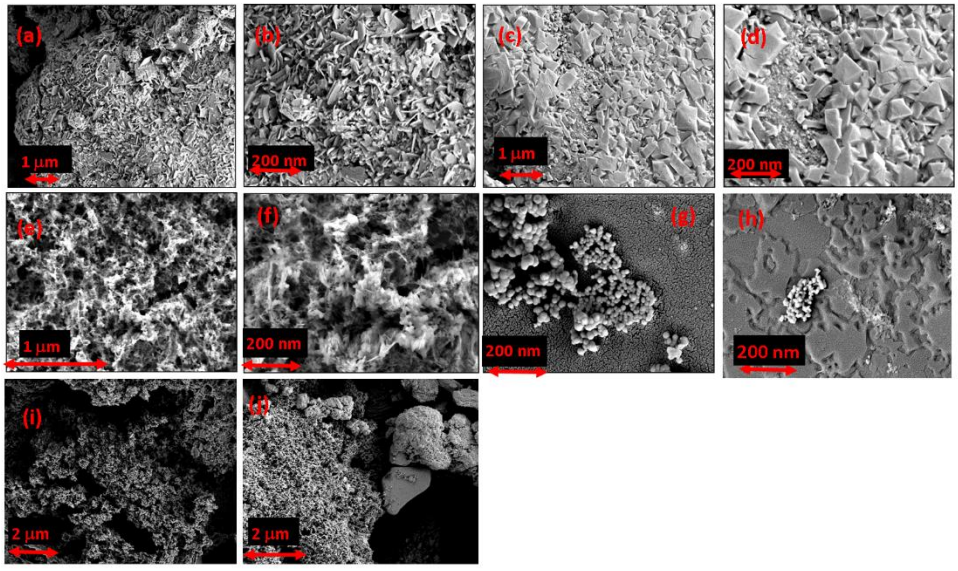

Figure 2.16. FE-SEM analysis of chronoamperometry electrodes at neutral pH as well as in acidic pH 3: (**a** and **b**) shows the flake type of particles for **POM-CoW(OH)$_2$**; (**c** and **d**) hexagonal/rhombohedral shaped particles were observed for **HIm@POM-MnW(OH)$_2$**; (**e** and **f**) *in-situ* generated W-FTO electrode shows foam/sponge particles; (**g** and **h**) *in-situ* prepared Co-FTO and Mn-FTO electrodes were formed spherical type particles; (**i** and **j**) shows the FE-SEM images of **POM-CoW(OH)$_2$** and **HIm@POM-MnW(OH)$_2$** electrodes at pH 3.

measurement show that there are some shifts and intensity difference of the peaks, when compared to PXRD patterns of parents **POM-CoW(OH)$_2$** and **HIm@POM-MnW(OH)$_2$** (**Figure 2.15**). These peak shifts and intensity difference are not surprising, because the preparation of coated samples was carried out by grinding the crystalline parent compounds into a very fine powder followed by its mixing with acetylene carbon as well as with Nafion.

Overall the PXRD patterns of the coated samples after CA experiments indicate that the parent compounds retain on the electrode surface after 10 hrs of CA measurement as molecular catalysts. In FESEM analysis after CA experiments (neutral pH as well as acidic pH), the **POM-CoW(OH)$_2$** has shown flake type of particles, whereas in the case of **HIm@POM-MnW(OH)$_2$** the rhombohedral/hexagonal particles are observed (**Figures 2.16**(**a-d**)); in the both the cases, spherical-shaped of metal nanoparticles were not observed. On the other hand, the electrochemically generated W–FTO, Co–FTO and Mn–FTO show spherical shaped nano-particles of respective metals in their FESEM images (**Figures 2.16**(**e-j**)). Thus, all the above-described experiments support that the POM based compounds **POM-CoW(OH)$_2$** and **HIm@POM-MnW(OH)$_2$** are true molecular catalysts for electrocatalytic HER in neutral pH as well as in acidic solution (pH 3).

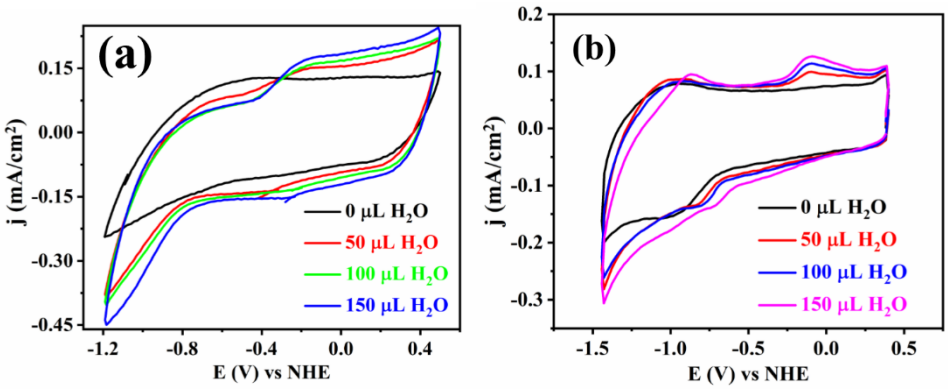

Figure 2.17. Non-aqueous medium cyclic voltammograms performed under inert atmosphere: (**a**) shows for **POM-CoW(OH)$_2$**; and (**b**) represent for **HIm@POM-MnW(OH)$_2$**. The CVs were collected during the sequential addition of a controlled amount of water and dry tetrahydrofuran (THF) solution containing 0.1 M tetrabutylammonium perchlorate (TBA-ClO_4) used as a supporting electrolyte.

In the present work, in order to investigate the basis of HER, *i.e.*, whether it is direct water reduction (eqn. 4) or just proton reduction (eqn. 2), we examined the CV studies of catalyst-coated electrodes in a non-aqueous medium, tetrahydrofuran (THF) medium containing 0.1 M tetrabutylammonium perchlorate (TBA-ClO_4) as supporting electrolyte by adding the controlled amount of water. The sequential addition of water (in micro-liter amounts) results in the chronological enhancement in cathodic onset current density for both **POM-CoW(OH)$_2$**– and **HIm@POM-MnW(OH)$_2$**–coated electrodes (**Figure 2.17**(**a** and **b**)). This conforms direct

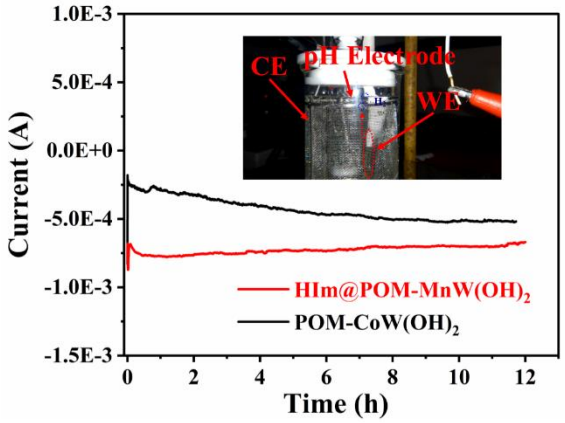

Figure 2.18. Chronoamperometry bulk-electrolysis (at -1.1 V for 12 hours), carried out in a two-electrode mode (at neutral pH, 0.1 M KCl) for **POM-CoW(OH)$_2$** and **HIm@POM-MnW(OH)$_2$**; the inset photograph shows the bulk-electrolysis experimental setup (CE: Pt net, WE: sample coated FTO and pH electrode).

electrocatalytic water reduction (eqn. 4) catalyzed by **POM-CoW(OH)$_2$** and **HIm@POM-MnW(OH)$_2$**. In order to comprehend further insights into the water reduction capability of the **POM-CoW(OH)$_2$** and **HIm@POM-MnW(OH)$_2$**, we performed the bulk chronoamperometry electrolysis using FTO electrode, coated with the catalyst at –1.1 V for 12 hrs in a two-electrode cell (FTO as working electrode and platinum counter electrode), connected to a digital pH meter with a pH electrode dipped into the electrolyte solution (**Figure 2.18**). During the electrolysis, changes in the pH value of the electrolyte were monitored with the pH meter. The initial pH value of the electrolyte was 6.96 (a neutral pH, before the electrolysis begins). After 12 hours of electrolysis, the final pH value was found to be 7.68 and 7.71 for **POM-CoW(OH)$_2$** and **HIm@POM-MnW(OH)$_2$**, respectively. This increase in pH value of the electrolyte solution from the neutral pH to an alkaline pH is consistent with direct water reduction at the cathode ($4H_2O + 4e^- \rightleftharpoons 2H_2 + 4OH^-$, eqn. 4) resulting in hydrogen evolution with the formation of hydroxyl ion making the electrolyte solution alkaline. This observation strengthens our claim of electrocatalytic water reduction to molecular hydrogen.

2.3.3.3. Kinetic insights

In order to understand the electrochemical HER kinetics catalyzed by **POM-CoW(OH)$_2$** and **HIm@POM-MnW(OH)$_2$**, the *iR* corrected Tafel plots were constructed by carrying out galvanostatic polarization under steady-state mass transfer control in neutral solution (pH 7) as well as in acidic solution (pH 3). The relevant electrolyte solutions were continuously stirred at 480 rpm to maintain the mass transfer control. The observed Tafel slope values are 180.17 and 170.14 mV dec^{-1} at neutral pH, and are 176.60 and 161.99 mV dec^{-1} at pH 3 for **POM-CoW(OH)$_2$** and **HIm@POM-MnW(OH)$_2$**, respectively indicating that **HIm@POM-MnW(OH)$_2$** is a better HER catalyst than **POM-CoW(OH)$_2$** (smaller Tafel slope is desired for an efficient catalyst) as shown in **Figure 2.19**.

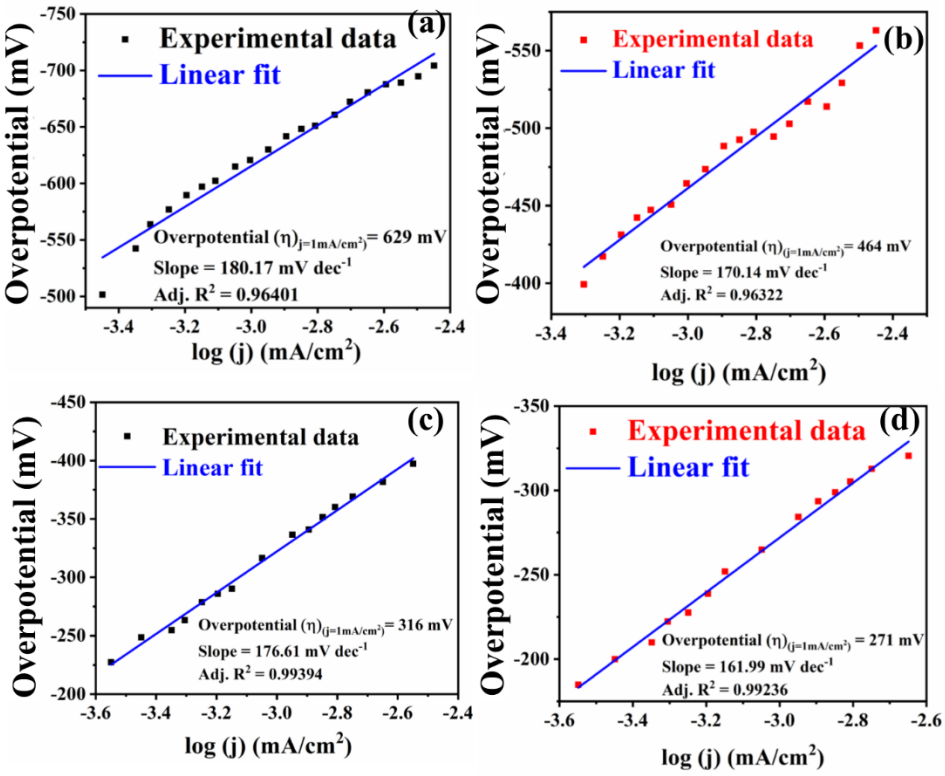

Figure 2.19. *iR*-corrected Tafel plots for **POM-CoW(OH)$_2$** and **HIm@POM-MnW(OH)$_2$** at neutral pH as well as in acidic pH 3: (**a** and **b**) shows the Tafel plots for **POM-CoW(OH)$_2$** and **HIm@POM-MnW(OH)$_2$** at neutral pH; (**c** and **d**) represent the Tafel plots for **POM-CoW(OH)$_2$** and **HIm@POM-MnW(OH)$_2$** in acidic pH 3.

We have already shown, in the present HER study, that we are dealing with water reduction $2H_2O + 2e^- \rightleftharpoons H_2 + 2OH^-$ (eqn. 4) and not hydronium ion reduction $2H_3O^+ + 2e^- \rightleftharpoons H_2 + 2H_2O$ (or $2H^+ + 2e^- \rightleftharpoons H_2$, eqn. 2). The water reduction step (eqn. 4), the mechanism of which is still not well-established, can be described by Volmer– and Heyrovsky–steps.

Volmer step: $H_2O + e^- + M \rightleftharpoons M–H + OH^-$

Heyrovsky step: $M–H + H_2O + e^- \rightleftharpoons H_2 + OH^- + M$, where M is the electrode surface site.

It has been established that if the rate determining step is water dissociation, *i.e.*, the Volmer step as shown above, the theoretical value of the Tafel slope would be 118 mV dec^{-1}.[56] In the present electrocatalytic HER study, the values of experimentally observed Tafel slopes are in the range of 162–180 mV dec^{-1}. Even this range of experimentally observed Tafel slope values is 50–60 mV dec^{-1} more than the theoretical values of Tafel slope, it indicates the Volmer step as the rate determining step in the present HER study. This increase in Tafel slope value from the theoretically predicted value could be due to the slow combination of H_{abs} to molecular hydrogen H_2 in the Heyrovsky step, high charge transfer resistance (R_{CT}) or low mass transfer rate, electrolyte solution resistance, *etc.*[120]

Besides Tafel slope, an overpotential (η), required to attain a current density (j) of 1 $mAcm^{-2}$ is an important parameter to understand the kinetics of HER. It is to be noted that the required overpotential to reach a current density of 1 $mAcm^{-2}$ is described in the present study, even though it is more convenient to report η in terms of the current density of 10 $mAcm^{-2}$. This is due to low concentration of the actual active species, two $–W(OH)_2$ moieties per formula units of both compounds$[\{Na_6(H_2O)_2\}][\{Co^{II}(H_2O)_3\}_2\{W^{VI}(OH)_2\}_2\{Bi^{III}W^{VI}_9O_{33})_2\}]\cdot 14H_2O$ (**POM-CoW(OH)$_2$**) and $[(W^{VI}(OH)_2)_2(Mn^{II}(H_2O)_3)_2(Na_4(H_2O)_{14}(BiW_9O_{33})_2](Him)_2\cdot 16H_2O$ (**HIm@POM-MnW(OH)$_2$**). The total amount of active species on the electrode surface is only ~0.6×10^{-9} mol, which makes quite difficult to obtain 10 $mAcm^{-2}$ current density. The overpotentials (η) at a current density of 1 $mAcm^{-2}$ are found to be 629 mV and 464 mV at neutral pH for **POM-CoW(OH)$_2$** and **HIm@POM-MnW(OH)$_2$**, respectively and those respectively are 316 mV and 271 mV in pH 3 (**Figure 2.19**).

2.3.3.4. Electrochemical impedance spectra

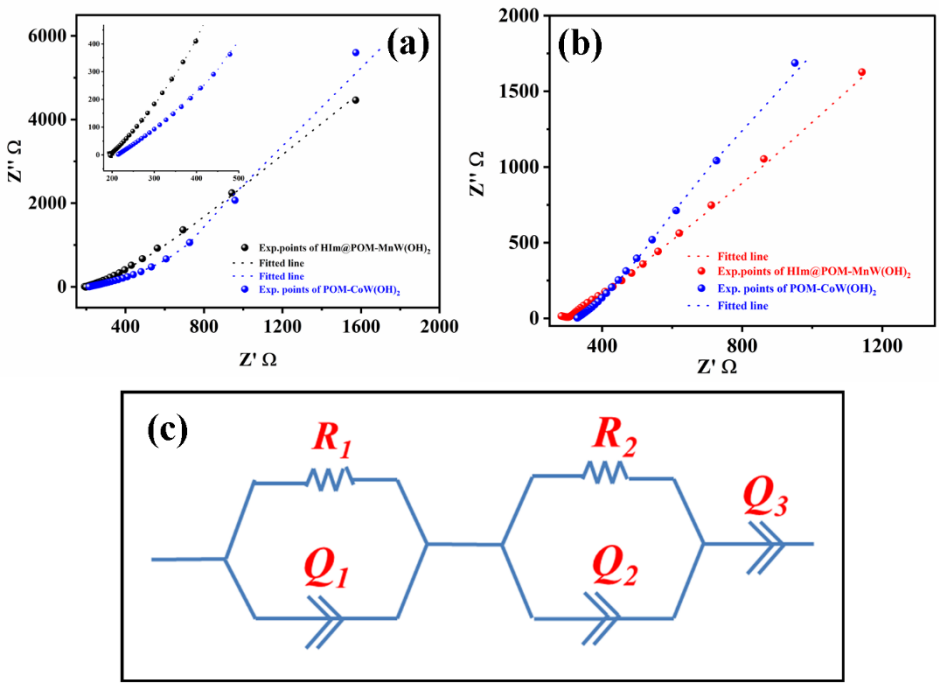

Figure 2.20. Nyquist plots of electrochemical impedance spectra for both catalysts (**POM-CoW(OH)$_2$** and **HIm@POM-MnW(OH)$_2$**): Nyquist plots of both the catalysts were collected (**a**) at neutral pH (inset image shows magnified view of Nyquist plot), and (**b**) represent the Nyquist plots at acidic pH 3; (**c**) equivalent circuit is used to fit the Nyquist plots of electrochemical impedance spectra data of **POM-CoW(OH)$_2$** and **HIm@POM-MnW(OH)$_2$**.

We performed electrochemical impedance spectroscopy (EIS) for both the compounds **POM-CoW(OH)$_2$** and **HIm@POM-MnW(OH)$_2$** to find out the charge transfer resistance (R_{CT}). **Figure 2.20**(**a** and **b**) represents the Nyquist plots of electrochemical impedance spectra for

POM-CoW(OH)$_2$ and **HIm@POM-MnW(OH)$_2$**. The impedance spectra were measured by alternative current electrochemical impedance spectroscopy (AC-EIS) by coating the samples on GC electrode at neutral pH as well as in acidic pH 3. The measurements were done in an identical condition to that of CV experiments, under the nitrogen atmosphere. The measured Nyquist plots of impedance data were constructed between the Z' (real impedance) *vs* Z'' (imaginary impedance) planes of Nyquist plot. The fitting of experimental impedance data of Nyquist plots were done by using the most appropriate equivalent circuit ($(R_1/Q_1) + (R_2/Q_2) + Q_3$) shown in **Figure 2.20**(**c**). The electrochemical lab (EC-lab) software was used to fit the experimentally obtained impedance data of Nyquist plots. The catalyst impedance (R_1/Q_1), electrode-electrolyte interface impedance (R_2/Q_2) and constant phase element (Q_3) are connected in a series. The Q_1, Q_2, and Q_3 are the constant phase elements. The (R_1/Q_1) and (R_2/Q_2) are present in the parallel. The origin of the Nyquist plot represents the bulk charge-transfer resistance (R_{CT}) of electrode material (in the present case R_1) at higher frequency region. On the other hand, the tail part of the Nyquist plot indicates the minor resistance (e.g. electrode-electrolyte inter-grain boundary, contact resistance, and electrolyte resistance, etc.) at lower frequency region, here it is R_2. The charge-transfer resistance of the **POM-CoW(OH)$_2$** and **HIm@POM-MnW(OH)$_2$** compounds were determined with no noticeable error, in terms of χ^2. **Figure 2.20**(**a** and **b**) show the Nyquist plots of electrochemical impedance spectra for **POM-CoW(OH)$_2$** and **HIm@POM-MnW(OH)$_2$** at neutral pH and pH 3.

In both pH mediums, we found that compound **HIm@POM-MnW(OH)$_2$** has less R_{CT} value (194.7 Ohms, at pH 7; 41.35 Ohms, at pH 3) than that of compound **POM-CoW(OH)$_2$** (212.8 Ohms, at pH 7; 131.8 Ohms, at pH 3). The relatively less R_{CT} value for **HIm@POM-MnW(OH)$_2$** is, probably, due to the presence of N–H···O hydrogen bonding interactions between the protonated imidazole and POM cluster surface oxo-groups (found in its single-crystal structure), which are not present in the compound **POM-CoW(OH)$_2$**. This facilitates the (fast) charge/electron transfer in the catalytic action of **HIm@POM-MnW(OH)$_2$**, which is consistent with relatively lower value of Tafel slope of **HIm@POM-MnW(OH)$_2$**.

2.3.3.5. Faradic efficiency

The other important related parameter *i.e.,* Faradic efficiency, for **POM-CoW(OH)$_2$** and **HIm@POM-MnW(OH)$_2$** was evaluated according to the procedure from recent relevant literature.[62-66,122] The Faradic efficiency was determined from the evolved hydrogen (H_2) gas over a period of the time. The chronopotentiometry electrolysis was carried out using a two-electrode system at 1 atm pressure. A known amount of sample coated on a 0.5 cm^2 area surface of Fluorinated Tin Oxide (FTO) was used as a working electrode (in the present case it works as a cathodic electrode), and a bulk area platinum spiral was used as a counter electrode (works as an anode). The catalyst loading on the FTO working electrode maintained as 1 mg/cm^2 and (0.1 M) potassium phosphate buffer was used as the electrolyte for both mediums (such as

neutral pH and acidic pH 3). The home-made setup was used to conduct the electrolysis process by employing a constant cathodic current -500 μA per 4 hours (**Figure 2.21**).

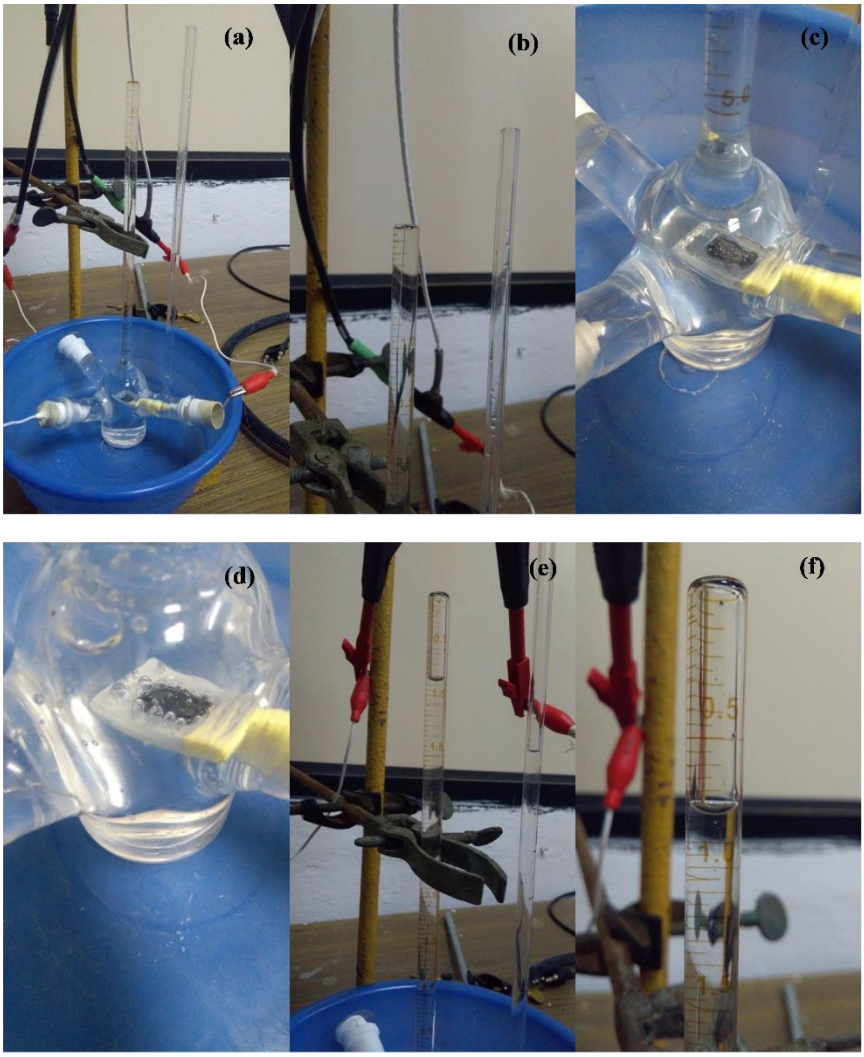

Figure 2.21. Photographs of bulk-chronopotentiometry electrolysis process of the **HIm@POM-MnW(OH)**$_2$: (**a**) A home-made inverted graduate tube setup was used for quantitative hydrogen evolution electrolysis experiment; (**b**) before electrolysis inverted graduated tube filled with electrolyte; (**c**) magnified view of the two-electrode setup separated by an inverted graduated tube; (**d**) the hydrogen gas production at working electrode during the electrolysis and the generated oxygen gas at the anode (i.e., counter electrode) was formed as a ring of gas bubbles outside the graduated tube; (**e** and **f**) shows hydrogen gas accumulation at the top of the inverted graduated tube by replacing the electrolyte.

Calculation of Faradic efficiency:

The Faradic efficiency could be express the efficiency of a catalyst in terms of electrical energy utilization in the electrochemical reaction. The Faradic efficiency of both the catalysts was determined as following.

For HER, Faradic efficiency

$$= \frac{\text{Number of moles of hydrogen evolved}}{\text{Number of moles of hydrogen that can evolve by utilizing the employed charge}} \times 100 \ldots\ldots\ldots (8)$$

In the quantitative measurement, the hydrogen gas was evolved in chronopotentiometry electrolysis by employing the constant cathodic current. The evolved molecular hydrogen gas was found to be 0.195 mL/hour (0.78 mL/4 hours) and 0.165 mL/hour (0.66 mL/4 hours) at neutral pH and 0.2 mL/hour (0.80 mL/4 hours) and 0.18 mL/hour (0.72 mL/4 hours) in acidic pH (*i.e.* at pH 3) under 1 atm pressure for **HIM@POM-MnW(OH)$_2$** and **POM-CoW(OH)$_2$**, respectively.

Thus, the number of moles of molecular hydrogen gas evolved per hour = (0.195/22400) mol = 8.705×10^{-6} mol

$$H_{2\ ideal} = \frac{\text{Q (Total Charge employed)}}{\text{n(number of electrons required for the chemical change)}\times 1\text{Farad}} \qquad \ldots\ldots\ldots\ldots(9)$$

Here, we employed a constant cathodic current -500 μA and n = 2 for HER (as it is a two-electron process).

Thus, the H_2 ideally should evolve = $\frac{(0.0005\times3600)}{2\times96500}$ mol = 9.32×10^{-6} mol ……...(10)

Faradic efficiency = $\frac{\text{Experimentally evolved hydrogen}}{\text{Ideally evolved hydrogen}} \times 100$ ……(11)

Therefore, the Faradic efficiency at neutral pH,

For **POM-CoW(OH)$_2$** found to be = $7.36\times10^{-6}/9.32\times10^{-6}\times100$

= **78.96**%.

For **Him@POM-MnW(OH)$_2$** found to be = $8.705\times10^{-6}/9.32\times10^{-6}\times100$

= **93.34**%.

The Faradic efficiency at pH 3,

For **POM-CoW(OH)$_2$** found to be = $8.03\times10^{-6}/9.32\times10^{-6}\times100$

= **86.15**%.

For **Him@POM-MnW(OH)$_2$** found to be = $8.92\times10^{-6}/9.32\times10^{-6}\times100$

= **95.70**%.

The Faradic efficiencies for **POM-CoW(OH)$_2$** and **HIm@POM-MnW(OH)$_2$** are found to be **78.96** and **93.34**% at neutral pH for **POM-CoW(OH)$_2$** and **HIm@POM-MnW(OH)$_2$**, respectively. At pH 3, the Faradic efficiencies, respectively are **86.15** and **95.70**%.

2.3.3.6. Turn over frequency (TOF)

The turn over frequency (TOF) is the finest parameter to represent the efficiency of a water splitting catalyst.[121,122] It is defined as the number of reactant molecules getting converted into the product molecules in a unit time per active site. The TOF of both the catalysts were calculated as.

The turnover frequency is calculated by using the below equation:

$$\text{TOF} = \frac{I}{2mF} \qquad \ldots\ldots\ldots\ldots\ldots (12)$$

Where;

I = current (A) value obtained from the chronoamperometry electrolysis (**Figure 2.13(c)**),

F = Faraday constant (C mol^{-1}),

m = number of active sites (mol),

2 = number of electrons required to form one mole of hydrogen,

Here; the number of active sites (m) calculated from bellow equation

$$m = \frac{Q}{nF} \qquad \ldots\ldots\ldots\ldots\ldots (13)$$

Q = charge (C mol^{-1}) calculated by integrating the current *vs* time plot generated from the cyclic voltammogram trace recorded under non-catalytic conditions using non-aqueous medium (CH_3CN medium),

n = number of electrons involved in the catalytic process.

From equation (12) and (13),

$$\text{TOF} = \frac{I}{2\times F\times Q/nF} \qquad \ldots\ldots\ldots\ldots\ldots (14)$$

$$\text{TOF} = \frac{I}{2Q/n} \qquad \ldots\ldots\ldots\ldots\ldots (15)$$

n = 2 for both the catalysts (two electrons are involving in HER);

$$\text{TOF} = \frac{I}{Q} \qquad \ldots\ldots\ldots\ldots\ldots (16)$$

Calculation of charge (Q) from non-catalytic cyclic voltammogram:

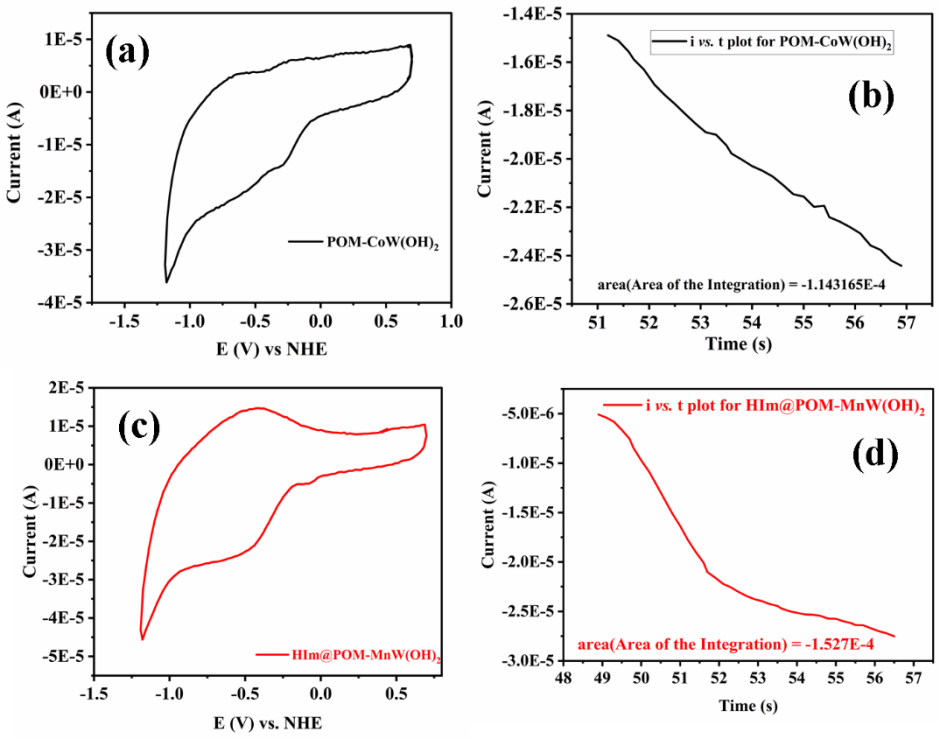

Figure 2.22. Cyclic voltammogram and its i-t plot: (**a** and **b**) for **POM-CoW(OH)$_2$**; (**c** and **d**) for **HIm@POM-MnW(OH)$_2$**. 0.1 M tetrabutylammonium perchlorate ($TBAClO_4$) in dry acetonitrile medium used as a supporting electrolyte under nitrogen atmosphere.

$$TOF = \frac{I}{Q} \qquad \ldots\ldots\ldots\ldots\ldots (16)$$

At neutral pH, the TOF values:

For **HIm@POM-MnW(OH)$_2$**,

The current (I) = -6.1513×10^{-5}A and Q = -1.5276×10^{-4} C

$$TOF = \frac{-6.1513E-5}{-1.5276E-4}$$

$$TOF = 0.4028 \text{ mol } (H_2)\ s^{-1}$$

For **POM-CoW(OH)$_2$**,

The current (I) = -3.638×10^{-5}A and Q = -1.143×10^{-4} C

$$TOF = \frac{-3.638E-5}{-1.143E-4}$$

$$TOF = 0.3182 \text{ mol } (H_2)\ s^{-1}$$

TOF of **HIM@POM-MnW(OH)$_2$ = 0.402 mol (H_2) s^{-1}**

TOF of **POM-CoW(OH)$_2$ = 0.318 mol (H_2) s^{-1}**

In acidic pH 3, a similar procedure was followed to calculate the TOF values for **HIm@POM-MnW(OH)$_2$** and **POM-CoW(OH)$_2$**.

TOF for **HIM@POM-MnW(OH)$_2$ = 1.289 mol (H_2) s^{-1}**

TOF for **POM-CoW(OH)$_2$ = 1.154 mol (H_2) s^{-1}**

The obtained TOF values are **0.318 s^{-1}** and **0.402 s^{-1}** at the neutral pH for **POM-CoW(OH)$_2$** and **HIm@POM-MnW(OH)$_2$**, respectively. But at pH 3, the TOF values respectively, are **1.154 s^{-1}** and **1.289 s^{-1}**. Thus in the present study, the TOF values can be enhanced more than three folds if pH of the neutral electrolyte solution is reduced to pH 3.

All these kinetic parameters (such as, pH measurement, R_{CT} value, Overpotential, Tafel slope, Faradic efficiency and TOF values) and stability experiments (CA electrolysis and 1000 cycles CV experiments) unambiguously establish that the title compounds **POM-CoW(OH)$_2$** and **HIm@POM-MnW(OH)$_2$** are efficient and robust electrocatalysts for hydrogen evolution reaction (HER), that work in a heterogeneous manner.

2.3.3.7. –W(OH)$_2$ functionality for HER and mechanistic view

We have already given a lot of emphasis on –W(OH)$_2$ functional group by claiming that, this functionality is responsible for electrocatalytic HER. We have reached this conclusion by performing a series of controlled experiments including detailed kinetic studies. We have shown that one of the title compounds, **POM-CoW(OH)$_2$** behaves like an inorganic acid at the neutral electrolyte solution by showing its deprotonation in an equlilibrium: POM–$\{W^{VI}(OH)_2\}_2] \rightleftharpoons [POM–\{W^{VI}(O)_2\}_2]^{2-} + 2H^+$ (eqn.7). Both these protonated and deprotonated forms of this equilibrium undergo electrochemical reduction; but only the protonated reduced form, $[POM–\{W^{V}(OH)_2\}_2]^{2-}$ reduces water to hydrogen. The deprotonated reduced form $[POM–\{W^{V}(O)_2\}_2]^{4-}$ undergoes electrochemical oxidation, but do not reduce water to molecular hydrogen, even it (deprotonated form) has more negative reduction potential (–0.655 V vs NHE) compared to its protonated form having reduction potential of –0.52 V vs NHE. A careful investigation on the electrocatalytic HER, $[POM–\{W^{V}(OH)_2\}_2]^{2-} + 2H_2O \rightarrow H_2(g) + 2OH^-$ $+[POM–\{W^{VI}(OH)_2\}_2$ (eqn. 6) shows that the number of protons is balanced properly. This will not be the case with deprotonated form $[POM–\{W^{VI}(O^-)_2\}_2]^{2-}$. That the protonated form $[POM–\{W^{VI}(OH)_2\}_2]$ is the active site for the HER in the present study can also be reasoned from the mechanistic point of view. An active site for electrocatalytic HER needs to bind the substrate, which is water (H_2O) here. One of the two reduced $\{W^{V}(OH)_2\}$ functionalities on

the POM cluster can release one hydroxyl group (known as a leaving group) and the substrate H_2O can bind to the $W^{(V)}$ center (in the place of released hydroxyl group) through its lone pair on oxygen atom. Then one electron transfer can happen from $W^{(V)}$ to the coordinated water (substrate) to form a coordinated hydroxyl group (thereby, retaining the protonated form of the catalyst active site) with the release of a H_* (can be described as Volmer step) which can combine with another H_*, formed from the other reduced $\{W^{V}(OH)_2\}$ functionality of the same cluster, to generate H_2 molecule (can be recognized as Heyrovsky step). Thus, essentially one formula unit POM cluster having two reduced $\{W^{V}(OH)_2\}^{-}$ functionalities, *i.e.*, $[POM–\{W^{V}(OH)_2\}_2]^{2-}$ binds with two substrate water molecules (by releasing two hydroxyl groups) generates a molecule of H_2 and the active sites get oxidized from $W^{(V)}$ to $W^{(VI)}$ as shown in equation 6. The deprotonated form $[POM–\{W^{VI}(O^{-})_2\}_2]^{2-}$ would not be able to do this, due to the lack of a leaving group, which can be substituted by the substrate molecule water.

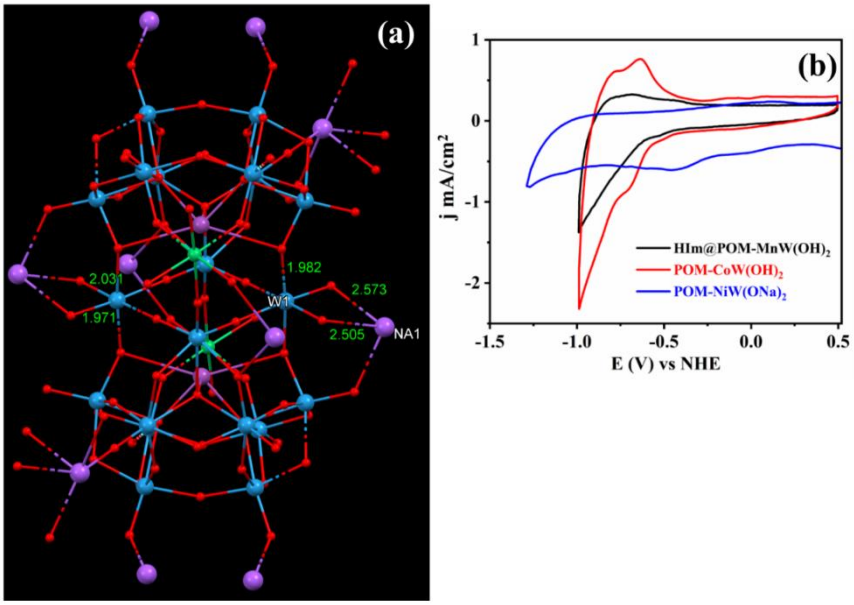

Figure 2.23. Single-crystal X-ray structure of **POM-NiW(ONa)$_2$** and its cyclic voltammogram: (a) single-crystal X-ray structure of **POM-NiW(ONa)$_2$**; (b) comparative cyclic voltammograms of **POM-CoW(OH)$_2$**, **HIm@POM-MnW(OH)$_2$,** and **POM-NiW(ONa)$_2$**. All the cyclic voltammograms were recorded in an identical condition (0.1 M potassium phosphate buffer used as a supporting electrolyte, neutral pH).

The ultimate evidence to support our model that protonated form $[POM–\{W^{VI}(OH)_2\}_2$ is accountable for HER, comes from our serendipitous isolation of nickel analogue of **POM-CoW(OH)$_2$**, The single-crystal X-ray structure of **POM-NiW(ONa)$_2$** shows that it has identical molecular structure of the cluster unit as that of **POM-CoW(OH)$_2$** except it has $\{W^{VI}(ONa)_2\}$ moieties instead of $\{W^{VI}(OH)_2\}$ moieties. As expected, **POM-NiW(ONa)$_2$** does not exhibit electrocatalytic HER (**Figure 2.23**) establishing that $\{W^{VI}(OH)_2\}$ moieties are active sites for HER.

2.4. Conclusions

We intended to establish that if W^{VI}–OH functionality is grafted on a polyoxometalate (POM) cluster surface, the resulting POM can be used as an electrocatalyst for HER. We have successfully demonstrated this structure-function relationship model by studying two POM based compounds **POM-CoW(OH)$_2$** and **HIm@POM-MnW(OH)$_2$**, each having two $\{W^{VI}(OH)_2\}$ moieties as active sites for HER. We have shown that the catalysts are more efficient in an acidic pH than the neutral pH. The obtained kinetic parameters suggest that the compound **HIm@POM-MnW(OH)$_2$** is relatively a better electrocatalyst than **POM-CoW(OH)$_2$** as far electrochemical HER is concerned. There are numerous POM compounds and many of these POM compounds have been used as OER as well as HER catalysts. There has never been an attempt/effort to designate a well-defined functional group on a POM surface that can be used for the most demanding hydrogen evolution reaction (HER). We have successfully demonstrated this. From this work, we predict that a POM compound, known or unknown, having M–OH group/functionality would function as a HER catalyst. This structure-function relation and the observed hierarchical HER trend at neutral pH provide the necessary toolkits for further introduction of more number of active sites (M–OH) and charge carriers as well as molecular modulation for the next generation catalysts to harvest the clean energy.

2.5. References

(1). Dresselhaus, M. S.; Thomas, I. L., Alternative Energy Technologies. *Nature* **2001**, *414*, 332-337.

(2). Schlapbach, L.; Züttel,A., Hydrogen-Storage Materials for Mobile Applications. *Nature* **2001**, *414*, 353-358.

(3). Subbaraman, R.; Tripkovic, D.; Chang, K.-C.; Strmcnik, D.; Paulikas, A. P.; Hirunsit, P.; Chan, M.; Greeley, J.; Stamenkovic, V.; Markovic, N. M.; Trends in Activity for The Water Electrolyser Reactions on 3*d* M(Ni,Co,Fe,Mn) Hydr(oxy)oxide Catalysts. *Nat. Mater.* **2012**, *11*, 550-557.

(4). Strmcnik, D.; Uchimura, M.; Wang, C.; Subbaraman, R.; Danilovic, N.; van der Vliet, D.; Paulikas, A. P.; Stamenkovic, V. R.; Markovic, N. M., Improving The Hydrogen Oxidation Reaction Rate by Promotion of Hydroxyl Adsorption. *Nat. Chem.* **2013**, *5*, 300-306.

(5). Subbaraman, R.; Tripkovic, D.; Strmcnik, D.; Chang, K.-C.; Uchimura, M.; Paulikas, A. P.; Stamenkovic, V.; Markovic, N. M., Enhancing Hydrogen Evolution Activity in Water Splitting by Tailoring Li^+-$Ni(OH)_2$-Pt Interfaces. *Science* **2011**, *334*, 1256.

(6). Turner, J. A., A Realizable Renewable Energy Future. *Science* **1999**, *285*, 687.

(7). Kanan, M. W.; Nocera, D. G., In Situ Formation of an Oxygen-Evolving Catalyst in Neutral Water Containing Phosphate and Co^{2+}. *Science* **2008**, *321*, 1072.

(8). Zhang, L.; Chen, Z., Polyoxometalates: Tailoring Metal Oxides in Molecular Dimension Toward Energy Applications. *Int. J. Energy Res.* **2020**, 44, 3316–3346.

(9). Roger, I.; Shipman, M. A.; Symes, M. D., Earth-Abundant Catalysts for Electrochemical and Photoelectrochemical Water Splitting. *Nat. Rev. Chem.* **2017**, *1*, 0003.

(10). Martin-Sabi, M.; Soriano-López, J.; Winter, R. S.; Chen, J.-J.; Vilà-Nadal, L.; Long, D.-L.; Galán-Mascarós, J. R.; Cronin, L., Redox Tuning The Weakley-type Polyoxometalate Archetype for the Oxygen Evolution Reaction. *Nat. Catal.* **2018**, *1*, 208-213.

(11). Chen, J.-J.; Symes, M. D.; Cronin, L., Highly Reduced and Protonated Aqueous Solutions of $[P_2W_{18}O_{62}]^{6-}$ for On-demand Hydrogen Generation and Energy Storage. *Nat. Chem.* **2018**, *10*, 1042-1047.

(12). Lei, Y.; Wang, Y.; Liu, Y.; Song, C.; Li, Q.; Wang, D.; Li, Y., Designing Atomic Active Centers for Hydrogen Evolution Electrocatalysts. *Angew. Chem. Int. Ed.* **2020** (https://doi.org/10.1002/anie.201914647).
(13). Xiu, L.; Pei, W.; Zhou, S.; Wang, Z.; Yang, P.; Zhao, J.; Qiu, J., Multilevel Hollow MXene Tailored Low-Pt Catalyst for Efficient Hydrogen Evolution in Full-pH Range and Seawater. *Adv. Funct. Mater.* **2020**, 1910028. (https://doi.org/10.1002/adfm.201910028).
(14). Xiong, B.; Zhao, W.; Chen, L.; Shi, J., One-Step Synthesis of W_2C@N, P-C Nanocatalysts for Efficient Hydrogen Electrooxidation Across the Whole pH Range. *Adv. Funct. Mater.* **2019**, *29*, 1902505.
(15). Zou, X.; Zhang, Y., Noble Metal-free Hydrogen Evolution Catalysts for Water Splitting. *Chem. Soc. Rev.* **2015**, *44*, 5148-5180.
(16). Du, Y.; Sheng, H.; Astruc, D.; Zhu, M., Atomically Precise Noble Metal Nanoclusters as Efficient Catalysts: A Bridge between Structure and Properties. *Chem. Rev.* **2020**, *120*, 526-622.
(17). Wang, Q.; Domen, K., Particulate Photocatalysts for Light-Driven Water Splitting: Mechanisms, Challenges, and Design Strategies. *Chem. Rev.* **2020**, *120*, 919-985.
(18). Zhu, J. Hu, L.; Zhao, P.; Lee, L. Y. S.; Wong, K.-Y., Recent Advances in Electrocatalytic Hydrogen Evolution Using Nanoparticles. *Chem. Rev.* **2020**, *120*, 851-918.
(19). Kim, J. H.; Hansora, D.; Sharma, P.; Jang, J.-W.; Lee, J. S., Toward Practical Solar Hydrogen Production – an Artificial Photosynthetic Leaf-to-Farm Challenge. *Chem. Soc. Rev.* **2019**, *48*, 1908-1971.
(20). Park, J.; Kwon, T.; Kim, J.; Jin, H.; Kim, H. Y.; Kim, B.; Joo, S. H.; Lee, K., Hollow Nanoparticles as Emerging Electrocatalysts for Renewable Energy Conversion Reactions. *Chem. Soc. Rev.* **2018**, *47*, 8173-8202.
(21). Ghosh, S.; Basu, R. N., Multifunctional Nanostructured Electrocatalysts for Energy Conversion and Storage: Current Status and Perspectives. *Nanoscale* **2018**, *10*, 11241-11280.
(22). Chisholm, G.; Cronin, L.; Symes, M. D., Decoupled Electrolysis using a Silicotungstic Acid Electron-Coupled-Proton Buffer in a Proton Exchange Membrane Cell. *Electrochim. Acta* **2020**, *331*, 135255.
(23). Hinnemann, B.; Moses, P. G.; Bonde, J.; Jørgensen, K. P.; Nielsen, J. H.; Horch, S.; Chorkendorff, I.; Nørskov, J. K., Biomimetic Hydrogen Evolution: MoS_2 Nanoparticles as Catalyst for Hydrogen Evolution. *J. Am. Chem. Soc* **2005**, *127*, 5308-5309.
(24). Karunadasa, H. I.; Montalvo, E.; Sun, Y.; Majda, M.; Long, J. R.; Chang, C. J., A Molecular MoS_2 Edge Site Mimic for Catalytic Hydrogen Generation. *Science* **2012**, *335*, 698.
(25). Kibsgaard, J.; Jaramillo, T. F.; Besenbacher, F., Building an Appropriate Active-Site Motif into a Hydrogen-Evolution Catalyst with Thiomolybdate $[Mo_3S_{13}]^{2-}$ Clusters. *Nat. Chem.* **2014**, *6*, 248-253.
(26). Tan, Y.; Liu, P.; Chen, L.; Cong, W.; Ito, Y.; Han, J.; Guo, X.; Tang, Z.; Fujita, T.; Hirata, A.; Chen, M. W., Monolayer MoS_2 Films Supported by 3D Nanoporous Metals for High-Efficiency Electrocatalytic Hydrogen Production. *Adv. Mater.* **2014**, *26*, 8023-8028.
(27). Shi, X.; Fields, M.; Park, J.; McEnaney, J. M.; Yan, H.; Zhang, Y.; Tsai, C.; Jaramillo, T. F.; Sinclair, R.; Nørskov, J. K.; Zheng, X., Rapid Flame Doping of Co to WS_2 for Efficient Hydrogen Evolution. *Energy Environ. Sci.* **2018**, *11*, 2270-2277.
(28). Tang, K.; Wang, X.; Li, Q.; Yan, C., High Edge Selectivity of In Situ Electrochemical Pt Deposition on Edge-Rich Layered WS2 Nanosheets. *Adv. Mater.* **2018**, *30*, 1704779.
(29). Faber, M. S.; Lukowski, M. A.; Ding, Q.; Kaiser, N. S.; Jin, S., Earth-Abundant Metal Pyrites (FeS_2, CoS_2, NiS_2, and Their Alloys) for Highly Efficient Hydrogen Evolution and Polysulfide Reduction Electrocatalysis. *J. Phys. Chem.* **2014**, *118*, 21347-21356.
(30). Henckel, D. A.; Lenz, O. M.; Krishnan, K. M.; Cossairt, B. M., Improved HER Catalysis through Facile, Aqueous Electrochemical Activation of Nanoscale WSe2. *Nano Lett.* **2018**, *18*, 2329-2335.
(31). Tsai, C.; Chan, K.; Abild-Pedersen, F.; Nørskov, J. K., Active Edge Sites in $MoSe_2$ and WSe_2 Catalysts for the Hydrogen Evolution Reaction: a Density Functional Study. *PhysChemChemPhys* **2014**, *16*, 13156-13164.

(32). Wan, C.; Regmi, Y. N.; Leonard, B. M., Multiple Phases of Molybdenum Carbide as Electrocatalysts for the Hydrogen Evolution Reaction. *Angew. Chem. Int. Ed.* **2014**, *53*, 6407-6410.
(33). Li, G.; Yu, J.; Zhou, Z.; Li, R.; Xiang, Z.; Cao, Q.; Zhao, L.; Wang, X.; Peng, X.; Liu, H.; Zhou, W., N-Doped Mo_2C Nanobelts/Graphene Nanosheets Bonded with Hydroxy Nanocellulose as Flexible and Editable Electrode for Hydrogen Evolution Reaction. *Science* **2019**, *19*, 1090-1100.
(34). Zhou, G.; Yang, Q.; Guo, X.; Chen, Y.; Xu, L.; Sun, D.; Tang, Y., Coupling Molybdenum Carbide Nanoparticles with N-doped Carbon Nanosheets as a High-Efficiency Electrocatalyst for Hydrogen Evolution Reaction. *Int. J. Hydrog. Energy* **2018**, *43*, 9326-9333.
(35). Han, N. Yang, K. R.; Lu, Z.; Li, Y.; Xu, W.; Gao, T.; Cai, Z.; Zhang, Y.; Batista, V. S.; Liu, W.; Sun, X., Nitrogen-doped Tungsten Carbide Nanoarray as an Efficient Bifunctional Electrocatalyst for Water Splitting in Acid. *Nat. Commun.* **2018**, *9*, 924.
(36). Xie, J.; Li, S.; Zhang, X.; Zhang, J.; Wang, R.; Zhang, H.; Pan, B.; Xie, Y., Atomically-thin Molybdenum Nitride Nanosheets with Exposed Active Surface Sites for Efficient Hydrogen Evolution. *Chem. Sci.* **2014**, *5*, 4615-4620.
(37). Chakrapani, V.; Thangala, J.; Sunkara, M. K., WO_3 and W_2N Nanowire Arrays for Photoelectrochemical Hydrogen Production. *Int. J. Hydrog. Energy* **2009**, *34*, 9050-9059.
(38). Yan, H.; Tian, C.; Wang, L.; Wu, A.; Meng, M.; Zhao, L.; Fu, H., Phosphorus-Modified Tungsten Nitride/Reduced Graphene Oxide as a High-Performance, Non-Noble-Metal Electrocatalyst for the Hydrogen Evolution Reaction. *Angew. Chem. Int. Ed.* **2015**, *54*, 6325-6329.
(39). Xu, Z.; Li, W. Yan, Y. Wang, H.; Zhu, H. Zhao, M.; Yan, S.; Zou, Z., In-Situ Formed Hydroxide Accelerating Water Dissociation Kinetics on Co_3N for Hydrogen Production in Alkaline Solution. *ACS Appl. Mater. Interfaces* **2018**, *10*, 22102-22109.
(40). Chen, Z.; Song, Y.; Cai, J.; Zheng, X.; Han, D.; Wu, Y.; Zang, Y.; Niu, S.; Liu, Y.; Zhu, J.; Liu, X.; Wang, G., Tailoring the d-Band Centers Enables Co_4N Nanosheets To Be Highly Active for Hydrogen Evolution Catalysis. *Angew. Chem. Int. Ed.* **2018**, *57*, 5076-5080.
(41). Zhang, Y.; Ouyang, B.; Xu, J.; Chen, S.; Rawat, R. S.; Fan, H. J., 3D Porous Hierarchical Nickel–Molybdenum Nitrides Synthesized by RF Plasma as Highly Active and Stable Hydrogen-Evolution-Reaction Electrocatalysts. *Adv. Energy Mater.* **2016**, *6*, 1600221.
(42). Gu, Y.; Chen, S. ; Ren, J.; Jia, Y. A.; Chen, C.; Komarneni, S.; Yang, D.; Yao, X., Electronic Structure Tuning in Ni_3FeN/r-GO Aerogel toward Bifunctional Electrocatalyst for Overall Water Splitting. *ACS Nano* **2018**, *12*, 245-253.
(43). Pei, Y.; Cheng, Y.; Chen, J.; Smith, W.; Dong, P.; Ajayan, P. M.; Ye, M.; Shen, J., Recent Developments of Transition Metal Phosphides as Catalysts in the Energy Conversion Field. *J. Mater. Chem. A* **2018**, *6*, 23220-23243.
(44). Popczun, E. J.; McKone, J. R. ; Read, C. G.; Biacchi, A. J.; Wiltrout, A. M. ; Lewis, N. S. ; Schaak, R. E., Nanostructured Nickel Phosphide as an Electrocatalyst for the Hydrogen Evolution Reaction. *J. Am. Chem. Soc.* **2013**, *135*, 9267-9270.
(45). Tian, J.; Liu, Q.; Asiri, A. M.; Sun, X., Self-Supported Nanoporous Cobalt Phosphide Nanowire Arrays: An Efficient 3D Hydrogen-Evolving Cathode over the Wide Range of pH 0–14. *J. Am. Chem. Soc.* **2014**, *136*, 7587-7590.
(46). Wang, M.-Q.; Ye, C.; Liu, H.; Xu, M.; Bao, S.-J., Nanosized Metal Phosphides Embedded in Nitrogen-Doped Porous Carbon Nanofibers for Enhanced Hydrogen Evolution at All pH Values. *Angew. Chem. Int. Ed.* **2018**, *57*, 1963-1967.
(47). Zheng, Y.; Jiao, Y.; Li, L. H.; Xing, T.; Chen, Y.; Jaroniec, M.; Qiao, S. Z., Toward Design of Synergistically Active Carbon-Based Catalysts for Electrocatalytic Hydrogen Evolution. *ACS Nano* **2014**, *8*, 5290-5296.

(48). Zou, X.; Huang, X.; Goswami, A.; Silva, R.; Sathe, B. R.; Mikmeková, E.; Asefa, T., Cobalt-Embedded Nitrogen-Rich Carbon Nanotubes Efficiently Catalyze Hydrogen Evolution Reaction at All pH Values. *Angew. Chem. Int. Ed.* **2014**, *53*, 4372-4376.

(49). Gao, S.; Li, G.-D.; Liu, Y.; Chen, H.; Feng, L.-L.; Wang, Y.; Yang, M.; Wang, D.; Wang, S.; Zou, X., Electrocatalytic H2 production from seawater over Co, N-codoped nanocarbons. *Nanoscale* **2015**, *7*, 2306-2316.

(50). Zheng, Y.; Jiao, Y.; Zhu, Y.; Li, L. H.; Han, Y.; Chen, Y.; Jaroniec, M.; Qiao, S.-Z., High Electrocatalytic Hydrogen Evolution Activity of an Anomalous Ruthenium Catalyst. *J. Am. Chem. Soc.* **2016**, *138*, 16174-16181.

(51). Lakadamyali, F.; Kato, M.; Muresan, N. M.; Reisner, E., Selective Reduction of Aqueous Protons to Hydrogen with a Synthetic Cobaloxime Catalyst in the Presence of Atmospheric Oxygen. *Angew. Chem. Int. Ed.* **2012**, *51*, 9381-9384.

(52). Artero, V.; Chavarot-Kerlidou, M.; Fontecave, M., Splitting Water with Cobalt. *Angew. Chem. Int. Ed.* **2011**, *50*, 7238-7266.

(53). Thoi, V. S.; Sun, Y.; Long, J. R.; Chang, C. J., Complexes of Earth-Abundant Metals for Catalytic Electrochemical Hydrogen Generation Under Aqueous Conditions. *Chem. Soc. Rev.* **2013**, *42*, 2388-2400.

(54). Nohra, B.; El Moll, H.; Rodriguez Albelo, L. M.; Mialane, P.; Marrot, J.; Mellot-Draznieks, C.; O'Keeffe, M.; Ngo Biboum, R.; Lemaire, J.; Keita, B.; Nadjo, L.; Dolbecq, A.; Polyoxometalate-Based Metal Organic Frameworks (POMOFs): Structural Trends, Energetics, and High Electrocatalytic Efficiency for Hydrogen Evolution Reaction. *J. Am. Chem. Soc.* **2011**, *133*, 13363-13374.

(55). Tourneur, J.; Fabre, B.; Loget, G.; Vacher, A.; Mériadec, C.; Ababou-Girard, S.; Gouttefangeas, F.; Joanny, L.; Cadot, E.; Haouas, M.; Leclerc-Laronze, N.; Falaise, C.; Guillon, E., Molecular and Material Engineering of Photocathodes Derivatized with Polyoxometalate-Supported $\{Mo_3S_4\}$ HER Catalysts. *J. Am. Chem. Soc.* **2019**, *141*, 11954-11962.

(56). Shinagawa, T.; Garcia-Esparza, A. T.; Takanabe, K., Insight on Tafel Slopes from A Microkinetic Analysis of Aqueous Electrocatalysis for Energy Conversion. *Sci. Rep.* **2015**, *5*, 13801.

(57). Yan, Y.; Xia, B. Y.; Zhao, B.; Wang, X., A Review on Noble-Metal-Free Bifunctional Heterogeneous Catalysts for Overall Electrochemical Water Splitting. *J. Mater. Chem. A* **2016**, *4*, 17587-17603.

(58). Lasia, A.; Rami, A., Kinetics of Hydrogen Evolution on Nickel Electrodes. *J. Electroanal. Chem.* **1990**, *294*, 123-141.

(59). Birry, L.; Lasia, A., Studies of the Hydrogen Evolution Reaction on Raney Nickel—Molybdenum Electrodes. *J. Appl. Electrochem.* **2004**, *34*, 735-749.

(60). Ye, K.-H.; Li, H.; Huang, D.; Xiao, S.; Qiu, W.; Li, M.; Hu, Y.; Mai, W.; Ji, H.; Yang, S., Enhancing Photoelectrochemical Water Splitting by Combining Work Function Tuning and Heterojunction Engineering. *Nat. Commun.* **2019**, *10*, 3687.

(61). Chandrasekaran, S.; Yao, L.; Deng, L.; Bowen, C.; Zhang, Y.; Chen, S.; Lin, Z.; Peng, F.; Zhang, P., Recent Advances in Metal Sulfides: from Controlled Fabrication to Electrocatalytic, Photocatalytic and Photoelectrochemical Water Splitting and Beyond. *Chem. Soc. Rev.* **2019**, *48*, 4178-4280.

(62). Mukhopadhyay, S.; Debgupta, J.; Singh, C.; Kar, A.; Das, S. K., A Keggin Polyoxometalate Shows Water Oxidation Activity at Neutral pH: POM@ZIF-8, an Efficient and Robust Electrocatalyst. *Angew. Chem. Int. Ed.* **2018**, *57*, 1918-1923.

(63). Singh, C.; Mukhopadhyay, S.; Das, S. K., Polyoxometalate-Supported Bis(2,2′-bipyridine)mono(aqua)nickel(II) Coordination Complex: an Efficient Electrocatalyst for Water Oxidation. *Inorg. Chem.* **2018**, *57*, 6479-6490.

(64). Mukhopadhyay, S.; Basu, O.; Kar, A.; Das, S. K., Efficient Electrocatalytic Water Oxidation by Fe(salen)–MOF Composite: Effect of Modified Microenvironment. *Inorg. Chem.* **2020**, *59*, 472-483.

(65). Manna, P.; Debgupta, J.; Bose, S.; Das, S. K., A Mononuclear Co(II) Coordination Complex Locked in a Confined Space and Acting as an Electrochemical Water-Oxidation Catalyst: A "Ship-in-a-Bottle" Approach. *Angew. Chem. Int. Ed.* **2016**, *55*, 2425-2430.

(66). Bose, S.; Debgupta, J.; Ramsundar, R. M.; Das, S. K., Electrochemical Water Oxidation Catalyzed by an In Situ Generated α-$Co(OH)_2$ Film on Zeolite-Y Surface. *Chem. Eur.* **2017**, *23*, 8051-8057.

(67). You, B.; Liu, X.; Hu, G.; Gul, S.; Yano, J.; Jiang, D.-e.; Sun, Y., Universal Surface Engineering of Transition Metals for Superior Electrocatalytic Hydrogen Evolution in Neutral Water. *J. Am. Chem. Soc.* **2017**, *139*, 12283-12290.

(68). Xie, X.; Song, M.; Wang, L.; Engelhard, M. H.; Luo, L.; Miller, A.; Zhang, Y.; Du, L.; Pan, H.; Nie, Z.; Chu, Y.; Estevez, L.; Wei, Z.; Liu, H.; Wang, C.; Li, D.; Shao, Y., Electrocatalytic Hydrogen Evolution in Neutral pH Solutions: Dual-Phase Synergy. *ACS Catal.* **2019**, *9*, 8712-8718.

(69). Danilovic, N.; Subbaraman, R.; Strmcnik, D.; Chang, K.-C.; Paulikas, A. P.; Stamenkovic, V. R.; Markovic, N. M., Enhancing the Alkaline Hydrogen Evolution Reaction Activity through the Bifunctionality of $Ni(OH)_2$/Metal Catalysts. *Angew. Chem. Int. Ed.* **2012**, *51*, 12495-12498.

(70). Singh, C.; Das, S. K., Anderson Polyoxometalate Supported $Cu(H_2O)$(phen) Complex as an Electrocatalyst for Hydrogen Evolution Reaction in Neutral Medium. *Polyhedron* **2019**, *172*, 80-86.

(71). Qin, J.-S.; Du, D.-Y.; Guan, W.; Bo, X.-J.; Li, Y.-F.; Guo, L.-P.; Su, Z.-M.; Wang, Y.-Y.; Lan, Y.-Q.; Zhou, H.-C., Ultrastable Polymolybdate-Based Metal–Organic Frameworks as Highly Active Electrocatalysts for Hydrogen Generation from Water. *J. Am. Chem. Soc.* **2015**, *137*, 7169-7177.

(72). Zhang, L.; Liu, P. F.; Li, Y. H.; Wang, C. W.; Zu, M. Y.; Fu, H. Q.; Yang, X. H.; Yang, H. G., Accelerating Neutral Hydrogen Evolution with Tungsten Modulated Amorphous Metal Hydroxides. *ACS Catal.* **2018**, *8*, 5200-5205.

(73). Sadakane, M.; Steckhan, E., Electrochemical Properties of Polyoxometalates as Electrocatalysts. *Chem. Rev.* **1998**, *98*, 219-238.

(74). Müller, A.; Krickemeyer, E.; Penk, M.; Walberg, H.-J.; Bögge, H., Spherical Mixed-Valence $[V_{15}O_{36}]^{5-}$, an Example from an Unusual Cluster Family. *Angew. Chem. Int. Ed. Eng.* **1987**, *26*, 1045-1046.

(75). Müller, A.; Sessoli, R.; Krickemeyer, E.; Bögge, H.; Meyer, J.; Gatteschi, D.; Pardi, L.; Westphal, J.; Hovemeier, K.; Rohlfing, R.; Döring, J.; Hellweg, F.; Beugholt, C.; Schmidtmann, M., Polyoxovanadates: High-Nuclearity Spin Clusters with Interesting Host−Guest Systems and Different Electron Populations. Synthesis, Spin Organization, Magnetochemistry, and Spectroscopic Studies. *Inorg. Chem.* **1997**, *36*, 5239-5250.

(76). Müller, A.; Peters, F.; Pope, M. T.; Gatteschi, D., Polyoxometalates: Very Large Clusters Nanoscale Magnets. *Chem. Rev.* **1998**, *98*, 239-272.

(77). Garai, S.; Haupt, E. T. K.; Bögge, H.; Merca, A.; Müller, A., Picking up 30 CO_2 Molecules by a Porous Metal Oxide Capsule Based on the Same Number of Receptors. *Angew. Chem. Int. Ed.* **2012**, *51*, 10528-10531.

(78). Chen, J. J.; Symes, M. D.; Fan, S. C.; Zheng, M. S.; Miras, H. N.; Dong, Q. F.; Cronin, L., High-Performance Polyoxometalate-Based Cathode Materials for Rechargeable Lithium-Ion Batteries. *Adv. Mater.* **2015**, *27*, 4649-4654.

(79). Chen, J. J.; Ye, J. C.; Zhang, X. G.; Symes, M. D.; Fan, S. C.; Long, D. L.; Zheng, M. S.; Wu, D. Y.; Cronin, L.; Dong, Q. F., Design and Performance of Rechargeable Sodium Ion Batteries, and Symmetrical Li-Ion Batteries with Supercapacitor-Like Power Density Based upon Polyoxovanadates. *Adv. Energy Mater.* **2017**, *8*, 1701021.

(80). Long, D.-L.; Burkholder, E.; Cronin, L., Polyoxometalate Clusters, Nanostructures and Materials: from Self-Assembly to Designer Materials and Devices. *Chem. Soc. Rev.* **2007**, *36*, 105-121.

(81). Miras, H. N.; Yan, J.; Long, D.-L.; Cronin, L., Engineering Polyoxometalates with Emergent Properties. *Chem. Soc. Rev.* **2012**, *41*, 7403-7430.

(82). Zang, H.-Y.; Chen, J.-J.; Long, D.-L.; Cronin, L.; Miras, H. N., Assembly of Thiometalate-Based $\{Mo_{16}\}$ and $\{Mo_{36}\}$ Composite Clusters Combining $[Mo_2O_2S_2]^{2+}$ Cations and Selenite Anions. *Adv. Mater.* **2013**, *25*, 6245-6249.

(83). Ibrahim, M.; Xiang, Y.; Bassil, B. S.; Lan, Y.; Powell, A. K.; de Oliveira, P.; Keita, B.; Kortz, U., A New Ni_{12} Cluster Based on Polyoxometalate Ligands. *Inorg. Chem.* **2013**, *52*, 8399-8408.

(84). Izarova, N. V.; Pope, M. T.; Kortz, U., Noble Metals in Polyoxometalates. *Angew. Chem. Int. Ed.* **2012**, *51*, 9492-9510.

(85). Fernandes, D. M.; Novais, H. C.; Bacsa, R.; Serp, P.; Bachiller-Baeza, B.; Rodríguez-Ramos, I.; Guerrero-Ruiz, A.; Freire, C., Polyoxotungstate@Carbon Nanocomposites As Oxygen Reduction Reaction (ORR) Electrocatalysts. *Langmuir* **2018**, *34*, 6376-6387.

(86). Ueda, T., Electrochemistry of Polyoxometalates: from Fundamental Aspects to Applications. *ChemElectroChem* **2018**, *5*, 823-838.

(87). Rhule, J. T.; Hill, C. L.; Judd, D. A.; Schinazi, R. F., Polyoxometalates in Medicine. *Chem. Rev.* **1998**, *98*, 327-358.

(88). Lv, H.; Geletii, Y. V.; Zhao, C.; Vickers, J. W.; Zhu, G.; Luo, Z.; Song, J.; Lian, T.; Musaev, D. G.; Hill, C. L., Polyoxometalate Water Oxidation Catalysts and the Production of Green Fuel. *Chem. Soc. Rev.* **2012**, *41*, 7572-7589.

(89). Zhao, C.; Kambara, C. S.; Yang, Y.; Kaledin, A. L.; Musaev, D. G.; Lian, T.; Hill, C. L., Synthesis, Structures, and Photochemistry of Tricarbonyl Metal Polyoxoanion Complexes, $[X_2W_{20}O_{70}\{M(CO)_3\}_2]^{12-}$ (X = Sb, Bi and M = Re, Mn). *Inorg. Chem.* **2013**, *52*, 671-678.

(90). Misra, A.; Kozma, K.; Streb, C.; Nyman, M., Beyond Charge Balance: Counter-Cations in Polyoxometalate Chemistry. *Angew. Chem. Int. Ed.* **2020**, *59*, 596-612.

(91). Sommers, J. A.; Hutchison, D. C.; Martin, N. P.; Kozma, K.; Keszler, D. A.; Nyman, M., Peroxide-Promoted Disassembly Reassembly of Zr-Polyoxocations. *J. Am. Chem. Soc.* **2019**, *141*, 16894-16902.

(92). Fernandes, D. M.; Araújo, M. P.; Haider, A.; Mougharbel, A. S.; Fernandes, A. J. S.; Kortz, U.; Freire, C., Polyoxometalate-Graphene Electrocatalysts for the Hydrogen Evolution Reaction. *ChemElectroChem* **2018**, *5*, 273-283.

(93). Lv, H.; Guo, W.; Wu, K.; Chen, Z.; Bacsa, J.; Musaev, D. G.; Geletii, Y. V.; Lauinger, S. M.; Lian, T.; Hill, C. L., A Noble-Metal-Free, Tetra-nickel Polyoxotungstate Catalyst for Efficient Photocatalytic Hydrogen Evolution. *J. Am. Chem. Soc.* **2014**, *136*, 14015-14018.

(94). Mulkapuri, S.; Kurapati, S. K.; Mukhopadhyay, S.; Das, S. K., A Fully Reduced $\{V^{IV}_{18}O_{42}\}$ Host and VO_4^{3-}, Cl^- as Guest Anions: Synthesis, Characterization and Proton Conductivity. *New J. Chem.* **2019**, *43*, 17670-17679.

(95). Mulkapuri, S.; Kurapati, S. K.; Das, S. K., Carbonate Encapsulation from Dissolved Atmospheric CO_2 into a Polyoxovanadate Capsule. *Dalton Trans.* **2019**, *48*, 8773-8781.

(96). Bösing, M.; Loose, I.; Pohlmann, H.; Krebs, B., New Strategies for the Generation of Large Heteropolymetalate Clusters: The β-B-SbW_9 Fragment as a Multifunctional Unit. *Chem. Eur.* **1997**, *3*, 1232-1237.

(97). Bösing, M.; Nöh, A.; Loose, I.; Krebs, B., Highly Efficient Catalysts in Directed Oxygen-Transfer Processes: Synthesis, Structures of Novel Manganese-Containing Heteropolyanions, and Applications in Regioselective Epoxidation of Dienes with Hydrogen Peroxide. *J. Am. Chem. Soc.* **1998**, *120*, 7252-7259.

(98). Loose, I.; Droste, E.; Bösing, M.; Pohlmann, H.; Dickman, M. H.; Rosu, C.; Pope, M. T.; Krebs, B., Heteropolymetalate Clusters of the Subvalent Main Group Elements Bi^{III} and Sb^{III}. *Inorg. Chem.* **1999**, *38*, 2688-2694.

(99). Wang, L.; Zhou, B.-B.; Yu, K.; Su, Z.-H.; Gao, S.; Chu, L.-L.; Liu, J.-R.; Yang, G.-Y., Novel Antitumor Agent, Trilacunary Keggin-Type Tungstobismuthate, Inhibits Proliferation and Induces Apoptosis in Human Gastric Cancer SGC-7901 Cells. *Inorg. Chem.* **2013**, *52*, 5119-5127.

(100). Wang, L.; Yu, K.; Zhou, B.-B.; Su, Z.-H.; Gao, S.; Chu, L.-L.; Liu, J.-R., The Inhibitory Effects of A New Cobalt-Based Polyoxometalate on The Growth of Human Cancer Cells. *Dalton Trans.* **2014**, *43*, 6070-6078.

(101). Zhang, W.; Liu, S.; Feng, D.; Zhang, C.; Sun, P.; Ma, F., Two Novel Krebs-type Polyoxoanions $[Cu^{I}_{2}(WO_2)_2(\beta\text{-}XW_9O_{33})_2]^{12-}$ (X = Sb^{III}, Bi^{III}) Resulting in 2D Layer Structures Linked by Copper(I) Ions and Copper(II) Complex Groups. *J. Mol. Struct.* **2009**, *936*, 194-198.

(102). Murphy, A. F.; McCormac, T., Urface Immobilisation of Transition Metal Substituted Krebs Type Polyoxometalates, $[X_2W_{20}M_2O_{70}(H_2O)_6]^{n-}$ (X = Bi or Sb, M = Co^{2+} or Cu^{2+}), by the Layer by Layer Technique. *Electrochim. Acta* **2011**, *56*, 10751-10761.

(103). Dolbecq, A.; Compain, J.-D.; Mialane, P.; Marrot, J.; Rivière, E.; Sécheresse, F.; Water Substitution on Iron Centers: from 0D to 1D Sandwich Type Polyoxotungstates. *Inorg. Chem.* **2008**, *47*, 3371-3378.

(104). Jiang, W.; Liu, L.; Hao, J., Polyoxometalate-Lyotropic Liquid Crystal Hybrid Material Formed in Room-Temperature Ionic Liquids. *J. Nanosci.* **2011**, *11*, 2168-2174.

(105). SAINT: Software for the CCD Detector System, Bruker Analytical X-ray Systems, Inc., Madison, WI, **1998**.

(106). Sheldrick, G. M., SADABS, Program for Absorption Correction, University of Gottingen, Gottingen, Germany, **1997**.

(107). Sheldrick, G. M., SHELXT – Integrated space-group and crystal-structure determination, *Acta Crystallogr., Sect. A: Found. Adv.*, **2015**, *71*, 3–8.

(108). Sheldrick, G. M., Crystal structure refinement with SHELXL, *Acta Crystallogr., Sect. C: Struct. Chem.*, **2015**, *71*, 3–8, (SHELXL-**2018/1** (Sheldrick, **2018**)).

(109). Bi, L.-H.; Kortz, U., Synthesis and Structure of the Pentacopper(II) Substituted Tungstosilicate $[Cu_5(OH)_4(H_2O)_2(A\text{-}\alpha\text{-}SiW_9O_{33})_2]^{10-}$. *Inorg. Chem.* **2004**, *43*, 7961-7962.

(110). Nellutla, S.; van Tol, J.; Dalal, N. S.; Bi, L.-H.; Kortz, U.; Keita, B.; Nadjo, L.; Khitrov, G. A.; Marshall, A. G., Magnetism, Electron Paramagnetic Resonance, Electrochemistry, and Mass Spectrometry of the Pentacopper(II)-Substituted Tungstosilicate $[Cu_5(OH)_4(H_2O)_2(A\text{-}\alpha\text{-}SiW_9O_{33})_2]^{10-}$, A Model Five-Spin Frustrated Cluster. *Inorg. Chem.* **2005**, *44*, 9795-9806.

(111). Topsoe, N. Y.; Dumesic, J. A.; Topsoe, H., Vanadia-Titania Catalysts for Selective Catalytic Reduction of Nitric-Oxide by Ammonia: I.I. Studies of Active Sites and Formulation of Catalytic Cycles. *J. Catal.* **1995**, *151*, 241-252.

(112). Topsoe, N. Y.; Topsoe, H.; Dumesic, J. A., Vanadia/Titania Catalysts for Selective Catalytic Reduction (SCR) of Nitric-Oxide by Ammonia: I. Combined Temperature-Programmed in-Situ FTIR and On-line Mass-Spectroscopy Studies. *J. Catal.* **1995**, *151*, 226-240.

(113). Kadir, P.; Attila, Y., Electrochemical Behavior of the Adsorbed Imidazolium Film on Platinum. *Zeitschrift für Physikalische Chemie, Bd.* **1996**, *196*, 109-123.

(114). Pekmez, K.; Özyöruk, H.; Yildiz, A., Electrochemistry in Aprotic Solvents Containing Anhydrous Perchloric Acid: Electroreduction of Imidazoles. *Ber. Bunsenges. Phys. Chem.* **1992**, *96*, 1805-1808.

(115). Magdić, K.; Kvastek, K.; Horvat-Radošević, V., Impedance Approach to Activity of Hydrogen Evolution Reaction on Spatially Heterogeneous GC Electrode Surfaces: Metal free vs. Ru Catalysed Case. *Electrochimica Acta* **2015**, *167*, 455-469.

(116). Garfinkel, D.; Edsall, J. T., Raman Spectra of Amino Acids and Related Compounds. X. The Raman Spectra of Certain Peptides and of Lysozyme. *J. Am. Chem. Soc.* **1958**, *80*, 3818-3823.

(117). Aberefa, O. A.; Daramola, M. O.; Iyuke, S. E., Production and Functionalization of Carbon Nanotubes for Application in Membrane Synthesis for Natural Gas Separation. *Micropor Mesopor Mat.* **2019**, *280*, 26-36.

(118). Zeng, J.; Jean, D.-i.; Ji, C.; Zou, S., In Situ Surface-Enhanced Raman Spectroscopic Studies of Nafion Adsorption on Au and Pt Electrodes. *Langmuir* **2012**, *28*, 957-964.

(119). Bribes, J. L.; El Boukari, M.; Maillols, J., Application of Raman Spectroscopy to Industrial Membranes. Part 2–Perfluorosulphonic Membrane. *J. Raman Spectrosc.* **1991**, *22*, 275-279.
(120). Shinagawa, T.; Takanabe, K., Towards Versatile and Sustainable Hydrogen Production through Electrocatalytic Water Splitting: Electrolyte Engineering. *ChemSusChem* **2017**, *10*, 1318-1336.
(121). Mahmood, J.; Li, F.; Jung, S.-M.; Okyay, M. S.; Ahmad, I.; Kim, S.-J.; Park, N.; Jeong, H. Y.; Baek, J.-B., An Efficient and pH-Universal Ruthenium-based Catalyst for the Hydrogen Evolution Reaction. *Nat. Nanotechnol.* **2017**, *12*, 441-446.
(122). S. Ghosh, A. K. Srivastava, R. Govu, U. Pal, S. Pal, A Diuranyl(VI) Complex and Its Application in Electrocatalytic and Photocatalytic Hydrogen Evolution from Neutral Aqueous Medium. *Inorg. Chem.* **2019**, *58*, 14410-14419.

CHAPTER 3

Barrel-shaped Polyoxometalates Exhibiting Electrocatalytic Hydrogen Evolution at Neutral pH

Overview:

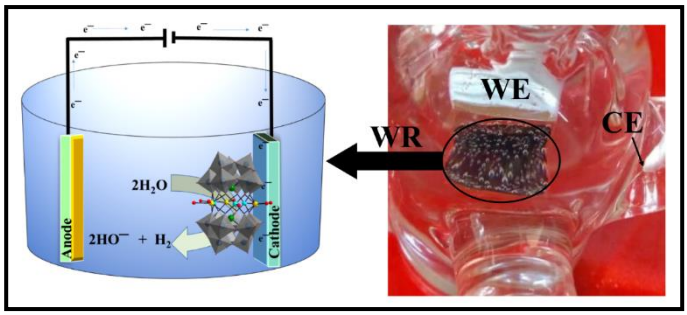

Two copper-based barrel-shaped POMs, namely $[\{H_3O\}_4\{Na_6(H_2O)_{22}\}][\{(Cu^{I}_{0.25}Cu^{I}_{0.75})(H_2O)_3\}_2\{Cu^{II}(H_2O)\}_3\{B\text{-}\alpha\text{-}Bi^{III}W^{VI}_9O_{33}\}_2]\cdot 7H_2O$ (**NaCu-POM**) and $Li_4[\{NH_4\}_2\{H_3O\}_3\{Li(H_2O)_5\}][\{Cu^{II}(SH)\}\{(Cu^{II}Cu^{I}_{1.5})(B\text{-}\alpha\text{-}Bi^{III}W^{VI}_9O_{33})\}_2]\cdot 9H_2O$ (**LiCu-POM**) were synthesized and characterized. The molecular structures of **NaCu-POM** and **LiCu-POM** are obtained from their single-crystal diffraction studies that reveal a penta- $\{Cu_5\}$- and hexa-nuclear copper $\{Cu_6\}$-wheels, sandwiched between two lacunary $\{B\text{-}\alpha\text{-}Bi^{III}W^{VI}_9O_{33}\}^{9-}$ POM units to form barrel-shaped title POM molecules. In both the compounds, the mixed-valent nature of copper centers in the penta- and hexa-nuclear copper wheels were confirmed by bond valence sum (BVS) calculations and XPS analysis. The core structures of **NaCu-POM** and **LiCu-POM** are quite similar, but the **LiCu-POM** additionally shows a sulfide ligand (SH^-) that is coordinated to one of the copper centers of $\{Cu_6\}$-wheel. The sulfide in **LiCu-POM** was expected to be generated from the *in-situ* reduction of sulfate anion since it was the only source of sulfur in the reaction (ammonia solution and lithium are expected to be involving as reducing agents). The presence of redox-active mixed-valent copper centers and their synergetic interactions with tungsten are probably driving the electrocatalytic activity of these compounds in water reduction at neutral pH. The Tafel slope values of 267 and 352 mV dec^{-1} are found for **NaCu-POM** and **LiCu-POM**, respectively. The respective turn over frequencies (TOFs) are 1.598 mol H_2 s^{-1} and 1.117 mol H_2 s^{-1} at pH 7. The Faradic efficiencies are 89% for **NaCu-POM** and 92% for **LiCu-POM** at pH 7. The catalysts are stable during 4 hours of chronoamperometric experiment and 100 cycles of cyclic voltammetric (CV) experiments. The controlled experiments exclude the chances of the decomposition of molecular catalysts to other electrochemically active species (such as, Cu or W metal nano-particles) during the course of the reaction which establish the true catalytic nature of concerned barrel-shaped POMs.

3.1. Introduction

Considering the fast growing energy demands and associated environmental concerns, hydrogen (H_2) is found to be one of the clean and efficient energy source owing to its high energy density (146 kJ g^{-1}) and carbon-free end product (*i.e.*, H_2O) formation after its usage.[1,2] There have been plenty of physical and chemical methods developed for hydrogen production. However, electrochemical hydrogen evolution/water splitting has been considered as one of the clean, efficient and sustainable methods owing to its demand for easily available reactant (water) and easily processable electrical energy, that are sole reactants and by products in the hydrogen energy cycle.[1-20] Generally, overall electrochemical water splitting (WS) reaction ($H_2O_{(l)} \rightarrow H_{2(g)} + 1/2\ O_{2(g)}$, $\Delta G° = +237.2$ kJ mol^{-1}, $\Delta E° = 1.23$ V *vs* NHE at 25 °C and 1 atm pressure) process demands high thermodynamic potential irrespective of the reaction medium.[1,18] But it could be achievable by employing a sustainable electrocatalyst. Besides, it is worthy to be noted that, hydrogen evolution is an acidic medium cathodic reaction (takes place at cathode: HER: $2H^+_{(aq)} + 2e^- \rightarrow H_{2(g)}$) and most often, used cathodic materials include noble metals (*e.g.*, Pt), which are costly and also not easily accessible. Therefore, enormous attention has been paid to develop an effective noble metal-free electrocatalysts, such as, transition metal-borides, carbides, nitrides, phosphides, selenides, sulfides, heteroatom-doped nano-carbons, polyoxometalates (POMs), metal-organic frameworks (MOFs), and polyoxometalate–metal–organic framework (POMOF) composites, *etc.* for hydrogen evolution reactions (HERs).[11-17,19] But, even after so many best efforts from pertinent science community, there is much void still left to develop an effective and robust electrocatalyst, to perform hydrogen evolution in non-acidic (alkaline/neutral pH) medium, because of its demand for an additional input energy (η) to break the H–O–H bond for water reduction reaction ($2H_2O + 2e^- \rightleftharpoons H_2 + 2OH^-$), thereby H_2 production in alkaline/neutral pH.[1,2,7,11-17,21-24] Hence, it is found to a need of the hour to develop a highly stable and active noble metal-free WR catalyst that works with minimal overpotential requirements. With this rationale in mind, our group has been actively working on developing noble metal-free POM based bio-compatible electrocatalyst for this cathodic half-cell reaction ($2H_2O + 2e^- \rightleftharpoons H_2 + 2OH^-$) at alkaline/neutral pH.

In the course of our journey, it was found that the transition metal and alkaline (such as Li^+ and Na^+) ion coupled polyoxometalates (POMs) have been identified as potential electrode materials for sustainable clean energy generation and its reversible storage.[19,20,25-37] Even though, there is a plethora of POMs combined with transition and alkaline metal ions, very limited number of examples of polyoxotungstates (POTs) with copper/lithium (or their combination in a single system)[38,39] have been reported (*Appendix Table 3(i)*).[25-28] Besides, with their potential applicability of small cation charge carriers (*i.e.* Li^+ and Na^+) in clean energy harnessing[40-44] and in reversible energy storage devices (solid-state batteries, battery electrodes, redox flow batteries),[19,45,46] curiosity to embed these small cations into POTs' matrix and

exploring the energy applications of the resulting Li/Na-POTs has exponentially been increasing.

In addition to small cationic charge carriers added POTs, transition metal ion anchored POTs have also been evolving parallelly. As a special mention, copper ion incorporated POTs have been well-known redox active systems and found to play a vital role in photochemical hydrogen evolution.[42-44] But, they are largely unexplored for their potential application in electrocatalytic hydrogen evolution reactions. Interestingly, among all reported copper containing POT systems, copper ion(s) sandwiched POTs have been in focus, owing to their interesting structural and functional properties. Thanks to some of the actively working groups in this area, who have been extensively explored tri- to hexa-nuclear copper-wheel substituted sandwich type POTs with As^{III} or Sb^{III} as hetero atom.[47-57] Though, a few reports have come out with tri- and tetra-nuclear copper-wheel substituted sandwich type POTs containing Bi^{III} ion as hetero atom,[42,58-60] tungstobimuthates with higher nuclear copper-wheels have not been much studied and opens door for their construction and exploration.

In the wake of these significant features and necessity associated with this class of materials, we attempted to synthesize copper containing POTs with small ion charge carriers. Here we are reporting two such (Na^+ and Li^+ containing) functional copper-polyoxotunstobismuthate barrels $[\{H_3O\}_4\{Na_6(H_2O)_{22}\}][\{(Cu^I_{0.25}Cu^I_{0.75})(H_2O)_3\}_2\{Cu^{II}(H_2O)\}_3\{B\text{-}\alpha\text{-}Bi^{III}W^{VI}_9O_{33}\}_2]\cdot 7H_2O$ (**NaCu-POM**) and $Li_4[\{NH_4\}_2\{H_3O\}_3\{Li(H_2O)_5\}][\{Cu^{II}(SH)\}\{(Cu^{II}Cu^I_{1.5})(B\text{-}\alpha\text{-}Bi^{III}W^{VI}_9O_{33})\}_2]\cdot 9H_2O$ (**LiCu-POM**), fabricated in a simple one-pot wet synthetic procedure. Careful structural analysis of fabricated systems revealed that, the copper centers are present as mixed-valent ions, arranged in the form of penta- and hexa-nuclear copper wheels sandwiched between POT clusters in compounds **NaCu-POM** and **LiCu-POM**, respectively. We have described their detailed electrochemical properties emphasizing the electrocatalytic hydrogen evolution reactions (HERs) at the neutral pH.

3.2. Experimental section

3.2.1. Materials and methods

All chemicals were of analytical grade and used as received. All the experiments were conducted in ambient conditions using deionized water. Both of the barrel type compounds were synthesized in a one-pot wet reaction method, as described below.

3.2.1.1. Synthesis of $[\{H_3O\}_4\{Na_6(H_2O)_{22}\}][\{(Cu^I_{0.25}Cu^I_{0.75})(H_2O)_3\}_2\{Cu^{II}(H_2O)\}_3\{B\text{-}\alpha\text{-}Bi^{III}W^{VI}_9O_{33}\}_2]\cdot 7H_2O$ (NaCu-POM)

3.0 g of $Na_2WO_4\cdot 2H_2O$ was dissolved in 50 mL of water and subsequently 0.5 mL of 6 M nitric acid (HNO_3) was added; then the reaction mixture was left on a hot plate for stirring at 90 °C for 15 min. The resulting reaction mixture was allowed to cool down to room temperature,

filtered and collected the filtrate. Later, an aqueous solution of copper sulphate (0.5 g $CuSO_4 \cdot 5H_2O$ dissolved in 2 mL of water) was added drop wise to the above filtrate with continuous stirring upon which the colour of the reaction mixture turned to parrot-green from colourless. Subsequently, an acidic solution of bismuth nitrate (0.48 g of $Bi(NO_3)_3 \cdot 5H_2O$ dissolved in 1 mL of 6M nitric acid) was added drop wise under constant stirring followed by adjusting pH of the reaction mixture to 6.85 using a 15% aqueous ammonia solution. The resulted reaction mixture was left for stirring for 1 hour at 90 °C while covering the reaction flask with a watch glass. The resulting reaction mixture was filtered twice to get a clear solution and was left for crystallization at room temperature. Block-shaped yellow-green crystals were isolated after one week, washed twice with minimum amount of ice-cold water and kept for drying at room temperature. Yield: 1.52 g (49.65% based on Tungsten). Anal. calc. % (Found from ICP-OES) for $H_{87}O_{108}Bi_2Cu_5Na_6$: Bi, 6.89 (7.07); Cu, 6.29 (6.54); Na, 2.28 (2.03); W, 54.59 (54.90); TGA: *ca.*% 12.0 (10.40); FTIR (cm^{-1}): 3360, 2060, 1629, 1415, 940, 873, 689; UV-Vis (nm): 1258, 520, 275.

3.2.1.2. Synthesis of $Li_4[\{NH_4\}_2\{H_3O\}_3\{Li(H_2O)_5\}][\{Cu^{II}(SH)\}\{(Cu^{II}Cu^{I}_{1.5})(B\text{-}\alpha\text{-}Bi^{III}W^{VI}_9O_{33})\}_2]\cdot 9H_2O$ (LiCu-POM)

0.6 g of Li_2WO_4 was dissolved in a 20 mL of water and heated at 90 °C on a hot plate followed by drop wise addition of bismuth nitrate solution (0.12 g of $Bi(NO_3)_3 \cdot 5H_2O$ dissolved in 1 mL of 6 M nitric acid) while maintaining the temperature. Later, after around 15 minutes of stirring, aq. $CuSO_4 \cdot 5H_2O$ solution (0.125 g in 2 mL) was added drop wise to the above colorless reaction mixture under stirring at the same temperature. The reaction mixture was then treated with 125 µl of 6 M nitric acid, and the stirring was continued for more 30 minutes. Then the pH of the reaction mixture was adjusted to 6.87, using a 15% aqueous ammonia solution. The resulting reaction mixture was again heated at 90 °C for additional 1 hour with continuous constant stirring (covering the reaction flask with a watch glass). The resulting reaction mixture was then filtered to get a clear filtrate, which was left for crystallization at room temperature. The golden yellow colored crystals, isolated after 10 days, were washed twice with a minimum amount of ice-cold water and kept for drying at room temperature. Yield: 0.33 g (46.74% based on Tungsten). Anal. calc. % (Found from ICP-OES) for $H_{46}N_2O_{83}S_1Bi_2Cu_6Li_5W_{18}$: Bi, 7.53 (7.32); Cu, 6.87 (7.24); Li, 0.63 (0.71); S, 0.58 (0.2); W, 59.63 (60.19); TGA: *ca.*% 7.40 (7.91); FTIR (cm^{-1}): 3375, 3170, 2840, 2060, 1621, 1415, 932, 865, 686; UV-Vis (nm): 1341, 545, 281.

3.2.2. Physical measurements

Both the compounds (**NaCu-POM** and **LiCu-POM**) were characterized by single-crystal X-ray diffraction (SCXRD) as well as other analytical techniques (such as FT-IR, Raman, TGA, PXRD, XPS, and ICP-OES *etc.*) including electrochemical studies. The FT-IR spectra were collected using Bruker Tensor II equipped with Platinum ATR (Attenuated Total Reflectance) accessory. Raman spectra were recorded with Wi-Tec alpha 300AR laser confocal optical

microscope (T-LCM) facility coupled with a Peltier cooled CCD detector using 785 nm Argon ion laser. Thermogravimetric analyses were performed on the Perkin Elmer – STA6000 analyzer. The powder X-ray diffraction (PXRD) patterns were recorded using Bruker D8-Advance diffractometer equipped with graphite monochromated CuKα1 (1.5406 Å) and Kα2 (1.54439 Å) radiation. X-ray photo electron spectra (XPS) of crystalline powder samples were collected with Thermo Scientific K-ALPHA surface analysis spectrometer using Al Kα radiation (1486.6 eV). Elemental analyses were carried out on inductive coupled plasma optical emission spectroscopy (ICP-OES) Varian 720ES. Field emission scanning electron microscopy-energy dispersive X-ray analysis was conducted on Carl Zeiss model Ultra 55 microscope equipped with Oxford Instruments X-MaxN SDD (50 mm^2) system functioned with INCA analysis software.

3.2.2.1. X-ray crystallography

Suitable nascent single-crystals of **LiCu-POM** and **NaCu-POM** were selected from the bunch of crystals present in the mother liquor and quickly mounted on a glass fiber-tip using the silicone grease. The X-ray diffraction data of **LiCu-POM** were collected at 293 K. Since the crystals of **NaCu-POM** are found to loose crystallinity under the ambient environment, the data collection was carried out at 100 K temperature and under nitrogen gas flow. A Bruker D8 Quest CCD diffractometer having a Mo–Kα (λ = 0.71073 Å) graphite monochromatic X-ray beam source was used to collect the diffraction data of both the compounds and 40 mm of the crystal-to-detector distance was maintained while collection. The ω scans were recorded with a width of 0.3°. Data reduction was performed by SAINT PLUS,[61] and empirical absorption corrections were done using equivalent reflections performed by the SADABS.[62] Structure solutions and full-matrix least-squares refinements were carried out using SHELXT-2015,[63] SHELXL-2015.[64] All the non-hydrogen atoms refined anisotropically. The following atoms Cu_4, Li_1, Li_3, O_1, O_2, O_{14}, O_{18}, O_{19} of **LiCu-POM** and O_{20}, O_{36} of **NaCu-POM** adapted atomic displacement parameter (ADP) disorder. The specified atoms were refined with EADP instruction. Attempts made to locate hydrogen atoms of lattice ammonia and water molecules in **LiCu-POM** and **NaCu-POM** were unsuccessful. The crystallographic details such as structure refinement parameters, bond distances, and bond angles of **LiCu-POM** and **NaCu-POM** are provided in **Table 3.1** and *Appendix 3(ii)* respectively. The **CSD–2033171**, **CSD–2033173** contains the supplementary crystallographic data files of **LiCu-POM** and **NaCu-POM** respectively. The crystal data of the **LiCu-POM** and **NaCu-POM** can be obtained free of charge via ttp://www.ccdc.cam.ac.uk/conts/retrieving.html, or from the Cambridge Crystallographic Data Centre, 12 Union Road, Cambridge CB2 1EZ, UK; fax: (+44) 1223-336-033; or e-mail: deposit@ccdc.cam.ac.uk.

Table 3.1. Crystal data and structural refinement parameters for LiCu-POM and NaCu-POM

Parameter	**NaCu-POM**	**LiCu-POM**
Empirical formula	$H_{87}O_{108}Bi_2Cu_5Na_6W_{18}$	$H_{46}N_2O_{83}S_1Bi_2Cu_6Li_5W_{18}$
Formula weight	5998.40	5549.44
T(K)/ λ (Å)	100(2) /0.71073	293(2)/0.71073
Crystal system	Monoclinic	Tetragonal
Space group	C2/m	P-421m
a Å	33.074(4)	16.7401(18)
b Å	19.569(2)	16.7401(18)
c Å	14.8466(17)	13.869(2)
α (°)	90	90
β (°)	90.589(4)	90
γ (°)	90	90
Volume ($Å^3$)	9608(2)	3886.6(10)
Z	2	2
P calc. (Mg/m^3)	4.086	4.726
μ (mm^{-1}), *F*(000)	26.331, 10292	32.767, 4762
Goodness-of-fit on F^2	1.020	1.050
R_1/wR_2 [$I > 2\sigma(I)$]	0.0355/0.0868	0.0309/0.0779
R_1/wR_2 (all data)	0.0471/0.0919	0.0324/0.0786
Largest diff. peak/hole (e $Å^{-3}$)	3.233/-2.323	2.849/-2.895

3.2.2.2. Electrochemical Measurements

All the electrochemical experiments were performed using three-electrode electrochemical cell. The catalyst modified glassy carbon was a working electrode, a home-made Ag/AgCl (3M) was a reference electrode, whereas Pt spring was used as a counter electrode. The neutral pH potassium phosphate buffer (0.1 M) was used as the supporting electrolyte for all the experiments. For catalyst modified electrode fabrication, 4 mg of sample along with 1 mg of acetylene carbon black was taken into 1 mL of the ethanol-water mixture (3:2 ratio). Later, 20 µL of 5 wt% aqueous Nafion binder was added to it and was sonicated at room temperature for around 30 minutes to obtain a homogeneous mixture. 10 µL of this homogeneous ink was coated on to a 3 mm diameter (0.0706 cm^2 geo-metrical area) glassy carbon (GC) electrode (which leaves around 40 µg of the material on the working electrode). Additionally, 5 wt % Nafion solution in the ethanol (4:6 ration of Nafion-ethanol mixture) was also prepared and coated drop of solution over above electrode coated material. The same amount of sample loading, was maintained for all the electrochemical experiments unless otherwise notified. The coated ink was dried under the IR-lamp (temp ~70 °C) and the electrode was left at room temperature for 5 min before using. For all the electrochemical experiments, UHP grade nitrogen gas was passed through electrolyte solution to obtain saturation, and continuous

nitrogen gas flow (1 atm) was maintained over the solution throughout the experiments. The experimentally obtained potential values were converted to the NHE scale (normal hydrogen electrode scale) following the relation of E(NHE) = E(Ag/AgCl) + 0.204V when the Ag/AgCl electrode is used as a standard reference electrode. The cyclic voltammogram (CV) scans were initiated at the open circuit potential (OCP), and five continuous cycles of the CV were recorded to make the quiescent electrolyte. Bulk-electrolysis experiments were conducted using 0.5 cm^2 area fluorinated tin oxide 'FTO' working, and large area Pt wire counter electrode. The catalyst loading of 1mg/cm^2 was maintained on the FTO electrode. Most of the cyclic voltammograms were recorded with a scan rate of 100 mVs^{-1}. The Nyquist data of an electrochemical impedance spectra were collected applying –796 mV (vs NHE) in an identical experimental conditions. The obtained complex impedance data of Nyquist plots were constructed as real impedance Z(Real) on X-axis and imaginary impedance Z(Im) on Y-axis, and was fitted with the following circuit $((R_1/Q_1)+(R_2/Q_2)+Q_3)$. Tafel data were obtained in the galvanostatic mode under study-state mass flow. The study-state mass was maintained by 480 rpm constant stirring of electrolyte throughout the experiment.

3.3. Results and Discussion

3.3.1. Detailed discussion on synthesis

In the present work, a mixed-valent $\{Cu_5\}$- penta- and $\{Cu_6\}$- hexa-nuclear copper-wheel coupled polyoxotungstate (POT) barrels with sodium (**NaCu-POM**) and lithium ions (**LiCu-POM**) were constructed following an one-pot wet synthetic protocol at 90 °C temperature and near neutral pH. Both the systems were water insoluble and considerably air stable, except slight degradation in the crystal quality with time in the case of **NaCu-POM**. The crystal quality degradation is a quite commonly expected phenomenon in POM chemistry as they tend to lose lattice water. These analogous molecular systems **NaCu-POM** and **LiCu-POM** were thoroughly characterized by SCXRD, ICP-OES and other analytical techniques *viz*. FT-IR, Raman, XPS, PXRD, TGA *etc*., wherever needed. Careful structural analysis reveals that, each molecule broadly consisting of mixed-valent penta- and hexa-nuclear copper-wheels at the center connecting two lacunary $\{B\text{-}\alpha\text{-}Bi^{III}W^{VI}_9O_{33}\}^{9-}$ POM units. The copper centers of wheels are found to be in two different oxidation states (Cu(I) and Cu(II)). These varying oxidation states of copper atoms were determined and confirmed by bond valence sum (BVS) calculations and other analytical method *viz.*, X-ray photoelectron spectroscopy (XPS) (discussed in later parts of this section). The appearance of mixed-valent species in product, points towards *in-situ* partial reduction of copper species in aqueous ammonium medium as stated in a few earlier reports.[56,65] The charge on the title Cu-POM clusters was mainly balanced with sodium and lithium counter cations, yielding **NaCu-POM** and **LiCu-POM**, respectively. Though the basic core structure of both Cu-POT barrels has been found to be similar, the careful SCXRD data analysis and elemental analysis show a few significant distinctions between **NaCu-POM** and **LiCu-POM**, especially in terms of coordination sphere of copper ions. To state it clearly, in

NaCu-POM, copper coordination spheres are made of only oxygen donor atoms, whereas in the case of **LiCu-POM**, one of the copper ions is coordinated to SH^- group. The newly appeared SH^- is assumed to be derived from lithium or ammonium ion assisted reduction of sulfate anion (as it was the only source of sulphur in the reaction system) in an aqueous ammonium solution. The presence of sulfide group coordinated to a boarder-line acidic copper(II) center is indicated by single crystal X-ray diffraction analysis and BVS calculations and later it was substantiated by other analytical confirmation techniques *viz*. ICP-OES and XPS analyses (*vide infra*). Finally, results from all of the analytical data led us to conclude and propose molecular formulas for **NaCu-POM** and **LiCu-POM** as $[\{H_3O\}_4\{Na_6(H_2O)_{22}\}][\{(Cu^{I}_{0.25}Cu^{I}_{0.75})(H_2O)_3\}_2\{Cu^{II}(H_2O)\}_3\{B\text{-}\alpha\text{-}Bi^{III}W^{VI}_9O_{33}\}_2]\cdot 7H_2O$ and $Li_4[\{NH_4\}_2\{H_3O\}_3\{Li(H_2O)_5\}][\{Cu^{II}(SH)\}\{(Cu^{II}Cu^{I}_{1.5})(B\text{-}\alpha\text{-}Bi^{III}W^{VI}_9O_{33})\}_2]\cdot 9H_2O$, respectively. Detailed data interpretations are presented in following sections:

3.3.2. Physical characterizations

3.3.2.1. Single-crystal X-ray crystallography

SCXRD analysis reveals that the **NaCu-POM** crystallizes in a monoclinic *C2/m* space group. There are four copper atoms in the pertinent asymmetric unit in the crystal structure of compound **NaCu-POM** with different occupancies (Cu1, 1.0; Cu2, 0.50; Cu3, 0.75; and Cu4, 0.25). Thus, Cu1 has full occupancy, Cu2 has half occupancy, Cu3 has three-fourth occupancy and Cu4 has one-fourth occupancy. Therefore, 2.5 copper atoms present in the asymmetric unit and thereby there are five copper centers per formula unit of this compound $[\{H_3O\}_4\{Na_6(H_2O)_{22}\}][\{(Cu^{I}_{0.25}Cu^{I}_{0.75})(H_2O)_3\}_2\{Cu^{II}(H_2O)\}_3\{B\text{-}\alpha\text{-}Bi^{III}W^{VI}_9O_{33}\}_2]\cdot 7H_2O$ **NaCu-POM**), even though the **Figure 3.1**(**a**) shows that there are apparent six copper centers per barrel molecule (all coppers in the barrel are not with full occupancies). The structural analysis shows that two units of the lacunary $\{B\text{-}\alpha\text{-}Bi^{III}W^{VI}_9O_{33}\}^{9-}$ POMs are coupled together by a penta-nuclear copper (Cu_5)-wheel *i.e.*, $[\{(Cu^{I}_{0.25}Cu^{I}_{0.75})(H_2O)_3\}_2\{Cu^{II}(H_2O)\}_3]^{8+}$ (**Figure 3.1**(**b**)). Based on the coordination environment and oxidation states (see BVS calculations and XPS analysis, *vide infra*), copper atoms in the (Cu_5)-wheel were divided into two types. Type-(a) consists of three alternatively arranged copper atoms (Cu1, $^{\#}$Cu1, and Cu2; $^{\#}$symmetrically equivalent) with square pyramidal geometry, whereas the remaining two copper atoms (Cu3, $^{\#}$Cu3 and Cu4) are with distorted octahedral geometry included in type-(b). These two types of atoms are having a sharp distinction not only in terms of their geometrical environment (**Figure 3.1**(**b**)), but also in terms of their oxidation states. Type-(a) includes Cu(II) ions and Cu(I) ions in type-(b)) that are consistent with BVS calculations and other analytical techniques (*vide infra*).

Additionally, sodium counter cations are found in the form of sodium-aqua wheels in the overall crystal structure. Each of these wheels was made up of twelve doubly aqua-bridged sodium atoms with four additional non-bridging coordinated water molecules (**Figure 3.1**(**c**)). In the crystal structure, each sodium-aqua wheel is bridged between two units of above

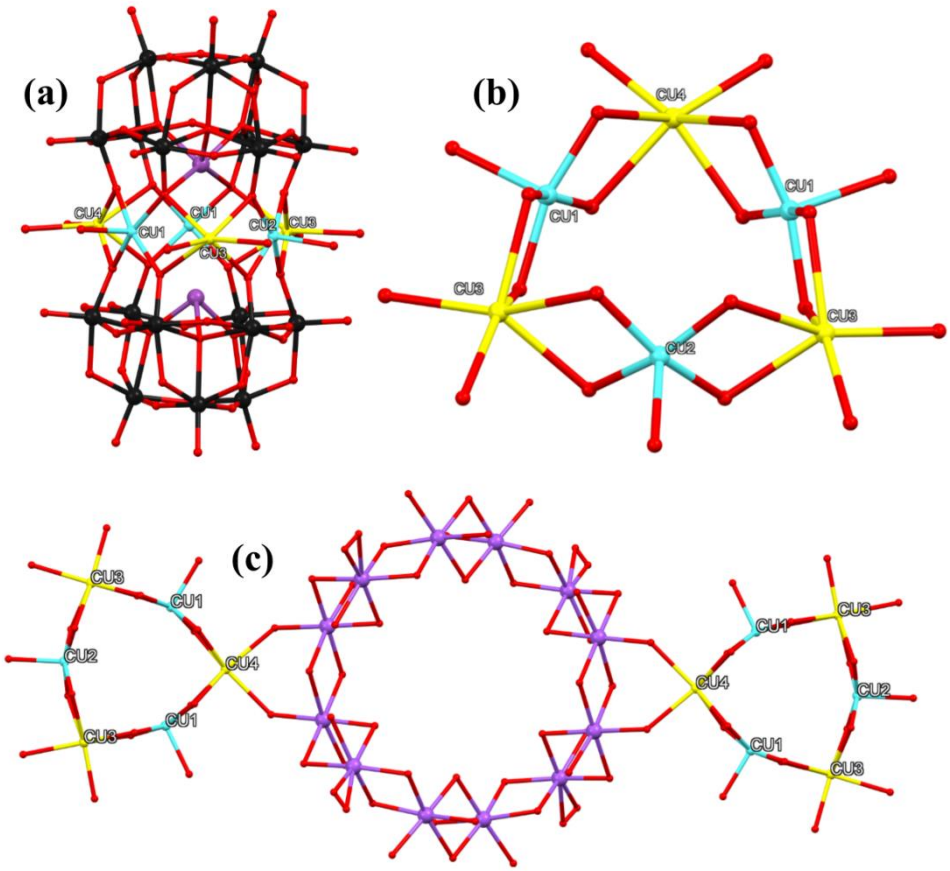

Figure 3.1. Single crystal-structure analysis of barrel-shaped **NaCu-POM**: (**a**) ball-stick representation of **NaCu-POM** cluster; (**b**) a penta-nuclear copper wheel of **NaCu-POM**; (**c**) connectivity of sodium aqua-wheel with two penta-nuclear copper wheels in side on ways (color code: cyan, Cu^{2+}; yellow, Cu^{1+}; dark-grey, tungsten; purple, bismuth; red, oxygen; sodium, violate).

discussed polyoxotungstate (POT) barrels in a 'side on' manner, by sharing a pair of copper wheel coordinated aqua-ligands; this leads to the formation of a {POT}-{Na-wheel}-{POT} type extended arrangement throughout the crystal structure (**Figure 3.1**(**c**)). This {POT}-{Na-wheel}-{POT} extended structure is further observed to interact with two such parallelly arranged neighbouring units with the plug-socket type of arrangement (**Figure 3.2**(**a** and **b**)) and yielding a 1D-supramolecular chain propagating in the crystallographic *c*-axis. These 1D chains are further closely packed and cemented by supramolecularly interacted crystal water molecules along with other inter chain secondary interactions that lead to a water-insoluble 3D-supra molecular network. In 2003, Weakley group isolated an iso-structural copper-tungstobismuthate barrel system $[\{Na(H_2O)_2\}_3\{Cu^{II}(H_2O)\}_3\{Bi^{III}W^{VI}_9O_{33}\}_2]^{9-}$ (**Cu_3BiW_9**).[58] But, the major difference between earlier report and present barrel lies in the composition of the center connecting wheel of the core barrel structure. In the case present (**NaCu-POM**) $[\{(Cu^{I}_{0.25}Cu^{I}_{0.75})(H_2O)_3\}_2\{Cu^{II}(H_2O)\}_3\{B\text{-}\alpha\text{-}Bi^{III}W^{VI}_9O_{33}\}_2]^{10-}$ system, the central belt is a penta-nuclear copper $\{Cu_5^{(II/I)}\}$-wheel whereas **Cu_3BiW_9** possess a hexa-nuclear tri-copper and

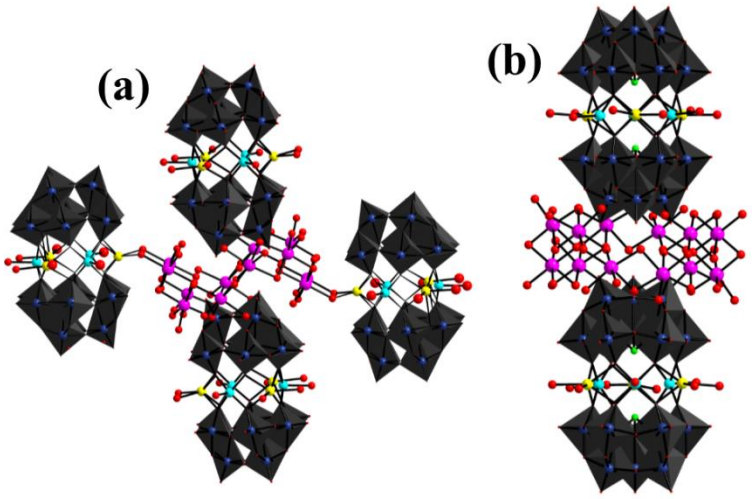

Figure 3.2. Single crystal-structure analysis of barrel-shaped **NaCu-POM**: (**a**) Ball-stick representation of crown ehter type sodium-aqua wheel connected with two barrel-shaped POMs in side-on manner and further sandwiched by other two POM barrels in plug-socket mode; (**b**) sodium aqua-wheel was sandwich by two POM barrels (plug-socket type) (color code: cyan, Cu^{2+}; yellow, Cu^{1+}; dark-grey polyhedral, tungsten (WO_6); red, oxygen; sodium, violate).

tri-sodium $\{Na_3^{(I)}Cu_3^{(II)}\}$-wheel. Further, the present **NaCu-POM** system consists of mixed-valent copper $\{Cu_5^{(II/I)}\}$-wheel, but in the case of **Cu_3BiW_9**, the copper in center wheel was only in divalent state Cu(II)-wheel. The structural similarity prompted us to crosscheck the possibility of the presence of sodium ions in the central copper wheel; thus the concerned distorted octahedral copper centers (in the present work) were attempted to refine as sodium. But, the refinement was unstable and increment in the residual electron density as well as R_1 factor were observed. On the other hand, respective atoms and cluster framework oxygen atoms were also affected with non-positive definition (NPD) alert. These crystallographic factors clearly suggest that the presence of only copper ions at the distorted octahedral geometric centers in the central metal belt. Besides, electronic resonance or disorder is commonly observed phenomenon in similar type of systems and in present case, the Cu3 center has occupancy factors of 0.75.[38,42] In addition to the crystallographic characterization, the molecular formula of the **NaCu-POM** system has also been deduced from ICP-OES analysis of the synthesized material.

On the other hand, **LiCu-POM** was crystallized in the tetragonal *P-42$_1$m* space group and similar to the structure of **NaCu-POM**, in this structure also, two identical lacunary [B-α-$Bi^{III}W^{VI}_9O_{33}]^{9-}$ POM units are linked together by a $\{Cu_6\}$-wheel $[\{Cu^I\}_3\{Cu^{II}(SH)\}\{Cu^{II}\leftarrow(O{=}W)\}_2]^{9+}$ (this +9 charge is based on the charges of only copper centers excluding the ligand charges) and have made it a barrel-shaped POM cluster anion $[\{Cu^{II}(SH)\}\{(Cu^{II}Cu^{I}_{1.5})(B\text{-}\alpha\text{-}Bi^{III}W^{VI}_9O_{33})\}_2]^{9-}$ (**Figure 3.3**(**a**)) with the only notable distinction (as mentioned earlier and in formula as well) of a presence of sulfide coordinating copper center in this **LiCu-POM** compound. Interestingly, the **LiCu-POM** also shows the

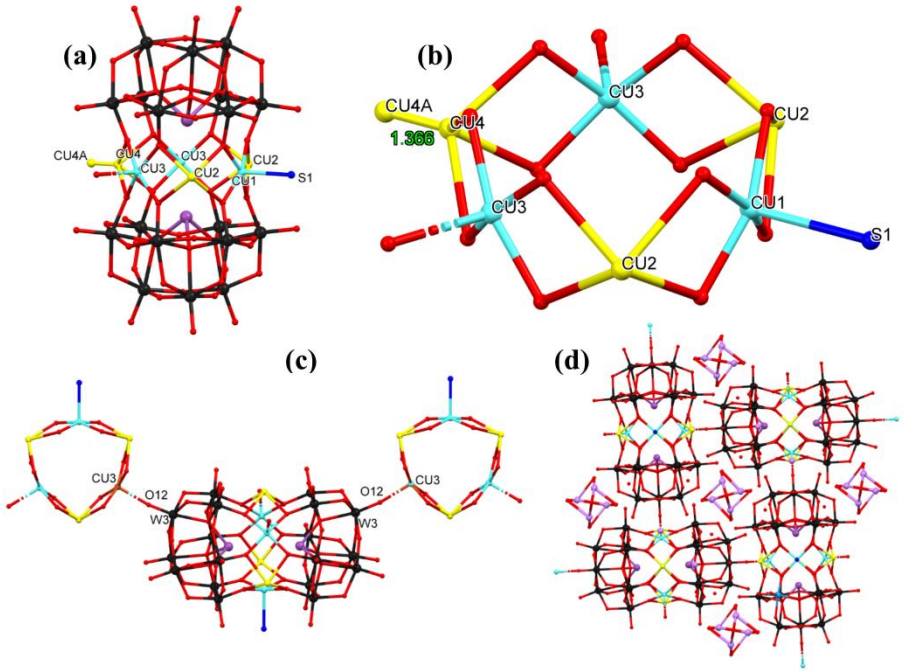

Figure 3.3. Single crystal-structure analysis of barrel-shaped compound **LiCu-POM**: (**a**) ball-stick representation of **LiCu-POM** cluster; (**b**) a hexa-nuclear copper wheel of **LiCu-POM** (the disordered copper center present outside the copper wheel labelled as Cu4a (yellow color ball)); (**c**) connectivity of barrel-shaped POM cluster with hexa-nuclear copper wheel through the W=O–Cu linkage; (**d**) layer-like two dimensional (2D) network (crystallographic *ab*-plane); the channels present in this 2D network are occupied by lithium aqua clusters (color code: cyan, Cu^{2+}; yellow, Cu^{1+}; dark-grey, tungsten; purple, bismuth; red, oxygen; lithium, violate).

presence of a mixed-valent but hexa-nuclear copper $\{Cu_6\}$-wheel *i.e.*, $[\{Cu^{I}\}_3\{Cu^{II}(SH)\}\{Cu^{II}\leftarrow(O=W)\}_2]^{9+}$ (**Figure 3.3**(**b**)). In this structure also, the central hexa-nuclear copper-wheel consists of two types of coordination geometries and it is sandwiched between two lacunary $[B\text{-}\alpha\text{-}Bi^{III}W^{VI}_9O_{33}]^{9-}$ POM anions. In type-(a), the copper(II) (Cu1, Cu3 and $^{\#}$Cu3) centers were present in square-pyramidal geometry (penta-coordinated). The four corners of the basal plane of the $\{Cu_6\}$-wheel are coordinated by bridged oxo groups from lacunary $[B\text{-}\alpha\text{-}Bi^{III}W^{VI}_9O_{33}]^{9-}$ POM clusters. Whereas the apical position of one of the coppers (Cu1) is coordinated by a hydrogen sulphide (SH^{-}) molecule (Cu^{II}–SH) and that of remaining two copper centers (Cu3 and $^{\#}$Cu3) are occupied by ($Cu^{II}\leftarrow$O=W) terminal oxygen of other adjacent POT barrels.

On the other hand, type-(b) copper(I) (Cu2, $^{\#}$Cu2 and Cu4) centers adopt distorted square-planar geometry (tetra-coordinated). All the four coordination sites of copper(I) centers ligated with oxo-groups of two lacunary $[B\text{-}\alpha\text{-}Bi^{III}W^{VI}_9O_{33}]^{9-}$ POM anions of the barrel. These Cu(I) centers are placed in the alternative sites of the copper-wheel (**Figure 3.3**(**b**)), similar to that of

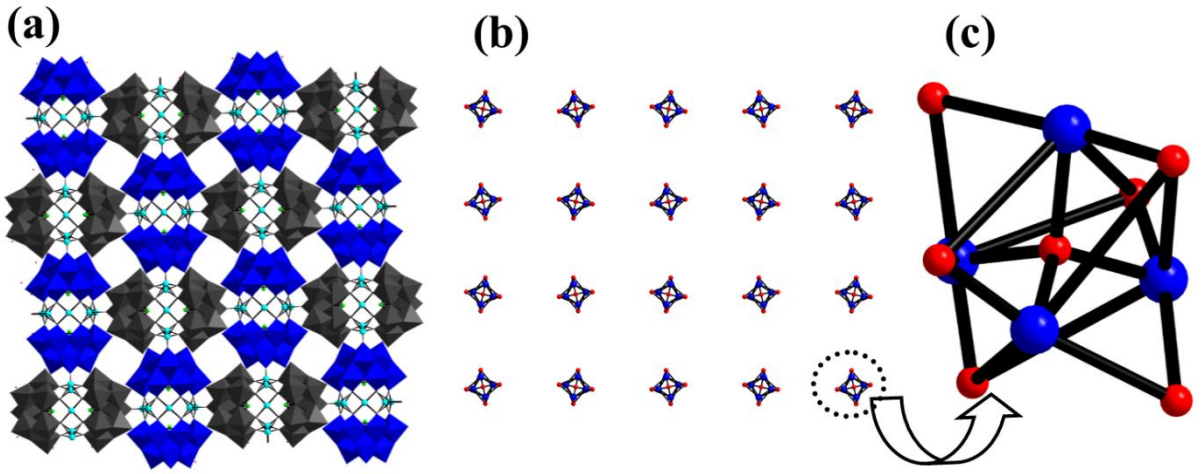

Figure 3.4. Single crystal-structure analysis of barrel-shaped compound **LiCu-POM**: (**a**) Overall packing diagram in the crystal structure of **LiCu-POM** showing 2D network structure, formed by coordinated covalent bonds among barrel-shaped clusters, leaving a 1D void spaces looking through crystallographic *c*-axis; (**b**) lithium-aqua clusters are separately shown which are present in the 1D channels looking through crystallographic *c*-axis; (**c**) magnified view of lithium-aqua cluster (color code: red, oxygen; blue color balls, lithium; cyan, copper wheel; green; bismuth; all the tungsten centers are shown in polyhedral representation (alternatively, blue and grey color).

NaCu-POM. Of note, it has been observed that, due to the disorder, some of the electron density of the Cu atom (with a partial site occupancy factor of 0.025) is located away from the Cu4 center (with a distance of 1.366Å) and it has been assigned as Cu4A (represented as yellow color ball; **Figure 3.3**(**b**)). This disorder might be expected due to the electron delocalization or strained squire-planar geometry or some other internal factors; this type of situations are commonly observed in the relevant systems.[42] Each of these anionic POT barrels were cross-linked with four neighbouring perpendicularly arranged barrel clusters through the strong coordinate covalent bonds (Cu^{II}←O=W bond distance: 2.307Å, **Figure 3.3**(**c**)) resulting in the formation of a two-dimensional (2D) layer-like wavy polymeric network (along crystallographic *ab* plane, **Figure 3.3**(**d**)). These 2D layered–networks are cemented by secondary interactions involving lattice water molecules, yielding a strong supramolecular 3D network, which is characterized by 1D open channels, parallel to crystallographic *c*-axis (**Figure 3.4**(**a**)). These channels were further occupied with lithium-aqua cationic $\{Li(H_2O)_5\}^{1+}$ clusters which are supramolecularly interacting and thereby further strengthening the **LiCu-POM** network (**Figure 3.4**(**b** and **c**)). The anionic charges of the copper coordinated POM cluster anion (barrel), $[\{Cu^{II}(SH)\}\{(Cu^{II}Cu^{I}_{1.5})(B\text{-}\alpha\text{-}Bi^{III}W^{VI}_{9}O_{33})\}_2]^{10-}$ are counterbalanced by five lithium ions, two ammonium ions and three hydronium ions as shown in the relevant formula $Li_4[\{NH_4\}_2\{H_3O\}_3\{Li(H_2O)_5\}][\{Cu^{II}(SH)\}\{(Cu^{II}Cu^{I}_{1.5})(B\text{-}\alpha\text{-}Bi^{III}W^{VI}_{9}O_{33})\}_2]\cdot 9H_2O$ (**LiCu-POM**).

In 2017, Patzke group isolated tri- and tetra-nuclear-copper(II) wheel containing polyoxotungstobismuthates from a reaction containing lacunary $[B\text{-}\alpha\text{-}Bi^{III}W^{VI}_{9}O_{33}]^{9-}$ POM and

Cu(II) ion precursors.[42] In the very same report, they also discussed about the possibility of formation of the copper wheel with higher nuclearity (penta– or hexa–nuclear), but, they were unsuccessful. Even in later period, very few examples of hexa–nuclear copper(II) wheel containing inorganic as well as organic-inorganic hybrid POTs were reported with As(III) and Sb(III) ions as hetero atoms.[47-57] Thus, the present two examples (**NaCu-POM** and **LiCu-POM**) are new addition to the polyoxotungstobismuthate class.

In the course of structural analysis, oxidation states of cluster elements were determined by bond valence sum (BVS) calculations. Bond valence sum (BVS) calculations[66] shows that copper centers exist in +2 as well as +1 oxidation states in the both compounds. In both the compounds, copper centers that are in square-pyramidal geometry are stabilized in cupric state (Cu^{2+}), whereas those are in distorted-octahedral geometry (Cu3, #Cu3, and Cu4 in **NaCu-POM**) and distorted square-planer geometry (Cu2, #Cu2 and Cu4 in **LiCu-POM**) are present in cuprous state (Cu^{1+}). Based on the BVS analysis, the sulfur present in the crystals of **LiCu-POM** may be considered as a hydrogen sulfide (SH^-). The oxidation states of the metals and sulfur, estimated from BVS calculations, are further experimentally analyzed by X-ray photoelectron spectroscopy (XPS) as described below.

3.3.2.2. X-ray photoelectron spectra (XPS)

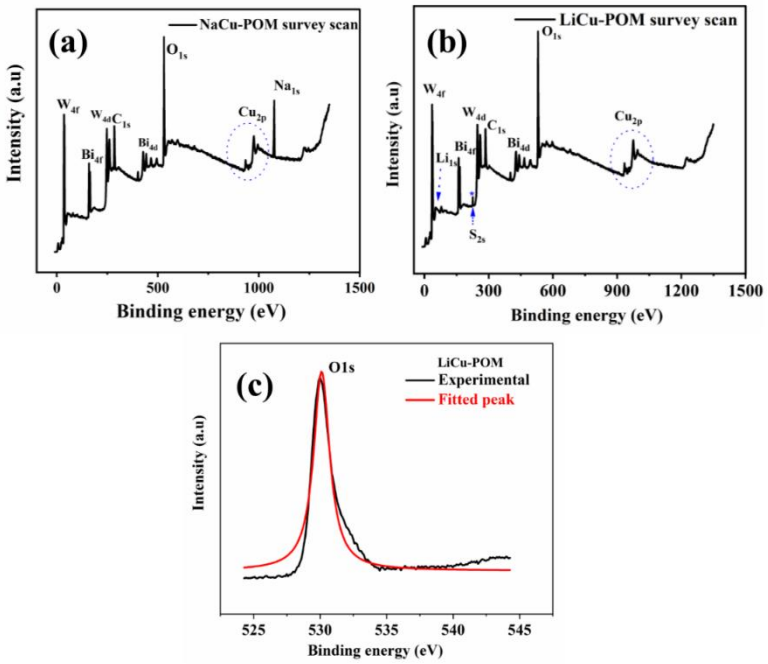

Figure 3.5. X-ray photoelectron spectra: (**a** and **b**) show survey scan XPS plots for **NaCu-POM** and **LiCu-POM** compounds; (**c**) displays high resolution XPS plot of O1s for **LiCu-POM**.

We have analyzed the title compounds by X-ray photoelectron spectroscopy (XPS) in order to understand more about oxidation states. The obtained data were de-convoluted using

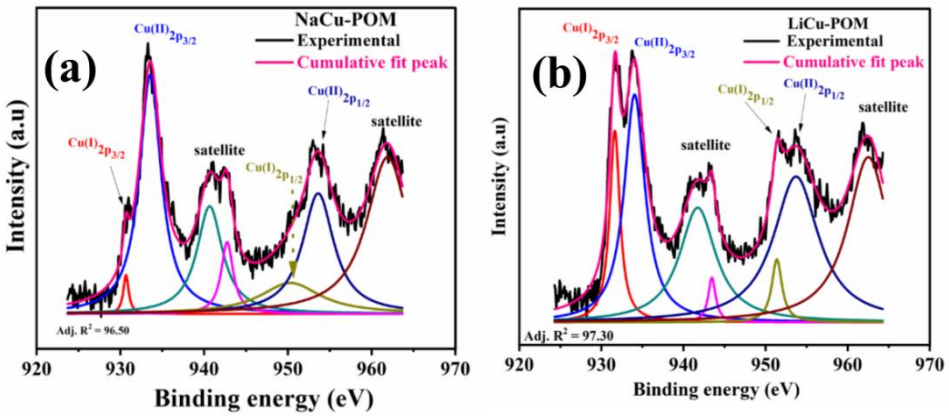

Figure 3.6. High resolution X-ray photoelectron spectra: (**a** and **b**) show XPS plot of Cu2p for **NaCu-POM** and **LiCu-POM** compounds.

Lorentzian-Gauguin (LG) fitting without noticeable error (in terms of Adj. R^2). The low resolution XPS plots of both compounds indicate the presence of O, Bi, Cu, and W elements; these plots also show presence of sodium and lithium in compounds **NaCu-POM** and **LiCu-POM**, respectively (**Figure 3.5**(**a** and **b**)). Additionally, the survey scan spectrum for **LiCu-POM** (**Figure 3.5**(**b**)) indicates the presence of sulfur at 224.63 eV. The oxygen (O1s) peak at 530 eV was taken as a reference in the interpretation of obtained XPS plots (**Figure 3.5**(**c**)). The **Figure 3.6**(**a** and **b**), displays the high resolution XPS plots of copper for compounds **NaCu-POM** and **LiCu-POM**, respectively; the copper $Cu2p_{3/2}$ signals positioned at 930.68 eV and 931.63 eV have been assigned to the monovalent copper (Cu^I) and their respective $Cu2p_{1/2}$ peaks appear at 950.62, 951.37 eV, respectively. Whereas, the $Cu2p_{3/2}$ peaks at 933.56 and 934.03 eV are consistent with copper(II) oxidation state and their respective $Cu2p_{1/2}$ signals appear at 953.87 and 953.68 eV. In both systems, additional two satellite peaks (around 942 eV and 962 eV) at higher energy side to the Cu2p signals signify multi-electronic transitions in the different energy levels of copper atom.[67] In accordance to the BVS calculations (three Cu^+ and three Cu^{2+} centers per formula unit), the LG fitting of the copper Cu2p peaks in **LiCu-POM** system shows two equivalent-intensities for Cu(I) and Cu(II) signals. On the other hand, the copper Cu2p peaks in **NaCu-POM** system are relatively broad with less intensity than that of **LiCu-POM**. This broadness in the Cu2p band in **NaCu-POM** suggests that some of the copper(I) center electron density participates in the resonance or delocalization within copper $\{Cu_5\}$-wheel, which can be realized by the occurrence of three-fourth occupancy (not full occupancy) of two copper(I) ions (namely Cu3 and its symmetry equivalent in the relevant crystal structure) in the SCXRD analysis. The tungsten XPS plots of both systems show two peaks at 34.98, 34.28 and 37.18, 36.72 eV corresponding to the $W4f_{7/2}$ and $W4f_{5/2}$, respectively (**Figure 3.7**(**a** and **b**)).[68] The high resolution XPS features for bismuth (Bi4f) of compounds **NaCu-POM** and **LiCu-POM** exhibit two peaks of $Bi4f_{7/2}$ and $Bi4f_{5/2}$ at 158.16, 158.88 and 164.54, 163.22 eV (**Figure 3.7**(**c** and **d**)), respectively.[69] Along with all these elements,

measurements were also performed to ascertain the presence sulphur (the presence of which was already hinted by ICP-OES, SCXRD analyses and BVS calculations). However, owing to its very minute content in the barrel (a single atom per unit formula) and overlap with bismuth (Bi4f) band binding energy, the sulphur 2p (S2p) XPS peak was not traceable from the overall XPS profile. Therefore, we performed further de-convolution analysis of high resolution Bi4f XPS band to confirm the presence of sulphur in **LiCu-POM**. The de-convolution of XPS plot of Bi4f essentially shows two weak band at 160.22 eV which has been assigned to binding energy of $S2p_{3/2}$.[69,70] The similar analysis was also carried out to the Bi4f XPS feature of **NaCu-POM**, but the trials were unsuccessful. This confirmed that sulphur is absent **NaCu-POM**. As shown in **Figure 3.5**(**b**), a small response (S2s) at 224.63 eV is found in XPS survey scan of **LiCu-POM** compound (S2s peak highlighted with *), which was a clear indication for the presence of sulphur in this compound. The binding energy value for this feature suggests that the sulphur is present in the form of sulphide in compound **LiCu-POM**. Hence, it has been assigned as hydrogen sulphide (SH^-), because it is coordinated to one of the copper(II) centers and Cu–S bond distance is 2.545Å (*vide supra*, crystallography section), which considerably larger than Cu=S bond. The presence of sodium and lithium can be confirmed based on appearance of the peaks at 1076.05 eV (attributed to Na1s of sodium; **Figure 3.5**(**a**)) and 52.48 eV (Li1s of lithium; **Figure 3.7**(**e**))[71] in the XPS plots of **NaCu-POM** and **LiCu-POM**, respectively.

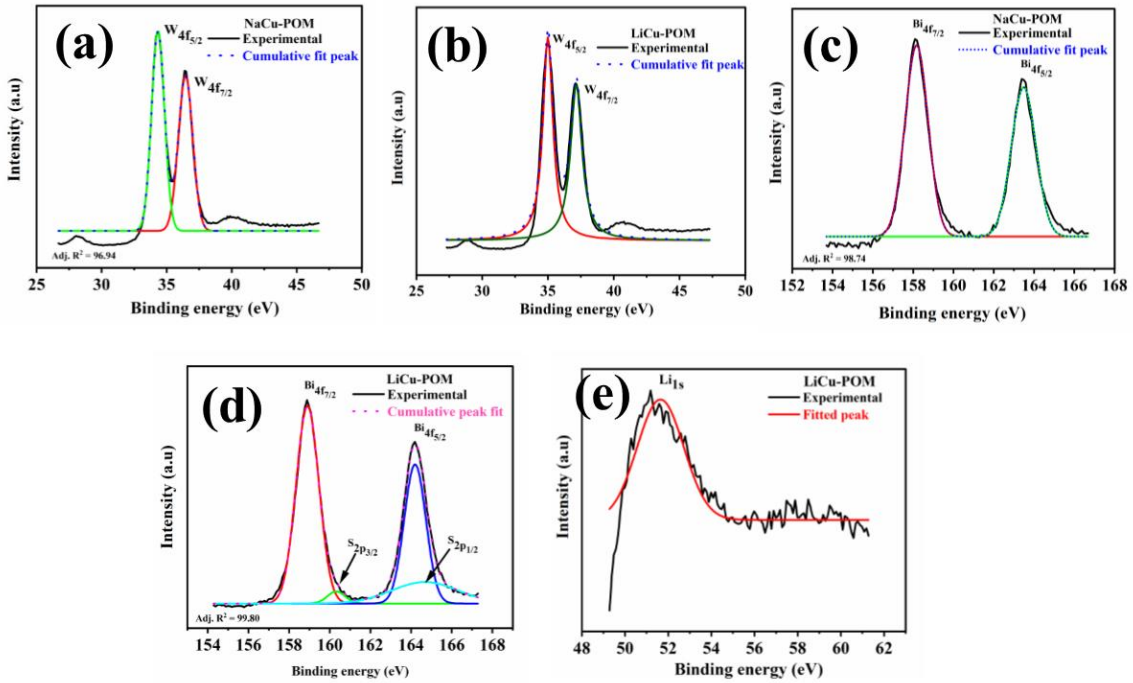

Figure 3.7. High resolution X-ray photoelectron spectra: (**a** and **b**) show XPS plots of W4f for **NaCu-POM** and **LiCu-POM** compounds respectively; (**c** and **d**) show XPS spectra of Bi4f for **NaCu-POM** and **LiCu-POM** compounds, respectively; (**e**) show XPS plot of Li1s for **LiCu-POM**.

3.3.2.3. FT-IR, Raman and UV-Vis spectra

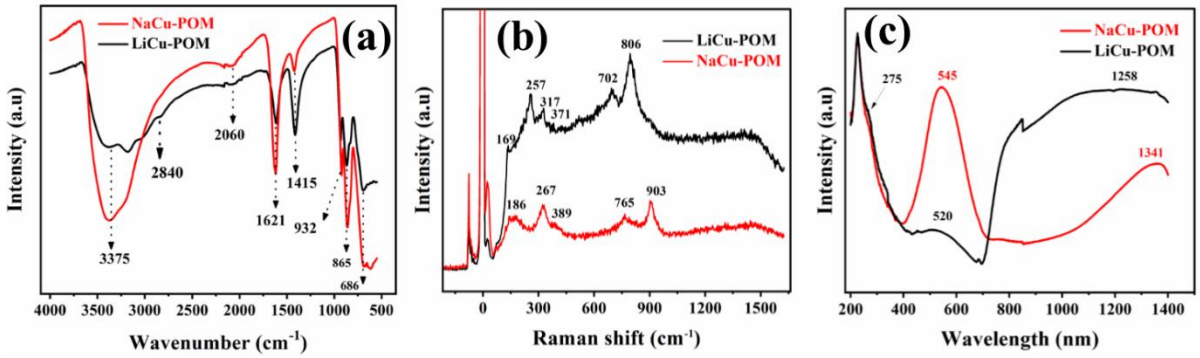

Figure 3.8. FT-IR, Raman, and electronic spectra: (**a**) FT-IR spectra; (**b**) Raman spectra; (**c**) electronic spectra for **NaCu-POM** and **LiCu-POM** compounds.

The FT-IR spectra were recorded to understand the inter-atomic bond vibrational behaviour of **NaCu-POM** and **LiCu-POM** systems. In the FT-IR spectra (**Figure 3.8**(**a**)), the bands at around 930–610 cm^{-1} are assigned to stretching and bending modes of polyoxotungstate (POT) barrel-like cluster (W=O, W–O–W, Cu–O–W, and Bi–O–W) and those appeared at around 1626, 3400 cm^{-1} can be correlated to bending and stretching modes of lattice and coordinated water, respectively.[40,58,59] The weak features at 2840 and 3180 cm^{-1} in the IR spectrum of **LiCu-POM** are ascribed to the S–H (transition metal ion coordinated hydrogen sulfide; here it is copper coordinated hydrogen sulfide) and N–H (present as ammonium cation) bonds, respectively. Whereas in the same region of the IR spectrum of **NaCu-POM**, no such S–H and N–H responses are found. Further, in the Raman spectra (**Figure 3.8**(**b**)), recorded for both the systems, the bands in the region of 950–280 cm^{-1} signify the Raman active modes of POT framework (W=O_{ter} and μ_2–O/μ_4–O). The observed electronic absorption bands in 800–540 nm region are attributed to copper d–d electronic transitions which in turn supports its presence in **NaCu-POM** and **LiCu-POM** systems.[58,59] On the other hand, bands located in 500–220 nm window are ascribed to the ligand to metal charge transfer (LMCT) transitions (**Figure 3.8**(**c**)).[59]

3.3.2.4. Powder X-ray diffraction studies

Powder X-ray diffraction (PXRD) profiles were carried out for **NaCu-POM** (**Figure 3.9**(**a**)) and **LiCu-POM** (**Figure 3.9**(**b**)) to get insights into their bulk properties, like phase purity and homogeneity of as synthesized compounds. The PXRD prifiles show, in close observation, that some of the minor peaks in experimental pattern have minute (more or less shift) shift in the peak position from their simulated pattern peaks, which can be expected due to the solvent water loss. The effect of lattice water loss from **NaCu-POM** and **LiCu-POM** systems can also be realized in the thermal analysis (see below). Other than this, the overall patterns are found

to be consistent together and it confirms the bulk phase purity and homogeneity of both compounds.

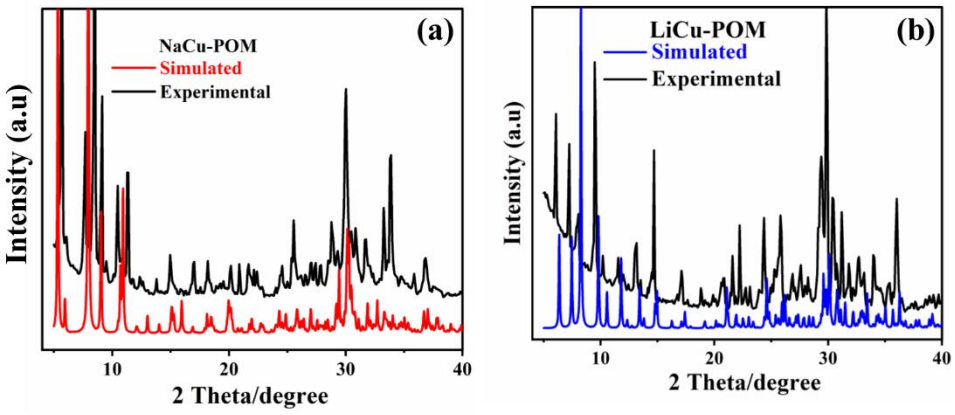

Figure 3.9. (**a** and **b**) Powder X-ray diffraction profiles for **NaCu-POM** and **LiCu-POM** compounds.

3.3.2.5. Thermogravimetric analysis

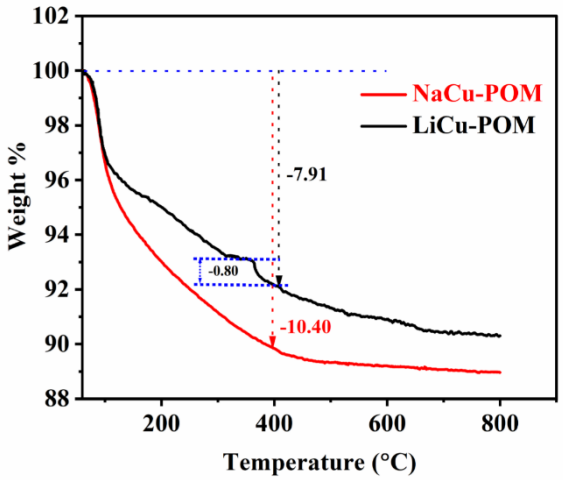

Figure 3.9. Thermogravimetric analysis profiles for **NaCu-POM** and **LiCu-POM** compounds.

Thermal stability analysis of both the compounds (**NaCu-POM** and **LiCu-POM**) were investigated using as-synthesized samples, under the He gas atmosphere. **Figure 3.9** shows the thermal stabilities for both the compounds. The **NaCu-POM** has gradual weight loss of 10.40% (*ca.* 12.0%) is observed from initial temperature to around 400 °C implying the loss of lattice water- and sodium-aqua wheel water-molecules as well as copper coordinated aqua ligands. While in the case of **LiCu-POM**, it has overall weight loss of 7.91% (*ca.* 7.40%) in two-stages from the initial temperature to 408 °C indicating the loss of lattice- and lithium-coordinated-water molecules and ammonium ions as well as hydrogen sulfide. A small hump of 0.8% (*ca.* 0.58%) weight loss around 390 °C in **LiCu-POM** is probably due to the loss of metal ion

coordinated sulfur (SH^-) ligand, which is not present on the TGA profile of **NaCu-POM** (as expected). The presence of high amount of residual mass around 89 and 91%, respectviely for **NaCu-POM** and **LiCu-POM**, reflected from their TGA curves, is due to degraded metal-oxide contents for both the compounds.

3.3.3. Electrochemical water reduction

3.3.3.1. Cyclic voltammograms

It is noteworthy to be mentioned here, that the tungsten (W^{VI}) assisted electron coupled proton reduction for polyoxotungstates/polyoxometalates is commonly observed in an acidic medium. But, it is observed to be significantly suppressed at neutral pH (in absence of redox induced protons).[72-74] Based on these observations, it could be concluded that, to achieve effective water reduction at neutral pH using tungsten based systems, their functionalization/activation would be vital. Structural alterations of polyoxotungstate clusters and combining them with redox active elements are some of the commonly adapted strategies for POM activation.

Along this line, Cronin and coworkers[20] recently functionalized a "Weakley-type POM" with molybdenum. They further investigated the effect of structural modulation on electrochemical properties and achieved an enhanced electrochemical water oxidation activity. Inspired from such studies, in the present work, lacunary $[B\text{-}\alpha\text{-}Bi^{III}W^{VI}_9O_{33}]^{9-}$ POM clusters were functionalized by means of incorporating redox-active copper ion (copper-wheel) between two lacunary cluster anions. Keen electrochemical investigation revealed that, newly generated two systems **NaCu-POM** and **LiCu-POM** are synergistically activated, exhibiting polyoxotungsten based water reduction reaction at the neutral pH.

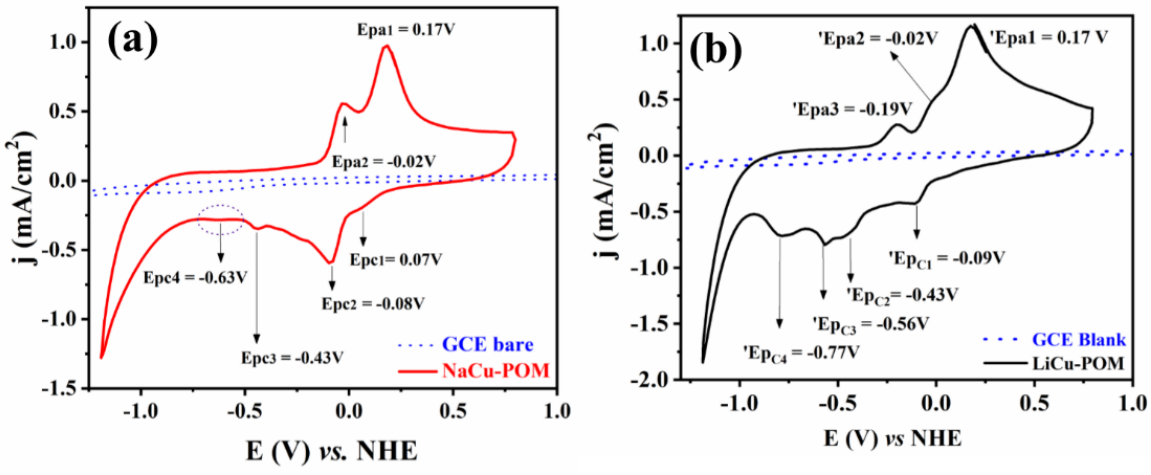

Figure 3.10. Cyclic voltammograms: (**a**) cyclic voltammogram of **NaCu-POM** compound; (**b**) cyclic voltammogram of **LiCu-POM** compound, recorded at neutral pH using 0.1 M potassium phosphate buffer used as supporting electrolyte (scan rate 100 mV/s).

In the course of present studies, hydrogen evolution reactions (HERs) of both the systems (**NaCu-POM** and **LiCu-POM**) were accessed at neutral pH in a three electrode mode unless otherwise mentioned. Both the systems have quite similar CV profiles (**Figure 3.10**) and they show two common quasi-reversible redox couples and two irreversible reductive responses followed by a substantial surge in the current corresponding to the electrocatalytic water reduction (**Figure 3.10**). Specifically, **Figure 3.10**(**a**) illustrates the CV of **NaCu-POM**, in which two redox couples at *ca.* $^{1}\Delta E_{1/2}$ = 0.12 V (*vs.* NHE; Epc$_1$ = 0.07 V and Epa$_1$ = 0.17 V) and $^{2}\Delta E_{1/2}$ = –0.05 V (*vs.* NHE; Epc$_2$ = –0.08 V and Epa$_2$ = –0.02 V) were assigned to two single-electron redox processes of copper (Cu^{II}/Cu^{I}) centers. Since it was already observed in SCXRD analysis, that the copper centers were present in two different coordination environments. Thus, these two different coordination environments may be the reason for these two redox couples separately.[75,76] Two irreversible reduction responses (Epc$_3$ and Epc$_4$) indicate the involvement of the reduction of cluster tungsten ($W^{VI} + e^{-} \rightarrow W^{V}$) centers.[38,41,72,77,78] These two irreversible reductions are followed by a large surge in the current (onset at *ca.* –0.75 V (*vs.* NHE)) along with the visual observation of gas bubbles on working electrode surface, indicating the electrocatalytic water reduction to molecular hydrogen. The CV of **LiCu-POM** is shown in **Figure 10**(**b**). On par with CV of **NaCu-POM**, two redox couples for **LiCu-POM** appear at $^{1}\Delta E_{1/2}$ = 0.04 V (*vs.* NHE; 'Epc$_1$ = –0.09 V and 'Epa$_1$ = 0.17 V) and $^{2}\Delta E_{1/2}$ = –0.31 V (*vs.* NHE; 'Epc$_3$ = –0.43 V and 'Epa$_2$ = –0.19 V). That are ascribed to two single electron redox processes (Cu^{II}/Cu^{I}) from two types of environmentally different copper centers. Right after these two Cu^{II}/Cu^{I} couples, two irreversible reduction peaks ('Epc$_3$ and 'Epc$_4$) appear due to the reduction of cluster tungsten centers ($W^{VI} + e^{-} \rightarrow W^{V}$) followed by large WR current surge (onset at *ca.* –0.92 V (*vs.* NHE)) and the observation of H_2 gas bubbles on the working electrode surface.

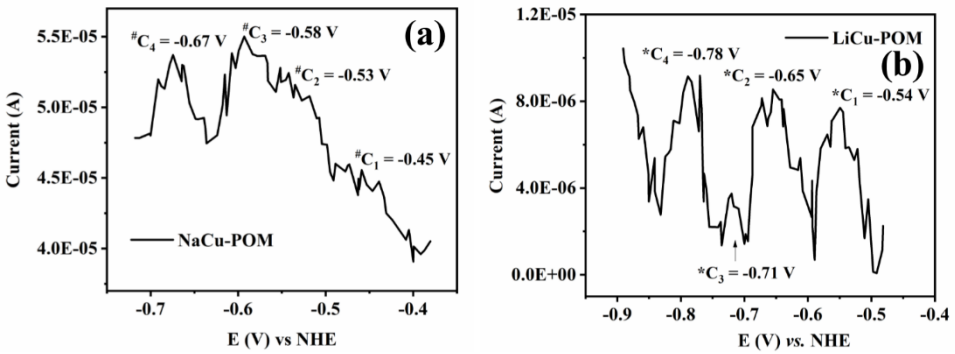

Figure 3.11. Differential pulse voltammogram (DPV): (**a**) DPV of **NaCu-POM** compound; (**b**) DPV of **LiCu-POM** compound, recorded at neutral pH using 0.1 M potassium phosphate buffer as supporting electrolyte.

The two irreversible reduction peaks in both compounds have been resolved by cathodic differential pulse voltammogram (DPV) measurement. The resolved DPV responses are $^{\#}C_1$, $^{\#}C_2$, $^{\#}C_3$, and $^{\#}C_4$ for **NaCu-POM** as shown in **Figure 3.11**(**a**). Thus the cathodic DPV

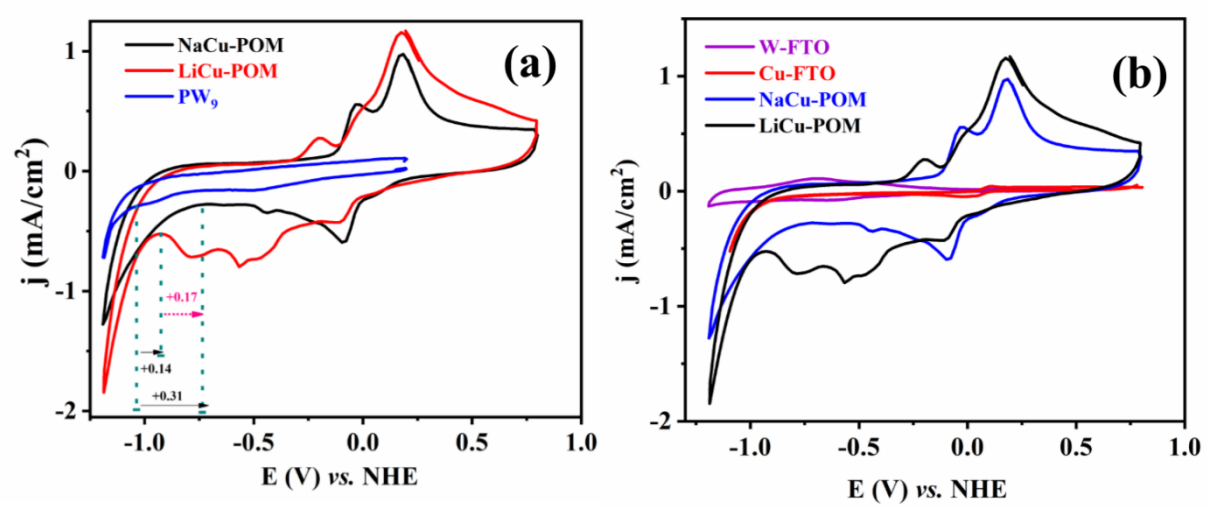

Figure 3.12. Controlled experiments: (**a**) cyclic voltammogram profiles for **NaCu-POM**, **LiCu-POM**, and **PW$_9$**, (**b**) cyclic voltammogram profiles for **NaCu-POM**, **LiCu-POM**, **Cu-FTO** and **W-FTO**, were collected in 0.1 M potassium phosphate buffer (neutral pH) used as electrolyte for all the cases (scan rate 100 mV/s).

measurement elucidates that the *E*pc$_3$ and *E*pc$_4$ responses, shown in **Figure 3.10**(**a**), are each two electron reduction waves that split into four DPV responses $^{\#}C_1$, $^{\#}C_2$, $^{\#}C_3$, and $^{\#}C_4$ (**Figure 3.11**(**a**)). Likewise, the resolved DPV responses $^{*}C_1$, $^{*}C_2$, $^{*}C_3$, and $^{*}C_4$ for **LiCu-POM** (**Figure 3.11**(**b**)) reveal that the irreversible reductions at *E*pc$_3$ and *E*pc$_4$ (**Figure 3.10**(**b**)) are each two-electron reduction waves for the compound **LiCu-POM**. Thus both the compounds, **NaCu-POM** and **LiCu-POM** show four electron reductions of the tungsten centers, that responsible for electrocatalytic water reduction to molecular hydrogen. This is because we do not observe the respective oxidative responses in their CVs for both compounds, instead we find large current surges right after these irreversible reductions indicating the electrocatalytic water reduction for both compounds. It is commonly known that, the reduced tungsten centers ($W^{VI} + e^- \rightarrow W^V$) of a POM cluster are highly reactive and capable of breaking H–OH bond through the plausible cathodic reaction pathway (eqns 1 and 2). After water reduction

Cathode:	$[\text{Cu-POM}] + 4e^- \rightarrow [\text{Cu-POM}]^{4-}$ (*)	(eqn 1)
	$[\text{Cu-POM}]^{4-}$ (*) $+ 4H_2O \rightarrow 2H_2 + [\text{Cu-POM}] + 4OH^-$	(eqn 2)
Anode:	$4OH^- \rightarrow O_2 + 4e^- + 2H_2O$	(eqn 3)

reaction (eqn 2), catalytically active tungsten sites [Cu-POM] (*), the highly reactive reduced species, regenerate to their original (oxidized) [Cu-POM] form ((*) refers to the electrochemically activated state of catalyst) in the catalytic cycles.

A small shoulder-type anodic response (labelled as '*E*pa$_2$, **Figure 3.10**(**b**)) at *ca.* 0.02V (*vs.* NHE) for the compound **LiCu-POM** may be due to the result of an irreversible oxidation of its copper coordinated hydrogen sulphide (Cu–SH) group.

A careful investigation on catalytic activities of **NaCu-POM** and **LiCu-POM** towards HER, **NaCu-POM** is found to be more efficient than **LiCu-POM** as far as the onset potential values are concerned. **NaCu-POM** has less cathodic HER onset potential by *ca.* 0.17 V (*vs.* NHE) than that of **LiCu-POM**. This difference in onset potential values can be attributed to their supramolecular level structural dissimilarities in their solid state. As we have already described in the crystallography section, **NaCu-POM** possess copper coordinated water molecules, that are not present in the crystal structure of **LiCu-POM**. Hence, it can conveniently be assumed that, the ligated water molecules in **NaCu-POM** can establish an extensive H-bonding network and making it more hydrophilic which could in turn allows larger number of reactant (water) molecules to interact with catalyst, allowing more amount of water reduction compared to that in the case of **LiCu-POM**. This solid state supramolecular level topological comparison is logical because in the present work, the electrocatalytic HER has been performed in a heterogeneous manner (in the solid state).

Importance of copper wheel in these barrel POMs: synergistic effect

We have already seen that the tungsten centers of the POM barrels are mainly responsible for the electrocatalytic HER in the present study. In order to strengthen our claim tungsten centers are responsible for HER, we perform CV studies of $Na_9[PW_9O_{34}]\cdot 7H_2O$ (**PW_9**)[79] because the title barrels are formed by fusing two identical lacunary Keggin anions$\{Bi^{III}W^{VI}_9O_{33}\}^{9-}$ by a mixed-valent copper wheel at the middle portion of the barrel. Thus, ideally we should have performed the CV studies of $\{Bi^{III}W^{VI}_9O_{33}\}^{9-}$ cluster containing compound; but unfortunately, $\{Bi^{III}W^{VI}_9O_{33}\}^{9-}$ cluster containing compound cannot be synthesized in a pure form. Thus we performed the CV studies of $\{P^{V}W^{VI}_9O_{34}\}^{9-}$ cluster containing compound to exclude the possibility of the participation of bismuth and other form of tungsten. Since **PW_9** (a sodium salt) is water soluble, the CV was recorded in a homogeneous manner using 1 mmol compound in 0.1 M phosphate buffer (pH 7) solution under identical operational condition as was used for the title compounds. The CV of **PW_9** shows two irreversible weak reduction responses *ca.* – 0.66 and – 1.04 V (*vs.* NHE) followed by a very small HER onset (**Figure 3.12**(**a**)). Thus, **NaCu-POM** and **LiCu-POM** systems have less cathodic HER onset potential by *ca.* 0.31 V and 0.14 V (*vs.* NHE), respectively, compared to the analogous constituent **PW_9** (**Figure 3.12**(**a**)). This clearly indicates that the mixed valent-copper wheel, joining two **BiW_9** clusters at the equatorial position POM clusters plays an important role in the synergetic enhancement of electrocatalytic HER activity.

In order to understand more about the active site of the catalysts, the cyclic voltammogram profiles of *in-situ* (electrochemically in the cathodic window) generated **Cu-FTO** and **W-FTO** (metal nano-particles) were also recorded and presented along with the CV profiles of **NaCu-POM** and **LiCu-POM** in **Figure 3.12**(**b**). As shown in Figure 3.12b, the electrochemically generated **W-FTO** and **Cu-FTO** do not show any considerable CV response as shown by **NaCu-POM** and **LiCu-POM**.

Similarly, comparative studies were also conducted with *in-situ* generated **W-FTO** electrode to understand the redox phenomena of electrochemically formed tungsten-metal particles and their involvement in the hydrogen evolution reaction. The obtained CV responses of **NaCu-POM** and **LiCu-POM** are not identical to the **Cu-FTO**, **PW_9** and **W-FTO** electrodes (where are those **Figure 3.12**(**b** and **b**)). This clearly indicates the true molecular catalytic nature of **NaCu-POM** and **LiCu-POM** and the intrinsic activation and involvement of cluster tungsten centers of the title compounds in the electrochemical water reduction to molecular hydrogen in the present work.

3.3.3.2. Stability test and controlled experiments

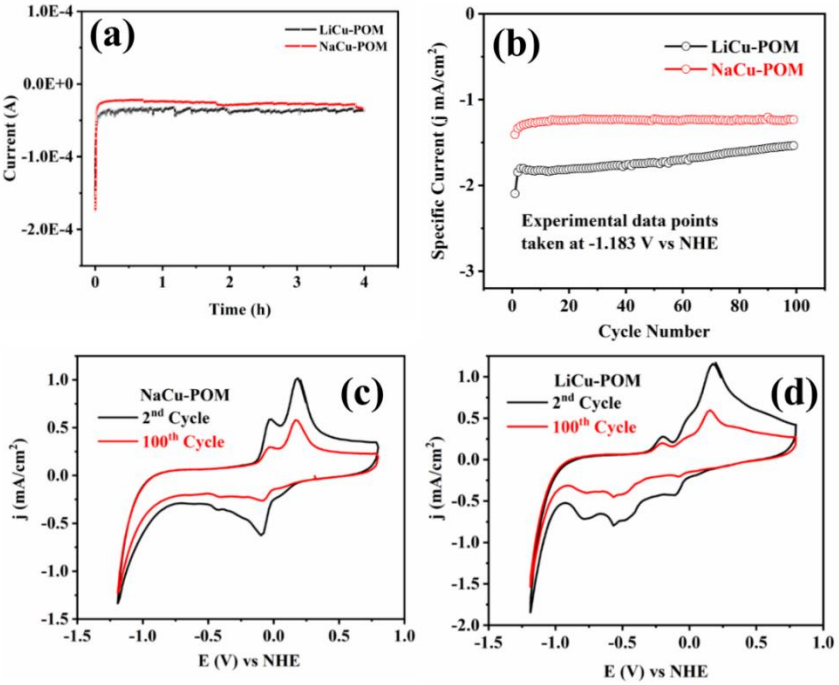

Figure 3.13. Stability tests: (**a**) chronoamperometry electrolysis responses for **NaCu-POM** and **LiCu-POM** compounds conducted for 4 hours at –1 V vs NHE; (**b**) a derivative plot constructed for cyclic voltammogram cycle numbers *vs* specific current density (each data point extracted at –1.183 V *vs* NHE; *i.e.* end point of each cycle' HER current) for both compounds; (**c** and **d**) 2nd and 100th cycles of cyclic voltammogram profiles for **NaCu-POM** and **LiCu-POM**, respectively; in all the cases, 0.1 M potassium phosphate buffer (neutral pH) has been used as an electrolyte (CV scan rate 100 mV/s).

We have investigated long-term stability of these two catalytic systems (**NaCu-POM** and **LiCu-POM**) by following means: (i) *chronoamperometric (CA) electrolysis* (performed at –1V *vs.* NHE for 4 hours) of both the systems as shown in **Figure 3.13**(**a**) showing stability over the period of 4 hours and (ii) *100 consecutive cycles of cyclic voltammogram (CV) scan* (**Figure 3.13**(**b-d**)). The specific current density is plotted against number of cyclic voltammogram cycles. All the data points of specific current density for this plot were extracted from the end points of the each cycle of HER current density (*i.e.*, at –1.183 V (*vs.* NHE)) and plotted against the respective cycle count (**Figure 3.13**(**b**)). Both the electrocatalysts produced stable and

study-state current density over 100 cycles and indicates a moderate durability of respective electrodes (**Figure 3.13**(**c** and **d**)). These two tests conveniently suggest that these **Cu-POT** electrocatalysts are enough stable and robust under operational condition. Despite of these estimated adequate stabilities, a little loss in catalytic activity and redox peak current were observed during the 100 cycles CV scan, which can be attributed to possible fractional delamination of the coated sample from the electrode surface, due to the continuous evolution of hydrogen bubbles.

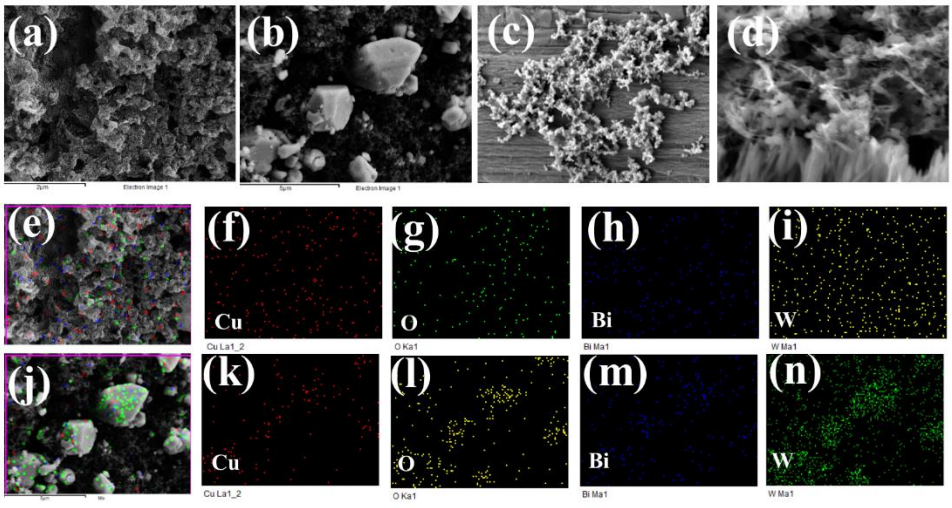

Figure 3.14. FESEM-EDX analysis on the post chronoamperometric electrolysis electrode surfaces: (**a** and **b**) FESEM images of chronoamperometric electrolysis electrodes surface for **NaCu-POM** and **LiCu-POM** compounds; (**c** and **d**) FESEM image of *in-situ* generated **Cu-FTO** and **W-FTO** electrodes; (**e-i**) EDX elemental mapping on chronoamperometric electrolysis electrode surface of **NaCu-POM**; (**j-n**) EDX elemental mapping on chronoamperometric electrolysis electrode surface of **LiCu-POM**.

The chemical nature of the catalyst is assumed to be intact even after prolonged CV cycle scan, there is no considerable similarities found between the CV patterns of **NaCu-POM** and **LiCu-POM**, and those of *in-situ* generated **Cu-FTO**, **W-FTO** and $\mathbf{PW_9}$ under similar operational conditions (**Figure 3.12**). In general, the change in surface morphology (*viz.* appearance of spherical metal nano-particles on the surface of the electrode) has been a very frequently observed phenomenon in the case of reductive degradation of POM clusters under cathodic hydrogen evolution reaction condition. Nevertheless, as illustrated by *FESEM imaging* of post-catalytic CA electrodes, there were no observable morphological changes like formation of spherical metal nano-particles over electrode surface (**Figure 3.14**(**a** and **b**)), found (which is inevitable on degradation of catalytic species to compounds similar to *in-situ* grown **Cu-FTO** and **W-FTO** electrodes (**Figure 3.14**(**c** and **d**))[68]. The EDX imaging on both catalysts shows their back-bone construction elements in the EDX elemental mapping of both the samples, **NaCu-POM** (**Figure 3.14**(**e-i**) and for **LiCu-POM** (**Figure 3.14**(**j-n**) after CA catalytic electrolysis. This is also supported by Raman spectra, which were recorded after 4 hours of CA measurement.

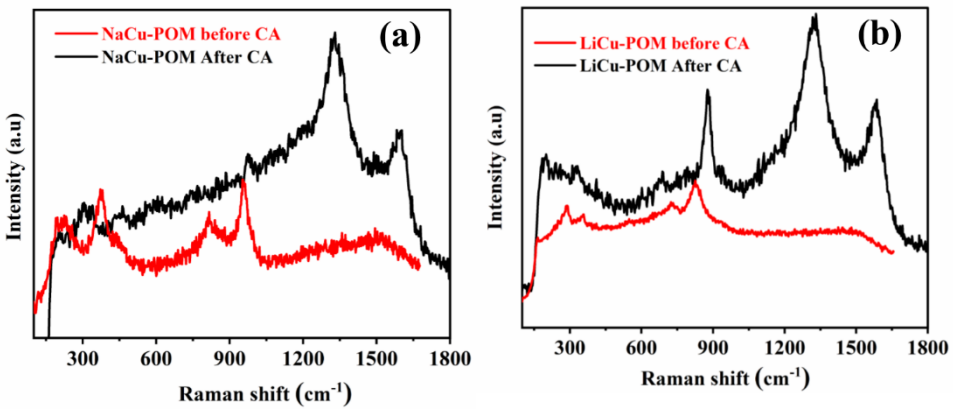

Figure 3.15. Raman spectral analysis of the electrodes after chronoamperometric experiments: (**a** and **b**) Raman spectra of chronoamperometric electrolysis electrode surfaces for **NaCu-POM** and **LiCu-POM** compounds, respectively.

Raman spectral data (**Figure 3.15**(**a** and **b**)), recorded for both the CA electrodes after electro-catalysis, have not shown noticeable deviation from that of parent material and it (along with all of the above electrochemical and spectroscopic outcomes) strongly advocate the unaltered identity of catalysts during electrochemical water reduction.

3.3.3.3. Kinetic insights

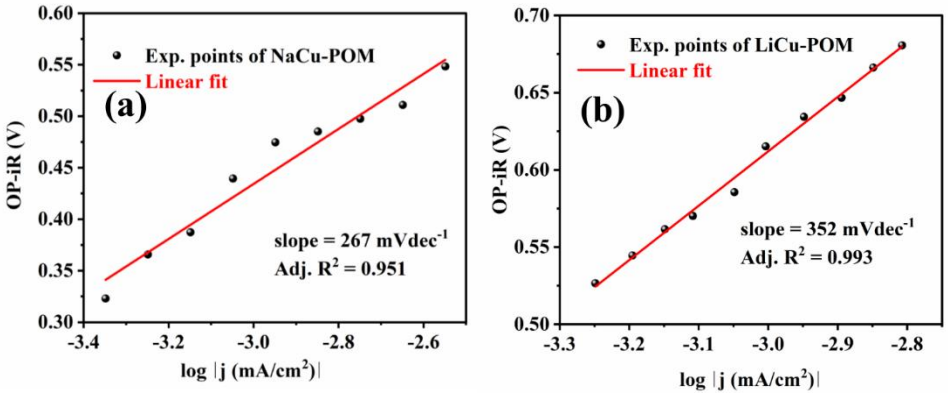

Figure 3.16. Hydrogen evolution reaction kinetics: (**a** and **b**) Tafel plots for **NaCu-POM** and **LiCu-POM** compounds, respectively were constructed at neutral pH condition; 0.1 M potassium phosphate buffer was used as supporting electrolyte.

To understand better the reaction kinetics of electrochemical HER, Tafel plots were plotted (**Figure 3.16**(**a**) for **NaCu-POM** and **Figure 3.16**(**b**) for **LiCu-POM**); the relevant data were collected in a galvanostatic mode under study-state mass flow at the neutral pH. The electrolyte was stirred constantly at 480 rpm to maintain the constant mass transfer in the HER.[8,68,74,76] The obtained Tafel slopes (267 and 352 mV dec^{-1} for **NaCu-POM** and **LiCu-POM**, respectively)

with respective overpotential values (430 and 612 mV; at j = 1 $mAcm^{-2}$) clearly indicate the enhanced catalytic water reduction based on tungsten active sites of the title catalysts.

Furthermore, the Tafel slope values can also predict the hydrogen evolution reaction path: the Volmer step (V), $H_2O + e^- \rightarrow OH^- + H_{ads}$ (adsorbed hydrogen atom on the catalyst active site), followed by the Heyrovsky step (H), $H_{ads} + H_2O + e^- \rightarrow H_2 + OH^-$ or the Tafel step (T), $2H_{ads} \rightarrow H_2$ or result of both in hydrogen evolution. The obtained Tafel slope (267 and 352 mV dec^{-1}) values for **NaCu-POM** and **LiCu-POM** are almost twice and thrice compared to the theoretically predicted Volmer step value (118 mV dec^{-1}; as rate determining step (RDS) in HER),[80] and are demonstrate that Volmer step as the RDS in title compounds catalytic HER process followed by the involvement of slow (both H-T steps) recombination of HER intermediates (H_{ads}). Among two catalysts, the **NaCu-POM** has shown efficient HER activity with 85 mV dec^{-1} (180 mV of less overpotential) of lower Tafel slop than the **LiCu-POM** under identical conditions.

3.3.3.4. Faradic efficiency

Faradic efficiencies [efficiency of a catalyst to convert reactants (here H_2O) into the product (here H_2) for a given amount electrical energy] of catalysts (**NaCu-POM** and **LiCu-POM**) were calculated from bulk electrolysis to assess their electrocatalytic ability. Here we have measured the amount of hydrogen gas, evolved from a constant current electrolysis, using a homemade setup (*vide infra*).[8,68,75]

Detailed Experimental procedure

Faradic efficiencies of both the catalysts (**NaCu-POM** and **LiCu-POM**) were determined from the experimentally evolved hydrogen (H_2) gas over a period of time, by the application of the constant current in a two-electrode electrolysis system at 1 atm. The known amount (1 mg/cm^2) of sample was coated on to Fluorinated Tin Oxide (FTO) with 0.5 cm^2 surface area and it was used as a working electrode (cathode), whereas the platinum net as a counter electrode (anode) for Faradic electrolysis. The 0.1 M potassium phosphate buffer with neutral pH was used as an electrolyte. The home-built setup was used to carry out the electrolysis with constant applied cathodic current -500 μA per 6 hours. The setup was constructed in such a way that, any gas evolved in the counter electrode chamber could not enter into the working electrode chamber, as they were separated from each other by the inverted glass tube. The counter and working components separating glass tube remains open at the bottom and also contains a small window between the working and counter electrode, to maintain the better electrical continuity. The design of this homemade setup not only maintains clear separation between hydrogen and oxygen generated at their respective electrolysis, but also measures the volume of collected hydrogen gas with a precession of 0.05 milliliters. During the electrolysis, hydrogen gas bubbles first accumulates at the surface of the working electrode then moves up and collected in an inverted graduated tube by displacing already present electrolyte. On the other hand, the oxygen

gas produced from the counter electrode was amassed as a ring of bubbles around the inverted graduated tube, but could not get inside the tube and do not mix up with the hydrogen.

Calculation of Faradic efficiency

The Faradic efficiency, is the efficiency with which charge is utilized in an electrochemical reaction. The Faradic efficiencies of both the catalysts were determined by following the reported method.[8,68,75]

For WRC, it could be formulated as

$$= \frac{\text{Number of moles of hydrogen evolved}}{\text{Moles of hydrogen that can evolve by utilizing the employed charge}} \times 100 \qquad \ldots\ldots\ldots\ldots (4)$$

From the quantitative measurement, the hydrogen gas evolved in constant current electrolysis, at neutral pH we found, was 0.186 mL/hour (1.12 mL/6 hours) and 0.193 mL/hour (1.16 mL/6 hours) under 1 atm pressure for **NaCu-POM** and **LiCu-POM** systems, respectively.

Detailled calculation given for NaCu-POM:

Thus, the moles of hydrogen evolved in one hour = (0.186/22400) mol = 8.33×10^{-6} mol

$$H_{2\ ideal} = \frac{\text{Q (Total Charge employed)}}{\text{n(number of electrons required for the chemical change)}\times 1\text{Farad}} \qquad \ldots\ldots\ldots\ldots\ldots (5)$$

Here, we employed a constant cathodic current -500 μA and 'n'= 2 for HER (as it is a two-electron process).

Thus, the H_2 ideally should evolve = $\frac{(0.0005\times3600)}{2\times96500}$ mol = 9.32×10^{-6} mol ..... (6)

$$\text{Faradic efficiency} = \frac{\text{Experimentally evolved hydrogen}}{\text{Ideally evolved hydrogen}} \times 100 \qquad \ldots\ldots\ldots\ldots\ldots (4)$$

However, the Faradic efficiency,

For **NaCu-POM** found to be = $8.33\times10^{-6}/9.32\times10^{-6}\times100$ = **89.37**% (≈ **89** %)

For **LiCu-POM** found to be = $8.61\times10^{-6}/9.32\times10^{-6}\times100$ = **92.39**% (≈ **92** %)

Thus, the experimental results reveal that, the HER Faradic efficiencies for **NaCu-POM** and **LiCu-POM** were found to be ~88 % and ~92 %, respectively. These values not only illustrate the effectiveness of catalysts, but also exclude the occurrence of any major side reactions during electrocatalytic HER. From the experimentally obtained values it is evident that **NaCu-POM** was having slightly lower efficiency compared to that of **LiCu-POM**. This difference in Faradic efficiency can be attributed to the combined effect of (a) presence of relatively lower number of catalytically active sites in unit area of electrode, and (b) probably low rate of mass

transportation or partial delamination of electrode film due to the high activity and more hydrogen gas production,[81] in the case of **NaCu-POM**. In order to establish these assumptions, number of active sites on specific surface area of glassy carbon (working) electrode (GCE) were calculated from the sample (i.e. 10μL) coated on electrode surface (see below) adopting a reported procedure.[82]

Calculation of number of electrochemically active sites present on electrode surface:[82]

The number of catalytically active sites present on the sample coated electrode was calculated as follows:

First we determined the number of grams of catalyst sample present in the 10 microliters of ink that was used to coat the GCE surface.

During the preparation of catalyst coating on the GC electrode, 4 milligram of the material (catalyst) was taken in 1 mL of ethanol-water solution. So, it was 4×10^{-3} gm per mL.

Then we found out the number of grams of sample present in 10 microliters of ink as follows.

- 10 microliters = 10×10^{-3} mL or 1×10^{-2} mL.
- Now the combination of both values = 4×10^{-3} g $mL^{-1} \times 1 \times 10^{-2}$ mL.
  $= 4 \times 10^{-5}$ g or 40×10^{-6} g.
- So, ~ 40×10^{-6} g of sample present in 10 microliters ink.

For NaCu-POM,

No. of catalytically active sites present in 10 μL ink.

- Molecular weight of **NaCu-POM** = 5998.4 g $mole^{-1}$.
- One mole of **NaCu-POM** cluster has five moles of copper and eighteen moles of tungsten ions (therefore in the calculation, we have assumed to be considered all the copper and tungsten ions (5+18 = 23) are active sites).
- No. of active sites = coated sample (g)/mole wt. of catalyst (g).
  = 0.00004 g/5998.4 g.
  = 6.668×10^{-9} moles.
- Now, how many moles of active sites present in the electrode coated 10 microliters ink.
- No. of active sites (Γ_0) = 6.598×10^{-9} moles × 23 moles of active sites.
  = 1.5337×10^{-7} moles of active sites present.

For LiCu-POM,

- Molecular weight of **LiCu-POM** = 5549.44 g $mole^{-1}$.
- No. of active sites = 0.00004 g/5549.44 g.
  = 7.207×10^{-9} moles.
- No. of active sites (Γ_0) = 7.207×10^{-9} moles × 24 moles of active sites
  = 1.7299×10^{-7} moles of active sites present.

In 10μL of suspension, the **NaCu-POM** and **LiCu-POM** consisted of 1.5337×10^{-7} and 1.7299×10^{-7} moles of active sites, respectively. Presence of lower number of active sites on the electrode surface can result the lower yield of product conversion. The second factor *i.e.*, low rate of mass transportation or lower number of accessible active sites due to the more surface blockage by hydrogen gas bubbling for **NaCu-POM** compared **LiCu-POM** can be found out by electrochemical impedance spectroscopy (EIS) measurements.

3.3.3.5. Electrochemical impedance spectra

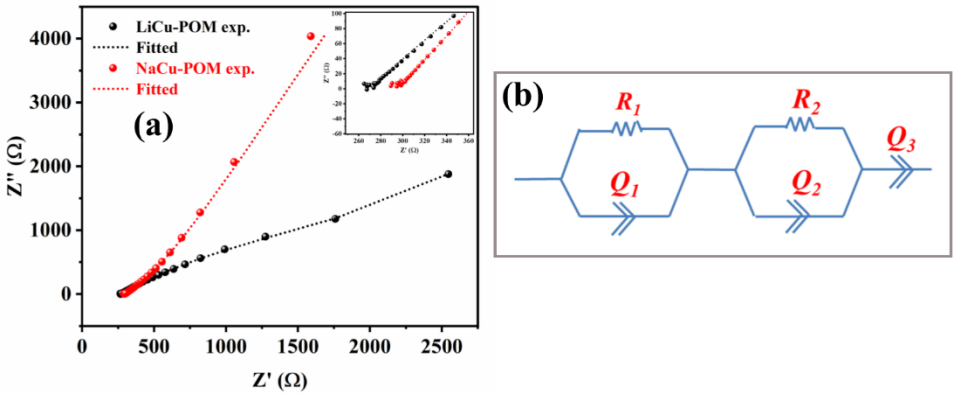

Figure 3.17. Eelectrochemical impedance study: (**a**) Nyquist plots for **NaCu-POM** and **LiCu-POM** compounds (inset represent the magnified view of higher frequency region Nyquist plot for both) recorded at neutral pH condition 0.1 M potassium phosphate buffer used as supporting electrolyte; (**b**) equivalent circuit used to fit impedance data.

Figure 3.17(**a**) represent the electrochemical impedance spectra of **NaCu-POM** and **LiCu-POM** which were measured from the alternative current electrochemical impedance spectroscopy (AC-EIS) for sample coated GC electrodes at neutral pH in an identical experimental condition, under nitrogen atmosphere. The EIS spectra for both the systems were measured at –796 mV (vs. NHE). The measured complex impedance data were constructed between the Z'(real) *vs* Z''(imaginary) impedance planes of Nyquist plots. The experimentally obtained impedance data of Nyquist plots were best fitted using the most appropriate equivalent circuit $((R_1/Q_1) + (R_2/Q_2) + Q_3)$ shown in **Figure 3.17**(**b**). The origin of the slanting line (having a very small semi-circle, shown as inset in **Figure 3.17**(**a**)) of the Nyquist plot at higher frequency region represents the bulk charge transfer resistance (R_{CT}) of electrode material (in the present case R_1), whereas the tail part of the Nyquist plot indicates the electrode-electrolyte inter-grain boundary and electrolyte resistance at lower frequency region (here it is R_2). The Q_1, Q_2, and Q_3 are constant phase elements used to determine the charge-transfer resistance of the **NaCu-POM** and **LiCu-POM** with no noticeable error in terms of χ^2 value.

As shown in **Figure 3.17**(**a**), the **NaCu-POM** has more charge transfer resistance (R_{CT} = 294 Ohms) than that of **LiCu-POM** (R_{CT} = 269 Ohms). As we have already seen that the **NaCu-POM** has relatively less number of active sites (1.5337×10^{-7} moles) than that of **LiCu-**

POM system (1.7299×10^{-7} moles). Thus, the less number of active sites along with more charge transfer resistence in **NaCu-POM** system can limit the overal rate of mass transportation than the **LiCu-POM** system. This can affect on overal Faradic efficiency of **NaCu-POM** system. It is apparent that the number of active sites also influence the overall rate of mass transportation which has been revealed in terms of R_{CT} value of the electrode. It suggested that the electrode with less number of active sites *i.e.* **NaCu-POM-GC** electrode (1.5337×10^{-7} moles) has more charge transfer resistance 294 Ω than the electrode with more number of surface active sites, *i.e.* **LiCu-POM-GC** (1.7299×10^{-7} moles) having less charge transfer resistance 269 Ω.

3.3.3.6. Scan rate variation

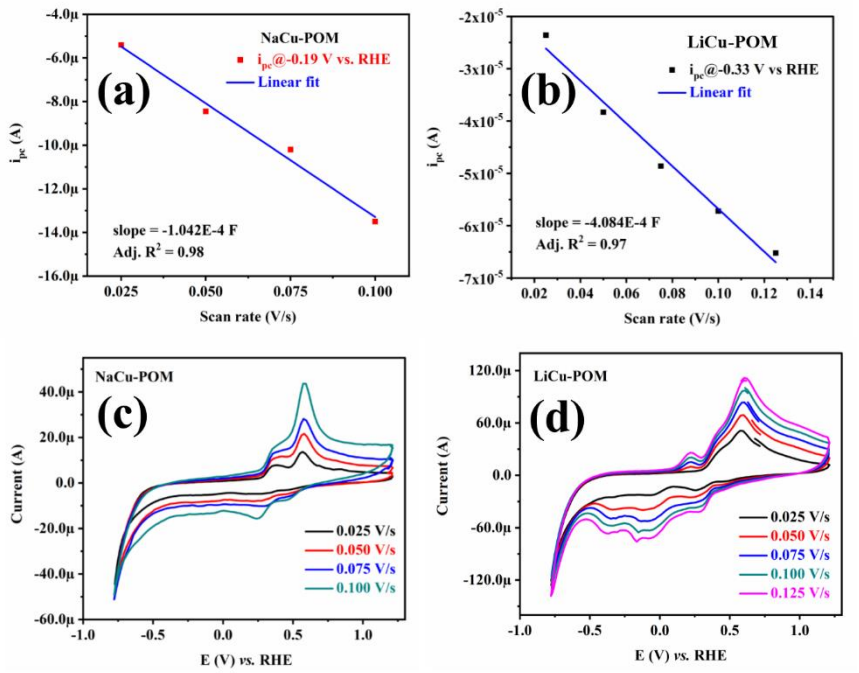

Figure 3.18. Scan rate plots: (**a** and **b**) derivative plots constructed from the peak current (i_{pc}) as a function of scan rate variation (-0.025 to -0.125 Vs^{-1}) for **NaCu-POM** and **LiCu-POM** compounds, respectively; (**c** and **d**) scan rate variation cyclic voltammogram plots for **NaCu-POM** and **LiCu-POM** compounds, respectively.

In addition to the calculation of number of active sites and EIS analysis, the derivative plots were also constructed by the cathodic peak current *vs* function of a scan rate (**Figure 3.18**(**a** and **b**)). The derivative plots show linear enhancement in the cathodic peak current. The linear fits of such plots were estimated as -1.042×10^{-4} and -4.084×10^{-4} F values for **NaCu-POM** and **LiCu-POM**, respectively, which signify the presence of lower number of active sites in **NaCu-POM** than that in **LiCu-POM** as these numbers directly relate to the quantities of active sites. These results are also pretty good support to the above analyses. Later, the effect of scan rate on the catalyst response was also studied. As illustrated in **Figure 3.18**(**c** and **d**), with raise in the scan rate (0.025–0.125 V/s), the enhancement in the peak current is also observed, which

clearly indicates the diffusion controlled electrochemical hydrogen evolution by both the catalysts.[83] Results from all these experiments, *i.e.* calculation of number of active sites, EIS, and scan rate variation measurements, suggest the effect of loading of catalytically active sites and charge carrier ions on the ion transportation as well as the Faradic efficiency (quantitative measurement) on the overall HERs.

3.3.3.7. Turn over frequency (TOF):

We calculated turn over frequencies (TOFs) to get further insights in to the catalysts' activity. The TOF values of respective systems were calculated following the reported procedures as described below.[8,84] The TOF is defined as the number of reactants getting converted into the product molecules in a unit time per active site. Thus, the TOF of both catalysts were calculated as, TOF = $\frac{I}{2mF}$ …… (7).

where

I = current (A) value obtained from chronoamperometry electrolysis,

F = Faraday constant (C mol^{-1}),

m = number of active sites (mol),

2 = number of electrons required to form one mole of hydrogen.

Here, the number of active sites being '*m*' calculated by the equation 8

$$m = \frac{Q}{nF} \qquad \text{.....…… (8)}$$

Q = charge (-3.667×10^{-5} and -6.6486×10^{-5} C mol^{-1} for **NaCu-POM** and **LiCu-POM**, respectively) calculated by integrating the current *vs* time plot generated from the trace of cyclic voltammogram recorded under non-catalytic conditions using non-aqueous medium (CH_3CN medium),

Calculation of charge (Q) from trace of non-catalytic cyclic voltammogram:

From equations (7) and (8),

$$\text{TOF} = \frac{I}{2\times F\times Q/nF} \qquad \text{…… (9)}$$

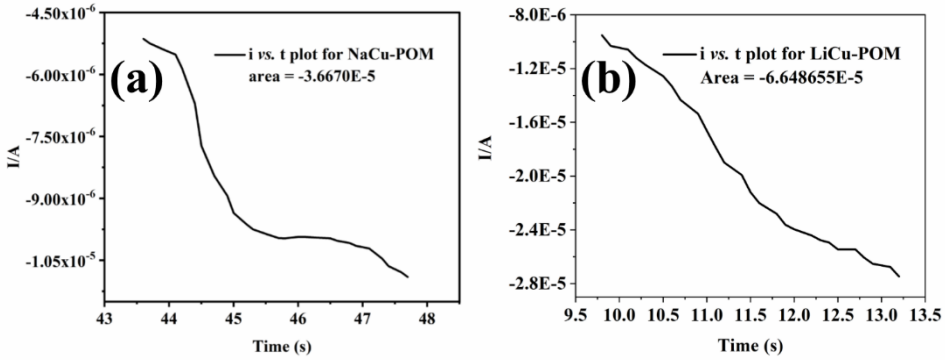

Figure 3.19. (**a** and **b**) *i-t* plots, constructed from the trace of cyclic voltammogram of **NaCu-POM** and **LiCu-POM** compounds [CVs were recorded in non-aqueous (acetonitrile) medium having 0.1 M $TBAClO_4$ as supporting electrolyte under nitrogen atmosphere].

Here, the factor n = 4 for both the catalysts, becuase four electrons are involved in the HER reaction.

$$TOF = \frac{I}{2Q/4} \qquad \ldots\ldots\ldots\ldots\ldots (10)$$

$$TOF = \frac{4\times I}{2\times Q} \qquad \ldots\ldots\ldots\ldots\ldots (11)$$

Calculation of TOF values for NaCu-POM and LiCu-POM using equation 11.

For NaCu-POM,

The current (*I*) value, obtained from CA electrolysis (**Figure 3.13**(**a**)) = -2.931×10^{-5}A

and charge (*Q*) (from **Figure 3.19**(**a**)) = -3.667×10^{-5} C.

$$TOF = \frac{4\times2.931E-5}{2\times3.667E-5}$$

TOF = **1.598** mol (H_2) s^{-1}

For LiCu-POM,

The current (*I*) value obtained from CA electrolysis (**Figure 3.13**(**a**)) = -3.716×10^{-5}A

and charge (*Q*) (from Figure 3.19b) = -6.648×10^{-5} C.

$$TOF = \frac{4\times3.716E-5}{2\times6.648E-5}$$

TOF = **1.117** mol (H_2) s^{-1}

This, the obtained TOF values of **1.598** and **1.117** sec^{-1} clearly demonstrate that **NaCu-POM** is a more efficient HER electrocatalyst compared to **LiCu-POM**.

3.4. Conclusion

In conclusion, two analogous higher nuclear mixed-valent copper wheel functionalized polyoxotungstobismuthates (**NaCu-POM** and **LiCu-POM**) were isolated adopting a facile one-pot wet synthetic method. Interestingly, presence suitable reaction conditions like reducing atmosphere in the **LiCu-POM** reaction mixture, the sulphate (source $CuSO_4$) gets converted into a hydrogen sulfide (SH^-) and coordinated to the one of the six copper centers. The functionalized **NaCu-POM** and **LiCu-POM** systems synergistically activate the cluster tungsten centers towards electrocatalytic water reduction to molecular hydrogen at neutral pH. The **NaCu-POM** and **LiCu-POM** catalysts exhibit enhanced electrocatalytic activity with less cathodic onset potentials, 0.31 and 0.14V, respectively along with a high WR (water reduction) current compared to the pristine $\mathbf{PW_9}$ system. The stability tests and controlled experiments reveal the robustness and true molecular electrocatalytic water reduction nature of the **NaCu-POM** and **LiCu-POM** catalysts. Besides, relatively low Tafel slope values 267 and 352 mV dec^{-1} with good Faradic efficiencies 88 and 92% confirm the high-end water reduction activity at neutral pH by the title compounds **NaCu-POM** and **LiCu-POM**, respectively. The high TOF values of 1.598 and 1.117 sec^{-1} demonstrate also the high efficiencies of **NaCu-POM** and **LiCu-POM** catalysts, respectively. Between these two catalysts, the **NaCu-POM** has shown better WR performance in terms of efficiency parameters. The design and functionalization strategy of these two POMs in the present investigation can open up new avenue for clean and sustainable energy production using noble metal free bio-compatible catalyst.

3.5. References

(1). Gray, H. B. Powering the Planet with Solar Fuel. *Nat. Chem*. **2009**, *1*, 7.
(2). Zhu, J.; Hu, L.; Zhao, P.; Lee, L. Y. S.; Wong, K.-Y., Recent Advances in Electrocatalytic Hydrogen Evolution Using Nanoparticles. *Chem. Rev*. **2020**, *120*, 851-918.
(3). Lewis, N. S.; Nocera, D. G. Powering the Planet: Chemical Challenges in Solar Energy Utilization. *Proc. Natl. Acad. Sci. U. S. A.* **2006**, *103*, 15729.
(4). REN21; Renewables 2018 Global Status Report, http://www. ren21.net/about-ren21/about-us/,2018.
(5). United States Department of Energy. A National Vision of America's Transition to a Hydrogen Economy-To 2030 and Beyond; Washington, *DC*, **2003**.
(6). Bae, S.-Y.; Mahmood, J.; Jeon, I.-Y.; Baek, J.-B., Recent Advances in Ruthenium-based Electrocatalysts for the Hydrogen Evolution Reaction. *Nanoscale Horiz*. **2020**, *5*, 43-56.
(7). Zou, X. X.; Zhang, Y. Noble Metal-free Hydrogen Evolution Catalysts for Water Splitting. *Chem. Soc. Rev*. **2015**, *44*, 5148-5180.
(8). Ghosh, S.; Srivastava, A. K.; Govu, R.; Pal, U.; Pal, S., A Diuranyl(VI) Complex and Its Application in Electrocatalytic and Photocatalytic Hydrogen Evolution from Neutral Aqueous Medium. *Inorg. Chem.* **2019**, *58*, 14410-14419.
(9). Frey, M., Hydrogenases: Hydrogen-Activating Enzymes. *ChemBioChem* **2002**, *3*, 153-160.
(10). Mondal, B.; Dey, A., Development of Air-Stable Hydrogen Evolution Catalysts. *Chem. Commun*. **2017**, *53*, 7707-7715.
(11). Morales-Guio, C. G.; Stern, L.-A.; Hu, X. Nanostructured Hydrotreating Catalysts for Electrochemical Hydrogen Evolution. *Chem. Soc. Rev.* **2014**, *43*, 6555−6569.
(12). Jiao, Y.; Zheng, Y.; Jaroniec, M.; Qiao, S. Z. Design of Electrocatalysts for Oxygen- and Hydrogen-Involving Energy Conversion Reactions. *Chem. Soc. Rev*. **2015**, *44*, 2060−2086.

(13). Wang, J.; Xu, F.; Jin, H.; Chen, Y.; Wang, Y. Non-Noble Metal based Carbon Composites in Hydrogen Evolution Reaction: Fundamentals to Applications. *Adv. Mater*. **2017**, *29*, 1605838.
(14). Zheng, Y.; Jiao, Y.; Vasileff, A.; Qiao, S.-Z. The Hydrogen Evolution Reaction in Alkaline Solution: From Theory, Single Crystal Models, to Practical Electrocatalysts. *Angew. Chem., Int. Ed.* **2018**, *57*, 7568−7579.
(15). Jin, H. Y.; Guo, C. X.; Liu, X.; Liu, J. L.; Vasileff, A.; Jiao, Y.; Zheng, Y.; Qiao, S. Z. Emerging Two-Dimensional Nanomaterials for Electrocatalysis. *Chem. Rev.* **2018**, *118*, 6337−6408.
(16). Hou, J.; Wu, Y.; Zhang, B.; Cao, S.; Li, Z.; Sun, L. Rational Design of Nanoarray Architectures for Electrocatalytic Water Splitting. *Adv. Funct. Mater*. **2019**, *29*, 1808367.
(17). Gao, Q. S.; Zhang, W. B.; Shi, Z. P.; Yang, L. C.; Tang, Y. Structural Design and Electronic Modulation of Transition-Metal Carbide Electrocatalysts toward Efficient Hydrogen Evolution. *Adv. Mater*. **2019**, *31*, 1802880.
(18). van Troostwijk, A. P.; Deiman, J. Sur Une Maniere De` Decopoer L´ 'eau en Air Inflammable et en Air Vital. *Obs. Phys. 1789*.
(19). Chen, J.-J.; Symes, M. D.; Cronin, L., Highly reduced and protonated aqueous solutions of $[P_2W_{18}O_{62}]^{6-}$ for on-demand hydrogen generation and energy storage. *Nat. Chem.* **2018**, *10*, 1042-1047.
(20). Martin-Sabi, M.; Soriano-López, J.; Winter, R. S.; Chen, J.-J.; Vilà-Nadal, L.; Long, D.-L.; Galán-Mascarós, J. R.; Cronin, L., Redox tuning the Weakley-type Polyoxometalate Archetype for the Oxygen Evolution Reaction. *Nat. Catal*. **2018**, *1*, 208-213.
(21). Danilovic, N.; Subbaraman, R.; Strmcnik, D.; Chang, K.-C.; Paulikas, A. P.; Stamenkovic, V. R.; Markovic, N. M., Enhancing the Alkaline Hydrogen Evolution Reaction Activity through the Bifunctionality of $Ni(OH)_2$/Metal Catalysts. *Angew. Chem. Int. Ed*. **2012**, *51*, 12495-12498.
(22). Subbaraman, R.; Tripkovic, D.; Strmcnik, D.; Chang, K.-C.; Uchimura, M.; Paulikas, A. P.; Stamenkovic, V.; Markovic, N. M., Enhancing Hydrogen Evolution Activity in Water Splitting by Tailoring Li^+-$Ni(OH)_2$-Pt Interfaces. *Science* **2011**, *334*, 1256.
(23). Subbaraman, R.; Tripkovic, D.; Chang, K.-C.; Strmcnik, D.; Paulikas, A. P.; Hirunsit, P.; Chan, M.; Greeley, J.; Stamenkovic, V.; Markovic, N. M., Trends in Activity for the Water Electrolyser Reactions on 3*d* M(Ni,Co,Fe,Mn) hydr(oxy)oxide catalysts. *Nat. Mater*. **2012**, *11*, 550-557.
(24). Zhang, L.; Liu, P. F.; Li, Y. H.; Wang, C. W.; Zu, M. Y.; Fu, H. Q.; Yang, X. H.; Yang, H. G., Accelerating Neutral Hydrogen Evolution with Tungsten Modulated Amorphous Metal Hydroxides. *ACS Catal*. **2018**, *8*, 5200-5205.
(25). Long, D.-L.; Burkholder, E.; Cronin, L., Polyoxometalate Clusters, Nanostructures and Materials: From Self-Assembly to Designer Materials and Devices. *Chem. Soc. Rev*. **2007**, *36*, 105-121.
(26). Miras, H. N.; Yan, J.; Long, D.-L.; Cronin, L., Engineering Polyoxometalates with Emergent Properties. *Chem. Soc. Rev*. **2012**, *41*, 7403-7430.
(27). Song, Y.-F.; Tsunashima, R., Recent Advances on Polyoxometalate-based Molecular and Composite Materials. *Chem. Soc. Rev.* **2012**, *41*, 7384-7402.
(28). Roger, I.; Shipman, M. A.; Symes, M. D., Earth-Abundant Catalysts for Electrochemical and Photoelectrochemical Water Splitting. *Nat. Rev. Chem*. **2017**, *1*, 0003.
(29). Chen, J. J.; Symes M. D.; Fan, S. C.; Zheng, M. S.; Miras H. N.; Dong, Q. F.; Cronin, L., High-Performance Polyoxometalate-Based Cathode Materials for Rechargeable Lithium-Ion Batteries. *Adv. Mater.* **2015**, *27*, 4649-4654.
(30). Chen, J. J.; Ye, J. C.; Zhang, X. G.; Symes M. D.; Fan, S. C.; Long, D. L.; Zheng, M. S.; Wu, D. Y.; Cronin, L.; Dong, Q. F., Design and Performance of Rechargeable Sodium Ion Batteries, and Symmetrical Li-Ion Batteries with Supercapacitor-Like Power Density Based upon Polyoxovanadates. *Adv. Energy Mater*. **2017**, *8*, 1701021.
(31). Ueda, T., Electrochemistry of Polyoxometalates: From Fundamental Aspects to Applications. *ChemElectroChem* **2018**, *5*, 823-838.
(32). Qin, J.-S.; Du, D.-Y.; Guan, W.; Bo, X.-J.; Li, Y.-F.; Guo, L.-P.; Su, Z.-M.; Wang, Y.-Y.; Lan, Y.-Q.; Zhou, H.-C., Ultrastable Polymolybdate-Based Metal–Organic Frameworks as Highly Active Electrocatalysts for Hydrogen Generation from Water. *J. Am. Chem. Soc.* **2015**, *137*, 7169-7177.
(33). Tourneur, J.; Fabre, B.; Loget, G.; Vacher, A.; Mériadec, C.; Ababou-Girard, S.; Gouttefangeas, F.; Joanny, L.; Cadot, E.; Haouas, M.; Leclerc-Laronze, N.; Falaise, C.; Guillon, E., Molecular and Material Engineering of Photocathodes Derivatized with Polyoxometalate-Supported $\{Mo_3S_4\}$ HER Catalysts. *J. Am. Chem. Soc.* **2019**, *141*, 11954-11962.

(34). Nohra, B.; El Moll, H.; Rodriguez Albelo, L. M.; Mialane, P.; Marrot, J.; Mellot-Draznieks, C.; O'Keeffe, M.; Ngo Biboum, R.; Lemaire, J.; Keita, B.; Nadjo, L.; Dolbecq, A., Polyoxometalate-Based Metal Organic Frameworks (POMOFs): Structural Trends, Energetics, and High Electrocatalytic Efficiency for Hydrogen Evolution Reaction. *J. Am. Chem. Soc.* **2011**, *133*, 13363-13374.

(35). Chisholm, G.; Cronin, L.; Symes, M. D., Decoupled Electrolysis using a Silicotungstic Acid Electron-Coupled-Proton Buffer in a Proton Exchange Membrane Cell. *Electrochim. Acta* **2020**, *331*, 135255.

(36). Fernandes, D. M.; Araújo, M. P.; Haider, A.; Mougharbel, A. S.; Fernandes, A. J. S.; Kortz, U.; Freire, C., Polyoxometalate-graphene Electrocatalysts for the Hydrogen Evolution Reaction. *ChemElectroChem* **2018**, *5*, 273-283.

(37). Miao, J.; Lang, Z.; Zhang, X.; Kong, W.; Peng, O.; Yang, Y.; Wang, S.; Cheng, J.; He, T.; Amini, A.; Wu, Q.; Zheng, Z.; Tang, Z.; Cheng, C., Polyoxometalate-Derived Hexagonal Molybdenum Nitrides (MXenes) Supported by Boron, Nitrogen Codoped Carbon Nanotubes for Efficient Electrochemical Hydrogen Evolution from Seawater. *Adv. Funct. Mater.* **2019**, *29*, 8.

(38). Pichon, C.; Mialane, P.; Dolbecq, A.; Marrot, J.; Rivière, E.; Keita, B.; Nadjo, L.; Sécheresse, F., Characterization and Electrochemical Properties of Molecular Icosanuclear and Bidimensional Hexanuclear Cu(II) Azido Polyoxometalates. *Inorg. Chem.* **2007**, *46*, 5292-5301.

(39). Bao, Y.-Y.; Bi, L.-H.; Wu, L.-X.; Mal, S. S.; Kortz, U., Preparation and Characterization of Langmuir−Blodgett Films of Wheel-Shaped Cu-20 Tungstophosphate and DODA by Two Different Strategies. *Langmuir* **2009**, *25*, 13000-13006.

(40). Kato, C.; Nishihara, S.; Tsunashima, R.; Tatewaki, Y.; Okada, S.; Ren, X.-M.; Inoue, K.; Long, D.-L.; Cronin, L., Quick and selective synthesis of $Li_6[\alpha\text{-}P_2W_{18}O_{62}]\cdot 28H_2O$ Soluble in Various Organic Solvents. *Dalton Trans.* **2013**, *42*, 11363-11366.

(41). Mal, S. S.; Bassil, B. S.; Ibrahim, M.; Nellutla, S.; van Tol, J.; Dalal, N. S.; Fernández, J. A.; López, X.; Poblet, J. M.; Biboum, R. N.; Keita, B.; Kortz, U., Wheel-Shaped Cu_{20}-Tungstophosphate $[Cu_{20}X(OH)_{24}(H_2O)_{12}(P_8W_{48}O_{184})]^{25-}$ Ion (X = Cl, Br, I) and the Role of the Halide Guest. *Inorg. Chem.* **2009**, *48*, 11636-11645.

(42). von Allmen, K. D.; Grundmann, H.; Linden, A.; Patzke, G. R., Synthesis and Characterization of 0D–3D Copper-Containing Tungstobismuthates Obtained from the Lacunary Precursor $Na_9[B\text{-}\alpha\text{-}BiW_9O_{33}]$. *Inorg. Chem.* **2017**, *56*, 327-335.

(43). Lv, H.; Gao, Y.; Guo, W.; Lauinger, S. M.; Chi, Y.; Bacsa, J.; Sullivan, K. P.; Wieliczko, M.; Musaev, D. G.; Hill, C. L., Cu-based Polyoxometalate Catalyst for Efficient Catalytic Hydrogen Evolution. *Inorg. Chem.* 2016, 55, 6750-6758.

(44). Su, Z.-M.; Zhang, M.; An, Q.; Qin, D.; Li, H.-L.; Lv, H.; Jia, Z.; Zhang, Q.; Yang, G.-Y., Synthesis of Two New Copper-Sandwiched Polyoxotungstates and the Influence of Nuclear Number on Catalytic Hydrogen Evolution Activity. *New J. Chem.* **2020**, *44*, 11035-11041.

(45). Kong, X.; Peng, Z., Low-Dimensional Materials for Alkaline Oxygen Evolution Electrocatalysis. *Mater. Today Chem.* **2019**, *11*, 119-132.

(46). Yuan, N.; Jiang, Q.; Li, J.; Tang, J., A Review on Non-Noble Metal Based Electrocatalysis for the Oxygen Evolution Reaction. *Arab. J. Chem.* **2020**, *13*, 4294-4309.

(47). Kortz, U.; Nellutla, S.; Stowe, A. C.; Dalal, N. S.; van Tol, J.; Bassil, B. S., Structure and Magnetism of the Tetra-Copper(II)-Substituted Heteropolyanion $[Cu_4K_2(H_2O)_8(\alpha\text{-}AsW_9O_{33})_2]^{8-}$. *Inorg. Chem.* **2004**, *43*, 144 -154.

(48). Yamase, T.; Ishikawa, H.; Abe, H.; Fukaya, K.; Nojiri, H.; Takeuchi, H., Molecular Magnetism of M_6 Hexagon Ring in D_3d Symmetric $[(MCl)_6(XW_9O_{33})_2]^{12-}$ (M = Cu^{II} and Mn^{II}, X = Sb^{III} and As^{III}). *Inorg. Chem.* **2012**, *51*, 4606-4619.

(49). Yamase, T.; Fukaya, K.; Nojiri, H.; Ohshima, Y., Ferromagnetic Exchange Interactions for Cu_6^{12+} and Mn_6^{12+} Hexagons Sandwiched by Two B-α-$[XW_9O_{33}]^{9-}$ (X = As^{III} and Sb^{III}) Ligands in *D3d*-Symmetric Polyoxotungstates. *Inorg. Chem.* **2006**, *45*, 7698-7704.

(50). Bi, L.-H.; Li, B.; Wu, L.-X.; Bao, Y.-Y., Synthesis, Characterization and Crystal Structure of a Novel 2D Network Structure Based on Hexa-Copper(II) Substituted Tungstoantimonate. *Inorg. Chimica Acta* **2009**, *362*, 3309-3313.

(51). Zhang, Z.; Sun, K.-N.; Yang, G.-Y., Two Series of Cu^{II}-Substituted Sandwich-Type Polyoxotungstates Constructed from Trivacant Germanotungstate Fragments. *ChemistrySelect* **2019**, *4*, 7559-7565.

(52). Yao, S.; Zhang, Z.; Li, Y.; Wang, E., A $\{Cu_6\}$-Containing Inorganic-Metal-Organic Sandwich-Type Tungstoantimonite and its 3D Supramolecular Framework. *Inorg. Chem. Commun.* **2009**, *12*, 937-940.

(53). Han, Q.; Ma, P.; Zhao, J.; Wang, J.; Niu, J., A novel 1D Tungstoarsenate with Mixed Organic Ligands Assembled by Hexa-Cu Sandwiched Keggin Units and Dinuclear Copper-Oxalate Complexes. *Inorg. Chem. Commun*. **2011**, *14*, 767-770.

(54). Zamstein, N.; Tarantul, A.; Tsukerblat, B., Magnetic Excitations in Cu_6 and Mn_6 Hexagons Embedded in D_3d-Symmetric Polyoxotungstates. *Inorg. Chem.* **2007**, *46*, 8851-8858.

(55). Niu, J.-Y.; Ma, X.; Zhao, J.-W.; Ma, P.-T.; Zhang, C.; Wang, J.-P., A Novel Organic–Inorganic Hybrid Turbine-Shaped Hexa-Zn Sandwiched Tungstoarsenate(III). *CrystEngComm* **2011**, *13*, 4834-4837.

(56). Li, D.; Ma, X.; Wang, Q.; Ma, P.; Niu, J.; Wang, J., Copper-Containing Polyoxometalate-Based Metal–Organic Frameworks as Highly Efficient Heterogeneous Catalysts toward Selective Oxidation of Alkylbenzenes. *Inorg. Chem.* **2019**, *58*, 15832-15840.

(57). Zhao, J.-W.; Zheng, S.-T.; Li, Z.-H.; Yang, G.-Y., Combination of Lacunary Polyoxometalates and High-Nuclear Transition-Metal Clusters Under Hydrothermal Conditions: first 65·8 $CdSO_4$-type 3-D Framework Built by Hexa-Cu(II) Sandwiched Polyoxotungstates. *Dalton Trans.* **2009**, 1300-1306.

(58). Rosu, C.; Rasu, D.; Weakley, T. J. R., X-ray Structure of Dodecasodium Tricopper(II)bis-nonatungstabismuthate(III) Hydrate, a Polyoxometalate Salt Containing $[\alpha\text{-B-}BiW_9O_{33}]^{9-}$ Units. *J. Chem. Crystallogr.* **2003**, *33*, 751-755.

(59). Rusu, D.; Tomasa, A. R.; Turdean, G. L.; Cojocaru, I.; Oana, B.; Rusu, M. Synthesis and Investigation of the Copper(II)-Substituted Polyoxotungstate Based on $[\alpha\text{-B-}BiW_9O_{33}]^{9-}$ Units. *Rev. Roum. Chim*. **2012**, *57*, 327–336.

(60). Rusu, D.; Roşu, C.; Crăciun, C.; David, L.; Rusu, M.; Marcu, G. FT-IR, UV–VIS and EPR Investigations of Multicopper Polyoxotungstates with Bi(III) as Heteroatom. *J. Mol. Struct.* **2001**, *563*, 427–433.

(61). SAINT: Software for the CCD Detector System, Bruker Analytical X-ray Systems, Inc., Madison, WI, **1998**.

(62). Sheldrick, G. M., SADABS, Program for Absorption Correction, University of Gottingen, Gottingen, Germany, **1997**.

(63). Sheldrick, G. M., SHELXT – Integrated space-group and crystal-structure determination, *Acta Crystallogr., Sect. A: Found. Adv.*, **2015**, *71*, 3–8.

(64). Sheldrick, G. M., Crystal structure refinement with SHELXL, *Acta Crystallogr., Sect. C: Struct. Chem.*, **2015**, *71*, 3–8, (SHELXL-**2018/1** (Sheldrick, **2018**)).

(65). Zhang, W.; Liu, S.; Feng, D.; Zhang, C.; Sun, P.; Ma, F., Two Novel Krebs-type Polyoxoanions $[Cu^{I}_2(WO_2)_2(\beta\text{-}XW_9O_{33})_2]^{12-}$ (X=SbIII, BiIII) Resulting in 2D Layer Structures Linked by Copper(I) ions and Copper(II) Complex Groups. *J. Mol. Struct.* **2009**, *936*, 194-198.

(66). O'Keefe, M.; Brese, N. E., Atom Sizes and Bond Lengths in Molecules and Crystals. *J. Am. Chem. Soc.* **1991**, *113*, 3226-3229.

(67). Swadźba-Kwaśny, M.; Chancelier, L.; Ng, S.; Manyar, H. G.; Hardacre, C.; Nockemann, P., Facile *In-Situ* Synthesis of Nanofluids Based on Ionic Liquids and Copper Oxide Clusters and Nanoparticles. *Dalton Trans.* **2012**, *41*, 219-227.

(68). Mukhopadhyay, S.; Debgupta, J.; Singh, C.; Kar, A.; Das, S. K., A Keggin Polyoxometalate Shows Water Oxidation Activity at Neutral pH: POM@ZIF-8, an Efficient and Robust Electrocatalyst. *Angew. Chem. Int. Ed.* **2018,** *57*, 1918-1923.

(69). Rauf, A.; Sher Shah, M. S. A.; Choi, G. H.; Humayoun, U. B.; Yoon, D. H.; Bae, J. W.; Park, J.; Kim, W.-J.; Yoo, P. J., Facile Synthesis of Hierarchically Structured Bi_2S_3/Bi_2WO_6 Photocatalysts for Highly Efficient Reduction of Cr(VI). *ACS Sustainable Chemistry & Engineering* **2015**, *3*, 2847-2855.

(70). Shi, Y.; Chen, Y.; Tian, G.; Fu, H.; Pan, K.; Zhou, J.; Yan, H., One-Pot Controlled Synthesis of Sea-Urchin Shaped Bi_2S_3/CdS Hierarchical Heterostructures with Excellent Visible Light Photocatalytic Activity. *Dalton Trans.* **2014**, *43*, 12396-12404.

(71). Aurbach, D.; Weissman, I.; Schechter, A.; Cohen, H., X-ray Photoelectron Spectroscopy Studies of Lithium Surfaces Prepared in Several Important Electrolyte Solutions. A Comparison with Previous Studies by Fourier Transform Infrared Spectroscopy. *Langmuir* **1996**, *12*, 3991-4007.

(72). Bassil, B. S.; Haider, A.; Ibrahim, M.; Mougharbel, A. S.; Bhattacharya, S.; Christian, J. H.; Bindra, J. K.; Dalal, N. S.; Wang, M.; Zhang, G.; Keita, B.; Rutkowska, I. A.; Kulesza, P. J.; Kortz, U., 15-Copper(II)-Containing 36-Tungsto-4-Silicates(IV) $[Cu_{15}O_2(OH)_{10}X(A\text{-}\alpha\text{-}SiW_9O_{34})_4]^{25-}$ (X = Cl, Br):

Synthesis, Structure, Magnetic Properties, and Electrocatalytic CO_2 Reduction. *Dalton Trans.* **2018**, *47*, 12439-12448.

(73). Kulesza, P. J.; Faulkner, L. R.; Chen, J.; Klemperer, W. G., Solid-State Electrochemistry: Voltammetric Monitoring of Redox Transitions in Single Crystals of Silicotungstic Acid. *J. Am. Chem. Soc*. **1991**, *113*, 379-381.

(74). Kulesza, P. J.; Faulkner, L. R., Solid-State Electroanalysis of Silicotungstic Acid Single Crystals at an Ultramicrodisk Electrode. *J. Am. Chem. Soc.* **1993**, *115*, 11878-11884.

(75). Singh, C.; Das, S. K., Anderson Polyoxometalate Supported Cu(H_2O)(phen) Complex as an Electrocatalyst for Hydrogen Evolution Reaction in Neutral Medium. *Polyhedron* **2019,** *172*, 80-86.

(76). Singh, C.; Mukhopadhyay, S.; Das, S. K., Polyoxometalate-Supported Bis(2,2′-bipyridine)mono(aqua)nickel(II) Coordination Complex: an Efficient Electrocatalyst for Water Oxidation. *Inorg. Chem.* **2018**, *57*, 6479-6490.

(77). Jabbour, D.; Keita, B.; Nadjo, L.; Kortz, U.; Mal, S. S., The Wheel-Shaped Cu_{20}–Tungstophosphate $[Cu_{20}Cl(OH)_{24}(H_2O)_{12}(P_8W_{48}O_{184})]^{25-}$, Redox and Electrocatalytic Properties. *Electrochem. commun*. **2005**, *7*, 841-847.

(78). Murphy, A. F.; McCormac, T., Surface Immobilisation of Ttransition Metal Substituted Krebs type Polyoxometalates, $[X_2W_{20}M_2O_{70}(H_2O)_6]^{n-}$ (X=Bi or Sb, M=Co^{2+} or Cu^{2+}), by the Layer by Layer Technique. *Electrochimica Acta* **2011**, *56*, 10751-10761.

(79). Ginsberg, A. P., *Inorganic Syntheses.* **1990**, *27*, p-100. *Online* ISBN:9780470132586, *DOI:10.1002/9780470132586*.

(80). Shinagawa, T.; Garcia-Esparza, A. T.; Takanabe, K., Insight on Tafel Slopes from a Microkinetic Analysis of Aqueous Electrocatalysis for Energy Conversion. *Sci. Rep*. **2015**, *5*, 13801.

(81). Shinagawa, T.; Takanabe, K., Towards Versatile and Sustainable Hydrogen Production Through Electrocatalytic Water Splitting: Electrolyte Engineering. *ChemSusChem* **2017**, *10*, 1318-1336.

(82). Mukhopadhyay, S.; Basu, O.; Kar, A.; Das, S. K., Efficient Electrocatalytic Water Oxidation by Fe(salen)–MOF Composite: Effect of Modified Microenvironment. *Inorg. Chem*. **2020**, *59*, 472-483.

(83). Kim, Y.; Shanmugam, S., Polyoxometalate–Reduced Graphene Oxide Hybrid Catalyst: Synthesis, Structure, and Electrochemical Properties. *ACS Applied Mater. Interfaces* **2013,** *5*, 12197-12204.

(84). Mahmood, J.; Li, F.; Jung, S.-M.; Okyay, M. S.; Ahmad, I.; Kim, S.-J.; Park, N.; Jeong, H. Y.; Baek, J.-B., An Efficient and pH-Universal Ruthenium-Based Catalyst for the Hydrogen Evolution Reaction. *Nat. Nanotechnol*. **2017**, *12*, 441-446.

CHAPTER 4

A Fully Reduced $\{V_{18}^{IV}O_{42}\}$ Host and VO_4^{3-}, Cl^- as Guest Anions: Synthesis, Characterization and Proton Conductivity

Overview:

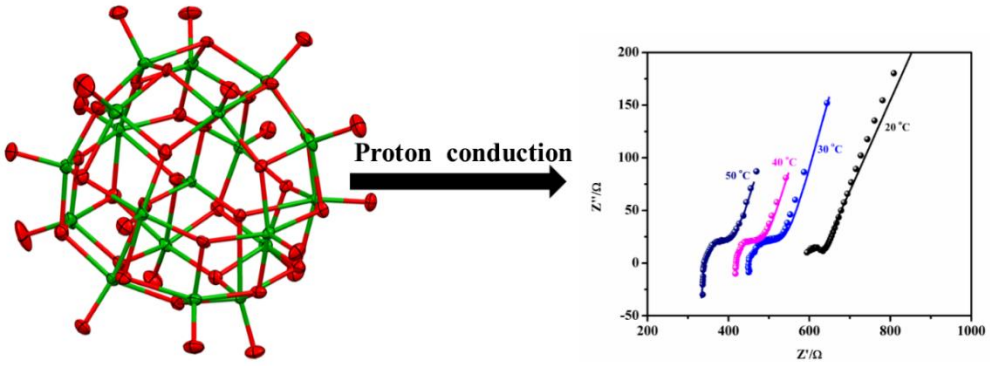

Fully reduced polyoxometalates (POMs), generally, have high negative charge that can be compensated by diverse cations including protons. The POMs with larger number of acidic protons often exhibit solid state proton conduction. We synthesized two polyoxovanadate (POV)-based compounds $[Na_7(H_2O)_{14}][H_8V^{IV}_{18}O_{42}(V^{V}O_4)]\cdot N_2H_4\cdot 7H_2O$ (**1**) and $[Na_5(H_2O)_{16}][H_8V^{IV}_{18}O_{42}(Cl)]\cdot 4N_2H_4\cdot 6H_2O$ (**2**), each of which accommodate eight acidic protons (per formula unit) acting as the cations. Compounds **1** and **2** have been characterized by routine analytical techniques, such as, IR, Raman, XPS, PXRD, TGA, *etc.* including elemental analysis and unambiguously by single crystal X-ray diffraction. As expected, compounds **1** and **2** having eight protons per formula unit exhibit proton conductivity in the solid state. Proton conductivity measurements of compounds **1** and **2** were performed (a) at variable temperature (20–50 °C), with constant humidity (70% RH) and (b) variable relative humidity (relative humidity from 40 % to 70%) under constant temperature (30 °C). The proton conductivity was observed to increase with increase in temperature and relative humidity. The best conductivity values were obtained at 50 °C under 70% RH and found to be 3.62×10^{-3} S cm^{-1} for compound **1** and 2.16×10^{-4} S cm^{-1} for compound **2**. Reproducibility of proton conductivity was verified by repetitive data recording over long time period and determining the mean value of conductivity of compounds **1** and **2** at 50 °C. The activation energy for **1** (23.34 kJ mol^{-1}) and **2** (18.40 kJ mol^{-1}) calculated from Arrhenius plots of temperature dependence of proton conductivity suggest a Grotthuss proton hoping mechanism for solid state proton conduction. Controlled experiments have shown that the synthesized compounds **1** and **2** are stable and robust under operational conditions.

4.1. Introduction

Polyoxometalates (POMs) are the compounds known over two hundred years for their structural diversities with various molecular motifs and sizes[1-12] and numerous applications in physical sciences like catalysis, medicinal chemistry, magnetism, nonlinear optics, solar cells and material science.[1-36] Being a subclass of POMs, polyoxovanadates (POVs) also gained a special attention because of their diverse structures,[1-12] supramolecular topologies,[4] and their applications such as catalysts,[13,14] electron reservoirs as well as supercapaciters,[13-18] single molecular magnets,[19-22] and sensors.[27-30] In general, the charge of anionic POVs/POMs were compensated by 1A group cations, *e.g.*, Li^+, Na^+, K^+ and Cs^+, organic cations as well as transition metal ions/complex cations (mostly 3*d* metals)[13-30] along with required number of protons. Due to the imparted acidity by these protons, the concerned POMs are regarded as heteropolyacids.[37] Solid state electrolytes with acidic protons are very important class of materials that show proton conduction. The magnitude of conductivity is proportional to the number of labile protons/ions (such as H_3O^+, $H_5O_2^+$ NH_4^+ etc.).[38] Hence, the presence of more the number of labile protons, can help to enhance the proton conductivity. Proton exchange membrane fuel cells (PEMFCs) are highly attractive, where proton conduction analogy is similar to that, occurred in photosynthesis.[39-41] So far, Nafion is used as proton conduction material in PEMFCs, as it show high proton conductivity (10^{-1} S cm^{-1}) and chemical stability.[43,44] However, its high manufacturing cost and low water holding capability still motivate researchers to search for suitable alternative materials.[45,46] In this regard, several materials including metal-organic frameworks (MOFs),[41,42] covalent organic frameworks (COFs),[47,48] functionalized zeolites,[49-53] and polyoxometalates have been studied for their proton conducting properties.[54-67] Here it is noteworthy to mention that, recently, Liu *et al*.[68] and Li *et al*.[69] reported stable mixed-valence molybdenum (VI/V) Mo_{132} spherical cluster containing- and reduced vanadium (IV) containing POM based-proton conducting materials, respectively.[68,69] In this context, fully reduced polyoxovanadates (POVs) are relatively more negatively charged compounds compared to their mixed-valent and oxidized analogues, resulting in a high probability of having protons on the relevant POV cluster surface,[6,7,21,2] thereby bringing about potential proton conducting materials. However, vanadium based POMs (i.e., POVs) are less explored as solid state proton conducting materials compared to the other POMs.[66-69] In general, POVs are well known for their host-guest chemistry.[7,21,22,70-88] The fully reduced $[V_{18}O_{42}]^{12-}$ host system as such (without any guest)[6] and the same reduced host system with a guest species $[V_{18}O_{42}(X)]^{n-}$ (X = H_2O, Cl^-, Br^-, I^-, VO_4^{3-}) are known.[21,22] In these cases, the number of protons are 1–4 and the relevant syntheses were carried out at relatively high pH (11–13). Keeping the fact that, an occurrence of more protons on the fully reduced POV cluster surface may give rise to proton conduction, in mind, we intended to use relatively lower pH in the relevant aqueous synthesis (around pH 8 instead of pH 11–13) to stabilize the same POV clusters $[V^{IV}_{18}O_{42}(V^{V}O_4)]^{15-}$ and $[V^{IV}_{18}O_{42}(Cl)]^{13-}$ in achieving more protons, associated with the fully reduced POV cluster. Thus, herein, we have described the synthesis and

characterization of $[Na_7(H_2O)_{14}][H_8V^{IV}_{18}O_{42}(V^{V}O_4)]\cdot N_2H_4\cdot 7H_2O$ (**1**) and $[Na_5(H_2O)_{16}][H_8V^{IV}_{18}O_{42}(Cl)]\cdot 4N_2H_4\cdot 6H_2O$ (**2**), each having eight protons per formula unit, emphasizing their solid state proton conducting properties. In this context, we must mention that similar fully reduced compounds $Na_6[H_9V^{IV}_{18}O_{42}(V^{V}O_4)]\cdot 21H_2O$[21] and $[K_{11}[H_2V^{IV}_{18}O_{42}(Cl)]\cdot 2N_2H_4\cdot 13H_2O$[22] were reported, but their proton conducting properties were never explored.

4.2. Experimental section

4.2.1. Materials and methods

All the chemicals were AR grade (purchased from available commercial sources) and used as received. Deionised water was used for all the experiments. Compounds **1** and **2** have been isolated by conventional wet synthesis methods under ambient atmosphere.

4.2.1.1. Synthesis of $[Na_7(H_2O)_{14}][H_8V^{IV}_{18}O_{42}(V^{V}O_4)]\cdot N_2H_4\cdot 7H_2O$ (1)

3.6 g (30 mmol) of $NaVO_3$ was added to 100 mL of hot water (temp. 85–90 °C) in a 250 mL conical flask to give a clear colourless solution. 0.71 g (17.75 mmol) of solid NaOH was added to the above solution (pH=8.47) and immediately covered with a watch glass. The mixture was stirred for 30 mins on a hot plate (temp. 85–90 °C). To this, 2.5 g (19.23 mmol) of $N_2H_5\cdot HSO_4$ was added in small portions. A dark green coloured solution, obtained, was further stirred for 15 mins. The hot reaction mixture was sealed in a vial with rubber septum and N_2 gas was purged for 1 h though the solution. The solution was then filtered and filtrate was left undisturbed for 24 hours in a vial closed with air tight septum. The dark brown coloured precipitate formed was filtered off and dark green colored filtrate was again kept undisturbed for crystallization in a closed vial at room temperature. The dark green crystals, settled after a week, were filtered, washed three times with a 20 mL of ice cold water and dried in air at room temperature. Yield: 2.09 g (63% based on vanadium). Anal. calc. % (Found) for $H_{54}N_2O_{67}Na_7V_{19}$: V, 42.39 (42.23); Na, 7.05 (7.20); H, 2.38 (2.49); N, 1.23 (1.42).

4.2.1.2. Synthesis of $[Na_5(H_2O)_{16}][H_8V^{IV}_{18}O_{42}(Cl)]\cdot 4N_2H_4\cdot 6H_2O$ (2)

3.6 g (30 mmol) of $NaVO_3$ was added to 100 mL of hot water (temp. 85–90 °C) in a 250 mL conical flask to give a clear colourless solution. 0.72 g (18 mmol) of solid NaOH was added subsequently to the above solution (pH=8.5) and immediately covered with a watch glass. The mixture was stirred for 30 mins on a hot plate (temp. 85–90 °C). To this, 2.5 g (19.23 mmol) of $N_2H_5\cdot HSO_4$ was added in small portions. A dark green coloured solution was obtained and was further stirred for 15 mins. The hot reaction mixture was sealed in a vial with rubber septum and N_2 gas was purged for 1 h though the solution. The solution was filtered and 4 g (68.44 mmol) of NaCl was added to the filtrate and stirred for 10 more minutes and left undisturbed for 24 hours in a closed vial. The dark brown coloured precipitate, formed, was filtered off and dark coloured filtrate was again kept undisturbed for crystallization in a closed vial at room

temperature. The dark crystals settled after a week, were filtered, washed three times with a 20 mL of ice cold water and dried in air at room temperature. Yield: 2.47g (67% based on Vanadium). Anal. calc. % (Found) for $H_{68}N_8O_{64}Na_5V_{18}Cl$: V, 40.36 (40.92); Na, 5.0 (65.20); Cl, 1.56 (1.63); H, 3.02 (3.39); N, 4.93 (4.82).

4.2.2. Physical measurements

Elemental analyses were performed using FLASH EA series 1112 CHNS analyser. Bruker Tensor II FTIR instrument equipped with Platinum ATR (Attenuated Total Reflectance) accessory was used to collect FT-IR spectra. TG analyses were carried out on PerkinElmer – STA 6000 thermo-gravimetric analyser, under UHP nitrogen gas flow. Raman spectra were recorded on Wi-Tec alpha 300AR laser confocal optical microscope (T-LCM) facility equipped with a Peltier cooled CCD detector using 785 nm Argon ion laser. ICP-OES elemental analyses were performed on ICP-OES Varian 720ES. XPS analyses of powdered samples were performed on Omicron Nano Tec. ESCA$^+$ Oxford instruments Germany. Powder X-ray diffraction (PXRD) patterns of **1** and **2** were recorded on a Bruker D8-Advance diffractometer using graphite mono chromated CuKα1 (1.5406 Å) and Kα2 (1.54439 Å) radiation.

4.2.2.1. X-ray crystallography

Single crystals of compounds **1** and **2**, suitable to collect diffraction data, were obtained directly from the crystallization solvent. Single crystal X-ray diffraction data of **1** and **2** were collected at 100 K and 301 K respectively on a Bruker SMARTAPPEX III single crystal X-ray diffractometer equipped with CCD area detector, graphite monochromator and sealed Mo-Kα fine-focus X-ray tube (λ = 0.71073 Å). The scans were recorded with a ω scan width of 0.3°. Data reduction was performed by SAINT PLUS,[89] and empirical absorption corrections using equivalent reflections were performed by the SADABS.[90] Structure solutions were done using SHELXT-2015,[91] and full-matrix least-squares refinement was carried out using SHELXL-2015.[92] The important crystallographic data of compound **1** and **2** was given in **Table 4.1**. The details of bond distances and angles corresponding to compound **1** and **2** were provided in *Appendix 4(i)*. **CCDC–1906755** and **CCDC–1906756** contain the supplementary crystallographic data for compounds **1** and **2**, respectively. The crystal data can be obtained free of charge via http://www.ccdc.cam.ac.uk/conts/retrieving.html, or from the Cambridge Crystallographic Data Centre, 12 Union Road, Cambridge CB2 1EZ, UK; fax: (+44) 1223-336-033; or e-mail: deposit@ccdc.cam.ac.uk.

Table 4.1 Crystal data and structural refinement parameters for compounds **1** and **2**.

	Compound 1	**Compound 2**
Empirical formula	$H_{54}N_2Na_7O_{67}V_{19}$	$ClH_{68}N_8Na_5O_{64}V_{18}$
Formula weight	2283.22	2271.90
T(K)/ λ (Å)	100(2)/0.71073	301(2) /0.71073

Crystal system	Monoclinic	Trigonal
Space group	*Cc*	*P 3121*
a Å	20.7093(14)	12.8267(8)
b Å	15.2374(9)	12.8267(8)
c Å	19.1923(11)	33.368(2)
α (°)	90	90
β (°)	97.834(3)	90
γ (°)	90	120
Volume (Å^3)	5999.7(6)	4754.3(7)
Z	4	3
P calcd (g cm^{-3})	2.467	2.309
μ (mm^{-1}), *F*(000)	2.989, 4256	2.719, 3162
Goodness-of-fit on F^2	1.043	1.105
R_1/wR_2 [$I > 2\sigma(I)$]	0.0513/0.1406	0.0291/0.0809
R_1/wR_2 (all data)	0.0547/0.1431	0.0296/0.0809
Largest diff. peak/hole (e Å^{-3})	1.445/-1.023	1.341/-0.655

4.2.2.2. Solid-state proton conductivity methods

Pure powdered samples of **1** and **2** (400mg) were kept in between the two carbon sheets and made as a tablet having, 1.1455 cm^2 in area (*a*) and 0.286 cm in thickness (*l*) for compound **1** and 1.149 cm^2 in area (*a*) and 0.279 cm in thickness (*l*) for compound **2**, with the help of KBr press at 3 tons for 2 mins. The tablet was sandwiched in between two probe stainless steel electrodes (electrode || sample || electrode). The alternative current electrochemical impedance spectra (AC-EIS) for **1** and **2** were recorded in the range of 1Hz to 1MHz frequency applied by 100 mV of DC potential in the temperature range 20–50 °C with an interval of 10 °C at 70% relative humidity (RH) as well as in the range 40–70% RH with 10% relative humidity increment at 30 °C. The conditions are maintained with the help of a homemade humidity chamber and 4h of interval time was given between the successive measurements to attain the required experimental conditions. The alternative current electrochemical impedance spectroscopy (AC-EIS) was recorded on a Zahner Zanium electrochemical work station that operates with a Thales software. The experimentally obtained data were simulated/fitted with the electrochemical lab (EC-Lab V10.21 version) software.

4.3. Results and Discussion

4.3.1. Detailed discussion on synthesis

The fully reduced and proton rich vanadate cluster compounds **1** and **2** were isolated in a similar aqueous synthetic procedure, carried out under ambient condition. The synthesis involves usage of sodium meta-vanadate ($NaVO_3$) as a vanadium source, hydrazinium sulphate ($N_2H_5{\cdot}HSO_4$)

as a reducing agent and the pH of reaction mixture is adjusted to 8−8.5 using NaOH pellets. At the end of the reaction, N_2 gas was purged through the hot reaction mixtures of **1** and **2** to avoid the aerial contact. The reaction mixture of **2** was treated with slight excess of solid NaCl. Both the reaction mixtures (of compounds **1** and **2**) were kept undisturbed in a closed Erlenmeyer flask for crystallization. The isolated compounds are highly soluble in water, but insoluble in common organic solvents, e.g., methanol, ethanol, chloroform, dichloromethane *etc*. The elemental analysis data were consistent with the formulas $[Na_7(H_2O)_{14}][H_8V^{IV}_{18}O_{42}(V^{V}O_4)]\cdot N_2H_4\cdot 7H_2O$ (**1**) and $[Na_5(H_2O)_{16}][H_8V^{IV}_{18}O_{42}(Cl)]\cdot 4N_2H_4\cdot 6H_2O$ (**2**), also derived from the respective single crystal X-ray data.

4.3.2. Physical characterizations

4.3.2.1. Powder X-ray diffraction

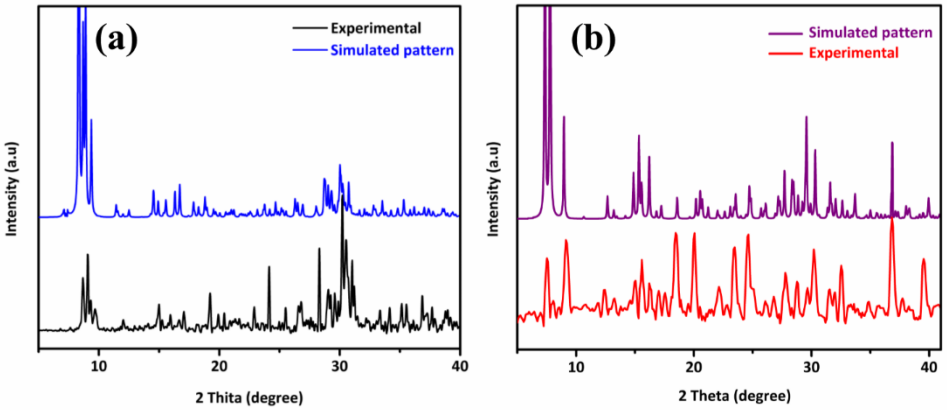

Figure 4.1. (**a** and **b**) powder X-ray diffraction analysis for compounds **1** and **2**.

The experimental powder XRD patterns recorded using powdered samples of compounds **1** and **2** were compared with the powder XRD patterns, simulated from respective single crystal data. The close matching of the observed PXRD pattern with their simulated profile indicates the bulk purity of the products **1** and **2** (**Figure 4.1**(**a** and **b**)). The compounds were further characterized by FTIR, Raman, UV-Vis and XPS spectroscopy. Thermogravimetric profiles of **1** and **2** were also collected to check their thermal stability.

4.3.2.2. Single-crystal X-ray crystallographic analysis

Compound $[Na_7(H_2O)_{14}][H_8V^{IV}_{18}O_{42}(V^{V}O_4)]\cdot N_2H_4\cdot 7H_2O$ (**1**) crystalized in a monoclinic space group *Cc*. The molecular structure of the concerned cluster is shown in **Figure 4.2**(**a**) as an ellipsoidal plot. The molecular structure reveals that a VO_4^{3-} ion is encapsulated by the metal-oxide cage made of spherically disposed 18 vanadyl $[\{V{=}O\}^{2+}]$ groups and 24 $\{\mu_3{-}O\}$ oxygen atoms. Each of the 18 vanadium atoms of the vanadyl groups coordinate to four bridging oxygens and one terminal oxygen atom to form a square pyramidal $\{VO_5\}$ unit. The central

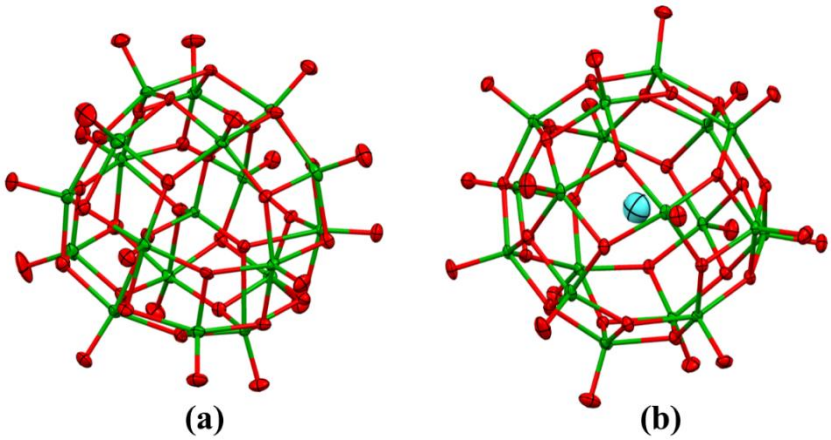

Figure 4.2. Single-crystal structures: (**a**) thermal ellipsoidal (60%) plot of the polyoxovanadate cluster anion in compound **1**; (**b**) thermal ellipsoidal (60%) diagram of the polyoxovanadate cluster anion of compound **2**.

encapsulated tetrahedral $\{VO_4^{3-}\}$ anion is connected to four $\{\mu_4–O\}$ oxygens and these $\{\mu_4–O\}$ oxygens are coordinated to twelve square pyramidal $\{VO_5\}$ units of the cluster and forms twelve octahedral $\{VO_6\}$ units. The remaining six $\{VO_5\}$ units do not have any interactions with central $\{VO_4^{3-}\}$ unit. The $V–\mu_4O(VO_4^{3-})$ distances fall within the range of 2.10–2.60 Å. The V=O terminal bond distances in the range 1.613–1.669 Å are similar to those of fully reduced POV cluster anions.[6,7,21,22] The details of bond distances and bond angles of **1** is listed in *Appendix VI(i)*. Bond valence sum calculations on the single crystal X-ray structure of compound **1** shows that all 18 cage vanadium centers are in +4 oxidation state and encapsulated tetrahedral vanadium has +5 oxidation state. The cluster ion $\{V^{IV}_{18}O_{42}(V^{V}O_4\}^{15-}$ demands fifteen positive charges; however in the crystal structure, only seven sodium ions are found to be located as cationic part. We therefore added eight protons (as cations) to compensate the fifteen negative charges of $\{V^{IV}_{18}O_{42}(V^{V}O_4\}^{15-}$. Similar proton addition has been shown by Müller and co-workers in the formulas of the similar fully reduced POV compounds.[21,22] In the crystal structure, the $[H_8V^{IV}_{18}O_{42}(V^{V}O_4)]^{7-}$ cluster units are inter-linked through the hydrated Na^+ cationic complexes and are hydrogen bonded lattice waters as well as hydrazine molecules to form a three-dimensional supra-molecular network shown in **Figure 4.3**(**a**).

Compound $[Na_5(H_2O)_{16}][H_8V^{IV}_{18}O_{42}(Cl)]\cdot4N_2H_4\cdot6H_2O$ (**2**) crystallized in a trigonal *P3121* space group. The molecular structure of cluster is shown in **Figure 4.2**(**b**) as ORTEP representation. The topology of cluster cage (compound **2**) is similar to that of **1**, except the encapsulation of Cl^- ion (compound **2**) instead of VO_4^{3-} ion (compound **1**). Unlike the VO_4^{3-} ion in **1**, the encapsulated Cl^- ion does not display any covalent interaction with the cluster cage and stabilized by establishing simple electrostatic interactions with the vanadium centers of cage. The V=O terminal bond distances in the range 1.606–1.636 Å are also similar to the same V=O distances of fully reduced clusters, reported earlier.[6,7,21,22] The details of bond distances

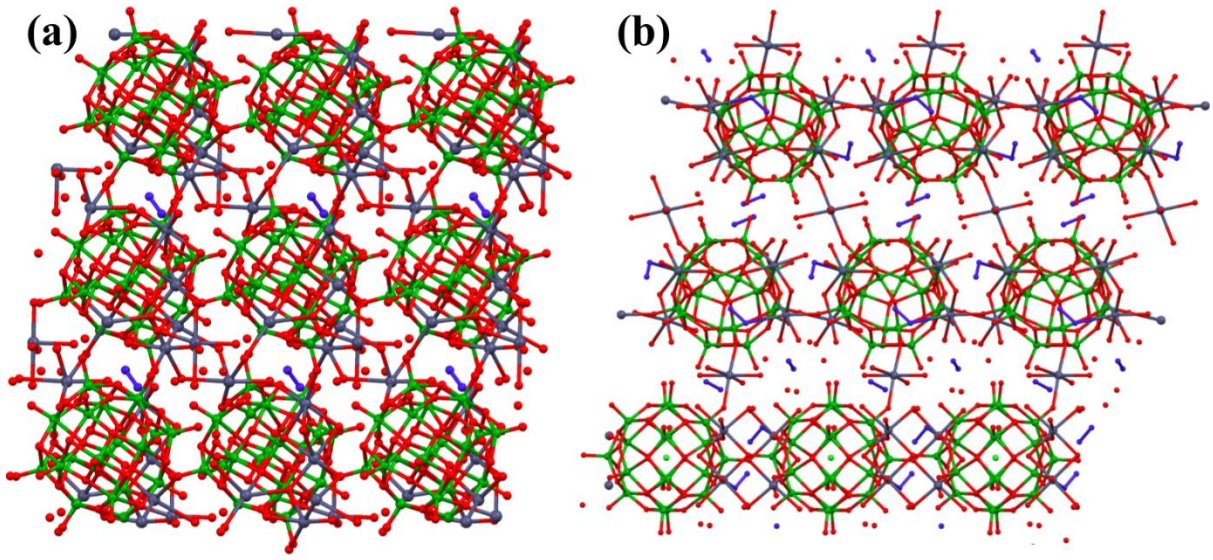

Figure 4.3. Single-crystal structures: (**a**) molecular packing, found in the crystal structure of compound **1**, viewed down to the crystallographic *b*-axis; (**b**) molecular packing, found in the crystal structure of compound **2**, viewed down to the crystallographic *b*-axis.

and bond angles of **2** listed in *Appendix 4(i)*. Bond valence sum calculations and the number of sodium cations found in the crystal structure of compound **2**, suggest the existence of eight protons (as cations) per formula unit of compound **2**. Notably, all the cage vanadium ions in both of these compounds are reduced ones (in +4 oxidation state) and both have lattice N_2H_4 molecules along with lattice water molecules. Compound **2** also shows three-dimensional supramolecular network in crystalline state, formed by the interactions of sodium ion coordinated water molecules with POV cluster anions (**Figure 4.3**(**b**)).

4.3.2.3. . FT-IR, Raman spectra

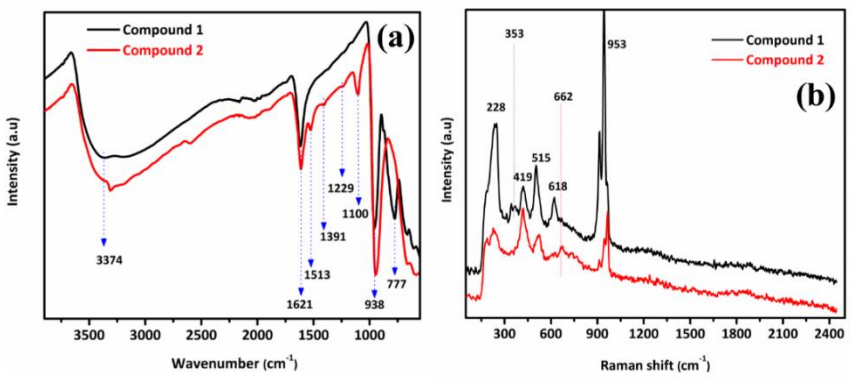

Figure 4.4. FT-IR and Raman spectra: (**a**) FT-IR spectra of compounds **1** and **2**; (**b**) Raman spectra of compounds **1** and **2**

The FTIR spectra of **1** and **2**, collected for powdered samples, display several bands in the region of 400–4000 cm^{-1} as shown in **Figure 4.4**(**a**). The V=O_t stretching bands, observed at 938, 927 cm^{-1} for compounds **1** and **2** respectively, are very close to the corresponding values reported for reduced POVs.[22] The V–O(μ_3–O and μ_4–O in **1** and μ_3–O in **2**) stretching bands are observed in the range of 450–780 cm^{-1}. Broad stretching bands, observed in the region of 3560–2850 cm^{-1} for compound **1** and compound **2** correspond to the O–H stretching of water as well as N–H stretching of lattice hydrazine molecules. In compound **2**, the corresponding band was further broadened in the range 3560–2750 cm^{-1} due to the presence of both O–H stretching bands of water as well as N–H stretchings of more lattice hydrazine molecules in the crystals of compound **2**. The Raman spectra of compounds **1** and **2** (**Figure 4.4**(**b**)) were recorded in the range of 100–2500 cm^{-1}. Both compounds **1** and **2** exhibit similar stretching bands, corresponding to V–Oμ_3 in the range of 200 to 680 cm^{-1} including a strong stretching band around 950 cm^{-1} for terminal V=O. In the Raman spectrum of compound **1**, one extra band, appeared around 350 cm^{-1}, is perhaps due to V–O$_{\mu4}$ bond of encapsulated VO_4^{3-} which is not found in the Raman spectrum of compound **2**.

4.3.2.4. Thermogravimetric analysis

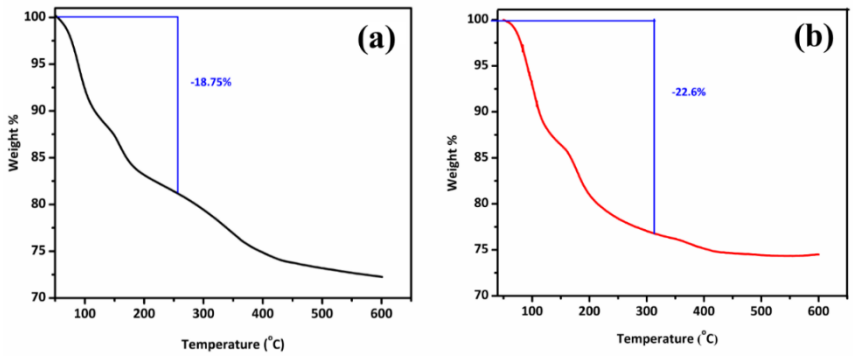

Figure 4.5. (**a** and **b**) thermogravimetric analysis of compound **1** and compound **2**.

Thermal stability of the compounds **1** and **2** were examined by TGA analysis under N_2 gas atmosphere (**Figure 4.5**). Thermogravimetric analysis inferred that compound **1** shows two stage mass loss corresponding to lattice water, hydrazine and sodium coordinated water molecules in the temperature ranges 50 to 320 °C respectively (**Figure 4.5**(**a**)). The cluster displays thermal stability until 350 °C; subsequently it gets decomposed. In case of compound **2**, there is a gradual weight loss in the temperature range 50 to 400 °C corresponding to loss of water of crystallization and hydrazine molecules as well as sodium coordinated water molecules (**Figure 4.5**(**b**)).

4.3.2.5. Bond valance sum (BVS) calculations

The reduction of vanadium centers in both compounds **1** and **2** was indicated by the longer $V{=}O_t$ bond distances measured through crystal structure and observation of stretching vibrations for $V{=}O_t$ bond at lower frequencies.[22] So, we calculated the bond valance sum (BVS) values for vanadium centers of both **1** and **2**. The BVS calculations reveal that all the 18 vanadium centers of host cage of **1** are in +4 oxidation state. The relevant BVS values are in the range 3.40–4.22 (Avg. = 3.89). The vanadium center of tetrahedral VO_4^{3-} guest was in +5 oxidation state (BVS = 4.72). Whereas in compound **2**, all the 18 vanadium centers of host cage are in +4 oxidation state and corresponding BVS values are in the range 3.87–4.28 (Avg. = 4.11). The details of BVS calculations are given in the *Appendix 4(ii)*.

4.3.2.6. X-ray photoelectron spectra (XPS)

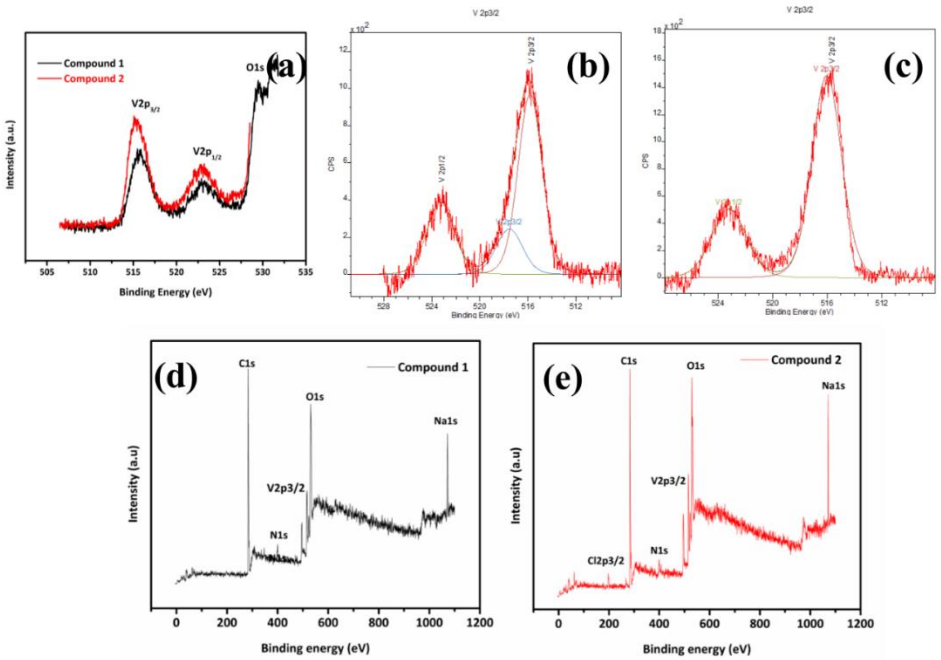

Figure 4.6. XPS spectra: (**a**) vanadium ($V2p_{3/2}$, $V2p_{1/2}$ and O1s) core scan XPS spectra of compounds **1** and **2**; (**b**) de-convoluted XPS spectrum of compound **1**; (**c**) de-convoluted XPS spectrum of compound **2**; (**d** and **e**) survey scan XPS spectrum of compounds **1** and **2**.

From the bond distances around vanadium centers, bond valance sum values calculated for vanadium centers and IR and Raman spectra, it is inferred that the vanadium centers of $\{V_{18}O_{42}\}$ cages in both **1** and **2** are in +4 oxidation state. To obtain further confirmation of oxidation states of vanadium centers, we have collected X-ray photoelectron spectra (XPS) of compounds **1** and **2** (**Figure 4.6**). The O1s response, observed at 530 eV, was taken as the reference (**Figure 4.6**(**a**)). $V^{IV}O_2$ powder is known to exhibit O1s peak at 530 eV along with $V^{IV}2p_{3/2}$ peak at 515.65 eV.[93] The same literature reported the XPS plot of $V^{V}_2O_5$ with O1s and $V^{V}2p_{3/2}$ binding energy peaks at 529.8 eV and 517 eV respectively.[93] In the present work,

Figure 4.6(**a**) displays vanadium core level XPS spectra plots of **1** and **2**. In XPS spectrum of **1**, a signal, observed at 515.7 eV with 3.0 eV FWHM (full width at half maximum), is for the cage $V^{IV}2p_{3/2}$ (**Figure 4.6**(**b**)). The corresponding cage $V^{(IV)}$ signal ($V^{IV}2p_{3/2}$) was observed at 515.6 eV with 2.8 eV FWHM in XPS plot of **2** (**Figure 4.6**(**c**)). These signals clearly indicate the +4 oxidation state of vanadium centres of the cluster cages in **1** and **2**.[93] Now, in compound **1**, even though, all cage vanadium ions are in reduced (+4) oxidation state, its encapsulated central vanadate (guest) has vanadium in +5 oxidation state, whose presence could not simply be figured out from its XPS plot (**Figure 4.6**(**a**), black curve). We thus performed de-convolution on the experimentally obtained XPS plot of compound **1** as shown in **Figure 4.6**(**b**), which shows two peaks: major (intense) peak at 515.70 eV with 2.43 eV FWHM, consistent with $V2p_{3/2}$ for reduced cage V^{4+} ions and a relatively weak intensity peak at 517.48 eV with 2.70 eV FWHM, consistent with $V2p_{3/2}$ of centrally encapsulated ortho-vanadate with V in +5 oxidation state.[93] We also performed de-convolution on the experimentally obtained XPS data of compound **2** as shown in **Figure 4.6**(**c**) and in this case (de-convoluted plot), we found that there is no resolution of the experimentally obtained plot retaining the original peak at around 516.0 eV with 2.46 eV FWHM, consistent with $V2p_{3/2}$ for reduced cage V^{4+} ions[93] of compound **2**. This peak clearly indicate the presence of +4 oxidation state of vanadium only in compound **2**. An additional XPS peak with relatively weak intensity (in both plots) is also been observed in the range of 521.50–525.62 eV with FWHM in the range of 2.71–2.84, that corresponds to $V2p_{1/2}$. The survey scan of both the compounds were shown in **Figure 4.6**(**d** and **e**).

4.3.2.7. UV-Vis absorption spectra

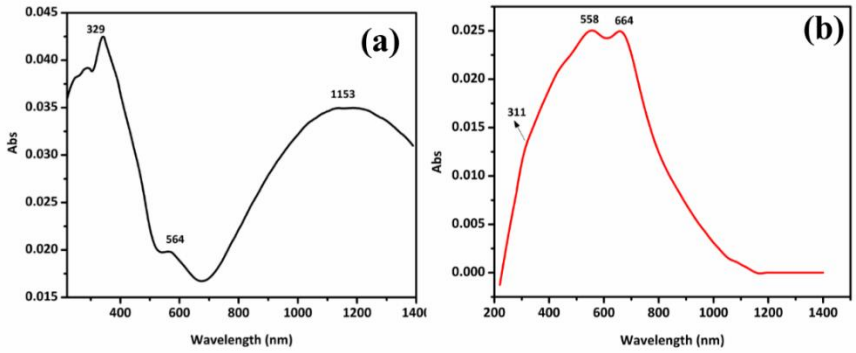

Figure 4.7. UV-visible spectra: (**a**) for compound **1** and (**b**) for compound **2**.

In addition to above mentioned XPS and BVS analyses, the solid state electronic absorption spectra of solid samples of compounds **1** and **2** were collected with background reference of $BaSO_4$ (**Figure 4.7**). The broad absorption feature present in the electronic spectrum of compound **1** in the near-IR region (with absorption maximum at 1130 nm) can tentatively be assigned to inter-valence charge transfer (IVCT) transition (cage V^{4+} to centrally encapsulated V^{5+} centre). Müller and Döring have described similar IVCT transition for the similar system,[21] as exhibited by compound **1** (**Figure 4.7**(**a**)). The small band around 574 nm may be due d-d

transitions of V^{4+} (d^1) ion. The response, appeared around 331 nm, might be due to ligand-to-metal charge transfer (LMCT) transition (O→V). In the case of compound **2** (**Figure 4.7**(**b**)), the broad absorption feature has two bands at 567 and 662 nm, that are attributed to d-d transitions of V^{4+} (d^1) ion,[94,95] and a shoulder at around 311 nm due to O→V charge transfer transition.

4.3.3. Solid state proton conductivity

4.3.3.1. Variable temperature proton conductivity

The reduction of all vanadium centres in the present system increase the overall charge (e^-/H^+) on the cluster and allows the concerned POV clusters to be protonated to a greater extent. Both compounds **1** and **2** are having eight protons per formula unit, associated with respective POV cluster anions. The proton conduction/transportation step is the key part in hydrogen fuel cells for viable energy production which requires an efficient, affordable and robust proton exchange membrane (PEM), which can be a solid electrolyte or proton exchange membrane with efficient water retention capability and should work for a prolonged period. In the present study, proton conductivity has been evaluated from alternative-current (A.C.) electrochemical impedance spectroscopy (EIS) of solid pelletized samples of compounds **1** and **2** under different particular

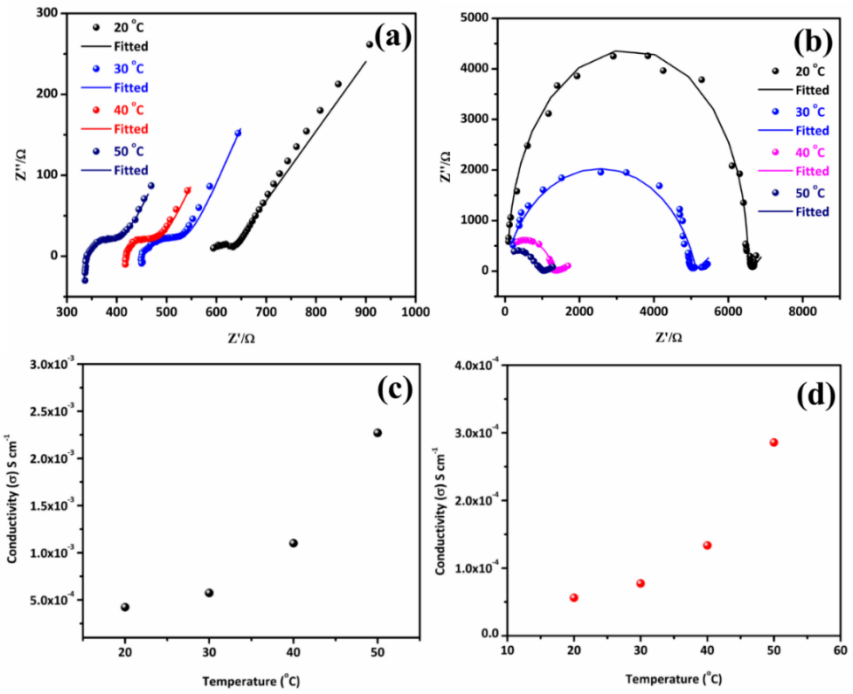

Figure 4.8. Proton conductivity: Nyquist plots of impedance spectra, collected during heating cycle (20 to 50 °C at 70% RH), (**a**) for compound **1** and (**b**) for compound **2**; (**c** and **d**) show the variation of proton conductivity with change in temperature for compounds **1** and **2** respectively. Measurements were done during heating cycle at a constant relative humidity (70% RH).

temperatures and relative humidity (RH). Before each proton conductivity measurement, fine powdered sample was sandwiched in between two carbon papers (thickness 50 µm) and pelletized under a pressure of 3 ton/cm^2 for 2 minutes. The use of conducting carbon paper was to lower the electrode-electrolyte contact resistance, which can contribute significantly to the observed impedance unless the conducting carbon paper is used. As the solid particles of powdered compounds **1** and **2** cannot form intimate microscopic contact with the metallic electrode surface, thus the use of conducting carbon paper was vital. Measurements were carried out using a home-made stainless steel two electrode set-up. The experimentally obtained proton conductivity data (Nyquist plots, **Figures 4.8**, **4.10** and **4.13**) were fitted with the most relevant equivalent circuit that can be explain the proton conducting behaviour of both the compounds i.e., compounds **1** and **2**. The $((R_1/Q_1)+(R_2/Q_2)+Q_3)$ circuit was used, where R_1, R_2, represents resistance components of the sample and Q_1, Q_2 and Q_3 are constant phase elements. In particular, the R_1 component accounts for the bulk conductivity or in other words the proton conductivity of compounds **1** and **2**. The constant phase elements account for the deviation of compounds **1** and **2** from the ideal behaviour (**Figure 4.9**). The conductance values are calculated from the equation: conductance (σ) = $L/(A\times R)$ $S\ cm^{-1}$ (where L = thickness, A = cross sectional area of the pellet and R is the experimentally observed resistance, in this case of the R_1).

Calculation of proton conductivity from impedance spectra by fitting with equivalent circuit as shown below:

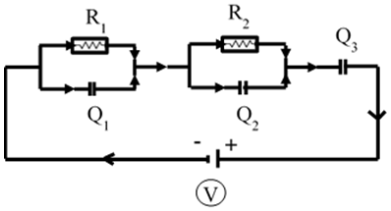

Figure 4.9. Equivalent circuit was used to fit the proton conductivity data of both the compounds.

Table 4.2. Fitting parameters were used to calculate the proton conductivity of compound **1** at various temperatures and 70% relative humidity (RH).

Temp. (°C)	$R_1(\Omega)$	Conductivity (S cm^{-1})
50	82.71	3.01×10^{-3}
40	226.3	1.10×10^{-3}
30	433.2	5.74×10^{-4}
20	587.2	4.24×10^{-4}

Table 4.3. Fitting parameters were used to calculate the proton conductivity of compound **2** at various temperatures and 70% relative humidity (RH).

Temp. (℃)	R_1(Ω)	Conductivity (S cm^{-1})
50	1228	1.97×10^{-4}
40	1818	1.33×10^{-4}
30	3137	7.73×10^{-5}
20	4319	5.61×10^{-5}

Calculation of proton conductivity for compound 1 from R_1 value at 50 ℃ using the formula, described below:

$$R = \rho \times \frac{l}{a} \quad \ldots\ldots\ldots\ldots\ldots \text{Eqn (1)}$$

Here we know that,

R = resistance of the electrolyte (R_1)

ρ = specific resistance of the electrolyte

l = thickness of the pallet (cm)

a = cross section area of pellet (cm^2)

Therefore, $x = \frac{l}{a}$

Then the Eqn (1) can be written as,

$$\rho = \frac{R}{x} \ldots\ldots\ldots\ldots\ldots\ldots \text{Eqn (2)}$$

R_1 = 82.71 (Ω)

l = 0.286 cm

a = 1.1455 cm^2

Therefore, x = 0.249 cm^{-1} (~ 0.25)

Specific resistance of the electrolyte (ρ) = 332.16 Ω cm

We calculated specific resistance from Eqn (2),

Then we know that, the conductance is inversely proportion to the resistance.

$$\sigma = \frac{1}{\rho} \ldots\ldots\ldots\ldots\ldots\ldots \text{Eqn (3)}$$

By putting the specific resistance value in Eqn (3), we get the specific conductivity of compound **1** at 50 ℃.

Thus, the proton conductivity of compound **1**, $(\boldsymbol{\sigma})_{50\ ℃}$ = **3.01×10^{-3} S cm^{-1}**.

* *Note:* Similar data fitting and calculation procedures were used to calculate proton conductivity values for **1** and **2** at various experimental conditions.

Nyquist plot at high frequency region which often resembles a semi-circular shape represents the impedance corresponds to the electrolyte bulk resistance (**Figure 4.8**). The proton conductivities of compounds **1** and **2** are 4.24×10^{-4} S cm^{-1} and 5.61×10^{-5} S cm^{-1} at 20 °C and 70% RH (relative humidity). Notably, these conductivity values are comparatively lower to that of traditional proton conducting material Nafion 117 (5×10^{-2} S cm^{-1}) under similar conditions but compounds **1** and **2** has a much lower manufacturing cost than commercial nafion.[43,44] The present conductivity values are comparable to those of many reported POM based proton conducting materials.[66-69] These conductivity values are found to increase, when we increase the temperature by keeping relative humidity constant (70% RH). The proton conductivities are found to reach to 10 times of its initial value when the temperature is increased from 20 to 50 °C keeping the RH constant at 70% (**Figure 4.8**).

4.3.3.2. Durability test

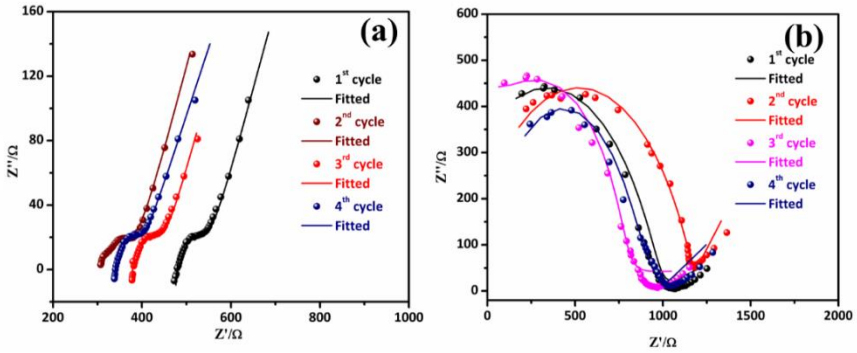

Figure 4.10. Stability test: Nyquist plots of impedance spectra recorded each cycle with a six hour time interval at 50 °C and 70% RH over a period of 24 hours, (**a**) for compounds **1** and (**b**) for compound **2**.

To check the reproducibility of the proton conductivity of compounds **1** and **2**, proton conductivity measurements were performed at each 6 hour time intervals for a total duration of 24 hours at 50 °C for both compounds (**Figure 4.10**). In this process, a total of four repetitive measurements were done and the mean value of the proton conductivity is being reported here as 3.62×10^{-3} S cm^{-1} for compound **1** and 2.16×10^{-4} S cm^{-1} for compound **2**. The standard deviation of measurement was calculated to be 8.62×10^{-4} S cm^{-1} for compound **1** and 4.62×10^{-5} S cm^{-1} for compound **2**. Thus, taking their standard deviation values, the proton conductivity values of compounds **1** and **2** at 50 °C (under 70% relative humidity) are 3.62×10^{-3} S cm^{-1} and 2.16×10^{-4} S cm^{-1} respectively.

4.3.3.3. Controlled experiments on residual electrolyte of compounds 1 and 2 after EIS measurements

Controlled experiments have shown consistent spectral futures as like synthesized compounds **1** and **2** even after long-term proton conductivity measurements (**Figures 4.11** and **4.12**).

Hence, confirms that the compounds **1** and **2** are stable and robust under operational conditions.

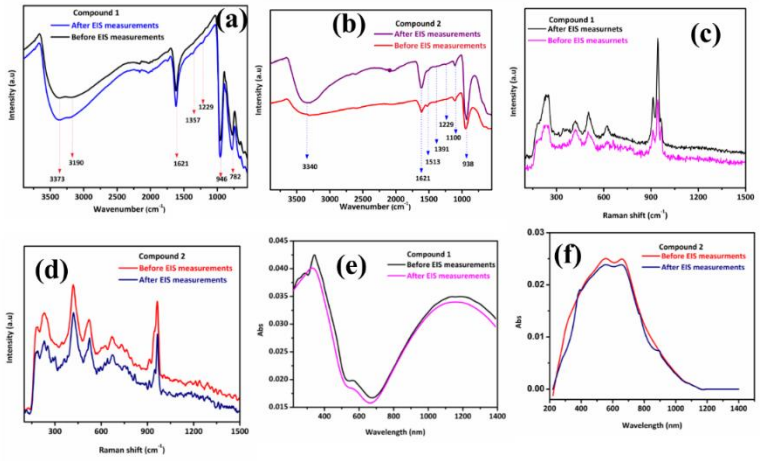

Figure 4.11. Controlled experiments: FTIR, Raman and UV-Vis spectra before and after EIS measurements of compounds **1** and **2**, (**a** and **b**) FTIR spectra of compounds **1** and **2**; (**c** and **d**) Raman spectra of compounds **1** and **2**; (**e** and **f**) UV-vis spectra of compounds **1** and **2**.

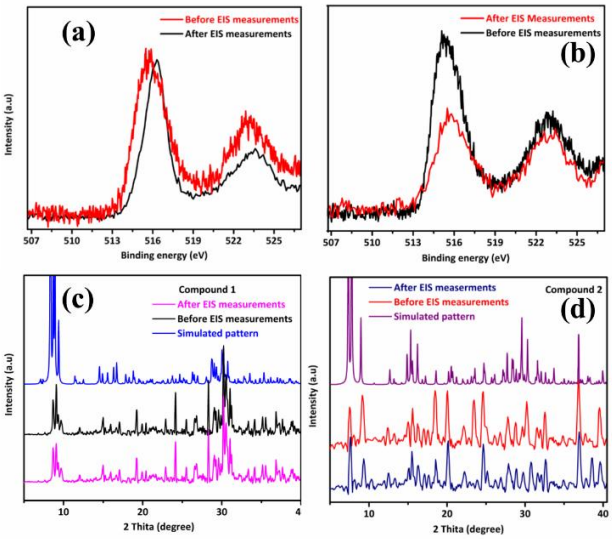

Figure 4.12. Controlled experiments: XPS spectra and PXRD profiles before and after EIS measurements of compounds **1** and **2**, (**a** and **b**) XPS spectra of compounds **1** and **2**; (**c** and **d**) PXRD of compounds **1** and **2**.

Detailed calculations of standard deviation of proton conductivity values for compounds 1 and 2:

The following equation (**1**) was used to calculate the standard deviation of compounds **1** and **2**. For this calculation, four proton conductivity measurements were recorded in 24 hours with 6 hours regular time intervals at a particular temperature and relative humidity (i.e., 50 °C and 70% RH). The obtained four proton conductivity values were used to calculate the standard deviation for compounds **1** and **2**.

$$S^2 = \frac{\sum(xi-xa)^2}{n-1} \text{ ..... equation (4)}$$

Hence here,
xi = Proton conductivity value,
xa = Mean value of total number of proton conductivity values, here is four data points,
n = Number of data points,
S = Standard deviation.

For compound 1:

Cycle number	xi	xa	$(xi - xa)$	$(xi - xa)^2$
1st	3.01×10^{-3}	3.62×10^{-3}	6.1×10^{-4}	3.72×10^{-7}
2nd	2.99×10^{-3}		6.3×10^{-4}	3.96×10^{-7}
3rd	3.68×10^{-3}		6.0×10^{-5}	3.6×10^{-9}
4th	4.83×10^{-3}		1.2×10^{-3}	1.46×10^{-6}

Note: the sign is taken as positive in the calculation of $(xi - xa)$ and$(xi - xa)$.

$$xa = \frac{sum\ \ of all\ xi\ values}{number\ of\ data\ points} \text{.....equation (5)}$$

$$xa = \frac{\{(3.01 \times 10\text{^}(-3)) + (2.99 \times 10\text{^}(-3)) + (3.68 \times 10\text{^}(-3)) + (4.83 \times 10\text{^}(-3))\}}{4}$$

$$xa = 3.627/1000$$

The total sum value of $(xi - xa)^2 = 2.231\times10^{-6}$

Equation **1** written as, $S = \sqrt{\frac{\sum(xi-xa)^2}{n-1}}$

$$S = \sqrt{\frac{\sum 2.231 \times 10\text{^}(-6)}{4-1}}$$

$$S = \sqrt{7.438 \times 10\text{^}(-7)}$$

Standard deviation(S) for compound **1** = **8.62×10^{-4} S cm^{-1}**

For compound 2:

The same calculation procedure of compound **1** followed to calculate the standard deviation of compound **2**.

Cycle number	xi	xa	$(xi - xa)$	$(xi - xa)^2$
1st	1.97×10^{-4}	2.16×10^{-4}	1.9×10^{-5}	3.61×10^{-10}
2nd	1.86×10^{-4}		3.0×10^{-5}	9.0×10^{-10}
3rd	1.96×10^{-4}		2.0×10^{-5}	4.0×10^{-10}
4th	2.85×10^{-4}		6.9×10^{-5}	4.76×10^{-9}

The total sum value of $(xi - xa)^2 = 6.421\times10^{-9}$

Standard deviation (S) for compound **2** = **4.621×10^{-5} S cm^{-1}**

4.3.3.4. Variable relative humidity proton conductivity

We also measured the proton conductivities of compounds **1** and **2** at 30 °C by varying the relative humidity in the range of 40 to 70%. The proton conductivities of compounds **1** and **2** are increased with the increase of relative humidity (**Figure 4.13**). The proton conductivity values of compounds **1** and **2** at 40% RH and 30 °C temperature are 5.57×10^{-4} S cm^{-1} and

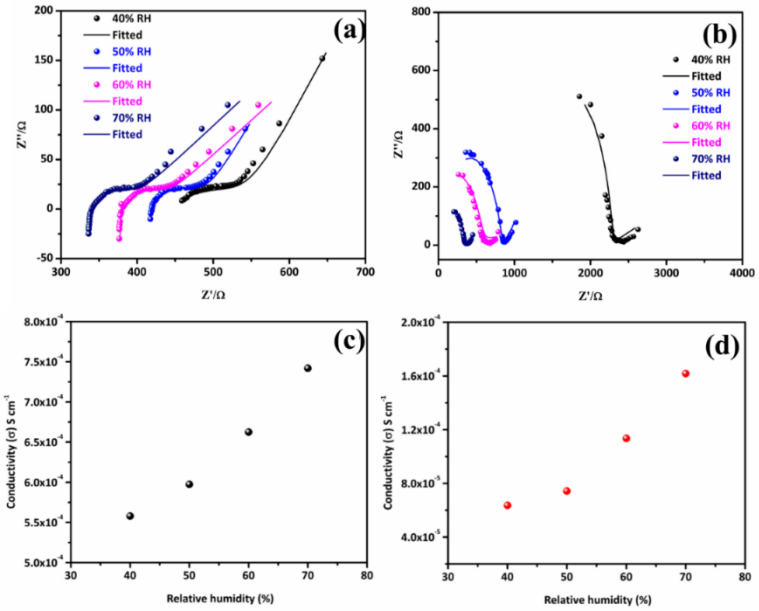

Figure 4.13. Proton conductivity: Nyquist plots of impedance spectra, collected under variable relative humidity condition (from 40 to 70% RH at 30 °C), (**a**) for compound **1** and (**b**) for compound **2**; (**c** and **d**) show the effect of variation of relative humidity on proton conductivity of compounds **1** and **2**.

6.35×10^{-5} S cm^{-1}, respectively. These values reach to 7.41×10^{-4} and 1.61×10^{-4} S cm^{-1} at 70% RH and 30 °C for **1** and **2**, respectively. This observation clearly indicates that the enhancement of proton conductivity is associated with the water as well as temperature. We believe that, high concentration of labile protons, negative charged domains on the cluster and presence of aqua-chain are the major factors to influence the proton conductivities in compounds **1** and **2**.

Calculation of activation energy (*Ea*) for compounds 1 and 2:

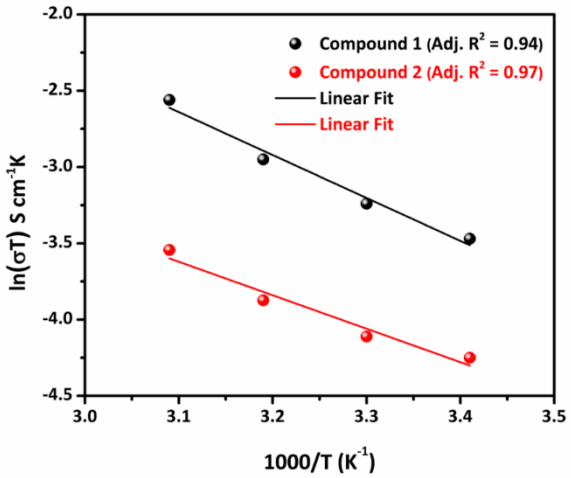

Figure 4.14. Activation energy plot: temperature dependent Arrhenius plots of proton conductivity for compounds **1** and **2**.

The Arrhenius activation energy (E_a) was calculated from Arrhenius plots (ln(σT) *vs 1000/T*) of the compounds **1** and **2** (**Figure 4.14**). Activation energies of **1** and **2** (E_a) from Arrhenius equation $\sigma = A.e^{-(Ea/RT)}$ (where, σ = conductance, E_a = activation energy, A = Arrhenius co-efficient/pre-exponential factor, R = ideal gas constant and T = temperature in K) are found to be, 23.34 kJ mol^{-1} (0.242 eV) and 18.40 kJ mol^{-1} (0.19 eV) respectively. This clearly suggests that the proton conduction in **1** and **2** follows Grotthuss mechanism.[42]

The slope value of the plot was used in Arrhenius equation to calculate the activation energies for compounds **1** and **2**.

From Arrhenius equation,

$$\boldsymbol{\sigma T = A.e^{\left(-\frac{Ea}{RT}\right)}} \quad \text{..... Eqn (6)}$$

Here, $\boldsymbol{\sigma}$ = conductivity of electrolyte, *i.e.*, proton conductivity;

$\boldsymbol{-Ea}$ = activation energy for proton conduction;

$\boldsymbol{R}$ = Ideal gas constant;

$\boldsymbol{T}$ = temperature in Kelvins (K) scale;

Eqn (6) can be written as,

$$\boldsymbol{ln(\sigma T) = lnA - \left(\frac{Ea}{RT}\right)} \quad \text{..... Eqn (7)}$$

Eqn (7) can be rewritten as,

$$\boldsymbol{ln(\sigma T) = lnA - \left(\frac{Ea}{R\times 1000}\right) \times \left(\frac{1000}{T}\right)} \quad \text{..... Eqn (8)}$$

Eqn (8) represent the straight line between **ln(σT)** and **1000/T**.

Thus, value of slope **(m)** = $\boldsymbol{-\left(\frac{Ea}{R\times 1000}\right)}$

For compound **1 s**lope (**m**) = -2.813 S cm^{-1} K^2.
And compound **2** slope (**m**) = -2.194 S cm^{-1} K^2.

Therefore,
the activation energy for compound **1**, ***Ea* = 0.24 eV (23.3 kJ mol^{-1})**,
Whereas for compound **2**, ***Ea* = 0.19 eV (18.4 kJ mol^{-1})**.

4.4. Conclusions

In conclusion, we have synthesized and structurally characterized two polyoxovanadate based host-guest compounds $[Na_7(H_2O)_{14}][H_8V^{IV}_{18}O_{42}(V^{V}O_4)]\cdot N_2H_4\cdot 7H_2O$ (**1**) and $[Na_5(H_2O)_{16}][H_8V^{IV}_{18}O_{42}(Cl)]\cdot 4N_2H_4\cdot 6H_2O$ (**2**), in which the host cages are fully reduced as far as metal centers are concerned. Both of these compounds have been characterized by routine spectral analyses including structural characterization by single crystal X-ray crystallography. Interestingly, in both compounds, the POV cluster is associated with eight protons and both structures have high amount of water molecules present in the crystal lattice. Thus we have performed solid state proton conductivity studies of the title polyoxovanadate compounds, which are very important in the context of sustainable/renewable energy, because the proton conducting membrane is one of the major component in the fuel cell. In general, protonated polyoxometalates are known to exhibit solid state proton conductivity. Among the polyoxometalates, polyoxovanadates are rarely explored as proton conducting materials. Therefore, this is one of seldom report of polyoxovanadates that show solid state proton conductivity.

4.5. References

(1). Katsoulis, D. E., A Survey of Applications of Polyoxometalates. *Chem. Rev.***1998**, *98*, 359-388.
(2). Gumerova, N. I.; Rompel, A., Synthesis, Structures and Applications of Electron-Rich Polyoxometalates. *Nat. Rev. Chem.* **2018**, *2*, 0112.
(3). Fang, W.-H.; Zhang, L.; Zhang, J., Synthetic Strategies, Diverse Structures and Tunable Properties of Polyoxo-Titanium Clusters. *Chem. Soc. Rev.* **2018**, *47*, 404-421.
(4). Izarova Natalya, V.; Pope Michael, T.; Kortz, U., Noble Metals in Polyoxometalates. *Angew. Chem. Int. Ed.* **2012**, *51*, 9492-9510.
(5). Long, D.-L.; Burkholder, E.; Cronin, L., Polyoxometalate Clusters, Nanostructures and Materials: From Self-Assembly to Designer Materials and Devices. *Chem. Soc. Rev.* **2007**, *36*, 105-121.
(6). Johnson, G. K.; Schlemper, E. O., Existence and Structure of the Molecular Ion 18-Vanadate(IV). *J. Am. Chem. Soc.* **1978**, *100*, 3645-3646.
(7). Wutkowski, A.; Niefind, F.; Näther, C.; Bensch, W., A New Mixed-Valent High Nuclearity Polyoxovanadate Cluster Based on the $\{V_{18}O_{42}\}$ Archetype. *Z. anorg. allg. Chem.* **2011**, *637*, 2198-2204.
(8). Johnson, G. K.; Murman, R. K.; Bowman, B., Isotopic Oxygen Exchange Rates Between $[V_{18}O_{42}]^{12-}$ and Water. *Trans. Met. Chem.* **1985**, *10*, 181-184.
(9). Monakhov, K. Y.; Bensch, W.; Kogerler, P., Semimetal-Functionalised Polyoxovanadates. *Chem. Soc. Rev.* **2015**, *44*, 8443-8483.

(10). Mahnke, L. K.; Kondinski, A.; Warzok, U.; Näther, C.; van Leusen, J.; Schalley, C. A.; Monakhov, K. Y.; Kögerler, P.; Bensch, W., Configurational Isomerism in Polyoxovanadates. *Angew. Chem. Int. Ed.* **2018**, *57*, 2972-2975.

(11). Wang, L.; Fan, H.; Du, C.; Xing, X.; Zhao, Y.; Chen, B.; Wang, L., Synthesis, Structure and Properties of a Co-Crystallized Complex Based on Polyoxovanadate $[V^{IV}_{12}V^{V}_{6}O_{42}]^{6-}$ and a Mononuclear Vanadium Complex $[VON(CH_2CH_2O)_3]$. *Inorg. Chem. Commun.* **2016**, *63*, 39-41.

(12). Crans, D. C.; Peters, B. J.; Wu, X.; McLauchlan, C. C., Does Anion-Cation Organization in Na^+-Containing X-Ray Crystal Structures Relate to Solution Interactions in Inhomogeneous Nanoscale Environments: Sodium-Decavanadate in Solid State Materials, Minerals, and Microemulsions. *Coord. Chem. Rev.* **2017**, *344*, 115-130.

(13). Wang, S.-S.; Yang, G.-Y., Recent Advances in Polyoxometalate-Catalyzed Reactions. *Chem. Rev.* **2015**, *115*, 4893-4962.

(14). Lv, H.; Geletii, Y. V.; Zhao, C.; Vickers, J. W.; Zhu, G.; Luo, Z.; Song, J.; Lian, T.; Musaev, D. G.; Hill, C. L., Polyoxometalate Water Oxidation Catalysts and The Production of Green Fuel. *Chem. Soc. Rev.* **2012**, *41*, 7572-7589.

(15). Fernando, A.; Weerawardene, K. L. D. M.; Karimova, N. V.; Aikens, C. M., Quantum Mechanical Studies of Large Metal, Metal Oxide, and Metal Chalcogenide Nanoparticles and Clusters. *Chem. Rev.* **2015**, *115*, 6112-6216.

(16). Miras, H. N.; Yan, J.; Long, D.-L.; Cronin, L., Engineering Polyoxometalates With Emergent Properties. *Chem. Soc. Rev.* **2012**, *41*, 7403-7430.

(17). Chen, J. J.; Symes Mark, D.; Fan, S. C.; Zheng, M. S.; Miras Haralampos, N.; Dong, Q. F.; Cronin, L., High-Performance Polyoxometalate-Based Cathode Materials for Rechargeable Lithium-Ion Batteries. *Adv. Mater.* **2015**, *27*, 4649-4654.

(18). Chen, J. J.; Ye, J. C.; Zhang, X. G.; Symes Mark, D.; Fan, S. C.; Long, D. L.; Zheng, M. S.; Wu, D. Y.; Cronin, L.; Dong, Q. F., Design and Performance of Rechargeable Sodium Ion Batteries, and Symmetrical Li-Ion Batteries with Supercapacitor-Like Power Density Based upon Polyoxovanadates. *Adv. Energy Mater.* **2017**, *8*, 1701021.

(19). Müller, A.; Peters, F.; Pope, M. T.; Gatteschi, D., Polyoxometalates: Very Large Clusters Nanoscale Magnets. *Chem. Rev.* **1998**, *98*, 239-272.

(20). Calzado, C. J.; Clemente-Juan, J. M.; Coronado, E.; Gaita-Arino, A.; Suaud, N., Role of the Electron Transfer and Magnetic Exchange Interactions in the Magnetic Properties of Mixed-Valence Polyoxovanadate Complexes. *Inorg. Chem.* **2008**, *47*, 5889-5901.

(21). Müller, A.; Döring, J., Topologisch Und Elektronisch Bemerkenswerte "Reduzierte" Cluster Des Typs $[V_{18}O_{42}(X)]^{N-}$ (X = SO_4^{2-}, VO_4^{3-}) Mit Td-Symmetrie Und Davon Abgeleitete Cluster $[V_{(18-p)}As_{2p}O_{42}(X)]^{m-}$ (X = SO_3^{2-}, SO_4^{2-}, H_2O; p = 3, 4). *Z. anorg. allg. Chem.* **1991**, *595*, 251-274.

(22). Müller, A.; Sessoli, R.; Krickemeyer, E.; Bögge, H.; Meyer, J.; Gatteschi, D.; Pardi, L.; Westphal, J.; Hovemeier, K.; Rohlfing, R.; Döring, J.; Hellweg, F.; Beugholt, C.; Schmidtmann, M., Polyoxovanadates: High-Nuclearity Spin Clusters with Interesting Host−Guest Systems and Different Electron Populations. Synthesis, Spin Organization, Magnetochemistry, and Spectroscopic Studies. *Inorg. Chem.* **1997**, *36*, 5239-5250.

(23). Rhule, J. T.; Hill, C. L.; Judd, D. A.; Schinazi, R. F., Polyoxometalates in Medicine. *Chem. Rev.* **1998**, *98*, 327-358.

(24). Yamase, T., Anti-Tumor, -Viral, and -Bacterial Activities of Polyoxometalates for Realizing an Inorganic Drug. *J. Mater. Chem.* **2005**, *15*, 4773-4782.

(25). Crans, D. C.; Woll, K. A.; Prusinskas, K.; Johnson, M. D.; Norkus, E., Metal Speciation in Health and Medicine Represented by Iron and Vanadium. *Inorg. Chem.* **2013**, *52*, 12262-12275.

(26). Zhang, L.; Zhang, H.; Zhang, W.; Gong, J.; Hu, H.; Yang, Y.; Liu, Y.; Kang, Z., Water-Capsule Strategy in Crystal Engineering for Water-Solubility Conversion from Insoluble to Soluble. *Dalton Trans.* **2012**, *41*, 13277-13279.

(27). Khan, M. I.; Putrevu, N. R.; Ayesh, S.; Yohannes, E. H.; Cage, B.; Doedens, R. J., Crystalline Framework Material Containing Arrays of Vanadium Oxide Nanoclusters: A Polyoxovanadate Framework with Room Temperature NOx Sensing Properties. *Cryst. Growth & Design* **2013**, *13*, 4667-4672.

(28). Ishaque Khan, M., Novel Extended Solids Composed of Transition Metal Oxide Clusters. *J. Solid State Chem.* **2000**, *152*, 105-112.

(29). Khan, M. I.; Yohannes, E.; Doedens, R. J., $[M_3V_{18}O_{42}(H_2O)_{12}(XO_4)]\cdot 24H_2O$ (M=Fe, Co; X=V, S): Metal Oxide Based Framework Materials Composed of Polyoxovanadate Clusters. *Angew. Chem. Int. Ed.* **1999**, *38*, 1292-1294.

(30). Khan, M. I.; Tabussum, S.; Marshall, C. L.; Neylon, M. K., Catalytic De-NO_x properties of Novel Vanadium Oxide Based Open-Framework Materials. *Catal. Lett.* **2006**, *112*, 1-12.

(31). Chen, L.; Chen, W.-L.; Wang, X.-L.; Li, Y.-G.; Su, Z.-M.; Wang, E.-B., Polyoxometalates in Dye-Sensitized Solar Cells. *Chem. Soc. Rev.* **2019**, *48*, 260-284.

(32). Ma, Y.-Y.; Wu, C.-X.; Feng, X.-J.; Tan, H.-Q.; Yan, L.-K.; Liu, Y.; Kang, Z.-H.; Wang, E.-B.; Li, Y.-G., Highly Efficient Hydrogen Evolution from Seawater by a Low-Cost and Stable Comop@C Electrocatalyst Superior to Pt/C. *Energy Environ. Sci.* **2017**, *10*, 788-798.

(33). Ma, Y.-Y.; Lang, Z.-L.; Yan, L.-K.; Wang, Y.-H.; Tan, H.-Q.; Feng, K.; Xia, Y.-J.; Zhong, J.; Liu, Y.; Kang, Z.-H.; Li, Y.-G., Highly Efficient Hydrogen Evolution Triggered by a Multi-Interfacial Ni/WC Hybrid Electrocatalyst. *Energy Environ. Sci.* **2018**, *11*, 2114-2123.

(34). Lechner, M.; Güttel, R.; Streb, C., Challenges in Polyoxometalate-Mediated Aerobic Oxidation Catalysis: Catalyst Development Meets Reactor Design. *Dalton Trans.* **2016**, *45*, 16716-16726.

(35). Ji, Y.; Huang, L.; Hu, J.; Streb, C.; Song, Y.-F., Polyoxometalate-Functionalized Nanocarbon Materials for Energy Conversion, Energy Storage and Sensor Systems. *Energy Environ. Sci.* **2015**, *8*, 776-789.

(36). Seliverstov, A.; Streb, C., Chirality Meets Visible-Light Photocatalysis in a Molecular Cerium Vanadium Oxide Cluster. *Chem. Commun.* **2014**, *50*, 1827-1829.

(37). Nakamura, O.; Kodama, T.; Ogino, I.; Miyake, Y., High-Conductivity Solid Proton Conductors: Dodecamolybdophosphoric Acid Anddodecatungst Ophosphoric Acid Crystals. *Chem. Lett.* **1979**, *8*, 17-18.

(38). West, A. R.; *Basic Solid State Chemistry*, Wiley, **1999**.

(39). Kreuer, K.-D.; Proton Conductivity: Materials and Applications. *Chem. Mater.*, **1996**, *8*, 610–641.

(40). Barboiu, M. and Gilles, A.; From Natural to Bioassisted and Biomimetic Artificial Water Channel Systems. *Acc. Chem. Res.*, **2013**, *46*, 2814–2823.

(41). Ramaswamy, P.; Wong, N. E.; Shimizu, G. K. H., MOFs as Proton Conductors - Challenges and Opportunities. *Chem. Soc. Rev.* **2014**, *43*, 5913-5932.

(42). Mukhopadhyay, S.; Debgupta, J.; Singh, C.; Sarkar, R.; Basu, O.; Das, S. K., Designing UiO-66-Based Superprotonic Conductor with the Highest Metal–Organic Framework Based Proton Conductivity. *ACS Applied Mater. Interfaces* **2019**, *11*, 13423-13432.

(43). Ochi, S.; Kamishima, O.; Mizusaki, J.; Kawamura, J., Investigation of Proton Diffusion in Nafion®117 Membrane by Electrical Conductivity And NMR. *Solid State Ionics* **2009**, *180*, 580-584.

(44). Schmidt-Rohr, K.; and Chen, Q.; Parallel Cylindrical Water Nanochannels in Nafion Fuel-Cell Membranes. *Nat. Mater.*, **2008**, *7*, 75–83.

(45). Kim, Y.; Ketpang, K.; Jaritphun, S.; Park, J. S.; Shanmugam, S., A Polyoxometalate Coupled Graphene Oxide–Nafion Composite Membrane for Fuel Cells Operating at Low Relative Humidity. *J. Mater. Chem. A* **2015**, *3*, 8148-8155.

(46). Lu, S.; Wang, D.; Jiang, S. P.; Xiang, Y.; Lu J.; and Zeng, J.; HPW/MCM-41 Phosphotungstic Acid/Mesoporous Silica Composites as Novel Proton-Exchange Membranes for Elevated-Temperature Fuel Cells. *Adv. Mater*., **2010**, *22*, 971–976.

(47). Kreuer, K.-D.; Paddison, S. J.; Spohr, E.; Schuster, M., Transport in Proton Conductors for Fuel-Cell Applications: Simulations, Elementary Reactions, and Phenomenology. *Chem. Rev.*, **2004**, *104*, 4637-4678.

(48). Chandra, S.; Kundu, T.; Kandambeth, S.; BabaRao, R.; Marathe, Y.; Kunjir, S. M.; Banerjee, R., Phosphoric Acid Loaded Azo (−N═N−) Based Covalent Organic Framework for Proton Conduction. *J. Am. Chem. Soc.* **2014**, *136*, 6570-6573.

(49). Han, W.; Kwan S.; and Yeung, K.; Zeolite Applications in Fuel Cells: Water Management and Proton Conductivity. *Chem. Eng. J.*, **2012**, *187*, 367-371.

(50). Han, W.; Kwan, S.; and Yeung, K.; Zeolite Proton Conducting Membrane for Micro Fuel Cell Applications. *Top. Catal.*, **2010**, *53*, 1394-1400.

(51). McKeen, J. C.; Yan, Y. S.; Davis, M. E., Proton Conductivity in Sulfonic Acid-Functionalized Zeolite Beta: Effect of Hydroxyl Group. *Chem. Mater.* **2008**, *20*, 3791-3793.

(52). Zhou, Y.; Yang, J.; Su, H.; Zeng, J.; Jiang, S. P.; Goddard, W. A., Insight into Proton Transfer in Phosphotungstic Acid Functionalized Mesoporous Silica-Based Proton Exchange Membrane Fuel Cells. *J. Am. Chem. Soc.* **2014**, *136*, 4954-4964.

(53). Wu, G.; Zhang, H.; Zhou, J.; Huang, A.; Wan, Q., Proton Conducting Zeolite Films for Low-Voltage Oxide-Based Electric-Double-Layer Thin-Film Transistors and Logic Gates. *J. Mater. Chem. C* **2013**, *1*, 5669-5674.

(54). Meng, X.; Wang, H.-N.; Song, S.-Y.; Zhang, H.-J., Proton-Conducting Crystalline Porous Materials. *Chem. Soc. Rev.* **2017**, *46*, 464-480.

(55). Yang, P.; Alsufyani, M.; Emwas, A.-H.; Chen, C.; Khashab, N. M., Lewis Acid Guests in a $\{P_8W_{48}\}$ Archetypal Polyoxotungstate Host: Enhanced Proton Conductivity via Metal-Oxo Cluster within Cluster Assemblies. *Angew. Chem. Inter. Ed.* **2018**, *57*, 13046-13051.

(56). Zhou, Y.; Yang, J.; Su, H.; Zeng, J.; Jiang S. P.; and Goddard, W. A.; Insight into Proton Transfer in Phosphotungstic Acid Functionalized Mesoporous Silica-Based Proton Exchange Membrane Fuel Cells. *J. Am. Chem. Soc.*, **2014**, *136*, 4954-4964.

(57). Yang, L.; Ma, P.; Zhou, Z.; Wang, J.; Niu, J., A Crown-Shaped 24-Molybdate Cluster Constructed by Organotriphosphonate Ligand. *Inorg. Chem.* **2013**, *52*, 8285-8287.

(58). Zang, H.-Y.; Chen, J.-J.; Long, D.-L.; Cronin, L.; Miras, H. N., Assembly of Thiometalate-Based $\{Mo_{16}\}$ and $\{Mo_{36}\}$ Composite Clusters Combining $[Mo_2O_2S_2]^{2+}$ Cations and Selenite Anions. *Adv. Mater.* **2013**, *25*, 6245-6249.

(59). Gao, Q.; Wang, X.-L.; Xu, J.; Bu, X.-H., The First Demonstration of the Gyroid in a Polyoxometalate-Based Open Framework with High Proton Conductivity. *Chem. Eur. J.* **2016**, *22*, 9082-9086.

(60). Wu, X.; Cai, H.; Wu, Q.; Yan, W., Synthesis and High Proton Conductive Performance of Vanadium-Substituted Dawson Structure Heteropoly Acid $H_8P_2W_{16}V_2O_{62}\cdot 20H_2O$. *Mater. Lett.* **2016**, *181*, 1-3.

(61). Tian, N.; Zhu, M.; Wu, Q.; Yan, W.; Yaroslavtsev, A. B., Preparation and Conductivity of The Keggin-Type Trivanadium-Substituted Tungstosilicic Acid $H_7SiW_9V_3O_{40}\cdot 9H_2O$. *Mater. Lett.* **2014**, *115*, 165-167.

(62). Dong, B.-X.; Wu, Y.-C.; Tian, H.; Liu, C.-B.; Liu, W.-L.; Teng, Y.-L., Synthesis, Crystal Structure and Electrochemical Properties of a New 2D Network Containing Linear $\{\varepsilon\text{-}H_2PMo_8{}^{V}Mo_4{}^{VI}O_{40}Zn_4\}\infty$ Inorganic Chain. *J. Clust. Sci.* **2016**, *27*, 361-371.

(63). Liu, J.-C.; Han, Q.; Chen, L.-J.; Zhao, J.-W.; Streb, C.; Song, Y.-F., Aggregation of Giant Cerium–Bismuth Tungstate Clusters into a 3D Porous Framework with High Proton Conductivity. *Angew. Chem. Int. Ed.* **2018**, *57*, 8416-8420.

(64). Wang, Y.-D.; Wang, J.-X.; Wei, M.-J.; Liu, B.-L.; Zang, H.-Y.; Tan, H.-Q.; Wang, Y.-H.; Li, Y.-G., Niobium Oxyhydroxide-Polyoxometalate Composite as an Efficient Proton-Conducting Solid Electrolyte. *ChemElectroChem* **2018**, *5*, 1125-1129.

(65). Wang, J.-X.; Wang, Y.-D.; Wei, M.-J.; Tan, H.-Q.; Wang, Y.-H.; Zang, H.-Y.; Li, Y.-G., Inorganic Open Framework Based on Lanthanide Ions and Polyoxometalates With High Proton Conductivity. *Inorg. Chem. Front.* **2018**, *5*, 1213-1217.

(66). Tong, X.; Tian, N.; Wu, W.; Zhu, W.; Wu, Q.; Cao, F.; Yan, W.; Yaroslavtsev, A. B., Preparation and Electrochemical Performance of Tungstovanadophosphoric Heteropoly Acid and Its Hybrid Materials. *J. Phys. Chem. C* **2013**, *117*, 3258-3263.

(67). Cai, H.; Wu, X.; Wu, Q.; Yan, W., Synthesis and High Proton Conductive Performance of a Quaternary Vanadomolybdotungstosilicic Heteropoly Acid. *Dalton Trans.* **2016**, *45*, 14238-14242.

(68). Liu, W.-J.; Dong, L.-Z.; Li, R.-H.; Chen, Y.-J.; Sun, S.-N.; Li, S.-L.; Lan, Y.-Q., Different Protonic Species Affecting Proton Conductivity in Hollow Spherelike Polyoxometalates. *ACS Applied Mater. Interfaces* **2019**, *11*, 7030-7036.

(69). Li, J.; Cao, X.-L.; Wang, Y.-Y.; Zhang, S.-R.; Du, D.-Y.; Qin, J.-S.; Li, S.-L.; Su, Z.-M.; Lan, Y.-Q., The Enhancement on Proton Conductivity of Stable Polyoxometalate-Based Coordination Polymers by the Synergistic Effect of MultiProton Units. *Chem. Eur. J.* **2016**, *22*, 9299-9304.

(70). Müller, A.; Krickemeyer, E.; Penk, M.; Rohlfing, R.; Armatage, A.; Bögge, H., Template-Controlled Formation of Cluster Shells or a Type of Molecular Recognition: Synthesis of $[HV_{22}O_{54}(ClO_4)]^{6-}$ and $[H_2V_{18}O_{44}(N_3)]^{5-}$. *Angew. Chem. Int. Ed. Eng.* **1991**, *30*, 1674-1677 and references therein.

(71). Müller, A.; Sessoli, R.; Krickemeyer, E.; Bögge, H.; Meyer, J.; Gatteschi, D.; Pardi, L.; Westphal, J.; Hovemeier, K.; Rohlfing, R.; Döring, J.; Hellweg, F.; Beugholt, C.; Schmidtmann, M., Polyoxovanadates: High-Nuclearity Spin Clusters with Interesting Host−Guest Systems and Different Electron Populations. Synthesis, Spin Organization, Magnetochemistry, and Spectroscopic Studies. *Inorg. Chem.* **1997**, *36*, 5239-5250.

(72). Khan, M. I.; Yohannes, E.; Doedens, R. J., $[M_3V_{18}O_{42}(H_2O)_{12}(XO_4)]\cdot 24H_2O$ (M=Fe, Co; X=V, S): Metal Oxide Based Framework Materials Composed of Polyoxovanadate Clusters. *Angew. Chem. Int. Ed.* **1999**, *38*, 1292-1294.

(73). Yamase, T.; Suzuki, M.; Ohtaka, K., Structures of photochemically prepared mixed-valence polyoxovanadate clusters: oblong $[V_{18}O_{44}(N_3)]^{14-}$, superkeggin $[V_{18}O_{42}(PO_4)]^{11-}$ and doughnut-shaped $[V_{12}B_{32}O_{84}Na_4]^{15-}$ anions. *J. Chem. Soc., Dalton Trans.* **1997**, 2463-2472.

(74). Kawanami, N.; Ozeki, T.; Yagasaki, A., NO- Anion Trapped in a Molecular Oxide Bowl. *J. Am. Chem. Soc.* **2000**, *122*, 1239-1240.

(75). Kuwajima, S.; Kikukawa, Y.; Hayashi, Y., Small-Molecule Anion Recognition by a Shape-Responsive Bowl-Type Dodecavanadate. *Chem. Asian J.* **2017**, *12*, 1909-1914.

(76). Inoue, Y.; Kikukawa, Y.; Kuwajima, S.; Hayashi, Y., A Chloride Capturing System via Proton-Induced Structure Transformation Between Opened- and Closed-Forms of Dodecavanadates. *Dalton Trans.* **2016**, *45*, 7563-7569.

(77). Kuwajima, S.; Ikinobu, Y.; Watanabe, D.; Kikukawa, Y.; Hayashi, Y.; Yagasaki, A., A Bowl-Type Dodecavanadate as a Halide Receptor. *ACS Omega* **2017**, *2*, 268-275.

(78). Müller, A.; Krickemeyer, E.; Penk, M.; Walberg, H.-J.; Bögge, H., Spherical Mixed-Valence $[V_{15}O_{36}]^{5-}$, an Example from an Unusual Cluster Family. *Angew. Chem. Int. Ed. Eng.* **1987**, *26*, 1045-1046.

(79). Dong, B.; Peng, J.; Chen, Y.; Kong, Y.; Tian, A.; Liu, H.; Sha, J., pH-Controlled Assembly of two Polyoxovanadates Based on $[V_{16}O_{38}(Cl)]^{8-}$ and $[V_{15}O_{36}(Cl)]^{6-}$ Building Blocks. *J. Mol. Struct.* **2006**, *788*, 200-205.

(80). Zhang, C.-D.; Liu, S.-X.; Gao, B.; Sun, C.-Y.; Xie, L.-H.; Yu, M.; Peng, J., Hybrid Materials Based on Metal–Organic Coordination Complexes and Cage-Like Polyoxovanadate Clusters: Synthesis, Characterization and Magnetic Properties. *Polyhedron* **2007**, *26*, 1514-1522.

(81). Chen, Y.; Peng, J.; Yu, H.; Han, Z.; Gu, X.; Shi, Z.; Wang, E.; Hu, N., A Supramolecular Assembly Of Chiral L/D-$[Cd(Cl)(H_2O)(Phen)_2]^+$ and L,L/D,D-Dinuclear Cd Complex Coordinated by Phen and $\{V_{16}O_{38}(Cl)\}$ Cluster. *Inorg. Chim. Acta* **2005**, *358*, 403-408.

(82). Dong, B.-x.; Peng, J.; Gómez-García, C. J.; Benmansour, S.; Jia, H.-q.; Hu, N.-h., High-Dimensional Assembly Depending on Polyoxoanion Templates, Metal Ion Coordination Geometries, and a Flexible Bis(imidazole) Ligand. *Inorg. Chem.* **2007**, *46*, 5933-5941.

(83). Teng, Y.-l.; Dong, B.-x.; Peng, J.; Zhang, S.-y.; Chen, L.; Song, L.; Ge, J., Spontaneous Resolution of 3D Chiral Hexadecavanadate-Based Frameworks Incorporating Achiral Flexible and Rigid Ligands. *CrystEngComm* **2013**, *15*, 2783-2785.

(84). Y. Chen, X. Gu, J. Peng, Z. Shi, H. Yu, E. Wang and N. Hu, The First Discrete Mixed-Valence Hexadecavanadate Host Shell Cluster Anions: Hydrothermal Synthesis, Structure and Characterization of $[V_{16}O_{38}(Cl)]^{8-}$. *Inorg. Chem. Commun.*, **2004**, *7*, 705-707.

(85). Ishaque Khan, M.; Ayesh, S.; Doedens, R. J.; Yu, M.; O'Connor, C. J., Synthesis and Characterization of a Polyoxovanadate Cluster Representing a New Topology. *Chem. Commun.* **2005**, 4658-4660.

(86). Kato, N.; Hayashi, Y., Discrete Spherical Hexadecavanadates Incorporating a Bromide with Oxidative Bromination Activity. *Dalton Trans.* **2013**, *42*, 11804-11811.

(87). Keene, T. D.; D'Alessandro, D. M.; Krämer, K. W.; Price, J. R.; Price, D. J.; Decurtins, S.; Kepert, C. J., $[V_{16}O_{38}(CN)]^{9-}$: A Soluble Mixed-Valence Redox-Active Building Block with Strong Antiferromagnetic Coupling. *Inorg. Chem.* **2012**, *51*, 9192-9199.

(88). Xiao, L.-N.; Xu, J.-N.; Hu, Y.-Y.; Wang, L.-M.; Wang, Y.; Ding, H.; Cui, X.-B.; Xu, J.-Q., Synthesis and characterizations of the first $[V_{16}O_{39}Cl]^{6-}$ (V16O39) polyanion. *Dalton Trans.* **2013**, *42*, 5247-5251.

(89). SAINT: Software for the CCD Detector System; Bruker Analytical X-ray Systems, Inc.: Madison, WI, **1998**.

(90). Sheldrick, G. M.; SADABS, Program for Absorption Correction; University of Gottingen: Gottingen, Germany, **1997**.

(91). Sheldrick, G. M.; *SHELXT* – Integrated Space-Group and Crystal-Structure Determination. *Acta Cryst.* **2015**, *A71*, 3–8.

(92). Sheldrick, G. M.; Crystal Structure Refinement with *SHELXL*. *Acta Cryst.* **2015**, *C71*, 3–8 (SHELXL-2018/1 (Sheldrick, 2018)).

(93). Silversmit, G.; Depla, D.; Poelman, H.; Marin, G. B.; De Gryse, R., Determination of the V2p XPS Binding Energies for Different Vanadium Oxidation States (V^{5+} to V^{0+}). *J. Electron. Spectrosc. Relat. Phenom.* **2004**, *135*, 167-175.

(94). Yuan, M.; Li, Y.; Wang, E.; Tian, C.; Wang, L.; Hu, C.; Hu, N.; Jia, H., Modified Polyoxometalates: Hydrothermal Syntheses and Crystal Structures of Three Novel Reduced and Capped Keggin Derivatives Decorated by Transition Metal Complexes. *Inorg. Chem.* **2003**, *42*, 3670-3676.

(95). Arumuganathan, T.; Das, S. K., Discrete Polyoxovanadate Cluster into an Organic Free Metal-Oxide-Based Material: Syntheses, Crystal Structures, and Magnetic Properties of a New Series of Lanthanide Linked-POV Compounds $[\{Ln(H_2O)_6\}_2As_8V_{14}O_{42}(SO_3)]\cdot 8H_2O$ (Ln = La^{3+}, Sm^{3+}, and Ce^{3+}). *Inorg. Chem.* **2009**, *48*, 496-507.

CHAPTER 5

Carbonate Encapsulation from Dissolved Atmospheric CO_2 into a Polyoxovanadate Capsule

Overview:

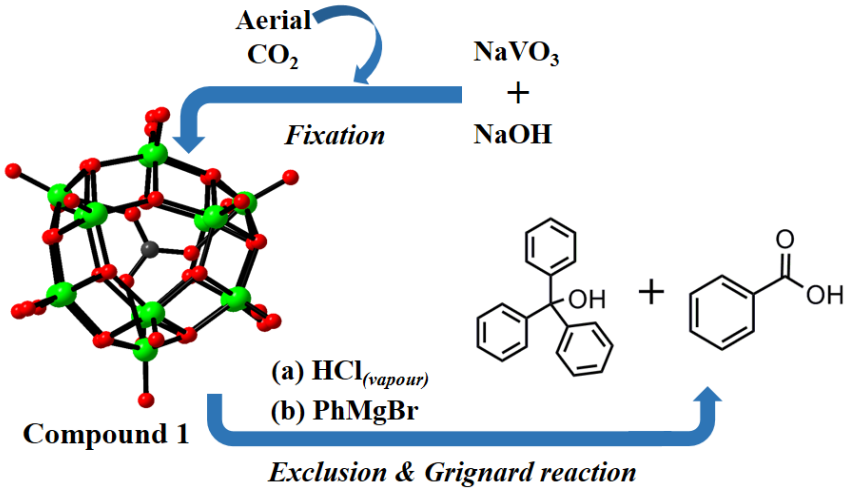

An aqueous synthesis, involving the reduction of VO_3^- anion in a mild alkaline pH in the presence of α-Bi_2O_3, leads to the formation of a fully reduced polyoxovanadate (POV) capsule, with CO_3^{2-} anion encapsulation in its internal cavity, in compound $[Na_6(H_2O)_{24}][H_8V^{IV}_{15}O_{36}(CO_3)]\cdot 3N_2H_4\cdot 10H_2O$ (**1**). This CO_3^{2-} anion encapsulation, the source of which is absorbed aerial CO_2 in the pertinent aqueous alkaline reaction mixture, occurs only in the presence of α-Bi_2O_3. Compound **1** crystals, upon exposure to HCl acid vapor, exclude CO_2 gas that can be reacted to Grignard reagent, PhMgBr to form triphenyl carbinol and benzoic acid; during this solid-vapor interface reaction, compound **1** itself is transformed into an amorphous material that includes Cl^- anion, but could not be characterized unambiguously. Thus, we have synthesized a chloride ion (Cl^-) encapsulated compound $[Na_{10}(H_2O)_{24}][H_3V^{IV}_{15}O_{36}(Cl)]\cdot 6H_2O$ (**2**) in a direct synthesis protocol, which has been characterized by crystallography as well as by other spectroscopic methods. Compounds **1** and **2**, each having fifteen vanadium(IV) centers, exhibit interesting magnetism in their solid state. The temperature dependence magnetic susceptibilities for compounds **1** and **2** have been recorded at 0.1 T in the temperature range of 3–300 K. The temperature dependence magnetic susceptibilities of compounds **1** and **2** are shown in the form of χ_M *vs* T and their product $\chi_M T$ *vs* T plots.

5.1. Introduction

Polyoxometalates (POMs), that are all-inorganic metal–oxygen cluster species having wide structural diversity[1-14] (in size as well as in shape) and diverse applications (in catalysis,[4-5] photochemistry,[5] electrochemistry,[4-11] medicine,[12] magnetism,[13-20] proton conduction[21] *etc.*), exhibit interesting host-guest chemistry.[21-29] Complete encapsulation of a guest molecule / ion in the internal cavity of host POM cluster is of considerable interest because it represents a unique supra-molecular core-shell entity, in which the guest species influence the electronic properties of the resulting host-guest system.[21-49] In this regard, among POMs, polyoxovanadates (POVs) draw special attention, because, a number of POVs are known to have well-defined internal cavities for encapsulation.[22-25] All these shell containing POV clusters, capable of encapsulating a guest species, have a common feature of the presence of square-pyramidal {O_4V=O} polyhedron, which is believed to have a tendency to form the cage or shell.[23-27, 30-49] The presence of the guest spices, such as, halide, pseudohalide, inorganic, or organic anions in the concerned synthesis reaction mixture, plays a key role in the isolation of resulting host-guest compounds. The guest-anionic-species like Cl^-, Br^-, I^-, CN^-, CO_3^{2-}, NO^-, NO_2^-, N_3^-, PO_4^{3-}, $HCOO^-$, CH_3COO^-, SH^-, SCN^-, SO_3^{2-}, SO_4^{2-}, ClO_4^- are known to get encapsulated by the following shell-containing POV hosts: $[V_{12}O_{32}(X)]^{5-}$ (X = NO^-, CN^-, OCN^-, NO_2^-, NO_3^-, HCO_2^-, CH_3COO^-, Cl^-, Br^-, I^-);[31-34] $[V_{12}O_{32}(X)]^{4-}$ (X = CO_2, CH_3CN, DCM, CH_3NO_2, CH_3Br);[26,30] $[V_{15}O_{36}(CO_3)]^{7-}$;[24,25] $[V_{15}O_{36}(X)]^{6-}$ (X = Cl^-, Br^-, I^-);[35,36] $[V_{16}O_{38}(X)]^{n-}$ (X = F^-, Cl^- , Br^-, CN^-, H_2O; n = 3, 4);[37-45] $[V_{16}O_{39}(Cl)]^{6-}$;[45] $[V_{16}O_{42}(Cl)]^{8-}$;[42] $[V_{18}O_{42}(X)]^{n-}$ and $[V_{18}O_{44}(X)]^{n-}$ (X = H_2O, Cl^-, Br^-, I^-, SO_4^{2-}, SO_3^{2-}, VO_4^{3-}, PO_4^{3-}, N_3^-, NO_2^-, NO_3^-, SH^-, $HCOO^-$; n = 5-15);[46-49] $[V_{22}O_{54}(X)]^{7-}$ (X = ClO_4^-, N_3^-); $[V_{30}O_{74}\{(V_4O_4)O_4\}]^{10-}$.[46] Thus, the chloride anion (Cl^-) encapsulation is found in diverse cage containing POV systems, reported by Müller,[35] Peng,[37] Khan,[42] Hayashi[43] and their Co-workers. Among these host-guest systems, carbonate anion (CO_3^{2-}) encapsulation by the mixed-valence POV cluster anion $[V^V_7V^{IV}_8O_{36}(CO_3)]^{7-}$ has drawn our special attention, because CO_3^{2-} anion can be derived from CO_2 gas ($CO_2 + OH^- \rightarrow CO_3^{2-} + H^+$), which is an important component on our earth-surface atmosphere in the context of global warming.[50,51] Müller and coworkers reported the first mixed-valent POV encapsulated carbonate compound $Li_7[V^V_7V^{IV}_8O_{36}(CO_3)]$~ca·$39H_2O$ in 1990, which was synthesized in the presence of Li_2CO_3.[24] Four years later, Yamase and Ohtaka prepared the same mixed-valent host-guest compound $K_5H_2[V^V_7V^{IV}_8O_{36}(CO_3)]\cdot 14.5H_2O$ (but with different cations), which was synthesized by photolyzing an aqueous CH_3OH solution mixture of $[V_4O_{12}]^{4-}$ in the presence of K_2CO_3.[25] There are reports on interactions between CO_2 and POMs.[52-57]

Here we report an unique aqueous synthesis of a POM-based host-guest system $[Na_6(H_2O)_{24}][H_8V^{IV}_{15}O_{36}(CO_3)]\cdot 3N_2H_4\cdot 10H_2O$ (**1**), in which the fully reduced POV capsule captures dissolved aerial CO_2 from an alkaline aqueous synthesis mixture in the form of carbonate anion. The absorption of aerial CO_2 by an aqueous alkaline solution is not surprising.

But, the fact, that the encapsulation of this dissolved aeiral CO_2 into the internal cavity of the POV capsule does not happen 'just like that' without the presence of some amount of α-Bi_2O_3 in the concerned reaction mixture, is surprising. We could isolated compound **1** from an aqueous alkaline solution of sodium vanadate under reducing condition, only in the presence of α-Bi_2O_3. Compound $[Na_6(H_2O)_{24}][H_8V^{IV}_{15}O_{36}(CO_3)]\cdot 3N_2H_4\cdot 10H_2O$ (**1**), on exposure to HCl vapor, excludes carbonate in the form of CO_2, whereby compound **1** gets transformed to an amporphous substance, which could not be characterized unambigiously, but it is found to contain chlorine element (from elemental analysis). We therefore synthesized a chloride included compound $[Na_{10}(H_2O)_{24}][H_3V^{IV}_{15}O_{36}(Cl)]\cdot 6H_2O$ (**2**), in which the same POV cluster capsule, as found in compound **1**, encapsulates chloride anion in its cavity as observed from its crystal structure determination.

5.2. Experimental section

5.2.1. Materials and methods

All the chemicals were of analytical grade and used as received. Deionised water was used for all the experiments. Compounds **1** and **2** have been synthesized by conventional wet synthesis methods under ambient atmosphere.

5.2.1.1. Synthesis of $[Na_6(H_2O)_{24}][H_8V^{IV}_{15}O_{36}(CO_3)]\cdot 3N_2H_4\cdot 10H_2O$ (1)

3.66 g of $NaVO_3$ was added to 100 mL of hot water (temp. 85–90 °C) in a 250 mL conical flask to give a clear colourless solution. 0.31 g of solid α-Bi_2O_3 and 0.72 g of solid NaOH were added subsequently to the above solution and immediately covered with a watch glass and stirred for 30 mins on a hot plate (temp. 85–90 °C). Afterwards, 2.5 g of $N_2H_5\cdot HSO_4$ was added in small portions (to avoid aggressive effervescence), to the above reaction mixture. After addition of $N_2H_5\cdot HSO_4$, the colour of the solution was changed from yellow to dark green and this was stirred for another 15 mins and cooled to room temperature. The solution was filtered and the filtrate was left undisturbed for 24 hours in an open atmosphere. The dark brown coloured precipitate, formed, was filtered off and dark green coloured filtrate was kept undisturbed for crystallization. After 10 days, the dark green crystals along with a minute amount of unidentified precipitate settled were filtered, washed three times with a little amount of ice cold water (~20 mL), twice with 20 mL of ethanol-ice cold water mixture (1:1 ratio) and dried in air at room temperature. Yield: 2.21 g (50% based on Vanadium). Anal. calc. for $V_{15}Na_6O_{79}C_1H_{88}N_6$: V, 33.81%; Na, 6.09%; C, 0.55%; H, 3.61%, N, 3.76%. Found: V, 34.96%; Na, 6.58%; C, 0.61%; H, 3.98%; N, 3.72%.

5.2.1.2. Synthesis of $[Na_{10}(H_2O)_{24}][H_3V_{15}O_{36}(Cl)]\cdot 6H_2O$ (2)

3.66 g of $NaVO_3$ was added to 100 mL of hot water (temp. 85–90 °C) in a 250 mL conical flask to give a colourless solution. 0.31 g of solid α-Bi_2O_3 and 0.72 g of solid NaOH were added

subsequently to the above solution and immediately covered with a watch glass and stirred for 30 mins on a hot plate (temp. 85–90 °C). 2.5 g of $N_2H_4{\cdot}H_2SO_4$ was added in small portions (to avoid effervescence) to the resulting reaction mixture. After addition of $N_2H_5{\cdot}HSO_4$, the colour of the solution was changed from yellow to dark green and this was stirred for another 15 mins. 4.5 g of solid NaCl was added to the reaction mixture and stirring was continued for 10 more minutes. The reaction contents were cooled to room temperature and the solution was filtered. The filtrate was kept undisturbed in an open atmosphere; after 4 days, black colored crystals along with a minute amount of unidentified precipitate, obtained, were filtered, washed three times with minimum amount of ice cold water (~20 mL), twice with 20 mL of ethanol-ice cold water mixture (1:1 ratio) and dried in air at room temperature. Yield: 2.35 g (55.5 % based on vanadium from product). Anal. calcd. for $V_{15}Na_{10}O_{66}Cl_1H_{63}$: V, 35.56%; Na, 10.70%; Cl, 1.65%. Found: V, 35.53%; Na, 10.58%; Cl, 1.68%.

5.2.2. Physical measurements

Elemental analyses were performed using FLASH EA series 1112 CHNS analyser. Bruker Tensor II equipped with Platinum ATR (Attenuated Total Reflectance) accessory was used to collect FT-IR spectra. TA instrument Q600 TG/DTA coupled with Bruker Tensor II ATR-IR was used to record TGA-FTIR measurements. TG analyses were carried out on PerkinElmer – STA 6000 and TG-Mass analyses were performed on PerkinElmer – STA 6000 coupled with PerkinElmer–Clarus SQ8S mass spectrometer. Raman spectra were recorded on Wi-Tec alpha 300AR laser confocal optical microscope (T-LCM) facility equipped with a Peltier cooled CCD detector using 785 nm Argon ion laser. Magnetic susceptibilities were measured in the temperature range of 3-300 K on a Quantum Design VSM SQUID. ICP-OES elemental analyses were performed on ICP-OES Varian 720ES. XPS analyses of powdered samples were performed on Omicron Nano Tec. ESCA$^+$ Oxford instruments Germany. Powder X-ray diffraction (PXRD) patterns of **1** and **2** were recorded on a Bruker D8-Advance diffractometer using graphite monochromated CuKα1 (1.5406 Å) and Kα2 (1.54439 Å) radiation.

5.2.2.1. X-ray crystallography

Single crystals of compounds **1** and **2**, suitable to collect diffraction data, were obtained directly from reaction mixture. Single crystal X-ray diffraction data of **1** and **2** were collected at100 K and 293 K respectively on a Bruker SMART APEX III single crystal X-ray diffractometer equipped with CCD area detector system, graphite monochromator and Mo-Kα fine-focus sealed tube (λ = 0.71073 Å). The scans were recorded with a ω scan width of 0.3°. Data reduction was performed by SAINT PLUS,[58] and empirical absorption corrections using equivalent reflections were performed by the program SADABS.[59] Structure solutions were done using SHELXT-2014,[60] and full-matrix least-squares refinement was carried out using SHELXL-2018.[61] All of the non-H atoms were refined anisotropically. Compound **1** crystallizes in hexagonal *P-62c* space group and compound **2** crystallizes in hexagonal *P-62m* space group.

Table 5.1. Crystal data and structural refinement parameters for compounds **1** and **2**

	Compound 1	**Compound 2**
Empirical formula	$C_1H_{88}N_6Na_6O_{73}V_{15}$	$Cl_1H_{63}Na_{10}O_{66}V_{15}$
Formula weight	2254.77	2148.93
T(K)/ λ (Å)	100(2)/0.71073	293(2) /0.71073
Crystal system	Hexagonal	Hexagonal
Space group	*P-62c*	*P-62m*
a Å	12.9910(6)	13.0800(18)
b Å	12.9910(6)	13.0800(18)
c Å	23.1099(12)	11.160(2)
α (°)	90	90
β (°)	90	90
γ (°)	120	120
Volume ($Å^3$)	3377.5(4)	1635.5(5)
Z	2	1
P calcd (g cm^{-3})	2.130	2.094
μ (mm^{-1}), *F*(000)	2.140, 2086	2.237, 1000
Goodness-of-fit on F^2	1.085	1.065
R_1/wR_2 [$I > 2\sigma(I)$]	0.0285/0.0769	0.0585/0.1753
R_1/wR_2 (all data)	0.018(6)	0.02(9)
Largest diff. peak/hole (e $Å^{-3}$)	2.384/-0.705	1.005/-0.797

The important crystallographic data of compounds **1** and **2** were given in **Table 5.1.** The supplementary crystallographic details such as bond distances and angles corresponding to compounds **1** and **2** were provided in *Appendix 5(i)*, respectively. **CCDC-1839257** and **CSD-434477** contain the supplementary crystallographic data for compounds **1** and **2**, respectively. The crystal data can be obtained free of charge via http://www.ccdc.cam.ac.uk/conts/retrieving.html, or from the Cambridge Crystallographic Data Centre, 12 Union Road, Cambridge CB2 1EZ, UK; fax: (+44) 1223-336-033; or e-mail: deposit@ccdc.cam.ac.uk.

5.3. Results and Discussion

5.3.1. Detailed discussion on synthesis

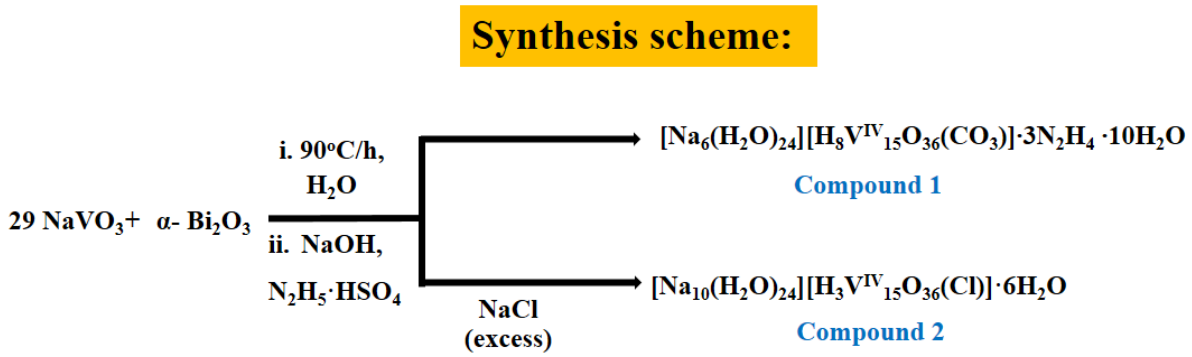

Scheme. 5.1. Scheme for fully reduced polyoxovanadate compounds synthesis in a one-pot wet reaction.

The synthesis of deep green colored compound $[Na_6(H_2O)_{24}][H_8V^{IV}_{15}O_{36}(CO_3)]\cdot 3N_2H_4\cdot 10H_2O$ (**1**) was carried out in an aqueous medium under an ambient condition (**Scheme. 5.1**). The synthesis involves $NaVO_3$ as the vanadium precursor, $N_2H_5\cdot HSO_4$ as the reducing agent, a small quantity (10 mol%) of α-Bi_2O_3 and solid NaOH (to adjust the pH to 8.5). Compound **1** (which does not have any bismuth atom in it) cannot be synthesized in absence of α-Bi_2O_3 from the concerned reaction mixture. It is also important to mention that, no external CO_3^{2-}source was used for the preparation of **1**, and spontaneous absorption of atmospheric CO_2 is the only possible source of encapsulated CO_3^{2-} in **1**. Thus α-Bi_2O_3 plays an important role in the encapsulation of dissolved atmospheric CO_2 (in the alkaline aqueous synthesis mixture) into the cavity of $\{V_{15}\}$ capsule in **1**. It is known that α-Bi_2O_3 shows a weak synergetic interaction with CO_2 in an alkaline solution.[62-65] Based on this, we speculate that, in the present aqueous alkaline synthesis of compound **1**, α-Bi_2O_3 establishes a reversible equilibrium with absorbed atmospheric CO_2: α-Bi_2O_3 + CO_2 ⇋ $(BiO)_2CO_3$ and supplies carbonate anion to compound **1** for its encapsulation. In order to understand, the survival of Bi_2O_3 in the concerned reaction mixture before and after crystallization, we performed the FESEM studies along with elemental map on the reaction mixture by analyzing sample solution after one day and after four days of the reaction (in this synthesis, crystallization starts after two days of the reaction). FESEM images of reaction mixture collected after one day show the presence of some flake-shaped particles decorated on sphere-shaped vanadium containing particles (**Figure 5.1**). In case of reaction mixture collected after four days, FESEM images show the presence of similar type of flake-shaped particles, but on needle-shaped vanadium containing crystals (since the crystallization was already started). The elemental map of these flake-shaped particles of two instances show mainly the existence of bismuth and oxygen. Thus, the solution contains some amount of bismuth and oxygen containing compounds that can be Bi_2O_3 (**Figure 5.2**). The existence of $Bi(OH)_3$ (in the alkaline reaction mixture) and elemental bismuth (under reducing condition) cannot be ruled out. Synthesis of compound **2** was carried out using similar synthetic protocol as of compound **1**, but at the end of the reaction an excess amount of NaCl was additionally supplied to the reaction mixture.

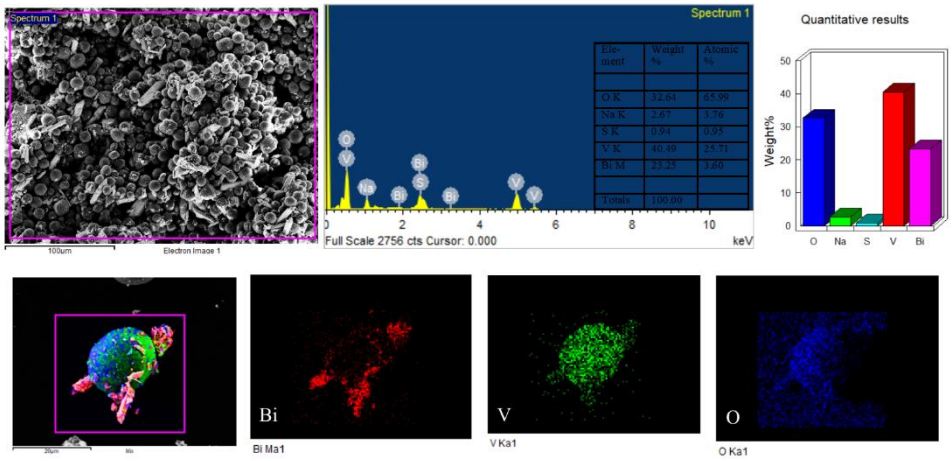

Figure 5.1. Reaction mixture analysis: FESEM-EDX elemental mapping of reaction mixture solution of compound **1** collected after one day.

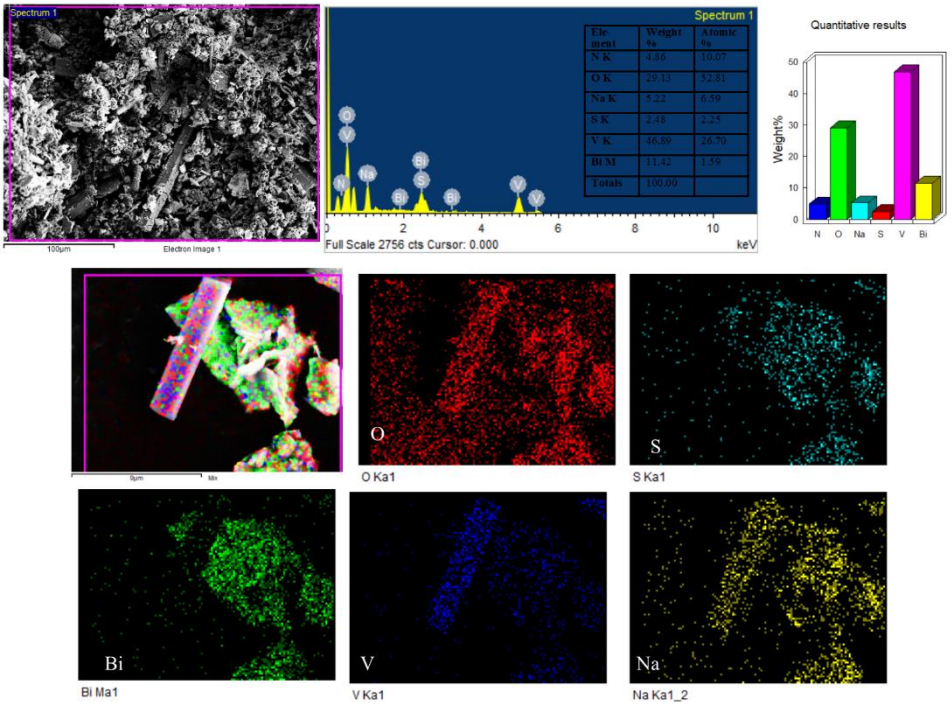

Figure 5.2. Reaction mixture analysis: FESEM-EDX elemental mapping of reaction mixture solution of compound **1** collected after four day.

5.3.2. Physical characterizations

5.3.2.1. Single-crystal X-ray crystallographic analysis

The crystal structure of **1** reveals that an encapsulated CO_3^{2-} anion is surrounded by 15 vanadium and 21 oxygen atoms spherically in the fully reduced POV capsule anion

$[H_8V^{IV}_{15}O_{36}(CO_3)]^{6-}$. The carbonate anion is stabilized by coordination with three vanadate units {V–O(CO_3^{2-}) = 2.30Å} in the cavity of the POV capsule. The POV cluster displays 12 $\{VO_5\}$ square pyramidal units and three distorted octahedral $\{VO_6\}$ units that are formed by coordination with central encapsulated CO_3^{2-} anion as shown in **Figure 5.3**. Each of these three vanadium centers, coordinated to the central CO_3^{2-}, is lying about 0.39 Å above the mean plane of four equatorial oxygen atoms. On the other hand, in each of twelve VO_5 centers, the vanadium is located about 0.631 Å above the mean plane of the concerned basal square-plane of four oxygen atoms. This implies that the interactions between peripheral vanadium atoms and the central carbonate ion is strong enough to consider these as coordinate covalent bonds. The overall topology of the POV cluster (compound **1**) is comparable to that of mixed-valent POV cluster in compound, $Li_7[V^V_7V^{IV}_8O_{36}(CO_3)]$ ~*ca.*·$39H_2O$, reported by Müller and co-workers.[24]

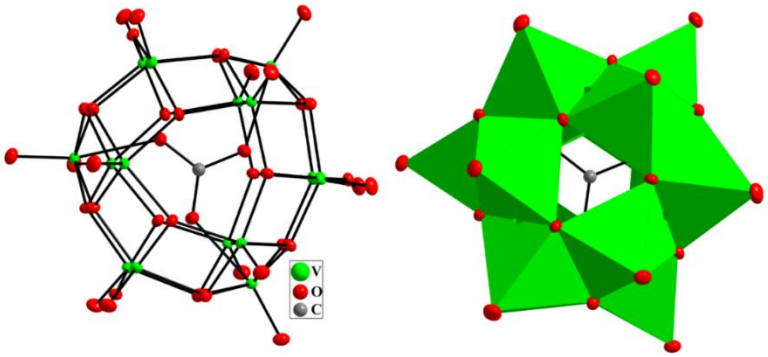

Figure 5.3. Single-crystal structure: thermal ellipsoidal and polyhedral plots (with 60% probability) of carbonate encapsulated cluster cage, $[H_8V^{IV}_{15}O_{36}(CO_3)]^{6-}$ (in compound **1**).

5.3.2.2. Spectroscopic characterization of the encapsulated carbonate ion

Since we did not supply any source of CO_3^{2-} anion (included in the cavity of the $\{V_{15}\}$ capsule in compound **1**) to the concerned reaction mixture and it is the aerial CO_2 dissolved in alkaline reaction mixture that gets encapsulated in the internal cavity of compound **1**, we have characterized the guest carbonate anion by IR and Raman spectral studies along with TGA-MS and TGA-IR studies besides single crystal X-ray crystallography. The presence of carbonate can be realized by Infrared (IR) bands observed at 1468 and 1406 cm^{-1} that can be assigned to stretching frequencies of carbonate ion (**Figure 5.4**(**a**)). The presence of CO_3^{2-} is also realized with the help of online coupled TGA-Infrared (**Figure 5.4**(**b-e**) and corresponding TGA response shown as inset in **Figure 5.4**(**f**)) and TGA-mass spectral analysis (**Figure 5.4**(**f**)). When the temperature of the sample reaches to 350 °C, the appearance of CO_2 stretching vibrations at 2295 cm^{-1} and 2345 cm^{-1} is started (i.e., decomposition of CO_3^{2-} as CO_2). The complete disappearance of CO_2 vibrations occurs around 445 °C. The TGA-mass spectra are also consistent with the TGA-IR data and show a mass loss response, corresponding to CO_2 at a similar temperature region (**Figure 5.4**(**f**)). The carrier gas (He) was flushed through the

sample port for 5 min prior to the measurement to eliminate the interference of atmospheric CO_2. The TGA profile was recorded in the temperature range 50 °C to 950 °C (10 °C/min,) and mass spectra were harvested between 3 to 42 min. A high intense mass peak at m/z = 44 corresponding to CO_2 observed in mass spectra of TGA effluent after 39th min in GC which corresponds to ~400 °C temperature in TGA.

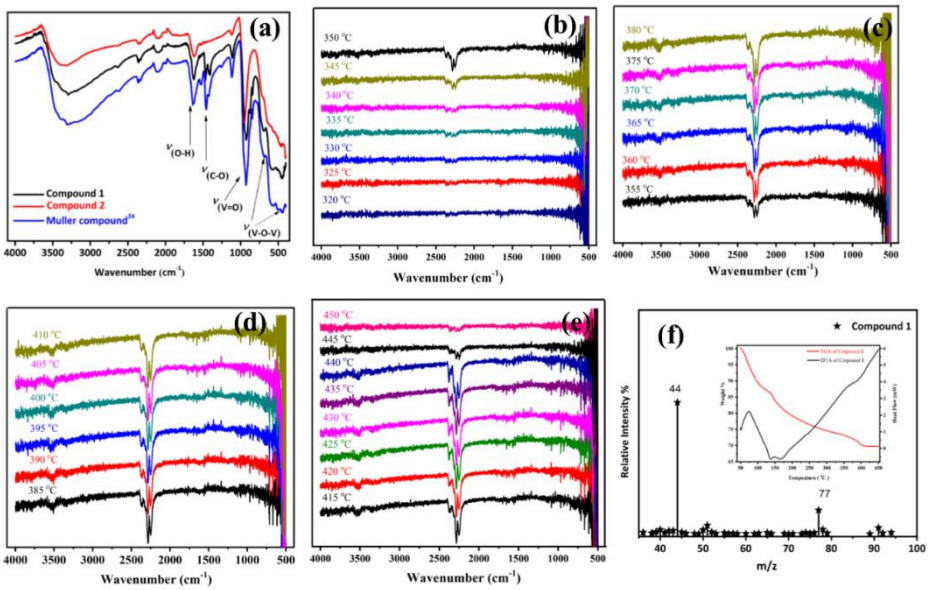

Figure 5.4. FT-IR, TGA-IR and TGA-mass spectra: (**a**) FTIR spectra of compounds **1**, **2** and Muller mixed-valent compound $Li_7[V^V_7V^{IV}_8O_{36}(CO_3)]$ ~*ca.*·$39H_2O$[24] (prominent carbonate stretching bands of **1** and Muller mixed-valent compound at 1468 and 1406 cm^{-1}, whereas compound **2** show none of these bands in that region); (**b**-**e**) TGA-IR spectral profile of compound **1** displaying stretching bands, corresponding to CO_2 evolved as a result of CO_3^{2-} decomposition in **1**; (**f**) TGA-mass spectrum of compound **1** displaying a peak corresponding to CO_2 evolved as a result of CO_3^{2-} decomposition in **1** (inset of Figure (**f**) can represent the thermogravimetric profile of compound **1** during the TGA-IR measurement).

5.3.2.3. Qualitative analysis of carbonate ion

The qualitative analysis test for CO_3^{2-} ion has also been performed and consistent positive results were obtained (**Figure 5.5**(**a** and **b**)).

Test 1: 0.1M calcium hydroxide solution was added drop-wise to a (0.1 mmol) 5 mL solution of compound **1** (deep green solution). A cloudy white precipitation was slowly formed which in turn confirms the presence of CO_3^{2-} ion in the compound **1**.

Test 2: In a 15 mL test tube, 5 mL of 0.1 mmol solution of compound **1** was treated with 5 mL of 0.1M hydrochloric acid. An immediate gas effervescence was observed along with generation of bright blue color solution. The effervescence confirms the presence of carbon

dioxide in the form of carbonate and the generation of bright blue color in solution indicates the presence of vanadium in their +4 oxidation state.

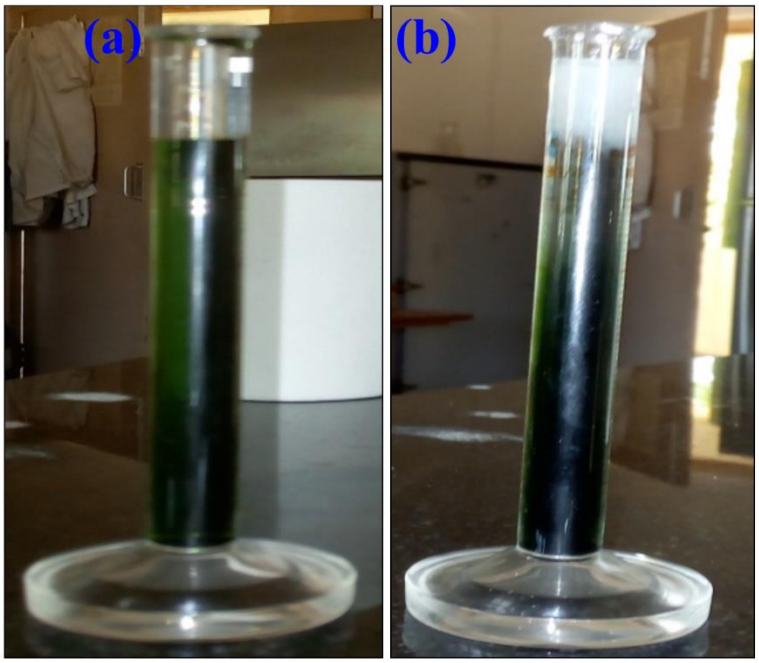

Figure 5.5. Carbonate ion test: (**a**) before addition of calcium hydroxide solution to the compound **1**; (**b**) after addition of calcium hydroxide solution to the compound **1**.

5.3.2.4. Carbonate ion exclusion as CO_2 from compound 1 in a gas-solid interface reaction followed by Grignard reaction

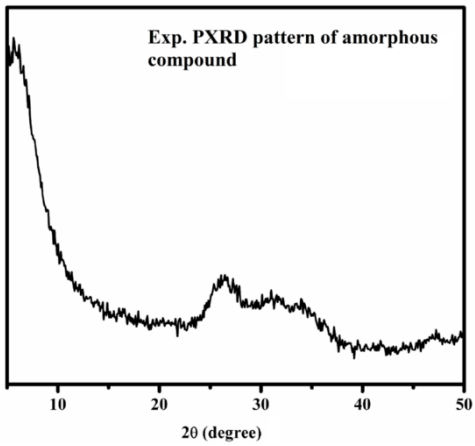

Figure 5.6. Powder X-ray diffraction pattern of an amorphous compound resulted in a gas-solid interface reaction.

Any carbonate salt, on reacting with a mineral acid, liberates CO_2 gas ($CO_3^{2-} + 2H^+ \rightarrow CO_2 + H_2O$), but not always with an acid vapor. Remarkably, the crystals of compound $[Na_6(H_2O)_{24}][H_8V^{IV}_{15}O_{36}(CO_3)]\cdot 3N_2H_4\cdot 10H_2O$ (**1**) (having a carbonate anion per formula unit) undergoes

gas-solid interface reaction with HCl vapor with the exclusion of CO_3^{2-} from the POV capsule as CO_2 gas resulting in the formation of an amorphous solid (eqn. 1), as confirmed from its PXRD studies (**Figure 5.6**).

$[Na_6(H_2O)_{24}][H_8V^{IV}_{15}O_{36}(CO_3)]\cdot 3N_2H_4\cdot 10H_2O$ (**1**, solid) + HCl (vapor) → CO_2 + an amorphous solid …… (eqn. 1)

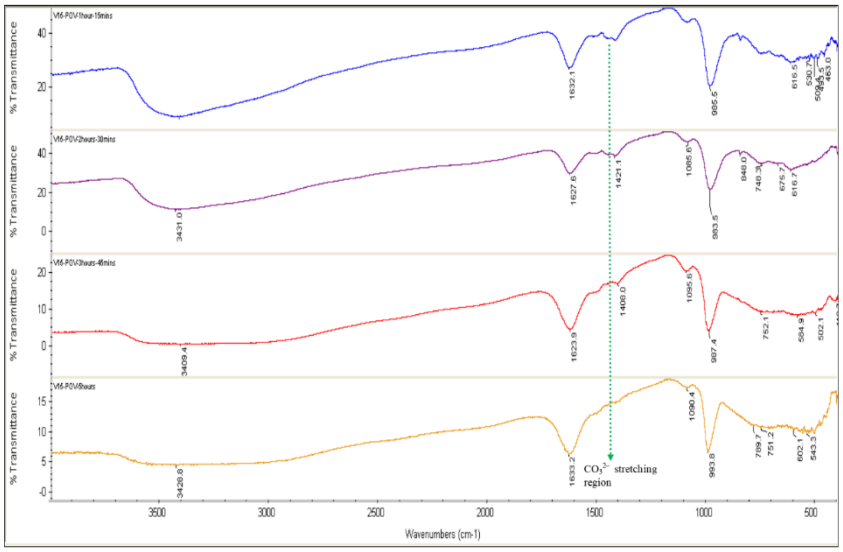

Figure 5.7. FTIR spectra: exclusion of carbonate as CO_2 gas from compound **1** was monitored by the FTIR spectra collected in the regular time intervals and the collected FTIR spectrums were represented in an overlay manner.

This exclusion of carbonate as CO_2 gas can simply be monitored by IR spectroscopy (**Figure 5.7**). The IR bands, observed at 1468 and 1406 cm^{-1} for **1**, disappears on exposing the crystals of **1** to HCl vapor resulting in the formation of amorphous substance in a solid to solid transformation (eqn. 1). We could not characterize unambiguously the resulting amorphous compound, formed by gas-solid reaction (eqn. 1). However, the elemental (ICP-OES; *Appendix 5(ii(d))*) analyses of this resulting amorphous solid shows the presence of chlorine element in it. The excluded CO_2 gas from encapsulated carbonate, as usually, can be reacted with Grignard reagent, PhMgBr to form triphenylmethanol and benzoic acid (**Scheme 5.2**). 2.2 g (1 mmol) of compound **1** having encapsulated carbonate anion was taken in a three neck round bottom flask and reacted with dry HCl vapours at 5 °C. The generated CO_2 was passed through dry tetrahydrofuran (THF) solution of trimethylamine to trap the unreacted HCl vapours and allowed to react with 2 mL of freshly prepared 0.1M PhMgBr reagent in 10 mL THF at -80 °C. The reaction mixture was mixed with water and pH was adjusted to 6.3 with 1M aqueous HCl solution and then extracted with diethyl ether. The resultant reaction mixture was analysed through the HRMS to identify the resulting products (***Appendix 5(ii(f))***).

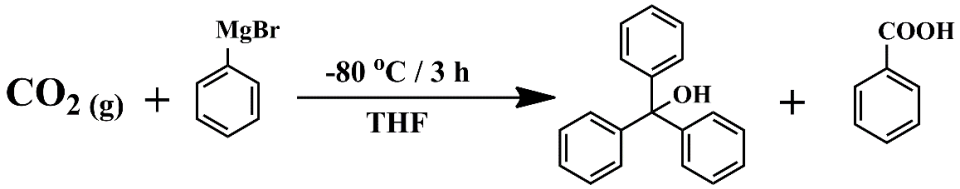

Scheme 5.2. Organic products formation: conversion of CO_2, excluded from compound **1**, to triphenylmethnol and benzoicacid by reacting with PhMgBr.

5.3.2.5. Understanding about molecular insights of gas-solid interface reaction material

As we could not characterize the amorphous compound formed in the gas-solid reaction (it loses crystallinity during its solid to solid state formation!) unambiguously and it is found to contain chlorine element, we intended to synthesize a chloride anion encapsulated compound in a direct synthesis. Thus, we have performed a synthesis similar to the synthesis of compound **1**, but added excess amount of NaCl at the end. We indeed have isolated and structurally characterized a Cl^- ion included compound $[Na_{10}(H_2O)_{24}][H_3V_{15}O_{36}(Cl)]\cdot 6H_2O$ (**2**), in which a chloride anion is found to be encapsulated in the internal cavity of same $\{V_{15}\}$ cluster, found in compound **1**. The crystal structure of this chloride anion encapsulated cluster cage is shown in **Figure 5.8**. As far as compositions are concerned, compound **2** POV cluster anion encapsulates a Cl^- in its cavity (**Figure 5.8**) and is tri-protonated in contrast to the compound **1** POV cluster anion, which encapsulates a CO_3^{2-} anion in its cavity and is protonated by 8 H^+. The Cl^- ion at the center of cluster shell (compound **2**) does not have any significant interactions with cluster cage and hence is stabilized by electrostatic interactions.

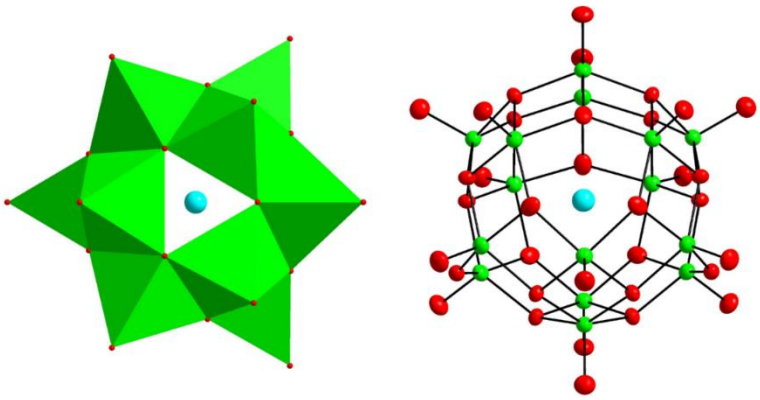

Figure 5.8. Single-crystal structure: polyhedral and thermal ellipsoidal plots (with 60% probability) of chloride encapsulated cluster cage, $[H_3V^{IV}_{15}O_{36}(Cl)]^{10-}$ (in compound **2**).

4.3.2.6. Raman spectra

The presence of same $\{V_{15}\}$ cluster cage in compound **2** can also be established by comparing its Raman signal with that of compound **1**. As shown in **Figure 5.9**, the Raman signals of

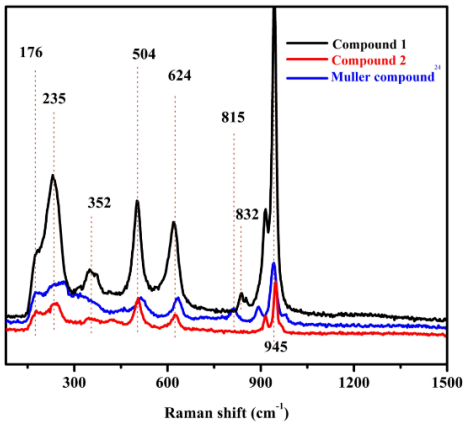

Figure 5.9. Raman spectra of compounds **1** and **2** along with Müller's mixed-valent compound $Li_7[V^V_7V^{IV}_8O_{36}(CO_3)]$ ~*ca.*·$39H_2O$.[24]

compounds **1**, **2** and known mixed-valent compound $Li_7[V^V_7V^{IV}_8O_{36}(CO_3)]$ ~*ca.*·$39H_2O$[24] are comparable. More specifically, the Raman bands corresponding to V–O(μ2-O/μ3-O) stretchings, observed for **1** and **2** in the range 200–650 cm^{-1}, are comparable to those found for the iso-structural mixed-valent compound $Li_7[V^V_7V^{IV}_8O_{36}(CO_3)]$ ~*ca.*·$39H_2O$.[24] The Raman spectral results are consistent with IR spectral results (**Figure 5.4a**, *vide supra*). Careful analysis shows an extra but small feature at around 800 cm^{-1} in the Raman spectra of **1** as well as in mixed-valent compound (both are carbonate anion containing compounds), which is not present in the Raman spectrum of **2** (chloride anion encapsulated compound **2**). We can thus assign this band at around 800 cm^{-1} in the Raman spectra of both compounds to Raman active A' mode of D_3h carbonate.[66]

5.3.2.7. Variable temperature magnetic susceptibility

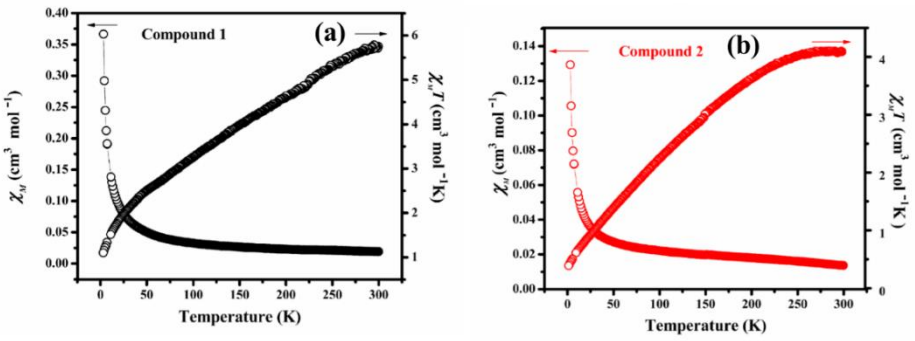

Figure 5.10. Variable temperature magnetic susceptibility: (**a** and **b**) χ_M *vs T* and $1/\chi_M T$ *vs T* plots of compounds **1** and **2**.

There are only very few organic free fully reduced polyoxovanadate (POV) cluster containing compounds; interestingly, all of them were reported by Müller group.[13,19,20,47] All these fully reduced organic free POV compounds were reported to exhibit remarkable magnetism.

Compounds **1** and **2** (present work) are new addition to this rare class of organic free fully reduced vanadium-based magnetic materials. Thus we have recorded magnetic susceptibilities of compounds **1** and **2** at 0.1 T in the temperature range 3–300 K. **Figure 5.10** shows the magnetic behaviors of compounds **1** and **2** in the form of χ_M versus T and product $\chi_M T$ versus T plots, respectively. The $\chi_M T$ value of compound **1** at 300 K is 5.758 cm^3 K mol^{-1} (6.786 μ_B), which is very close to the total spin only value 5.626 cm^3 K mol^{-1} (6.708 μ_B), expected for 15 non interacting electrons. In the case of compound **2**, the corresponding value is 4.104 cm^3 K mol^{-1} at 300 K, which is significantly less compared to their total spin only value (6.708 μ_B, expected for 15 non interacting electrons). As shown in **Figure 5.10**, as the temperature decreases, the $\chi_M T$ value of **1** was linearly decreased and reached to 2.36 cm^3 K mol^{-1} at 42 K. The value decreased rapidly below 42 K and reached to 1.104 cm^3 K mol^{-1} at 3 K. This behaviour does not follow curie and curie-wies law and seems to be antiferromagnetic interactions of individual spins in **1**. On the other hand, the $\chi_M T$ value of **2** is constant when the temperature is varied from 300 K to 250 K, but decreased linearly to 0.39 cm^3 K mol^{-1} with the decrease of temperature from 250 K to 3 K. The $\chi_M T$ value of 0.39 cm^3 K mol^{-1} at 3 K for **2** is close to zero and infers a S = 0 ground state for **2**. Thus the magnetic susceptibilities of **1** as a function of temperature is considerably different from **2** as a function of temperature. This clearly suggests that the encapsulated and coordinated carbonate anion in **1** as guest facilitates a different magnetic pathway compared to the magnetic exchange pathways, shown by compound **2** having non-coordinated encapsulated Cl^- anions as guest. However, the detailed account of magnetic interactions including theoretical studies in these compounds **1** and **2** are not possible at this stage and will be reported later in details.

5.3.2.8. BVS and XPS spectra

The bond valence sum calculations concludes that, all vanadium centers in **1** and **2** are in +4 oxidation state in contrast to the vanadium centers of same cluster cage containing compound $Li_7[V^V_7V^{IV}_8O_{36}(CO_3)]$ ~*ca.*·$39H_2O$ (mixed-valent compound),[24] that has 7 vanadium atoms in +5 oxidation state and 8 vanadium atoms in +4 oxidation state. Accordingly, the bond distances around the vanadium centres in **1** and **2** are quite different from those in $Li_7[V^V_7V^{IV}_8O_{36}(CO_3)]$ ~*ca.*·$39H_2O$[24] and other mixed-valent $\{V_{18}O_{42}\}$ systems.[40] The bond valance sum calculations (BVS) on **1** and **2** (*Appendix 5(iii)*) furnishes that the relevant BVS values are in the ranges of 3.40–4.22 (Avg. = 3.89) and 3.87–4.28 (Avg. = 4.11) for **1** and **2** respectively. The average V–O terminal bond distances (1.62–1.64) are significantly longer in **1** and **2** compared to the same distances reported for mixed-valent and fully oxidized polyoxovandates.[67] This observation is also consistent with +4 oxidation state of vanadium centers in **1** and **2**. In order to support the BVS calculations, we recorded X-ray photoelectron spectra (XPS) of compounds **1** and **2**, whereby O1s response at 530 eV was taken as the reference. **Figure 5.11** shows partial and survey scan XPS plots of **1** and **2**. Both compounds display a signal in the range of 514.96–515.73 eV for $V2p_{3/2}$ with FWHM (full width at half maximum) of 2.73–4.27 eV, which is

characteristic for a vanadium (IV) oxidation state.[68] An another XPS signal with relatively weak intensity has also been observed in the range of 522.50–523.12 eV corresponding to $V2p_{1/2}$.

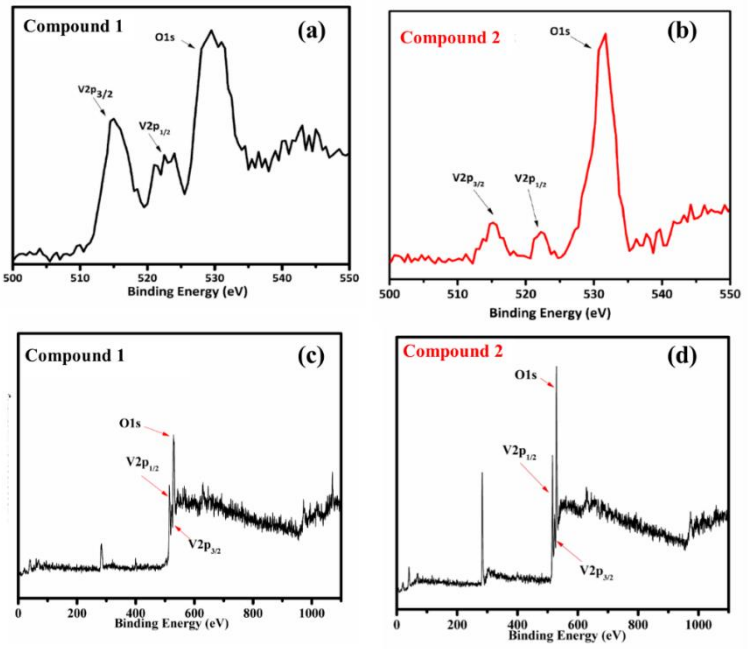

Figure 5.11. XPS spectra: (**a** and **b**) vanadium 2p core level XPS spectra of compounds **1** and **2**; (**c** and **d**) areal scan XPS spectra of compounds **1** and **2**.

5.3.2.9. Manganometric redox titrations

Prior to preparation of solutions, the solvents used were saturated with UHP nitrogen gas to remove the dissolved oxygen. 0.05N potassium permanganate solution ($KMnO_4$) was prepared and standardized with 0.05N ammonium ferrous sulphate ($(NH_4)_2Fe(SO_4)_2 \cdot 6H_2O$) in 0.2N sulphuric acid solution. The titrations are completely carried out under nitrogen atmosphere at room temperature to prevent the interaction of air with vanadium (IV) ion solution. 0.05N solution was freshly prepared by dissolving corresponding vanadium(IV) compound in 0.2N H_2SO_4 solution. 10 mL of the above solution was transferred into an Erlenmeyer flask and 0.2 mL of H_3PO_4 85% (syrupy phosphoric acid) as catalyst and 2 drops of ferroin as redox indicator were added. The mixture was titrated against standardized 0.05N potassium permanganate solution ($KMnO_4$). The end point was realized by a colour change from red to pale green. The experiment was repeated for two concurrent values.

Calculations for manganometric determination of vanadium oxidation states in compounds 1 and 2:

Compound 1

S No.	0.05N vanadium(IV) in 0.2N H_2SO_4 solution (mL)	Taken amount of 0.05N $KMnO_4$ (in Burette)	
		Initial (mL)	End point (mL)
1	10	0	10.3
2	10	0	10.4
3	10	0	10.4
4	Average titre value		10.36

Compound 2

S No.	0.05N vanadium(IV) in 0.2N H_2SO_4 solution (mL)	Taken amount of 0.05N $KMnO_4$ (in Burette)	
		Initial (mL)	End point (mL)
1	10	0	10.5
2	10	0	10.5
3	10	0	10.5
4	Average titre value		10.5

Formula for calculation:

$\{V^{IV}_{15}\} + 3\ KMnO_4 + 24\ H^+ \rightarrow \{V^{V}_{15}\} + 3\ Mn^{2+} + 12H_2O$

10 mL of 0.05 N of $KMnO_4$ = 15 no. of V^{IV} centres (in 10 mL of 0.05 N of V15 cluster)

x mL of 0.05 N of $KMnO_4$ = No. of V^{IV} centres (in 10 mL of 0.05 N of V15 cluster)

$$\text{No. of V(IV) centers present(in 10 mL of 0.05 N of V15 cluster)} = \frac{15 \times \text{x mL of KMnO4 (0.05 N)}}{\text{10 mL of KMnO4 (0.05 N)}}$$

For **Compound 1**,

$$\text{No. of V(IV) centers present (in 10 mL of 0.05 N of V15 cluster)} = \frac{15 \times \text{10.36 mL of KMnO4 (0.05 N)}}{\text{10 mL of KMnO4 (0.05 N)}}$$

$$= 15.54$$

For **Compound 2**,

$$\text{No. of V(IV) centers present(in 10 mL of 0.05 N of V15 cluster)} = \frac{15 \times \text{10.5 mL of KMnO4 (0.05 N)}}{\text{10 mL of KMnO4 (0.05 N)}}$$

$$=15.75$$

The obtained volumetric redox titrations results of **1** and **2** using standardized $KMnO_4$ solution and ferrion as an indicator was also revealed the presence of 15 electrons per formula unit of each of these compounds **1** and **2**.

5.3.2.10. UV-Vis absorption spectra

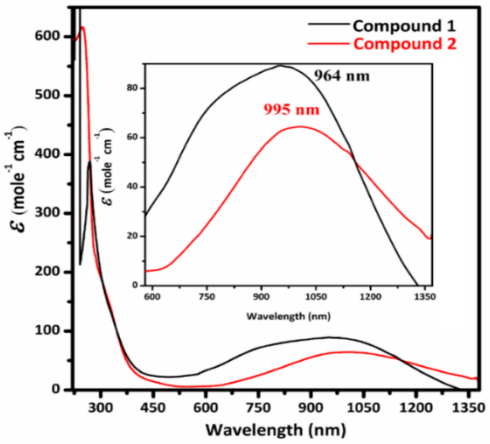

Figure 5.12. UV-Vis absorption (solution) spectra of compounds **1** and **2** in water.

Apart from above mentioned BVS, XPS, and volumetric redox titration confirmations, the presence of V(IV) oxidation states of **1** and **2** can be realized with the help of d-d transitions in UV-Vis spectra. For this, 0.1M lit^{-1} aqueous solutions (based on V^{4+} metal ion 0.1M per mL) of compounds **1** and **2** were used to record UV-Vis absorption (solution) spectra. The d–d transitions corresponding to V^{4+} (d^1) ion in the region of 600 to 1200 nm with an absorption maxima at 964 nm for **1** and at 995 nm for **2** (**Figure 5.12**) were observed.[69,70] The bands below 400 nm are perhaps due to ligand-to-metal charge transfer 'LM-CT' (O→V) transitions.

5.3.2.11. Thermogravimetric analyses

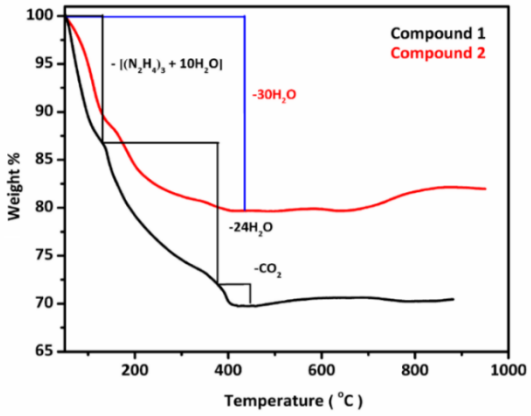

Figure 5.13. Thermogravimetric analyses plots of compounds **1** and **2**.

Thermal stability of the compounds **1** and **2** were examined by TGA analysis under helium gas atmosphere (**Figure 5.13**). The TGA analysis reveals that the compound **1** shows two stage dissociation of lattice water and hydrazine molecules as well as sodium coordinated water molecules and fallowed by CO_2 evaluation with the decomposition of CO_3^{2-} ion. However cluster show much thermal stability up to 495 °C then gets decomposed. Whereas compound **2** has a gradual weight loss in the temperature range 50 to 400 °C corresponding to water of crystallization and remains stable up to 600 °C.

5.3.2.12. Powder X-ray diffraction profiles

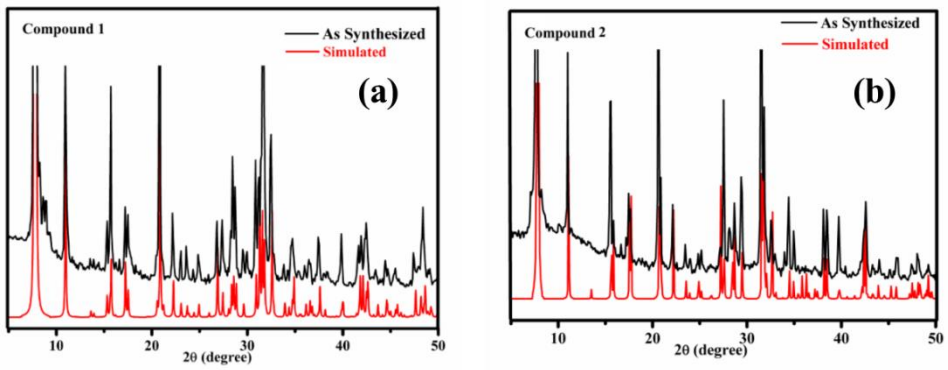

Figure 5.14. Powder X-ray diffraction patterns of compounds **1** and **2**.

Finally, the powder X-ray diffraction (PXRD) patterns were recorded to understand the phase purity and homogeneity of synthesized compounds **1** and **2**. **Figure 5.14** show the PXRD profiles of compounds **1** and **2**, the resulted experimental patterns were consistent with their calculated profiles hence confirmed that the homogeneity and phase purity of as synthesized compounds **1** and **2**.

5.4. Conclusions

In conclusion, even it is known that an alkaline aqueous solution absorbs aerial CO_2 gas and aqueous polyoxometalate chemistry had long been known (more than 200 years!), not a single polyoxometalate compound is known until today, in which this absorbed aerial CO_2 gets encapsulated. We have made this inclusion (as carbonate) possible by using some amount of α-Bi_2O_3 in the relevant reaction mixture. We have characterized this confined carbonate anion by IR, TGA-mass, TGA-IR spectral studies including single crystal X-ray crystallography. We have to admit that, even though, the terminal source of this carbonate encapsulation is air, this will not solve the global warming problem (one big cluster anion encapsulates only one carbonate anion!). But the present host-guest system is a unique one in the sense that, this on exposure to HCl vapor excludes the guest carbonate anion as CO_2 gas leading to the formation of an amorphous material. The excluded CO_2 can be reacted with PhMgBr (a Grignard reagent) to produce useful organic products (triphenyl carbinol and benzoic acid). We could not

characterize the resulting amorphous material (formed after CO_2 exclusion with HCl vapor in a solid to solid transformation). Elemental analysis of this amorphous material shows the presence of not only chlorine element but also a good amount hydrogen content even after thorough washing with water. A preliminary measurement on this amorphous material shows that it exhibits excellent proton conduction in the solid state. The detailed studies in this direction is under progress.

5.5. References

(1). Katsoulis, D. E., A Survey of Applications of Polyoxometalates. *Chem. Rev.* **1998**, *98*, 359-388.
(2). Fang, W.-H.; Zhang, L.; Zhang, J., Synthetic Strategies, Diverse Structures and Tuneable Properties of Polyoxo-Titanium Clusters. *Chem. Soc. Rev.* **2018**, *47*, 404-421.
(3). Izarova Natalya, V.; Pope Michael, T.; Kortz, U., Noble Metals in Polyoxometalates. *Angew. Chem. Int. Ed.* **2012**, *51*, 9492-9510.
(4). Wang, S.-S.; Yang, G.-Y., Recent Advances in Polyoxometalate-Catalyzed Reactions. *Chem. Rev.* **2015**, *115*, 4893-4962.
(5). Lv, H.; Geletii, Y. V.; Zhao, C.; Vickers, J. W.; Zhu, G.; Luo, Z.; Song, J.; Lian, T.; Musaev, D. G.; Hill, C. L., Polyoxometalate Water Oxidation Catalysts and the Production of Green Fuel. *Chem. Soc. Rev.* **2012**, *41*, 7572-7589.
(6). Long, D.-L.; Burkholder, E.; Cronin, L., Polyoxometalate Clusters, Nanostructures and Materials: From Self-Assembly to Designer Materials and Devices. *Chem. Soc. Rev.* **2007**, *36*, 105-121.
(7). Gumerova, N. I.; Rompel, A., Synthesis, Structures and Applications of Electron-Rich Polyoxometalates. *Nat. Rev. Chem.* **2018**, *2*, 0112.
(8). Fernando, A.; Weerawardene, K. L. D. M.; Karimova, N. V.; Aikens, C. M., Quantum Mechanical Studies of Large Metal, Metal Oxide, and Metal Chalcogenide Nanoparticles and Clusters. *Chem. Rev.* **2015**, *115*, 6112-6216.
(9). Miras, H. N.; Yan, J.; Long, D.-L.; Cronin, L., Engineering Polyoxometalates with Emergent Properties. *Chem. Soc. Rev.* **2012**, *41*, 7403-7430.
(10). Chen, J. J.; Symes Mark, D.; Fan, S. C.; Zheng, M. S.; Miras Haralampos, N.; Dong, Q. F.; Cronin, L., High-Performance Polyoxometalate-Based Cathode Materials for Rechargeable Lithium-Ion Batteries. *Adv. Mater.* **2015**, *27*, 4649-4654.
(11). Chen, J. J.; Ye, J. C.; Zhang, X. G.; Symes Mark, D.; Fan, S. C.; Long, D. L.; Zheng, M. S.; Wu, D. Y.; Cronin, L.; Dong, Q. F., Design and Performance of Rechargeable Sodium Ion Batteries, and Symmetrical Li-Ion Batteries with Supercapacitor-Like Power Density Based upon Polyoxovanadates. *Adv. Energy Mater.* **2017**, *8*, 1701021.
(12). Rhule, J. T.; Hill, C. L.; Judd, D. A.; Schinazi, R. F., Polyoxometalates in Medicine. *Chem. Rev.* **1998**, *98*, 327-358.
(13). Müller, A.; Peters, F.; Pope, M. T.; Gatteschi, D., Polyoxometalates: Very Large Clusters Nanoscale Magnets. *Chem. Rev.* **1998**, *98*, 239-272.
(14). Monakhov, K. Y.; Bensch, W.; Kogerler, P., Semimetal-Functionalised Polyoxovanadates. *Chem. Soc. Rev.* **2015**, *44*, 8443-8483.
(15). Winpenny, R. E. P., High-Nuclearity Paramagnetic 3*d*-Metal Complexes with Oxygen- and Nitrogen-Donor Ligands. *Adv. Inorg. Chem.*, **2001**, *52*, 1-11.
(16). Barbour, A.; Luttrell, R. D.; Choi, J.; Musfeldt, J. L.; Zipse, D.; Dalal, N. S.; Boukhvalov, D. W.; Dobrovitski, V. V.; Katsnelson, M. I.; Lichtenstein, A. I.; Harmon, B. N.; Kögerler, P., Understanding the Gap in Polyoxovanadate Molecule-Based Magnets. *Phys. Rev. B* **2006**, *74*, 014411.
(17). Chiorescu, I.; Wernsdorfer, W.; Müller, A.; Bögge, H.; Barbara, B., Non-Adiabatic Landau-Zener Transitions in Low-Spin Molecular Magnet V_{15}. *J. Magn. Magn. Mater.* **2000**, *221*, 103-109.
(18). Hegetschweiler, K.; Morgenstern, B.; Zubieta, J.; Hagrman Pamela, J.; Lima, N.; Sessoli, R.; Totti, F., Strong Ferromagnetic Interactions in $[V_8O_{14}(H{-}2taci)_2]$: An Unprecedented Large Spin Ground State for a Vanadyl Cluster. *Angew. Chem. Inte. Ed.* **2004**, *43*, 3436-3439.

(19). Gatteschi, D.; Pardi, L.; Barra, A. L.; Müller, A.; Döring, J., Layered magnetic structure of a metal cluster ion. *Nature* **1991**, *354*, 463.

(20). Barra, A. L.; Gatteschi, D.; Pardi, L.; Mueller, A.; Doering, J., Magnetic Properties of High-Nuclearity Spin Clusters Fourteen- and Fifteen-Oxovanadium(IV) Clusters. *J. Am. Chem. Soc.* **1992**, *114*, 8509-8514.

(21). Yang, P.; Alsufyani, M.; Emwas, A.-H.; Chen, C.; Khashab, N. M., Lewis Acid Guests in a $\{P_8W_{48}\}$ Archetypal Polyoxotungstate Host: Enhanced Proton Conductivity via Metal-Oxo Cluster within Cluster Assemblies. *Angew. Chem. Int. Ed.* **2018**, *57*, 13046-13051.

(22). Müller, A.; Das, S. K.; Kögerler, P.; Bögge, H.; Schmidtmann, M.; Trautwein, A. X.; Schünemann, V.; Krickemeyer, E.; Preetz, W., A New Type of Supramolecular Compound: Molybdenum-Oxide-Based Composites Consisting of Magnetic Nano capsules with Encapsulated Keggin-Ion Electron Reservoirs Cross-Linked to a Two-Dimensional Network. *Angew. Chem. Int. Ed.* **2000**, *39*, 3413-3417.

(23). Müller, A.; Reuter, H.; Dillinger, S., Supramolecular Inorganic Chemistry: Small Guests in Small and Large Hosts. *Angew. Chem. Int. Ed. Eng.* **1995**, *34*, 2328-2361.

(24). Müller, A.; Penk, M.; Rohlfing, R.; Krickemeyer, E.; Döring, J., Topologically Interesting Cages for Negative Ions with Extremely High "Coordination Number": An Unusual Property of V-O Clusters. *Angew. Chem. Int. Ed. Eng.* **1990**, *29*, 926-927.

(25). Yamase, T.; Ohtaka, K., Photochemistry of polyoxovanadates. Part 1. Formation of the Anion-Encapsulated Polyoxovanadate $[V_{15}O_{36}(CO_3)]^{7-}$ and Electron-Spin Polarization of α-Hydroxy Alkyl Radicals in the Presence of Alcohols. *J. Chem. Soc., Dalton Trans.* **1994**, 2599-2608.

(26). Day, V. W.; Klemperer, W. G.; Yaghi, O. M., Synthesis and Characterization of a Soluble Oxide Inclusion Complex, $[CH_3CN.cntnd.\ (V_{12}O_{32})]^{4-}$. *J. Am. Chem. Soc.* **1989**, *111*, 5959-5961.

(27). Müller, A.; Rohlfing, R.; Krickemeyer, E.; Bögge, H., Control of the Linkage of Inorganic Fragments of V–O Compounds: From Cluster Shells as Carcerands via Cluster Aggregates to Solid-State Structures. *Angew. Chem. Int. Ed. Eng.* **1993**, *32*, 909-912.

(28). Watfa, N.; Melgar, D.; Haouas, M.; Taulelle, F.; Hijazi, A.; Naoufal, D.; Avalos, J. B.; Floquet, S.; Bo, C.; Cadot, E., Hydrophobic Effect as a Driving Force for Host–Guest Chemistry of a Multi-Receptor Keplerate-Type Capsule. *J. Am. Chem. Soc.* **2015**, *137*, 5845-5851.

(29). Moussawi, M. A.; Leclerc-Laronze, N.; Floquet, S.; Abramov, P. A.; Sokolov, M. N.; Cordier, S.; Ponchel, A.; Monflier, E.; Bricout, H.; Landy, D.; Haouas, M.; Marrot, J.; Cadot, E., Polyoxometalate, Cationic Cluster, and γ-Cyclodextrin: From Primary Interactions to Supramolecular Hybrid Materials. *J. Am. Chem. Soc.* **2017**, *139*, 12793-12803.

(30). Kikukawa, Y.; Seto, K.; Uchida, S.; Kuwajima, S.; Hayashi, Y., Solid-State Umbrella-type Inversion of a VO_5 Square-Pyramidal Unit in a Bowl-type Dodecavanadate Induced by Insertion and Elimination of a Guest Molecule. *Angew. Chem. Int. Ed.* **2018**, *57*, 16051-16055.

(31). Kawanami, N.; Ozeki, T.; Yagasaki, A., NO- Anion Trapped in a Molecular Oxide Bowl. *J. Am. Chem. Soc.* **2000**, *122*, 1239-1240.

(32). Kuwajima, S.; Kikukawa, Y.; Hayashi, Y., Small-Molecule Anion Recognition by a Shape-Responsive Bowl-Type Dodecavanadate. *Chem. – Asian J.* **2017**, *12*, 1909-1914.

(33). Inoue, Y.; Kikukawa, Y.; Kuwajima, S.; Hayashi, Y., A Chloride Capturing System via Proton-Induced Structure Transformation between Opened- and Closed-Forms of Dodecavanadates. *Dalton Trans.* **2016**, *45*, 7563-7569.

(34). Kuwajima, S.; Ikinobu, Y.; Watanabe, D.; Kikukawa, Y.; Hayashi, Y.; Yagasaki, A., A Bowl-Type Dodecavanadate as a Halide Receptor. *ACS Omega* **2017**, *2*, 268-275.

(35). Müller, A.; Krickemeyer, E.; Penk, M.; Walberg, H.-J.; Bögge, H., Spherical Mixed-Valence $[V_{15}O_{36}]^{5-}$, an Example from an Unusual Cluster Family. *Angew. Chem. Int. Ed. Eng.* **1987**, *26*, 1045-1046.

(36). Dong, B.; Peng, J.; Chen, Y.; Kong, Y.; Tian, A.; Liu, H.; Sha, J., pH-Controlled Assembly of two Polyoxovanadates based on $[V_{16}O_{38}(Cl)]^{8-}$ and $[V_{15}O_{36}(Cl)]^{6-}$ Building Blocks. *J. Mol. Struct.* **2006**, *788*, 200-205.

(37). Zhang, C.-D.; Liu, S.-X.; Gao, B.; Sun, C.-Y.; Xie, L.-H.; Yu, M.; Peng, J., Hybrid Materials based on Metal–Organic Coordination Complexes and Cage-Like Polyoxovanadate Clusters: Synthesis, Characterization and Magnetic Properties. *Polyhedron* **2007**, *26*, 1514-1522.

(38). Chen, Y.; Peng, J.; Yu, H.; Han, Z.; Gu, X.; Shi, Z.; Wang, E.; Hu, N., A Supramolecular Assembly of Chiral l/d-$[Cd(Cl)(H_2O)(phen)_2]^+$ and l,l/d,d-Dinuclear Cd Complex Coordinated by Phen and $\{V_{16}O_{38}(Cl)\}$ Cluster. *Inorg. Chim. Acta* **2005**, *358*, 403-408.

(39). Dong, B.-x.; Peng, J.; Gómez-García, C. J.; Benmansour, S.; Jia, H.-q.; Hu, N.-h., High-Dimensional Assembly Depending on Polyoxoanion Templates, Metal Ion Coordination Geometries, and a Flexible Bis(imidazole) Ligand. *Inorg. Chem.* **2007**, *46*, 5933-5941.

(40). Teng, Y.-l.; Dong, B.-x.; Peng, J.; Zhang, S.-y.; Chen, L.; Song, L.; Ge, J., Spontaneous Resolution of 3D Chiral Hexadecavanadate-based Frameworks Incorporating Achiral Flexible and Rigid Ligands. *CrystEngComm* **2013**, *15*, 2783-2785.

(41). Chen, Y.; Gu, X.; Peng, J.; Shi, Z.; Yu, H.; Wang, E.; Hu, N., The First Discrete Mixed-Valence Hexadecavanadate Host Shell Cluster Anions: Hydrothermal Synthesis, Structure and Characterization of $[V_{16}O_{38}(Cl)]^{8-}$. *Inorg. Chem. Commun.* **2004**, *7*, 705-707.

(42). Ishaque Khan, M.; Ayesh, S.; Doedens, R. J.; Yu, M.; O'Connor, C. J., Synthesis and Characterization of a Polyoxovanadate Cluster Representing a New Topology. *Chem. Commun.* **2005**, 4658-4660.

(43). Kato, N.; Hayashi, Y., Discrete Spherical Hexadecavanadates Incorporating a Bromide with Oxidative Bromination Activity. *Dalton Trans.* **2013**, *42*, 11804-11811.

(44). Keene, T. D.; D'Alessandro, D. M.; Krämer, K. W.; Price, J. R.; Price, D. J.; Decurtins, S.; Kepert, C. J., $[V_{16}O_{38}(CN)]^{9-}$: A Soluble Mixed-Valence Redox-Active Building Block with Strong Antiferromagnetic Coupling. *Inorg. Chem.* **2012,** *51*, 9192-9199.

(45). Xiao, L.-N.; Xu, J.-N.; Hu, Y.-Y.; Wang, L.-M.; Wang, Y.; Ding, H.; Cui, X.-B.; Xu, J.-Q., Synthesis and Characterizations of the First $[V_{16}O_{39}Cl]^{6-}$ ($V_{16}O_{39}$) Polyanion. *Dalton Trans.* **2013**, *42*, 5247-5251.

(46). Müller, A.; Krickemeyer, E.; Penk, M.; Rohlfing, R.; Armatage, A.; Bögge, H., Template-Controlled Formation of Cluster Shells or a Type of Molecular Recognition: Synthesis of $[HV_{22}O_{54}(ClO_4)]^{6-}$ and $[H_2V_{18}O_{44}(N_3)]^{5-}$. *Angew. Chem. Int. Ed. Eng.* **1991**, *30*, 1674-1677 and references therein.

(47). Müller, A.; Sessoli, R.; Krickemeyer, E.; Bögge, H.; Meyer, J.; Gatteschi, D.; Pardi, L.; Westphal, J.; Hovemeier, K.; Rohlfing, R.; Döring, J.; Hellweg, F.; Beugholt, C.; Schmidtmann, M., Polyoxovanadates: High-Nuclearity Spin Clusters with Interesting Host−Guest Systems and Different Electron Populations. Synthesis, Spin Organization, Magnetochemistry, and Spectroscopic Studies. *Inorg. Chem.* **1997,** *36*, 5239-5250.

(48). Khan, M. I.; Yohannes, E.; Doedens, R. J., $[M_3V_{18}O_{42}(H_2O)_{12}(XO_4)]\cdot 24\ H_2O$ (M=Fe, Co; X=V, S): Metal Oxide Based Framework Materials Composed of Polyoxovanadate Clusters. *Angew. Chem. Int. Ed.* **1999**, *38*, 1292-1294.

(49). Yamase, T.; Suzuki, M.; Ohtaka, K., Structures of Photochemically Prepared Mixed-Valence Polyoxovanadate Clusters: Oblong $[V_{18}O_{44}(N_3)]^{14-}$, Super Keggin $[V_{18}O_{42}(PO_4)]^{11-}$ and Doughnut-Shaped $[V_{12}B_{32}O_{84}Na_4]^{15-}$ Anions. *J. Chem. Soc., Dalton Trans.* **1997**, 2463-2472.

(50). Climate Change 2007: Synthesis Report, International Panel on Climate Change, Cambridge University Press, Cambridge, UK, **2007**.

(51). Falkowski, P.; Scholes, R. J.; Boyle, E.; Canadell, J.; Canfield, D.; Elser, J.; Gruber, N.; Hibbard, K.; Högberg, P.; Linder, S.; Mackenzie, F. T.; Moore Iii, B.; Pedersen, T.; Rosenthal, Y.; Seitzinger, S.; Smetacek, V.; Steffen, W., The Global Carbon Cycle: A Test of Our Knowledge of Earth as a System. *Science* **2000**, *290*, 291.

(52). Yu, B.; Zou, B.; Hu, C.-W., Recent Applications of Polyoxometalates in CO_2 Capture and Transformation. *Journal of CO_2 Utilization* **2018**, *26*, 314-322.

(53). Garai, S.; Haupt, E. T. K.; Bögge, H.; Merca, A.; Müller, A., Picking up $30CO_2$ Molecules by a Porous Metal Oxide Capsule Based on the Same Number of Receptors. *Angew. Chem. Int. Ed.* **2012**, *51*, 10528-10531.

(54). Gao, G.; Li, F.; Xu, L.; Liu, X.; Yang, Y., CO_2 Coordination by Inorganic Polyoxoanion in Water. *J. Am. Chem. Soc.* **2008**, *130*, 10838-10839.

(55). Khenkin, A. M.; Efremenko, I.; Weiner, L.; Martin, J. M. L.; Neumann, R., Photochemical Reduction of Carbon Dioxide Catalyzed by a Ruthenium-Substituted Polyoxometalate. *Chem. Eur. J.* **2010,** *16*, 1356-1364.

(56). Levinger, N. E.; Rubenstrunk, L. C.; Baruah, B.; Crans, D. C., Acidification of Reverse Micellar Nanodroplets by Atmospheric Pressure CO_2. *J. Am. Chem. Soc.* **2011,** *133*, 7205-7214.

(57). Cheng, W.; Xue, Y.-s.; Luo, X.-M.; Xu, Y., A Rare Three-Dimensional POM-based Inorganic Metal Polymer Bonded by CO_2 with High Catalytic Performance for CO_2 Cycloaddition. *Chem. Commun.* **2018**, *54*, 12808-12811.

(58). SAINT: Software for the CCD Detector System; Bruker Analytical X-ray Systems, Inc.: Madison, WI, **1998**.

(59). G. M. Sheldrick, SADABS, Program for Area Detector Absorption Correction; University of Gottingen: Gottingen, Germany, **1997**.
(60). Sheldrick, G. M., SHELXT – Integrated Space-Group and Crystal-Structure Determination, *Acta Crystallogr., Sect. A: Found. Adv.*, **2015**, *71*, 3–8.
(61). Sheldrick, G. M., Crystal Structure Refinement with SHELXL, *Acta Crystallogr., Sect. C: Struct. Chem.*, **2015**, *71*, 3–8, (SHELXL-**2018/1** (Sheldrick, **2018**)).
(62). Taylor, P.; Sunder, S.; Lopata, V. J., Structure, Spectra, and Stability of Solid Bismuth Carbonates. *Can. J. Chem.* **1984**, *62*, 2863-2873.
(63). Esaka, T.; Moto-ike, K., CO_2 Absorption and Desorption of Bi_2O_3–La_2O_3 Powders Prepared by Mechanical Synthesis. *Mater. Res. Bull.* **2004**, *39*, 1581-1587.
(64). M. Nolan, CO_2 Activation on Heterostructures of Bi_2O_3-Nanocluster Modified TiO_2: Promoting the Critical First Step in CO_2 Conversion, **2018**. https://doi.org/10.26434/chemrxiv.5917351.v1.
(65). Yin, S.-F.; Maruyama, J.; Yamashita, T.; Shimada, S., Efficient Fixation of Carbon Dioxide by Hyper Valent Organobismuth Oxide, Hydroxide, and Alkoxide. *Angew. Chem. Int. Ed.* **2008**, *47*, 6590-6593.
(66). Greenaway, A. M.; Dasgupta, T. P.; Koshy, K. C.; Sadler, G. G., A Correlation between Infra-red Stretching Mode Absorptions and Structural Angular Distortions for the Carbonato Ligand in a Wide Variety of Complexes. *Spectrochim. Acta.* **1986**, *42*, 949-954.
(67). Queen, W. L.; West, J. P.; Hudson, J.; Hwu, S.-J., Extended Utility of Molten-Salt Chemistry: Unprecedented Synthesis of a Water-Soluble Salt-Inclusion Solid Comprised of High-Nuclearity Vanadium Oxide Clusters. *Inorg. Chem.* **2011**, *50*, 11064-11068.
(68). Silversmit, G.; Depla, D.; Poelman, H.; Marin, G. B.; De Gryse, R., Determination of the V2p XPS Binding Energies for Different Vanadium Oxidation States (V^{5+} to V^{0+}). *J. Electron Spectrosc. Relat. Phenom.* **2004**, *135*, 167-175.
(69). Yuan, M.; Li, Y.; Wang, E.; Tian, C.; Wang, L.; Hu, C.; Hu, N.; Jia, H., Modified Polyoxometalates: Hydrothermal Syntheses and Crystal Structures of Three Novel Reduced and Capped Keggin Derivatives Decorated by Transition Metal Complexes. *Inorg. Chem.* **2003**, *42*, 3670-3676.
(70). Arumuganathan, T.; Das, S. K., Discrete Polyoxovanadate Cluster into an Organic Free Metal-Oxide-Based Material: Syntheses, Crystal Structures, and Magnetic Properties of a New Series of Lanthanide Linked-POV Compounds $[\{Ln(H_2O)_6\}_2As_8V_{14}O_{42}(SO_3)]\cdot 8H_2O$ (Ln = La^{3+}, Sm^{3+}, and Ce^{3+}). *Inorg. Chem.* **2009**, *48*, 496-507.

Concluding Remarks and Future Scope of the Present Thesis Work

Concluding Remarks:

The present thesis has highlighted the necessity of polyoxometalates (POMs), earth-abundant bio-compatible materials, for carbon free-energy production (*i.e.*, electrocatalytic hydrogen evolution and solid-state proton conduction) and environmental cleaning (CO_2 sequestration). Throughout the thesis work, simple and energy efficient one-pot wet synthetic methodologies were adapted for POM materials production, using a green solvent (*i.e.*, water) and earth-abundant metal-oxides precursors. All the compounds, presented in this thesis work, were characterized by routine analytical techniques as well as unambiguously by single-crystal X-ray diffraction studies.

Chapter 2, the first working chapter, presents isolation and exploration of two $\mathbf{W^{VI}–(OH)_2}$ functional sites containing POM systems, *i.e.*, (**POM-CoW(OH)$_2$** and **Him@POM-MnW(OH)$_2$**). The $W^{VI}–(OH)_2$ sites on the surface of POMs are found to be electrochemically active for electrocatalytic hydrogen evolution reaction in a wide pH range (from acidic to neutral pH medium). The electrochemical controlled experiments have clearly established the structure-function relationship and also revealed the crucial role of $W^{VI}–(OH)_2$ functional sites on electrocatalytic hydrogen evolution reaction. Both the catalysts, studied in this chapter, have been shown to be stable and to exhibit efficient hydrogen evolution reaction activity in a wide pH range under the given electrochemical operational condition. Between the two compounds presented in this section,, the **Him@POM-MnW(OH)$_2$** is found to have better catalytic efficiency towards electrocatalytic hydrogen evolution reaction than that shown by **POM-CoW(OH)$_2$**. The enhanced activity in the case of **Him@POM-MnW(OH)$_2$** is expected due to the presence of an additional charge carrier ions (*i.e.*, protonated imidazole). This chapter opens up the doors and strengthens the idea of introducing more number of transition metal-hydroxyl (M^{n+}–OH) groups and charge carriers into the POMs for further enhancement in the hydrogen evolution reaction activity.

Chapter 3 describes the functionalization of lacunary (*in-situ* generated **BiW$_9$**) clusters by redox-active hexa-nuclear and penta-nuclear mixed-valent copper wheel and isolated as barrel-shaped POM (**LiCu-POM** and **NaCu-POM**) clusters containding compounds. Among two barrel-shaped POM clusters, studied in this chapter, one of the POM cluster (**LiCu-POM**) contains lithium counter cations and grown in to a 2D layered network though the Cu–O=W linkage and the void spaces of the 2D network were occupied by lithium aqua-clusters. Interestingly, in the **LiCu-POM** compound, a sulphide group was found to be coordinated to

the apical position of one of the copper center, which seems to be derived from *in situ* reduction of sulphate to sulfide. Ammonia solution and lithium ions are expected to take the leading role in this reduction of sulphate to sulfide. In contrast, the same observation is not made in the other compound (**NaCu-POM**). On the other hand, the **NaCu-POM** cluster containing compound contains sodium ions as counter cations in the form of a sodium aqua-wheel that connect to two POM barrels in a side on manner. In another view, the sodium aqua-wheel is sandwiched by two POM barrels in a plug-socket type and has made it a strong supramolecular network. The electrochemical studies of these barrel-type compounds reveal that both the functionalized compounds are synergistically activated and exhibit efficient electrocatalytic hydrogen evolution at neutral pH. In a close observation, the **NaCu-POM** has leading catalytic hydrogen evolution reaction activity over that of **LiCu-POM** catalyst. This enhanced activity in **NaCu-POM** could be attributed to the presence of extensive H-bonding, which further helps to interact with water and make the catalytic hydrogen evolution more feasible.

Chapter 4 depicts the role of reduced POMs on proton conductivity. It is commonly known that the higher the number of labile protons on POM surface and the higher is the conductivity. The higher number of protons on the concerned compounds surface prompted us to investigate the proton conductivity studies. In this chapter, we have studied the solid-state proton conductivity using such two simple, fully reduced, and proton-rich polyoxovanadate compounds (named as compounds **1** and **2**). The proton conductivity studies reveal that both the compounds are found to be stable under operational condition. Among two compounds, compound **1** has been shown to have better proton conductivity compared to that of compound **2**.

In **Chapter 5**, we have demonstrated the carbonate (CO_3^{2-}) ion encapsulation into the fully reduced polyoxovanadate capsule cavity from absorbed atmospheric CO_2 in the concerned synthesis reaction mixture. Interestingly, the encapsulated CO_3^{2-} has been excluded by gas-solid interface reaction under the controlled experimental condition and is further reacted with the Grignard (PhMgBr) reagent for its transformation to value added organic products (triphenyl carbinol and benzoic acid as the products). The resulted residual material from the gas-solid interface reaction was found to exhibit excellent proton conductivity in the order of 10^{-2} S cm^{-1} and its membrane fabrication is under progress. This chapter has also described the variable temperature magnetic studies of the title host guest compounds, that are fully reduced in terms of vanadium centers. This chapter demonstrates an immense attention of the modern scientific community for post-synthetic modifications on such fully reduced POMs (*e.g.,* gas-solid interface reaction) for next-generation materials for clean energy applications.

Future Scope:

In **Chapters 2-5**, we have already emphasized the role of functional polyoxometalates in clean energy management. In addition to this, direct utilization of solar energy is vital to produce

energy in a continuous manner. It is known that in total solar energy, around 70% of red light is present. Converting this form of energy into usable energy is most important and crucial to avoid global warming effect (fossil fuel burning) and sustainable life on the earth surface. We need a stable and efficient catalyst to capture and conversion of this energy in the form of fuels (H_2 molecules). On the other hand, the development of highly efficient energy processing devices is also most important to use the produced fuels efficiently. Hence, the construction of sustainable hydrogen fuel cell (FC) is also vital. The efficiency of FC largely depends on the efficiency of the proton exchange membrane (PEM) material. Besides, solar energy conversion, the fabrication of PEMs can make the fulfilment for overall energy management.

On the other hand, storage of electrical energy in the form of charge (*e.g.*, solid-state lithium/sodium-ion batteries, redox flow batteries *etc.*) is another important challenge for energy management in portable device applocations. For this, we need to develop the high-energy density charge carrier and conversion devices safely. In this area of technology, founctional polyoxometalates may be found to be the most potential candidates to address most of these energy management issues not only due to their very fast multi-electron redox reactions but also because of their structural integrity even after multiple number of electron transfer involeved in the concerned red-ox reactions. In addition to all these characteristics, their earth-abundancy, bio-compatible nature, and 'easy to synthesize for industrial demand in a one-pot aqueous methodology' are added advantages in employing these materials in clean energy management. The following attempts can be described as future scopes of this thesis work.

(1) Red-light driven photocatalytic hydrogen evolution using polyoxometalates.

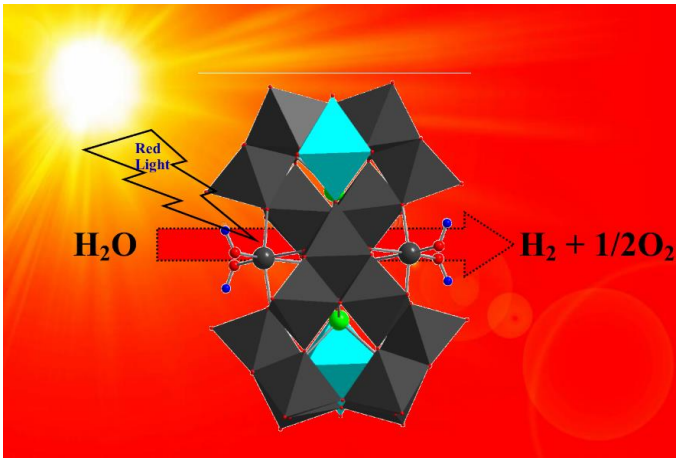

Figure 1. The representation of the red-light driven photocatalytic water splitting reaction using polyoxometalate molecular catalyst.

As we have seen in Chapters **2** and **3**, presence of redox-active 3*d*- metal ions, such as, Mn^{2+}, Co^{2+}, Cu^{2+} and W^{6+} in the POM based molecular compounds can make them potential photocatalysts for red-light driven photocatalytic water-splitting reaction. Thus, these materials

can be employed for the red-light driven photocatalytic water splitting reaction for solar fuel production, and this work is under progress in our laboratory and will completed in near future **(Figure 1)**.

(2) Fabrication of proton exchange membrane (PEM) using proton-rich polyoxometalates for fuel cell application

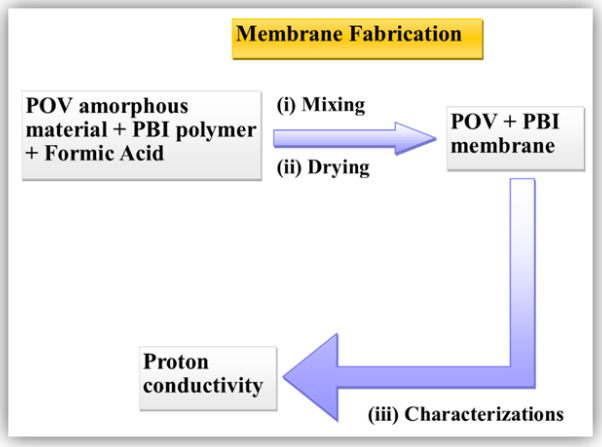

Figure 2. A schematic representation of the PBI supported membrane fabrication using POV amorphous material.

Polyoxometalates can be potential candidates for the development of proton exchnage membranes (PEMs) for fuel cell application because of their proton rich surface and can perform proton transportation through the surface oxo-groups. But their direct application in fuel cell being limited due to their high ionic nature. To overcome these drawbacks, it is required to dope these materials into the polymers (e.g. polybenzimidazole (PBI)) for the preparation of membranes. In this direction, *i.e.*, membrane fabrication work is under progress using polyoxovanadate (POV) amorphous material obtained from gas-solid interface reaction (**Chapter 5**). The prepared membrane is expected to be more stable and efficient for its direct application in real-life fuel cells **(Figure 2)**.

(3) Fabrication of lithium-ion cell using lithium-containing polyoxometalates

Rechargeable lithium-ion batteries are promising candidates to store high-density energy for various applications (*e.g.*, portable electronic devices, electric vehicles and grid balancing). Among cathodic materials, polyoxometalates (POMs) are considered as potential candidates to develop the high electrical energy storage materials due to their versatile redox properties and multi-electrons storage capacity without structural alterations. These properties largely motivate us to research for efficient and high energy storage cathode materials based on polyoxometalates. In this regard, here, lithium-ion coupled POM (like **LiCu-POM**, **chapter 4**) material has drawn our immense attention to fabricate the POM–based cathodic batteries **(Figure 3)**.

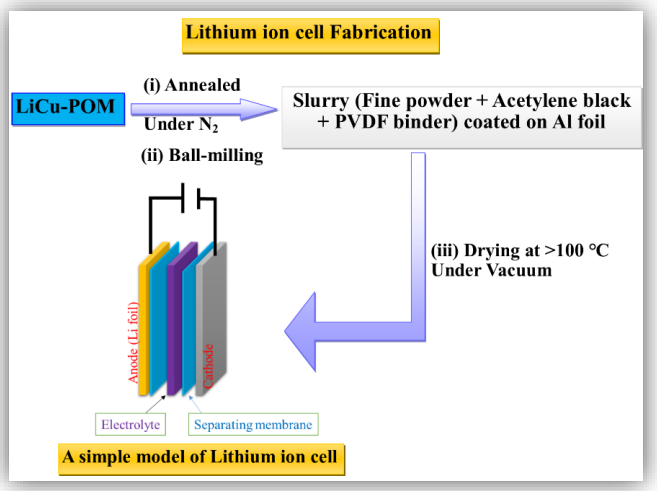

Figure 3. A schematic representation of the Lithium-ion cell fabrication using LiCu-POM material.

Appendix

Appendix 2(i). Details of bond distances and angles of POM-CoW(OH)$_2$

Bond distances (Å) and angles (°) of POM-CoW(OH)$_2$

Bi(1)-O(10)	2.131(15)	Co(1)-O(18)#1	2.165(13)
Bi(1)-O(1)	2.156(9)	Co(1)-O(18)	2.165(13)
Bi(1)-O(1)#1	2.156(9)	Co(1)-O(12)#3	2.259(17)
W(1)-O(2)	1.714(12)	Na(1)-O(23)	2.91(5)
W(1)-O(4)	1.886(12)	Na(1)-O(19)	2.95(3)
W(1)-O(6)	1.899(12)	Na(2)-O(16)	2.81(2)
W(1)-O(3)	1.914(4)	Na(2)-O(20)#4	2.86(2)
W(1)-O(5)	1.957(13)	Na(2)-O(21)#5	2.87(4)
W(1)-O(1)	2.289(10)	Na(2)-O(18)#5	2.94(2)
W(2)-O(7)	1.720(12)		
W(2)-O(11)	1.861(11)	O(10)-Bi(1)-O(1)	88.2(4)
W(2)-O(9)	1.895(11)	O(10)-Bi(1)-O(1)#1	88.2(4)
W(2)-O(8)	1.943(8)	O(1)-Bi(1)-O(1)#1	85.1(5)
W(2)-O(4)	1.981(12)	O(2)-W(1)-O(4)	101.8(6)
W(2)-O(10)	2.302(10)	O(2)-W(1)-O(6)	101.8(6)
W(3)-O(12)	1.747(16)	O(4)-W(1)-O(6)	156.1(5)
W(3)-O(13)	1.780(10)	O(2)-W(1)-O(3)	98.2(7)
W(3)-O(13)#1	1.780(10)	O(4)-W(1)-O(3)	89.6(7)
W(3)-O(11)	2.058(11)	O(6)-W(1)-O(3)	91.0(6)
W(3)-O(11)#1	2.058(11)	O(2)-W(1)-O(5)	98.3(6)
W(3)-O(10)	2.212(15)	O(4)-W(1)-O(5)	86.2(6)
W(4)-O(14)	1.715(13)	O(6)-W(1)-O(5)	86.5(5)
W(4)-O(15)	1.868(12)	O(3)-W(1)-O(5)	163.4(6)
W(4)-O(16)	1.918(13)	O(2)-W(1)-O(1)	171.6(6)
W(4)-O(9)	1.954(11)	O(4)-W(1)-O(1)	83.5(4)
W(4)-O(5)	1.963(12)	O(6)-W(1)-O(1)	72.6(4)
W(4)-O(1)	2.236(10)	O(3)-W(1)-O(1)	88.2(6)
W(5)-O(17)	1.707(12)	O(5)-W(1)-O(1)	75.4(4)
W(5)-O(18)	1.791(13)	O(7)-W(2)-O(11)	99.6(6)
W(5)-O(19)	1.928(5)	O(7)-W(2)-O(9)	101.1(7)
W(5)-O(16)	1.993(13)	O(11)-W(2)-O(9)	93.8(5)
W(5)-O(6)	2.027(13)	O(7)-W(2)-O(8)	97.7(7)
W(5)-O(1)	2.191(11)	O(11)-W(2)-O(8)	90.4(6)
W(6)-O(20)#2	1.837(16)	O(9)-W(2)-O(8)	159.8(5)
W(6)-O(20)	1.837(16)	O(7)-W(2)-O(4)	100.9(6)
W(6)-O(15)	1.996(11)	O(11)-W(2)-O(4)	159.3(5)
W(6)-O(15)#2	1.996(11)	O(9)-W(2)-O(4)	85.0(5)
W(6)-O(13)#3	2.121(10)	O(8)-W(2)-O(4)	84.2(6)
W(6)-O(13)#1	2.121(11)	O(7)-W(2)-O(10)	170.0(6)
Co(1)-O(22)	1.97(5)	O(11)-W(2)-O(10)	73.9(5)
Co(1)-O(21)#1	2.13(4)	O(9)-W(2)-O(10)	87.1(4)
Co(1)-O(21)	2.13(4)	O(8)-W(2)-O(10)	75.1(5)

O(4)-W(2)-O(10)	85.4(5)
O(12)-W(3)-O(13)	103.7(6)
O(12)-W(3)-O(13)#1	103.7(6)
O(13)-W(3)-O(13)#1	96.1(8)
O(12)-W(3)-O(11)	94.1(6)
O(13)-W(3)-O(11)	160.2(5)
O(13)#1-W(3)-O(11)	87.9(5)
O(12)-W(3)-O(11)#1	94.1(6)
O(13)-W(3)-O(11)#1	87.9(5)
O(13)#1-W(3)-O(11)#1	160.2(5)
O(11)-W(3)-O(11)#1	82.1(7)
O(12)-W(3)-O(10)	162.0(8)
O(13)-W(3)-O(10)	88.2(4)
O(13)#1-W(3)-O(10)	88.2(4)
O(11)-W(3)-O(10)	72.5(4)
O(11)#1-W(3)-O(10)	72.5(4)
O(14)-W(4)-O(15)	103.3(6)
O(14)-W(4)-O(16)	98.9(6)
O(15)-W(4)-O(16)	93.7(5)
O(14)-W(4)-O(9)	100.4(6)
O(15)-W(4)-O(9)	87.4(5)
O(16)-W(4)-O(9)	159.9(5)
O(14)-W(4)-O(5)	99.2(6)
O(15)-W(4)-O(5)	156.9(5)
O(16)-W(4)-O(5)	87.9(6)
O(9)-W(4)-O(5)	83.4(5)
O(14)-W(4)-O(1)	172.1(5)
O(15)-W(4)-O(1)	81.7(4)
O(16)-W(4)-O(1)	74.5(5)
O(9)-W(4)-O(1)	85.9(4)
O(5)-W(4)-O(1)	76.5(4)
O(17)-W(5)-O(18)	104.6(7)
O(17)-W(5)-O(19)	101.7(7)
O(18)-W(5)-O(19)	91.5(6)
O(17)-W(5)-O(16)	95.9(6)
O(18)-W(5)-O(16)	90.0(6)
O(19)-W(5)-O(16)	161.3(6)
O(17)-W(5)-O(6)	94.2(6)
O(18)-W(5)-O(6)	161.2(5)
O(19)-W(5)-O(6)	85.0(6)
O(16)-W(5)-O(6)	87.6(5)
O(17)-W(5)-O(1)	163.5(6)
O(18)-W(5)-O(1)	88.8(5)
O(19)-W(5)-O(1)	87.2(6)
O(16)-W(5)-O(1)	74.2(5)
O(6)-W(5)-O(1)	72.6(4)
O(20)#2-W(6)-O(20)	99.9(11)
O(20)#2-W(6)-O(15)	92.7(5)
O(20)-W(6)-O(15)	95.4(5)
O(20)#2-W(6)-O(15)#2	95.4(5)
O(20)-W(6)-O(15)#2	92.7(5)
O(15)-W(6)-O(15)#21	67.3(7)
O(20)#2-W(6)-O(13)#3	90.3(6)
O(20)-W(6)-O(13)#31	69.8(6)
O(15)-W(6)-O(13)#3	84.2(5)
O(15)#2-W(6)-O(13)#3	86.0(5)
O(20)#2-W(6)-O(13)#1	169.8(6)
O(20)-W(6)-O(13)#1	90.3(6)
O(15)-W(6)-O(13)#1	86.0(5)
O(15)#2-W(6)-O(13)#1	84.2(5)
O(13)#3-W(6)-O(13)#1	79.5(7)
O(22)-Co(1)-O(21)#1	93.8(13)
O(22)-Co(1)-O(21)	93.8(13)
O(21)#1-Co(1)-O(21)	91.4(18)
O(22)-Co(1)-O(18)#1	95.6(13)
O(21)#1-Co(1)-O(18)#1	94.5(10)
O(21)-Co(1)-O(18)#1	168.5(10)
O(22)-Co(1)-O(18)	95.6(13)
O(21)#1-Co(1)-O(18)	168.5(10)
O(21)-Co(1)-O(18)	94.5(10)
O(18)#1-Co(1)-O(18)	78.0(7)
O(22)-Co(1)-O(12)#3	178.0(16)
O(21)#1-Co(1)-O(12)#3	84.8(9)
O(21)-Co(1)-O(12)#3	84.8(9)
O(18)#1-Co(1)-O(12)#3	86.0(5)
O(18)-Co(1)-O(12)#3	86.0(5)
O(23)-Na(1)-O(19)	133.8(14)
O(16)-Na(2)-O(20)#4	98.6(7)
O(16)-Na(2)-O(21)#5	102.2(9)
O(20)#4-Na(2)-O(21)#5	153.9(9)
O(16)-Na(2)-O(18)#5	118.4(7)
O(20)#4-Na(2)-O(18)#5	117.1(7)
O(21)#5-Na(2)-O(18)#5	65.7(9)
Bi(1)-O(1)-W(5)	111.0(4)
Bi(1)-O(1)-W(4)	111.7(4)
W(5)-O(1)-W(4)	96.3(4)
Bi(1)-O(1)-W(1)	139.1(5)
W(5)-O(1)-W(1)	97.1(4)
W(4)-O(1)-W(1)	93.3(4)
W(1)-O(3)-W(1)#1	153.1(9)
W(1)-O(4)-W(2)	146.8(7)
W(1)-O(5)-W(4)	114.2(6)
W(1)-O(6)-W(5)	117.6(5)
W(2)-O(8)-W(2)#1	117.4(8)
W(2)-O(9)-W(4)	146.5(6)
Bi(1)-O(10)-W(3)	106.1(6)

Bi(1)-O(10)-W(2)#1	129.1(4)	W(4)-O(16)-Na(2)	117.0(7)
W(3)-O(10)-W(2)#1	95.9(5)	W(5)-O(16)-Na(2)	124.8(6)
Bi(1)-O(10)-W(2)	129.1(4)	W(5)-O(18)-Co(1)	133.6(7)
W(3)-O(10)-W(2)	95.9(5)	W(5)-O(18)-Na(2)#5	124.0(7)
W(2)#1-O(10)-W(2)	92.3(5)	Co(1)-O(18)-Na(2)#5	92.7(6)
W(2)-O(11)-W(3)	117.5(6)	W(5)-O(19)-W(5)#1	143.8(8)
W(3)-O(12)-Co(1)#3	172.1(11)	W(5)-O(19)-Na(1)	107.9(4)
W(3)-O(13)-W(6)#3	177.8(7)	W(5)#1-O(19)-Na(1)	107.9(4)
W(4)-O(15)-W(6)	133.1(6)	Co(1)-O(21)-Na(2)#5	95.4(14)
W(4)-O(16)-W(5)	115.0(6)	W(6)-O(20)-Na(2)#6	105.9(7)

Symmetry transformations used to generate equivalent atoms:

#1 x,-y+2,z #2 -x+2,y,-z+1 #3 -x+2,-y+2,-z+1

#4 x-1/2,-y+3/2,z #5 -x+3/2,-y+3/2,-z+1 #6 x+1/2,-y+3/2,z

Appendix 2(ii). Bond valence sum (BVS) calculations for compounds (POM-CoW(OH)$_2$, Him@POM-MnW(OH)$_2$ and BWCN)

```
Bond valence calculation. Numbers in brackets after atom symbols are at. no.,
r and c - see O"Keeffe and Brese, J.A.C.S. 1991, 113, 3226

......O1 of W-OH for [POM-CoW(OH)2]

  O   ( 8,   .63, 3.15)                          Rij    Dij    Vij
                      -W   (74, 1.38, 1.40) 1.93   1.84   1.29

  Bond valence sum for O    1.29

......O2 of W-OH for [POM-CoW(OH)2]

  O   ( 8,   .63, 3.15)                          Rij    Dij    Vij
                      -W   (74, 1.38, 1.40) 1.93   1.84   1.29

  Bond valence sum for O    1.29

......O1 of W-OH for [BWCN]
 O   ( 8,   .63, 3.15)                         Rij    Dij    Vij
                      -W   (74, 1.38, 1.40) 1.93   1.85   1.26
 Bond valence sum for O    1.26

......O2 of W-OH for [BWCN]
 O   ( 8,   .63, 3.15)                         Rij    Dij    Vij
                      -W   (74, 1.38, 1.40) 1.93   1.89   1.11
  Bond valence sum for O    1.11

......O1 of W-OH for [HIm@POM-MnW(OH)2]
```

```
  O   ( 8,   .63, 3.15)                          Rij    Dij    Vij
                      -W   (74, 1.38, 1.40) 1.93   1.86   1.23

  Bond valence sum for O   1.23

......O2 of W-OH for [HIm@POM-MnW(OH)2]

  O   ( 8,   .63, 3.15)                          Rij    Dij    Vij
                      -W   (74, 1.38, 1.40) 1.93   1.84   1.30

 Bond valence sum for O   1.30
```

Appendix 2*(iii)*. Elemental analysis report

PBMDIDKBKGICIC
LAOBMHLF
PNBEAMJBBKBFID
IHDBLBFF
PFLIJBAPKEIFNC
BONIOHCF

Issued to:
Prof Samar K.Das
School Of Chemistry
University of Hyderabad, Gachibowli,
Hyderabad-500046
Kind Attn.:Dr.Sathish Kumar.K

Report No. :LL/DR/19-20/001238
Issue Date : 23/10/2019
Customer Ref.: TRF
Ref.Date : 01/10/2019

Sample Particulars : **[CoW(OH)$_2$]**

Qty. Received : 100mg X 1 No Vial

Test Parameters : Tungsten as W,Sodium as Na,Cobalt as Co,Bismuth as Bi

Date of Receipt of Sample : 01/10/2019 **Date of Starting of Analysis** : 22/10/2019
Date of completion of analysis : 23/10/2019 *SAMPLE TESTED AS RECEIVED*

TEST RESULTS

S.No.	Parameters	UOM	Results
1	Tungsten as W	% by mass	62.89
2	Sodium as Na	% by mass	2.17
3	Cobalt as Co	% by mass	1.96
4	Bismuth as Bi	% by mass	7.25

Instrument Used: ICP-OES Varian 720-ES

NOTE : This report and results relate only to the sample / items tested.

Page No. 1/1

Srinivasu.G
Authorized Signatory

Appendix Figure 2. Elemental analysis report of POM-CoW(OH)$_2$ compound.

Appendix 3(i). Reported Cu-wheel substituted sandwich type tungstobismuthates.

Sandwich Polyoxometalate	Copper Motif	No. of Coppers	HER Studies	Ref.
$[\{H_3O\}_4\{Na_6(H_2O)_{22}\}][\{(Cu^{I}_{0.25}Cu^{I}_{0.75})(H_2O)_3\}_2\{Cu^{II}(H_2O)\}_3\{B\text{-}\alpha\text{-}Bi^{III}W^{VI}_9O_{33}\}_2]\cdot 7H_2O$ (**NaCu-POM**)	**$[\{(Cu^{I}_{0.25}Cu^{I}_{0.75})(H_2O)_3\}_2\{Cu^{II}(H_2O)\}_3]$**	**$\{Cu\}_5$**	Electrochemical	**This work**
$Li_4[\{NH_4\}_2\{H_3O\}_3\{Li(H_2O)_5\}][\{Cu^{II}(SH)\}\{(Cu^{II}Cu^{I}_{1.5})(B\text{-}\alpha\text{-}Bi^{III}W^{VI}_9O_{33})\}_2]\cdot 9H_2O$ (**LiCu-POM**)	**$[\{Cu^{I}\}_3\{Cu^{II}(SH)\}\{Cu^{II}(O{=}W)\}_2]$**	**$\{Cu\}_6$**	Electrochemical	**This work**
• $K_{6.56}Cu_{0.43}H_{2.20}[(Cu_3Cl)(K_{2.68}Cu_{0.38}(H_2O)_3(B\text{-}\alpha\text{-}BiW_9O_{33})_2]\cdot 13H_2O$ • $Na_6Rb_6[Cu_3(H_2O)_3(B\text{-}\beta\text{-}BiW_9O_{33})_2]\cdot 21H_2O$	$[(Cu^{II}_3Cl)(K_{2.68}Cu^{II}_{0.38}(H_2O)_3]$ $[Cu^{II}_3(H_2O)_3]$	**$\{Cu\}_4$** **$\{Cu\}_3$**	Photochemical	1
$Na_{12}[Cu_3(H_2O)_3(B\text{-}\alpha\text{-}BiW_9O_{33})_2]\cdot 47H_2O$	$[Cu^{II}_3(H_2O)_3]$	**$\{Cu\}_3$**		2
$Na_{12}[Cu_3(H_2O)_3(B\text{-}\alpha\text{-}BiW_9O_{33})_2]$	$[Cu^{II}_3(H_2O)_3]$	**$\{Cu\}_3$**		3
• $Na_{12}[Cu_3(H_2O)_3(B\text{-}\alpha\text{-}BiW_9O_{33})_2]\cdot 29H_2O$ • $Na_{10}[Cu_4(H_2O)_2(B\text{-}\alpha\text{-}BiW_9O_{33})_2]\cdot 43H_2O$	$[Cu^{II}_3(H_2O)_3\}]$ $[Cu^{II}_4(H_2O)_2]$	**$\{Cu\}_3$** **$\{Cu\}_4$**		4
$2D\text{-}Na_5(TEOA\text{-}H)_4[(Cu(H_2O))_3(B\text{-}\alpha\text{-}BiW_9O_{33})_2]$	$[Cu_3(H_2O)_3]$	**$\{Cu\}_3$**		5
$Na_{12}[\{Cu(H_2O)_2\}_3(B\text{-}\alpha\text{-}BiW_9O_{33})_2]\cdot 42H_2O$	$[Cu^{II}_3(H_2O)_3O_3]$	**$\{Cu\}_3$**		6
Other X-atoms				
$NaK_6[Cu_6Cl(SbW_9O_{33})_2]\cdot 14H_2O$	$[Cu^{II}_6Cl]$	**$\{Cu\}_6$**		7
$(n\text{-}BuNH_3)_{12}[(CuCl)_6(B\text{-}\alpha\text{-}AsW_9O_{33})_2]\cdot 6H_2O$	$[Cu^{II}Cl]_6$	**$\{Cu\}_6$**		8
$[n\text{-}BuNH_3]_{12}[(CuCl)_6(B\text{-}\alpha\text{-}SbW_9O_{33})_2]\cdot 6H_2O$	$[Cu^{II}Cl]_6$	**$\{Cu\}_6$**		9
$\{K_7Na\text{-}[Cu_4K_2(H_2O)_6(\alpha\text{-}AsW_9O_{33})_2]\text{`}5.5H_2O\}n$	$[Cu^{II}_4K_2(H_2O)_6]$	**$\{Cu\}_4$**		10
$Na_3K_7[Cu_4(H_2O)_2(B\text{-}\alpha\text{-}PW_9O_{34})_2]\cdot 30H_2O$	$[Cu^{II}_4(H_2O)_2]$	**$\{Cu\}_4$**	Photochemical	11
• $[Cu^{I}_6(trz)_6\{PW_{12}O_{40}\}_2]$ (HENU-2) • $[Cu^{I}_3(trz)_3\{PMo_{12}O_{40}\}]$ (HENU-3)	**$[Cu^{I}_6(trz)_6]$** **$[Cu^{I}_3(trz)_3]$**	**$\{Cu\}_6$** **$\{Cu\}_3$**		12
$[Cu_3(H_2O)_3(B\text{-}\alpha\text{-}XW_9O_{33})_2]^{n-}$ (X = As, Sb, Se, Te; n = 10 for Te and Se, 12 for Sb, As)	$[Cu^{II}_3(H_2O)_3]$	**$\{Cu\}_3$**		13
• $2D\text{-}[enH_2]_5[Cu^{II}(en)_2][Cu^{I}_2(WO_2)_2(B\text{-}\beta\text{-}SbW_9O_{33})_2]\cdot 16H_2O$ • $2D\text{-}[enH_2]_5[Cu^{II}(en)_2][Cu^{I}_2(WO_2)_2(B\text{-}\beta\text{-}BiW_9O_{33})_2]\cdot 22H_2O$	**$[Cu^{I}_2(H_2O)_2W_2O_4]$** **$[Cu^{I}_2(H_2O)_2W_2O_4]$**	**$\{Cu\}_2$** **$\{Cu\}_2$**		14
$Na_6H_4[Bi_2Cu_2W_{20}O_{70}(H_2O)_6]\cdot 36H_2O$	$[Cu^{II}_2(H_2O)_2W_2O_4]$	**$\{Cu\}_2$**		15
Lithium and higher nuclear copper containing polyoxometalates				
$LiK_{14}Na_9[P_8W_{48}O_{184}Cu_{20}(N_3)_6(OH)_{18}]\cdot 60H_2O$	$\{Cu^{II}_5(OH)_4\}\{Cu^{II}_5(OH)_2(\mu\text{-}1,1,3,3\text{-}N_3)\}_2^{26+}$	**$\{Cu\}_{20}$**		16
$K_{12}Li_{13}[Cu_{20}X(OH)_{24}(H2O)_{12}(P_8W_{48}O_{184})]\cdot 22H_2O$ (X = Cl, Br, I)	$[Cu^{II}_{20}X(OH)_{24}(H2O)_{12}]$	**$\{Cu\}_{20}$**		17, 18
$[Cu_{15}O_2(OH)_{10}Cl(A\text{-}\alpha\text{-}SiW_9O_{34})_4]^{25-}$	$[Cu^{II}_{15}O_2(OH)_{10}Cl]$	**$\{Cu\}_{15}$**	Electrocatalytic CO_2 reduction	19
$Li_6[\alpha\text{-}P_2W_{18}O_{62}]\cdot 28H_2O$	---	---		20

Appendix 3(ii). Details of bond distances and angles of NaCu-POM and LiCu-POM compounds

Bond lengths [Å] and angles [°] for NaCu-POM

O(25)-Bi(2)	2.105(8)	O(37)-W(6)#1	1.905(8)
O(25)-W(9)	2.239(8)	O(37)-W(10)	1.928(8)
O(25)-W(10)	2.246(8)	O(27)-W(7)	1.897(8)
O(25)-W(8)	2.273(8)	O(27)-W(6)	1.996(9)
O(24)-Bi(2)	2.103(10)	O(26)-W(6)	1.969(6)
O(24)-W(6)	2.237(7)	O(26)-W(6)#1	1.969(6)
O(24)-W(6)#1	2.237(7)	O(21)-W(6)	1.811(8)
O(24)-W(7)	2.295(11)	O(21)-Cu(1)	1.959(9)
O(34)-W(9)	1.736(9)	O(21)-Cu(2)	2.395(9)
O(31)-W(8)	1.715(9)	O(1)-Bi(1)	2.101(11)
O(41)-W(10)	1.738(8)	O(1)-W(1)	2.244(7)
O(28)-W(7)	1.727(13)	O(1)-W(1)#1	2.244(7)
O(23)-W(6)	1.722(8)	O(1)-W(2)	2.271(11)
O(38)-W(9)	1.809(9)	O(2)-Bi(1)	2.102(7)
O(38)-Cu(4)	1.951(8)	O(2)-W(4)	2.243(8)
O(38)-Cu(3)	2.422(9)	O(2)-W(5)	2.260(8)
O(36)-W(9)#1	1.923(4)	O(2)-W(3)	2.263(8)
O(36)-W(9)	1.924(4)	O(3)-W(1)	1.718(8)
O(35)-W(10)	1.949(8)	O(7)-W(2)	1.735(12)
O(35)-W(9)	1.960(8)	O(9)-W(3)	1.725(8)
O(32)-W(8)	1.914(8)	O(17)-W(5)	1.818(8)
O(32)-W(9)	1.995(9)	O(17)-Cu(1)	1.955(8)
O(30)-W(8)	1.919(3)	O(17)-Cu(3)#1	2.429(8)
O(30)-W(8)#1	1.919(3)	O(16)-W(5)	1.735(8)
O(33)-W(8)	1.912(8)	O(13)-W(4)	1.739(8)
O(33)-W(10)	1.979(8)	O(19)-W(1)	1.824(8)
O(29)-W(7)	1.903(8)	O(19)-Cu(1)#1	1.935(8)
O(29)-W(8)	1.921(8)	O(19)-Cu(2)	2.402(9)
O(39)-W(10)	1.810(8)	O(4)-W(1)	1.918(8)
O(39)-Cu(1)#1	1.947(8)	O(4)-W(5)#1	1.931(8)
O(39)-Cu(3)	2.436(8)	O(6)-W(2)	1.902(8)

O(6)-W(1)	1.994(8)	O(52)-Na(3)	2.416(11)
O(5)-W(1)	1.969(6)	O(53)-Na(3)#3	2.663(12)
O(5)-W(1)#1	1.969(6)	O(53)-Na(3)	2.663(12)
O(8)-W(2)	1.902(8)	O(54)-Na(3)	2.443(11)
O(8)-W(3)#1	1.923(8)	O(55)-Na(3)	2.464(10)
O(11)-W(3)	1.920(3)	O(55)-Na(3)#3	2.464(10)
O(11)-W(3)#1	1.920(3)	Na(1)-Na(1)#2	3.540(12)
O(10)-W(3)	1.891(8)	Na(1)-Na(2)	3.598(8)
O(10)-W(4)	2.011(8)	Na(2)-O(48)	2.421(18)
O(12)-W(3)	1.916(8)	Na(2)-Na(3)	3.541(8)
O(12)-W(5)	1.991(9)	Na(3)-Na(3)#3	3.799(11)
O(15)-W(4)	1.951(8)		
O(15)-W(5)	1.960(8)	Bi(2)-O(25)-W(9)	111.6(3)
O(14)-W(4)	1.923(4)	Bi(2)-O(25)-W(10)	110.6(3)
O(14)-W(4)#1	1.923(4)	W(9)-O(25)-W(10)	95.5(3)
O(18)-W(4)	1.804(8)	Bi(2)-O(25)-W(8)	139.7(4)
O(18)-Cu(4)	1.947(8)	W(9)-O(25)-W(8)	95.6(3)
O(40)-Cu(3)	2.344(10)	W(10)-O(25)-W(8)	95.1(3)
O(22)-Cu(4)	2.263(16)	Bi(2)-O(24)-W(6)	111.9(3)
O(20)-Cu(1)	2.183(9)	Bi(2)-O(24)-W(6)#1	111.9(3)
O(43)-Na(1)	2.451(14)	W(6)-O(24)-W(6)#1	95.9(4)
O(42)-Na(1)#2	2.427(16)	Bi(2)-O(24)-W(7)	139.2(5)
O(42)-Na(1)	2.427(16)	W(6)-O(24)-W(7)	94.7(3)
O(44)-Na(1)	2.435(15)	W(6)#1-O(24)-W(7)	94.7(3)
O(45)-Na(1)	2.400(12)	W(9)-O(38)-Cu(4)	143.8(5)
O(45)-Na(1)#2	2.400(12)	W(9)-O(38)-Cu(3)	112.2(4)
O(46)-Na(2)	2.436(11)	Cu(4)-O(38)-Cu(3)	100.3(4)
O(46)-Na(1)	2.447(12)	W(9)#1-O(36)-W(9)	146.3(8)
O(47)-Na(2)	2.425(11)	W(10)-O(35)-W(9)	116.3(4)
O(47)-Na(1)	2.470(12)	W(8)-O(32)-W(9)	117.5(4)
O(50)-Na(2)	2.420(12)	W(8)-O(30)-W(8)#1	151.1(7)
O(49)-Na(3)	2.367(11)	W(8)-O(33)-W(10)	118.0(4)
O(49)-Na(2)	2.473(12)	W(7)-O(29)-W(8)	153.3(5)
O(51)-Na(2)	2.359(11)	W(10)-O(39)-Cu(1)#1	144.1(5)
O(51)-Na(3)	2.465(11)	W(10)-O(39)-Cu(3)	111.3(3)

Cu(1)#1-O(39)-Cu(3)	100.8(3)	Na(1)#2-O(42)-Na(1)	93.6(8)
W(6)#1-O(37)-W(10)	148.6(5)	Na(1)-O(45)-Na(1)#2	95.0(6)
W(7)-O(27)-W(6)	117.7(4)	Na(2)-O(46)-Na(1)	94.9(4)
W(6)-O(26)-W(6)#1	115.0(5)	Na(2)-O(47)-Na(1)	94.6(4)
W(6)-O(21)-Cu(1)	143.0(5)	Na(3)-O(49)-Na(2)	94.0(4)
W(6)-O(21)-Cu(2)	114.3(4)	Na(2)-O(51)-Na(3)	94.4(4)
Cu(1)-O(21)-Cu(2)	100.5(3)	Na(3)#3-O(53)-Na(3)	91.0(5)
Bi(1)-O(1)-W(1)	112.1(4)	Na(3)-O(55)-Na(3)#3	100.9(5)
Bi(1)-O(1)-W(1)#1	112.1(4)	O(45)-Na(1)-O(42)	85.7(5)
W(1)-O(1)-W(1)#1	95.8(4)	O(45)-Na(1)-O(44)	174.9(5)
Bi(1)-O(1)-W(2)	138.1(5)	O(42)-Na(1)-O(44)	92.3(5)
W(1)-O(1)-W(2)	95.2(3)	O(45)-Na(1)-O(46)	95.4(5)
W(1)#1-O(1)-W(2)	95.2(3)	O(42)-Na(1)-O(46)	168.2(4)
Bi(1)-O(2)-W(4)	111.5(3)	O(44)-Na(1)-O(46)	87.5(5)
Bi(1)-O(2)-W(5)	109.6(3)	O(45)-Na(1)-O(43)	88.6(4)
W(4)-O(2)-W(5)	95.0(3)	O(42)-Na(1)-O(43)	82.5(3)
Bi(1)-O(2)-W(3)	141.0(4)	O(44)-Na(1)-O(43)	95.8(6)
W(4)-O(2)-W(3)	95.1(3)	O(46)-Na(1)-O(43)	85.8(4)
W(5)-O(2)-W(3)	95.3(3)	O(45)-Na(1)-O(47)	94.1(4)
W(5)-O(17)-Cu(1)	141.5(4)	O(42)-Na(1)-O(47)	107.3(3)
W(5)-O(17)-Cu(3)#1	111.8(3)	O(44)-Na(1)-O(47)	81.9(5)
Cu(1)-O(17)-Cu(3)#1	100.8(3)	O(46)-Na(1)-O(47)	84.4(4)
W(1)-O(19)-Cu(1)#1	143.1(5)	O(43)-Na(1)-O(47)	170.0(5)
W(1)-O(19)-Cu(2)	112.8(4)	O(45)-Na(1)-Na(1)#2	42.5(3)
Cu(1)#1-O(19)-Cu(2)	101.0(4)	O(42)-Na(1)-Na(1)#2	43.2(4)
W(1)-O(4)-W(5)#1	147.0(5)	O(44)-Na(1)-Na(1)#2	135.3(4)
W(2)-O(6)-W(1)	117.6(4)	O(46)-Na(1)-Na(1)#2	136.7(3)
W(1)-O(5)-W(1)#1	115.5(5)	O(43)-Na(1)-Na(1)#2	83.9(4)
W(2)-O(8)-W(3)#1	151.8(5)	O(47)-Na(1)-Na(1)#2	104.5(4)
W(3)-O(11)-W(3)#1	151.4(7)	O(45)-Na(1)-Na(2)	99.8(3)
W(3)-O(10)-W(4)	116.8(4)	O(42)-Na(1)-Na(2)	149.0(3)
W(3)-O(12)-W(5)	117.6(4)	O(44)-Na(1)-Na(2)	79.5(4)
W(4)-O(15)-W(5)	116.2(4)	O(46)-Na(1)-Na(2)	42.4(3)
W(4)-O(14)-W(4)#1	144.6(6)	O(43)-Na(1)-Na(2)	127.8(4)
W(4)-O(18)-Cu(4)	145.0(5)	O(47)-Na(1)-Na(2)	42.2(3)

Na(1)#2-Na(1)-Na(2)	134.2(2)	O(49)-Na(3)-O(51)	85.6(4)
O(51)-Na(2)-O(50)	81.5(4)	O(52)-Na(3)-O(51)	84.3(3)
O(51)-Na(2)-O(48)	104.9(5)	O(54)-Na(3)-O(51)	94.7(4)
O(50)-Na(2)-O(48)	97.1(7)	O(55)-Na(3)-O(51)	178.1(4)
O(51)-Na(2)-O(47)	86.1(4)	O(49)-Na(3)-O(53)	88.1(4)
O(50)-Na(2)-O(47)	158.6(5)	O(52)-Na(3)-O(53)	169.7(5)
O(48)-Na(2)-O(47)	102.9(7)	O(54)-Na(3)-O(53)	93.7(4)
O(51)-Na(2)-O(46)	171.6(4)	O(55)-Na(3)-O(53)	84.0(4)
O(50)-Na(2)-O(46)	106.2(4)	O(51)-Na(3)-O(53)	94.2(4)
O(48)-Na(2)-O(46)	78.0(6)	O(49)-Na(3)-Na(2)	44.2(3)
O(47)-Na(2)-O(46)	85.6(4)	O(52)-Na(3)-Na(2)	83.5(3)
O(51)-Na(2)-O(49)	85.6(4)	O(54)-Na(3)-Na(2)	136.2(3)
O(50)-Na(2)-O(49)	81.8(4)	O(55)-Na(3)-Na(2)	138.3(4)
O(48)-Na(2)-O(49)	169.2(5)	O(51)-Na(3)-Na(2)	41.6(2)
O(47)-Na(2)-O(49)	80.0(4)	O(53)-Na(3)-Na(2)	88.6(3)
O(46)-Na(2)-O(49)	92.0(4)	O(49)-Na(3)-Na(3)#3	94.3(3)
O(51)-Na(2)-Na(3)	44.0(3)	O(52)-Na(3)-Na(3)#3	136.8(3)
O(50)-Na(2)-Na(3)	75.5(3)	O(54)-Na(3)-Na(3)#3	86.7(3)
O(48)-Na(2)-Na(3)	148.3(5)	O(55)-Na(3)-Na(3)#3	39.6(3)
O(47)-Na(2)-Na(3)	83.4(3)	O(51)-Na(3)-Na(3)#3	138.6(2)
O(46)-Na(2)-Na(3)	133.7(4)	O(53)-Na(3)-Na(3)#3	44.5(3)
O(49)-Na(2)-Na(3)	41.8(3)	Na(2)-Na(3)-Na(3)#3	122.45(13)
O(51)-Na(2)-Na(1)	129.1(3)	O(18)#1-Cu(4)-O(18)	86.7(5)
O(50)-Na(2)-Na(1)	147.0(3)	O(18)#1-Cu(4)-O(38)	90.6(3)
O(48)-Na(2)-Na(1)	87.2(6)	O(18)-Cu(4)-O(38)	163.3(4)
O(47)-Na(2)-Na(1)	43.2(3)	O(18)#1-Cu(4)-O(38)#1	163.3(4)
O(46)-Na(2)-Na(1)	42.7(3)	O(18)-Cu(4)-O(38)#1	90.6(3)
O(49)-Na(2)-Na(1)	88.0(3)	O(38)-Cu(4)-O(38)#1	87.2(5)
Na(3)-Na(2)-Na(1)	116.0(2)	O(18)#1-Cu(4)-O(22)	101.5(5)
O(49)-Na(3)-O(52)	81.7(4)	O(18)-Cu(4)-O(22)	101.5(5)
O(49)-Na(3)-O(54)	178.1(4)	O(38)-Cu(4)-O(22)	95.2(5)
O(52)-Na(3)-O(54)	96.5(4)	O(38)#1-Cu(4)-O(22)	95.2(5)
O(49)-Na(3)-O(55)	94.5(5)	O(19)#1-Cu(1)-O(39)#1	163.5(4)
O(52)-Na(3)-O(55)	97.6(4)	O(19)#1-Cu(1)-O(17)	88.2(3)
O(54)-Na(3)-O(55)	85.3(5)	O(39)#1-Cu(1)-O(17)	89.5(3)

O(19)#1-Cu(1)-O(21)	88.6(3)	O(30)-W(8)-O(25)	86.3(4)
O(39)#1-Cu(1)-O(21)	88.6(3)	O(29)-W(8)-O(25)	86.6(3)
O(17)-Cu(1)-O(21)	162.3(4)	O(41)-W(10)-O(39)	105.3(4)
O(19)#1-Cu(1)-O(20)	97.5(4)	O(41)-W(10)-O(37)	98.5(4)
O(39)#1-Cu(1)-O(20)	99.0(4)	O(39)-W(10)-O(37)	88.8(3)
O(17)-Cu(1)-O(20)	97.6(4)	O(41)-W(10)-O(35)	101.1(4)
O(21)-Cu(1)-O(20)	100.1(4)	O(39)-W(10)-O(35)	90.9(3)
O(34)-W(9)-O(38)	104.3(4)	O(37)-W(10)-O(35)	159.8(3)
O(34)-W(9)-O(36)	100.8(5)	O(41)-W(10)-O(33)	96.6(4)
O(38)-W(9)-O(36)	89.9(5)	O(39)-W(10)-O(33)	158.1(3)
O(34)-W(9)-O(35)	98.3(4)	O(37)-W(10)-O(33)	85.7(3)
O(38)-W(9)-O(35)	90.1(4)	O(35)-W(10)-O(33)	87.2(4)
O(36)-W(9)-O(35)	160.3(4)	O(41)-W(10)-O(25)	168.6(4)
O(34)-W(9)-O(32)	97.4(4)	O(39)-W(10)-O(25)	85.3(3)
O(38)-W(9)-O(32)	158.3(4)	O(37)-W(10)-O(25)	85.9(3)
O(36)-W(9)-O(32)	86.9(5)	O(35)-W(10)-O(25)	73.9(3)
O(35)-W(9)-O(32)	85.9(3)	O(33)-W(10)-O(25)	73.1(3)
O(34)-W(9)-O(25)	167.9(4)	O(28)-W(7)-O(27)	99.6(4)
O(38)-W(9)-O(25)	85.3(3)	O(28)-W(7)-O(27)#1	99.6(4)
O(36)-W(9)-O(25)	86.5(4)	O(27)-W(7)-O(27)#1	89.8(5)
O(35)-W(9)-O(25)	73.9(3)	O(28)-W(7)-O(29)	100.7(4)
O(32)-W(9)-O(25)	73.1(3)	O(27)-W(7)-O(29)	159.6(4)
O(31)-W(8)-O(33)	99.8(4)	O(27)#1-W(7)-O(29)	89.5(4)
O(31)-W(8)-O(32)	99.4(4)	O(28)-W(7)-O(29)#1	100.7(4)
O(33)-W(8)-O(32)	89.6(4)	O(27)-W(7)-O(29)#1	89.5(4)
O(31)-W(8)-O(30)	100.6(5)	O(27)#1-W(7)-O(29)#1	159.6(4)
O(33)-W(8)-O(30)	159.5(4)	O(29)-W(7)-O(29)#1	84.2(5)
O(32)-W(8)-O(30)	89.3(4)	O(28)-W(7)-O(24)	170.7(5)
O(31)-W(8)-O(29)	100.6(4)	O(27)-W(7)-O(24)	74.0(3)
O(33)-W(8)-O(29)	89.0(4)	O(27)#1-W(7)-O(24)	74.0(3)
O(32)-W(8)-O(29)	160.0(4)	O(29)-W(7)-O(24)	86.2(3)
O(30)-W(8)-O(29)	85.2(4)	O(29)#1-W(7)-O(24)	86.2(3)
O(31)-W(8)-O(25)	170.3(4)	O(23)-W(6)-O(21)	104.3(4)
O(33)-W(8)-O(25)	73.7(3)	O(23)-W(6)-O(37)#1	100.1(4)
O(32)-W(8)-O(25)	73.8(3)	O(21)-W(6)-O(37)#1	90.2(4)

O(23)-W(6)-O(26)	99.1(4)	O(6)-W(2)-O(8)#1	161.0(4)
O(21)-W(6)-O(26)	90.8(4)	O(8)-W(2)-O(8)#1	86.1(5)
O(37)#1-W(6)-O(26)	159.8(4)	O(7)-W(2)-O(1)	168.2(5)
O(23)-W(6)-O(27)	96.3(4)	O(6)#1-W(2)-O(1)	74.1(3)
O(21)-W(6)-O(27)	159.4(4)	O(6)-W(2)-O(1)	74.1(3)
O(37)#1-W(6)-O(27)	86.7(3)	O(8)-W(2)-O(1)	87.3(3)
O(26)-W(6)-O(27)	85.2(4)	O(8)#1-W(2)-O(1)	87.3(3)
O(23)-W(6)-O(24)	168.1(4)	O(9)-W(3)-O(10)	99.8(4)
O(21)-W(6)-O(24)	85.9(4)	O(9)-W(3)-O(12)	98.7(4)
O(37)#1-W(6)-O(24)	85.7(3)	O(10)-W(3)-O(12)	90.9(4)
O(26)-W(6)-O(24)	74.3(3)	O(9)-W(3)-O(11)	101.2(5)
O(27)-W(6)-O(24)	73.6(3)	O(10)-W(3)-O(11)	88.9(4)
O(3)-W(1)-O(19)	104.7(4)	O(12)-W(3)-O(11)	159.9(4)
O(3)-W(1)-O(4)	100.7(4)	O(9)-W(3)-O(8)#1	99.9(4)
O(19)-W(1)-O(4)	89.9(4)	O(10)-W(3)-O(8)#1	160.2(3)
O(3)-W(1)-O(5)	98.1(4)	O(12)-W(3)-O(8)#1	87.9(3)
O(19)-W(1)-O(5)	90.2(4)	O(11)-W(3)-O(8)#1	85.5(4)
O(4)-W(1)-O(5)	160.5(4)	O(9)-W(3)-O(2)	170.8(3)
O(3)-W(1)-O(6)	97.4(4)	O(10)-W(3)-O(2)	74.9(3)
O(19)-W(1)-O(6)	157.9(4)	O(12)-W(3)-O(2)	74.2(3)
O(4)-W(1)-O(6)	86.5(3)	O(11)-W(3)-O(2)	86.3(4)
O(5)-W(1)-O(6)	86.2(4)	O(8)#1-W(3)-O(2)	85.8(3)
O(3)-W(1)-O(1)	167.9(4)	O(16)-W(5)-O(17)	105.1(4)
O(19)-W(1)-O(1)	85.0(4)	O(16)-W(5)-O(4)#1	100.4(4)
O(4)-W(1)-O(1)	86.4(3)	O(17)-W(5)-O(4)#1	89.7(3)
O(5)-W(1)-O(1)	74.2(3)	O(16)-W(5)-O(15)	97.9(4)
O(6)-W(1)-O(1)	73.1(4)	O(17)-W(5)-O(15)	91.1(3)
O(7)-W(2)-O(6)#1	97.7(4)	O(4)#1-W(5)-O(15)	160.7(3)
O(7)-W(2)-O(6)	97.7(4)	O(16)-W(5)-O(12)	97.9(4)
O(6)#1-W(2)-O(6)	89.2(5)	O(17)-W(5)-O(12)	157.0(3)
O(7)-W(2)-O(8)	101.3(4)	O(4)#1-W(5)-O(12)	85.8(3)
O(6)#1-W(2)-O(8)	161.0(4)	O(15)-W(5)-O(12)	85.9(3)
O(6)-W(2)-O(8)	89.2(3)	O(16)-W(5)-O(2)	167.8(4)
O(7)-W(2)-O(8)#1	101.3(4)	O(17)-W(5)-O(2)	84.3(3)
O(6)#1-W(2)-O(8)#1	89.2(3)	O(4)#1-W(5)-O(2)	87.1(3)

O(15)-W(5)-O(2)	73.8(3)	O(24)-Bi(2)-O(25)	87.3(3)
O(12)-W(5)-O(2)	72.9(3)	O(25)#1-Bi(2)-O(25)	86.2(4)
O(13)-W(4)-O(18)	103.5(4)	O(1)-Bi(1)-O(2)	87.2(3)
O(13)-W(4)-O(14)	99.8(4)	O(1)-Bi(1)-O(2)#1	87.2(3)
O(18)-W(4)-O(14)	90.9(4)	O(2)-Bi(1)-O(2)#1	84.8(4)
O(13)-W(4)-O(15)	99.3(4)	O(21)#1-Cu(2)-O(21)	77.9(4)
O(18)-W(4)-O(15)	91.1(4)	O(21)#1-Cu(2)-O(19)	69.1(3)
O(14)-W(4)-O(15)	159.8(4)	O(21)-Cu(2)-O(19)	115.4(3)
O(13)-W(4)-O(10)	97.6(4)	O(21)#1-Cu(2)-O(19)#1	115.4(3)
O(18)-W(4)-O(10)	159.0(3)	O(21)-Cu(2)-O(19)#1	69.1(3)
O(14)-W(4)-O(10)	84.8(4)	O(19)-Cu(2)-O(19)#1	77.4(4)
O(15)-W(4)-O(10)	86.1(3)	O(40)-Cu(3)-O(38)	137.7(4)
O(13)-W(4)-O(2)	169.0(4)	O(40)-Cu(3)-O(17)#1	93.9(4)
O(18)-W(4)-O(2)	86.0(3)	O(38)-Cu(3)-O(17)#1	112.9(3)
O(14)-W(4)-O(2)	85.6(4)	O(40)-Cu(3)-O(39)	83.9(3)
O(15)-W(4)-O(2)	74.4(3)	O(38)-Cu(3)-O(39)	76.8(3)
O(10)-W(4)-O(2)	73.2(3)	O(17)#1-Cu(3)-O(39)	68.8(3)
O(24)-Bi(2)-O(25)#1	87.3(3)		

Symmetry transformations used to generate equivalent atoms:
#1 x,-y+1,z #2 -x+1,y,-z #3 x,-y+2,z

Bond lengths [Å] and angles [°] for LiCu-POM

Bi(1)-O(2)	2.066(15)	W(2)-O(9)	1.906(13)
Bi(1)-O(1)	2.124(11)	W(2)-O(7)	1.917(11)
Bi(1)-O(1)#1	2.124(11)	W(2)-O(10)	1.921(13)
W(1)-O(3)	1.716(13)	W(2)-O(1)	2.268(12)
W(1)-O(4)	1.826(14)	W(3)-O(12)	1.697(17)
W(1)-O(5)	1.922(5)	W(3)-O(13)	1.908(12)
W(1)-O(6)	1.979(12)	W(3)-O(13)#1	1.908(12)
W(1)-O(7)	1.987(13)	W(3)-O(10)	1.916(14)
W(1)-O(1)	2.245(10)	W(3)-O(10)#1	1.916(14)
W(2)-O(11)	1.725(11)	W(3)-O(2)	2.315(16)
W(2)-O(8)	1.904(4)	W(4)-O(14)	1.728(12)

W(4)-O(16)	1.833(13)	Cu(6)-Cu(7)	1.37(4)
W(4)-O(6)	1.927(11)	Li(1)-Li(1)#7	2.55(19)
W(4)-O(15)	1.938(11)	Li(1)-Li(1)#5	2.55(19)
W(4)-O(9)	2.011(13)	Li(1)-Li(1)#6	2.6(2)
W(4)-O(1)	2.232(12)		
W(5)-O(17)	1.719(12)	O(2)-Bi(1)-O(1)	86.6(4)
W(5)-O(19)	1.881(12)	O(2)-Bi(1)-O(1)#1	86.6(4)
W(5)-O(15)	1.907(12)	O(1)-Bi(1)-O(1)#1	88.0(6)
W(5)-O(18)	1.958(8)	O(3)-W(1)-O(4)	103.5(7)
W(5)-O(13)#1	1.980(13)	O(3)-W(1)-O(5)	101.8(7)
W(5)-O(2)	2.262(10)	O(4)-W(1)-O(5)	89.4(7)
Cu(1)-O(4)#2	1.948(14)	O(3)-W(1)-O(6)	97.9(6)
Cu(1)-O(4)#1	1.948(14)	O(4)-W(1)-O(6)	90.3(6)
Cu(1)-O(4)#3	1.948(14)	O(5)-W(1)-O(6)	159.8(6)
Cu(1)-O(4)	1.948(14)	O(3)-W(1)-O(7)	98.8(6)
Cu(1)-S(1)	2.545(11)	O(4)-W(1)-O(7)	157.7(5)
Cu(2)-O(16)	2.279(13)	O(5)-W(1)-O(7)	86.7(7)
Cu(2)-O(16)#2	2.279(13)	O(6)-W(1)-O(7)	85.9(5)
Cu(2)-O(4)	2.417(15)	O(3)-W(1)-O(1)	167.9(6)
Cu(2)-O(4)#2	2.417(15)	O(4)-W(1)-O(1)	84.7(5)
Cu(3)-O(16)#2	1.938(13)	O(5)-W(1)-O(1)	87.0(6)
Cu(3)-O(16)	1.938(13)	O(6)-W(1)-O(1)	72.9(4)
Cu(3)-O(19)#2	1.939(12)	O(7)-W(1)-O(1)	73.2(4)
Cu(3)-O(19)	1.939(12)	O(11)-W(2)-O(8)	100.3(6)
Cu(3)-O(12)#4	2.307(18)	O(11)-W(2)-O(9)	99.9(5)
O(21)-Li(1)#5	1.50(11)	O(8)-W(2)-O(9)	159.7(6)
O(21)-Li(1)	2.48(12)	O(11)-W(2)-O(7)	97.2(6)
O(21)-Li(1)#6	2.65(12)	O(8)-W(2)-O(7)	88.8(6)
O(20)-Li(1)	2.02(11)	O(9)-W(2)-O(7)	90.9(5)
O(20)-Li(1)#6	2.02(11)	O(11)-W(2)-O(10)	102.3(6)
O(22)-Li(1)	1.58(11)	O(8)-W(2)-O(10)	85.4(7)
O(22)-Li(1)#5	1.58(11)	O(9)-W(2)-O(10)	88.0(6)
O(22)-Li(1)#6	1.58(11)	O(7)-W(2)-O(10)	160.3(6)
O(22)-Li(1)#7	1.58(11)	O(11)-W(2)-O(1)	169.2(5)
O(19)-Cu(6)	2.296(11)	O(8)-W(2)-O(1)	85.9(6)

O(9)-W(2)-O(1)	74.5(5)	O(19)-W(5)-O(15)	89.3(5)
O(7)-W(2)-O(1)	73.9(5)	O(17)-W(5)-O(18)	98.1(6)
O(10)-W(2)-O(1)	86.9(5)	O(19)-W(5)-O(18)	88.9(6)
O(12)-W(3)-O(13)	99.1(5)	O(15)-W(5)-O(18)	160.4(5)
O(12)-W(3)-O(13)#1	99.1(5)	O(17)-W(5)-O(13)#1	99.2(6)
O(13)-W(3)-O(13)#1	88.9(7)	O(19)-W(5)-O(13)#1	157.4(5)
O(12)-W(3)-O(10)	101.4(6)	O(15)-W(5)-O(13)#1	87.3(5)
O(13)-W(3)-O(10)	159.4(5)	O(18)-W(5)-O(13)#1	86.9(6)
O(13)#1-W(3)-O(10)	88.9(6)	O(17)-W(5)-O(2)	169.8(6)
O(12)-W(3)-O(10)#1	101.4(6)	O(19)-W(5)-O(2)	83.6(5)
O(13)-W(3)-O(10)#1	88.9(6)	O(15)-W(5)-O(2)	86.0(5)
O(13)#1-W(3)-O(10)#1	159.4(5)	O(18)-W(5)-O(2)	74.4(5)
O(10)-W(3)-O(10)#1	86.0(9)	O(13)#1-W(5)-O(2)	73.9(5)
O(12)-W(3)-O(2)	170.0(7)	O(4)#2-Cu(1)-O(4)#1	159.1(9)
O(13)-W(3)-O(2)	73.9(4)	O(4)#2-Cu(1)-O(4)#3	88.9(9)
O(13)#1-W(3)-O(2)	73.9(4)	O(4)#1-Cu(1)-O(4)#3	87.3(9)
O(10)-W(3)-O(2)	85.8(5)	O(4)#2-Cu(1)-O(4)	87.3(9)
O(10)#1-W(3)-O(2)	85.8(5)	O(4)#1-Cu(1)-O(4)	88.9(9)
O(14)-W(4)-O(16)	104.9(6)	O(4)#3-Cu(1)-O(4)	159.1(9)
O(14)-W(4)-O(6)	98.9(5)	O(4)#2-Cu(1)-S(1)	100.4(4)
O(16)-W(4)-O(6)	90.8(6)	O(4)#1-Cu(1)-S(1)	100.4(4)
O(14)-W(4)-O(15)	100.7(5)	O(4)#3-Cu(1)-S(1)	100.4(4)
O(16)-W(4)-O(15)	88.8(5)	O(4)-Cu(1)-S(1)	100.4(4)
O(6)-W(4)-O(15)	159.8(5)	O(16)-Cu(2)-O(16)#2	72.4(7)
O(14)-W(4)-O(9)	94.7(5)	O(16)-Cu(2)-O(4)	80.4(5)
O(16)-W(4)-O(9)	160.4(6)	O(16)#2-Cu(2)-O(4)	119.4(5)
O(6)-W(4)-O(9)	87.4(5)	O(16)-Cu(2)-O(4)#2	119.4(5)
O(15)-W(4)-O(9)	86.3(5)	O(16)#2-Cu(2)-O(4)#2	80.4(5)
O(14)-W(4)-O(1)	166.2(5)	O(4)-Cu(2)-O(4)#2	67.6(7)
O(16)-W(4)-O(1)	87.3(5)	O(16)#2-Cu(3)-O(16)	88.0(8)
O(6)-W(4)-O(1)	74.1(5)	O(16)#2-Cu(3)-O(19)#2	89.4(5)
O(15)-W(4)-O(1)	85.7(5)	O(16)-Cu(3)-O(19)#2	161.1(6)
O(9)-W(4)-O(1)	73.4(5)	O(16)#2-Cu(3)-O(19)	161.1(6)
O(17)-W(5)-O(19)	103.4(6)	O(16)-Cu(3)-O(19)	89.4(5)
O(17)-W(5)-O(15)	101.3(6)	O(19)#2-Cu(3)-O(19)	86.9(7)

O(16)#2-Cu(3)-O(12)#4	98.5(5)	Li(1)-O(20)-Li(1)#6	80(7)
O(16)-Cu(3)-O(12)#4	98.5(5)	Li(1)-O(22)-Li(1)#5	108(4)
O(19)#2-Cu(3)-O(12)#4	100.5(5)	Li(1)-O(22)-Li(1)#6	112(8)
O(19)-Cu(3)-O(12)#4	100.5(5)	Li(1)#5-O(22)-Li(1)#6	108(4)
Bi(1)-O(1)-W(4)	112.4(5)	Li(1)-O(22)-Li(1)#7	108(4)
Bi(1)-O(1)-W(1)	110.6(5)	Li(1)#5-O(22)-Li(1)#7	112(8)
W(4)-O(1)-W(1)	95.9(4)	Li(1)#6-O(22)-Li(1)#7	108(4)
Bi(1)-O(1)-W(2)	138.6(6)	W(5)-O(19)-Cu(3)	140.3(7)
W(4)-O(1)-W(2)	95.5(4)	W(5)-O(19)-Cu(6)	115.0(5)
W(1)-O(1)-W(2)	95.4(4)	Cu(3)-O(19)-Cu(6)	100.8(5)
Bi(1)-O(2)-W(5)#1	112.2(5)	Cu(7)-Cu(6)-O(19)#1	119.9(3)
Bi(1)-O(2)-W(5)	112.2(5)	Cu(7)-Cu(6)-O(19)#3	119.9(3)
W(5)#1-O(2)-W(5)	94.7(6)	O(19)#1-Cu(6)-O(19)#3	71.0(6)
Bi(1)-O(2)-W(3)	140.5(8)	Cu(7)-Cu(6)-O(19)#2	119.9(3)
W(5)#1-O(2)-W(3)	93.8(5)	O(19)#1-Cu(6)-O(19)#2	120.2(6)
W(5)-O(2)-W(3)	93.8(5)	O(19)#3-Cu(6)-O(19)#2	80.1(6)
W(1)-O(4)-Cu(1)	140.7(8)	Cu(7)-Cu(6)-O(19)	119.9(3)
W(1)-O(4)-Cu(2)	113.4(6)	O(19)#1-Cu(6)-O(19)	80.1(6)
Cu(1)-O(4)-Cu(2)	102.2(6)	O(19)#3-Cu(6)-O(19)	120.2(6)
W(1)#1-O(5)-W(1)	148.4(10)	O(19)#2-Cu(6)-O(19)	71.0(6)
W(4)-O(6)-W(1)	116.7(6)	O(21)#7-Li(1)-O(22)	90(6)
W(2)-O(7)-W(1)	117.5(6)	O(21)#7-Li(1)-O(20)	171(8)
W(2)-O(8)-W(2)#1	153.8(10)	O(22)-Li(1)-O(20)	84(5)
W(2)-O(9)-W(4)	116.5(6)	O(21)#7-Li(1)-O(21)	100(5)
W(3)-O(10)-W(2)	151.4(8)	O(22)-Li(1)-O(21)	60(4)
W(3)-O(13)-W(5)#1	118.5(6)	O(20)-Li(1)-O(21)	82(4)
W(5)-O(15)-W(4)	149.1(7)	O(21)#7-Li(1)-Li(1)#7	70(6)
W(4)-O(16)-Cu(3)	144.3(8)	O(22)-Li(1)-Li(1)#7	35.9(19)
W(4)-O(16)-Cu(2)	114.8(6)	O(20)-Li(1)-Li(1)#7	101(5)
Cu(3)-O(16)-Cu(2)	99.2(5)	O(21)-Li(1)-Li(1)#7	94(4)
W(5)-O(18)-W(5)#1	116.4(8)	O(21)#7-Li(1)-Li(1)#5	77(6)
W(3)-O(12)-Cu(3)#8	171.3(9)	O(22)-Li(1)-Li(1)#5	35.9(19)
Li(1)#5-O(21)-Li(1)	75(7)	O(20)-Li(1)-Li(1)#5	101(5)
Li(1)#5-O(21)-Li(1)#6	70(6)	O(21)-Li(1)-Li(1)#5	35(3)
Li(1)-O(21)-Li(1)#6	61(5)	Li(1)#7-Li(1)-Li(1)#5	62(5)

O(21)#7-Li(1)-Li(1)#6	124(5)	O(22)-Li(1)-O(21)#6	55(3)
O(22)-Li(1)-Li(1)#6	34(4)	O(20)-Li(1)-O(21)#6	78(4)
O(20)-Li(1)-Li(1)#6	50(3)	O(21)-Li(1)-O(21)#6	114(4)
O(21)-Li(1)-Li(1)#6	63(4)	Li(1)#7-Li(1)-O(21)#6	33(3)
Li(1)#7-Li(1)-Li(1)#6	59(2)	Li(1)#5-Li(1)-O(21)#6	89(3)
Li(1)#5-Li(1)-Li(1)#6	59(2)	Li(1)#6-Li(1)-O(21)#6	56(4)
O(21)#7-Li(1)-O(21)#6	93(5)		

Symmetry transformations used to generate equivalent atoms:

#1 -y+1/2,-x+1/2,z #2 y+1/2,x-1/2,z #3 -x+1,-y,z

#4 -y+1,x,-z+1 #5 y,-x+1,-z #6 -x+1,-y+1,z

#7 -y+1,x,-z #8 y,-x+1,-z+1

Appendix 3(iii). Details of bond valence (BVS) calculation for NaCu-POM and LiCu-POM compounds

Bond valence calculation for NaCu-POM compound

```
Bond valence calculation. Numbers in brackets after atom symbols are
at.no., r and c - see O"Keeffe and Brese, J.A.C.S. 1991, 113, 3226.

......Cu1

  Cu (29,  .87, 1.75)                        Rij   Dij   Vij
                      -O  ( 8,  .63, 3.15) 1.47  1.94   .28
                      -O  ( 8,  .63, 3.15) 1.47  1.95   .27
                      -O  ( 8,  .63, 3.15) 1.47  1.95   .27
                      -O  ( 8,  .63, 3.15) 1.47  1.96   .27
                      -O  ( 8,  .63, 3.15) 1.47  2.18   .14

  Bond valence sum for Cu  1.24

......Cu1a

  Cu (29,  .87, 1.75)                        Rij   Dij   Vij
                      -O  ( 8,  .63, 3.15) 1.47  1.94   .28
                      -O  ( 8,  .63, 3.15) 1.47  1.95   .27
                      -O  ( 8,  .63, 3.15) 1.47  1.95   .27
                      -O  ( 8,  .63, 3.15) 1.47  1.96   .27
                      -O  ( 8,  .63, 3.15) 1.47  2.18   .14
```

```
  Bond valence sum for Cu  1.24

......Cu2

  Cu (29,  .87, 1.75)                          Rij   Dij   Vij
                     -O  ( 8,  .63, 3.15) 1.47  1.95   .27
                     -O  ( 8,  .63, 3.15) 1.47  1.95   .27
                     -O  ( 8,  .63, 3.15) 1.47  1.95   .27
                     -O  ( 8,  .63, 3.15) 1.47  1.95   .27
                     -O  ( 8,  .63, 3.15) 1.47  2.26   .12

  Bond valence sum for Cu  1.21

......Cu3

  Cu (29,  .87, 1.75)                          Rij   Dij   Vij
                     -O  ( 8,  .63, 3.15) 1.47  2.52   .06
                     -O  ( 8,  .63, 3.15) 1.47  2.35   .09
                     -O  ( 8,  .63, 3.15) 1.47  2.46   .07
                     -O  ( 8,  .63, 3.15) 1.47  2.43   .07
                     -O  ( 8,  .63, 3.15) 1.47  2.43   .07
                     -O  ( 8,  .63, 3.15) 1.47  2.42   .08

  Bond valence sum for Cu   .44

......Cu3a

  Cu (29,  .87, 1.75)                          Rij   Dij   Vij
                     -O  ( 8,  .63, 3.15) 1.47  2.52   .06
                     -O  ( 8,  .63, 3.15) 1.47  2.35   .09
                     -O  ( 8,  .63, 3.15) 1.47  2.46   .07
                     -O  ( 8,  .63, 3.15) 1.47  2.43   .07
                     -O  ( 8,  .63, 3.15) 1.47  2.43   .07
                     -O  ( 8,  .63, 3.15) 1.47  2.42   .08

  Bond valence sum for Cu   .44

......Cu4

  Cu (29,  .87, 1.75)                          Rij   Dij   Vij
                     -O  ( 8,  .63, 3.15) 1.47  2.40   .08
                     -O  ( 8,  .63, 3.15) 1.47  2.40   .08
                     -O  ( 8,  .63, 3.15) 1.47  2.39   .08
                     -O  ( 8,  .63, 3.15) 1.47  2.39   .08
                     -O  ( 8,  .63, 3.15) 1.47  2.62   .04
                     -O  ( 8,  .63, 3.15) 1.47  2.62   .04

  Bond valence sum for Cu   .41
```

Bond valence calculation for LiCu-POM compound

```
Bond valence calculation. Numbers in brackets after atom symbols are
at.no., r and c - see O"Keeffe and Brese, J.A.C.S. 1991, 113, 3226.

......Cu1

  Cu (29,  .87, 1.75)                          Rij   Dij   Vij
                      -O  ( 8,  .63, 3.15) 1.47  1.95   .27
                      -O  ( 8,  .63, 3.15) 1.47  1.95   .27
                      -O  ( 8,  .63, 3.15) 1.47  1.95   .27
                      -O  ( 8,  .63, 3.15) 1.47  1.95   .27
                      -S  (16, 1.03, 2.35) 1.89  2.55   .17

  Bond valence sum for Cu  1.26

......Cu2

  Cu (29,  .87, 1.75)                          Rij   Dij   Vij
                      -O  ( 8,  .63, 3.15) 1.47  2.28   .11
                      -O  ( 8,  .63, 3.15) 1.47  2.28   .11
                      -O  ( 8,  .63, 3.15) 1.47  2.42   .08
                      -O  ( 8,  .63, 3.15) 1.47  2.42   .08

  Bond valence sum for Cu   .38

......Cu2a

  Cu (29,  .87, 1.75)                          Rij   Dij   Vij
                      -O  ( 8,  .63, 3.15) 1.47  2.28   .11
                      -O  ( 8,  .63, 3.15) 1.47  2.28   .11
                      -O  ( 8,  .63, 3.15) 1.47  2.42   .08
                      -O  ( 8,  .63, 3.15) 1.47  2.42   .08

  Bond valence sum for Cu   .38

......Cu3

  Cu (29,  .87, 1.75)                          Rij   Dij   Vij
                      -O  ( 8,  .63, 3.15) 1.47  1.94   .28
                      -O  ( 8,  .63, 3.15) 1.47  1.94   .28
                      -O  ( 8,  .63, 3.15) 1.47  1.94   .28
                      -O  ( 8,  .63, 3.15) 1.47  1.94   .28
                      -O  ( 8,  .63, 3.15) 1.47  2.31   .10

  Bond valence sum for Cu  1.23

......Cu3a
```

```
  Cu (29,  .87, 1.75)                          Rij   Dij   Vij
                      -O  ( 8,  .63, 3.15) 1.47  1.94   .28
                      -O  ( 8,  .63, 3.15) 1.47  1.94   .28
                      -O  ( 8,  .63, 3.15) 1.47  1.94   .28
                      -O  ( 8,  .63, 3.15) 1.47  1.94   .28
                      -O  ( 8,  .63, 3.15) 1.47  2.31   .10

  Bond valence sum for Cu  1.23

......Cu4

  Cu (29,  .87, 1.75)                          Rij   Dij   Vij
                      -O  ( 8,  .63, 3.15) 1.47  2.30   .11
                      -O  ( 8,  .63, 3.15) 1.47  2.30   .11
                      -O  ( 8,  .63, 3.15) 1.47  2.30   .11
                      -O  ( 8,  .63, 3.15) 1.47  2.30   .11

  Bond valence sum for Cu   .43

......S

  S  (16, 1.03, 2.35)                          Rij   Dij   Vij
                      -Cu (29,  .87, 1.75) 1.89  2.55   .17

  Bond valence sum for S    .17
```

Appendix 3(iv). Elemental analysis reports for NaCu-POM and LiCu-POM compounds

PBMDIDKBKGIDIC
LBOHKHLF
PNEEAMJEEKEFID
ILOHBKFF
PFLIJBAPKEIFMB
AGPJAGCF

Issued to:
Prof Samar K.Das
School Of Chemistry
University of Hyderabad, Gachibowli,
Hyderabad-500046
Kind Attn.:Dr.Sathish Kumar.K, 9908652965

Report No. : LL/DR/19-20/008408
Issue Date : 05/12/2019
Customer Ref. : TRF
Ref.Date : 28/11/2019

Sample Particulars : **Cu-POM**

Qty. Received : 100mg X 1 No Polythene Cover

Test Parameters : Copper as Cu, Sodium as Na,Tungsten as W,Bismuth as Bi

Date of Receipt of Sample : 28/11/2019
Date of completion of analysis : 02/12/2019
Date of Starting of Analysis : 02/12/2019
SAMPLE TESTED AS RECEIVED

TEST RESULTS

S.No.	Parameters	UOM	Results
1	Copper as Cu	% by mass	6.54
2	Sodium as Na	% by mass	2.03
3	Tungsten as W	% by mass	54.90
4	Bismuth as Bi	% by mass	7.01

Instrument Used: ICP-OES Varian 720-ES

NOTE : This report and results relate only to the sample / items tested.

Srinivasu.G
Authorized Signatory

Page No. 1/1

Appendix Figure 3(a). Elemental analysis report of NaCu-POM compound.

PEMDIDKEKGIDIC
LEOHKHLF
PNEEAMJEEKEFID
ILOHEKFF
PFLIJEAPKEIFME
AGPJAGCF

Issued to:
Prof Samar K.Das
School Of Chemistry
University of Hyderabad, Gachibowli,
Hyderabad-500046
Kind Attn.:Dr.Sathish Kumar.K, 9908652965

Report No. : LL/DR/19-20/001239
Issue Date : 23/10/2019
Customer Ref. : TRF

Ref.Date : 01/10/2019

Sample Particulars : LiCu-POM (Barrel)

Qty. Received : 100mg X 1 No Polythene Cover

Test Parameters : Copper as Cu,Lithium as Li,Tungsten as W,Bismuth as Bi

Date of Receipt of Sample : 01/10/2019
Date of completion of analysis : 23/10/2019

Date of Starting of Analysis : 22/10/2019

SAMPLE TESTED AS RECEIVED

TEST RESULTS

S.No.	Parameters	UOM	Results
1	Copper as Cu	% by mass	7.24
2	Lithium as Li	% by mass	0.71
3	Tungsten as W	% by mass	60.19
4	Bismuth as Bi	% by mass	7.32

Instrument Used: ICP-OES Varian 720-ES

NOTE : This report and results relate only to the sample / items tested.

Srinivasu.G
Authorized Signatory

Page No. 1/1

Appendix Figure 3(b). Elemental analysis report of LiCu-POM compound.

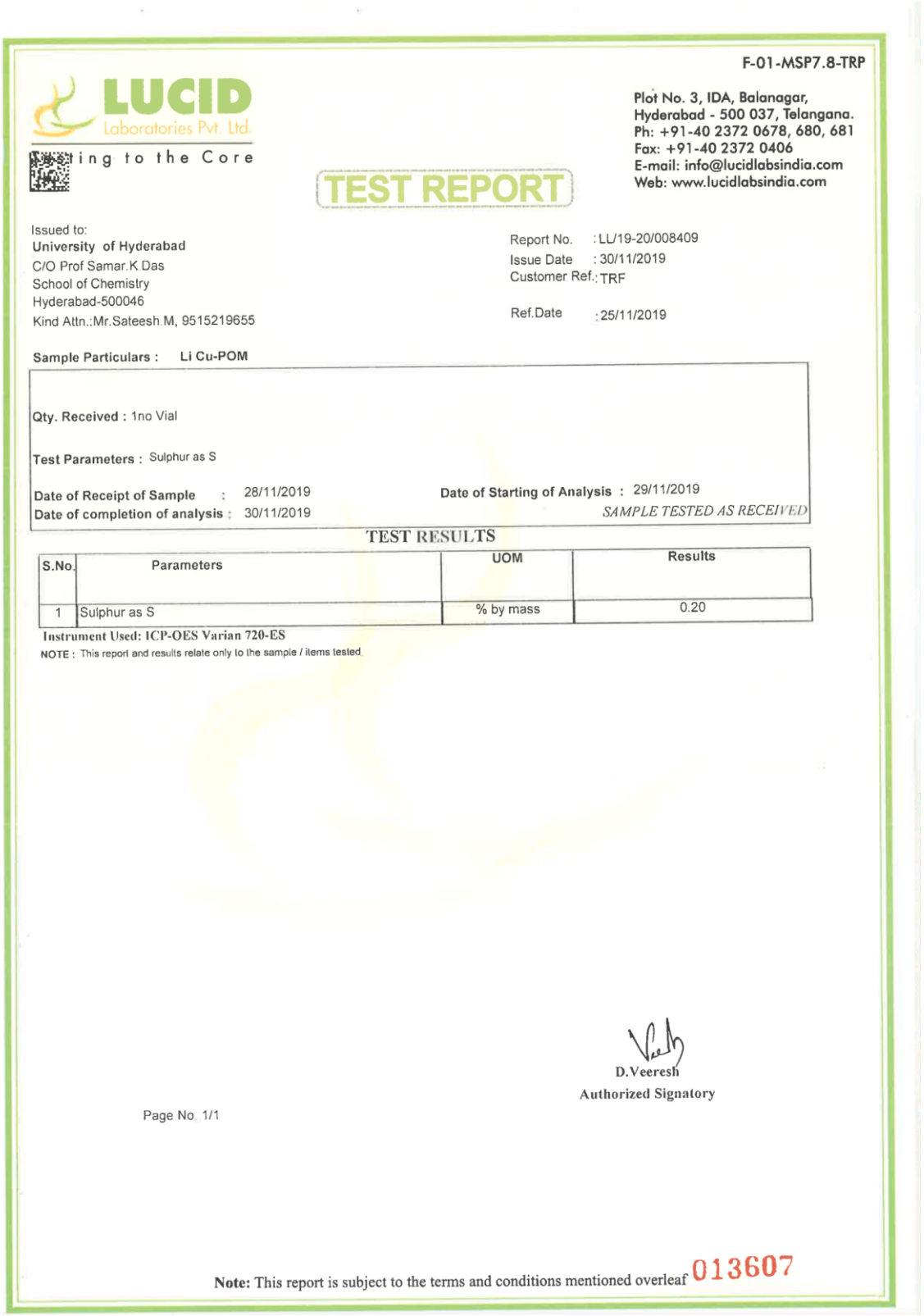

F-01-MSP7.8-TRP

LUCID Laboratories Pvt. Ltd.

ing to the Core

Plot No. 3, IDA, Balanagar,
Hyderabad - 500 037, Telangana.
Ph: +91-40 2372 0678, 680, 681
Fax: +91-40 2372 0406
E-mail: info@lucidlabsindia.com
Web: www.lucidlabsindia.com

TEST REPORT

Issued to:
University of Hyderabad
C/O Prof Samar.K Das
School of Chemistry
Hyderabad-500046
Kind Attn.:Mr.Sateesh.M, 9515219655

Report No. : LL/19-20/008409
Issue Date : 30/11/2019
Customer Ref.: TRF
Ref.Date : 25/11/2019

Sample Particulars : Li Cu-POM

Qty. Received : 1no Vial

Test Parameters : Sulphur as S

Date of Receipt of Sample : 28/11/2019
Date of completion of analysis : 30/11/2019
Date of Starting of Analysis : 29/11/2019
SAMPLE TESTED AS RECEIVED

TEST RESULTS

S.No.	Parameters	UOM	Results
1	Sulphur as S	% by mass	0.20

Instrument Used: ICP-OES Varian 720-ES

NOTE : This report and results relate only to the sample / items tested.

D.Veeresh
Authorized Signatory

Page No. 1/1

Note: This report is subject to the terms and conditions mentioned overleaf 013607

Appendix Figure 3(c). Elemental analysis report of sulfur for LiCu-POM compound.

***References for Appendix Table 3(i)*:**

[1]. von Allmen, K. D.; Grundmann, H.; Linden, A.; Patzke, G. R., Synthesis and Characterization of 0D–3D Copper-Containing Tungstobismuthates Obtained from the Lacunary Precursor $Na_9[B\text{-}\alpha\text{-}BiW_9O_{33}]$. *Inorg. Chem.* **2017**, *56*, 327-335.

[2]. Rusu, D.; Tomasa, A. R.; Turdean, G. L.; Cojocaru, I.; Oana, B.; Rusu, M. Synthesis and investigation of the copper(II)-substituted polyoxotungstate based on α-B-$[BiW_9O_{33}]^{9-}$ units. *Rev. Roum. Chim.* **2012**, *57*, 327–336.

[3]. Roşu, C.; Rasu, D.; Weakley, T. J. R. X-ray structure of dodecasodium tricopper(II)bis[nonatungstabismuthate(III) hydrate, a polyoxometalate salt containing α-B-BiW9O33 units. *J. Chem. Crystallogr*. **2003**, *33*, 751–755.

[4]. Rusu, D.; Roşu, C.; Crăciun, C.; David, L.; Rusu, M.; Marcu, G. FT-IR, UV–VIS and EPR investigations of multicopper polyoxotungstates with BiIII as heteroatom. *J. Mol. Struct.* **2001**, *563*, 427–433.

[5]. Xu, X.; Zhang, L.; Zhang, Y.; Qi, B.; Fang, L. Synthesis and Crystal Structure of a Sandwich-type Transition Metal Complex with Tungstobismutate and Triethanolamine. *Z. Naturforsch. B.* **2009**, *64*, 821–825.

[6]. Xue, G.-L.; Wang, H.-L.; Xie, Z.-H.; Shi, Q.-Z.; Wang, J.-W.; Wang, D.-Q. Synthesis, Crystal Structure and Magnetic Property of Sandwich-Type Heteropolyoxometalate $Na_9[(Na(H_2O)_3Cu(H_2O)_3(BiW_9O_{33})_2]\cdot 42H_2O$. *Chinese J. Chem.* **2004**, *22*, 159–161.

[7]. Bi, L.-H.; Li, B.; Wu, L.-X.; Bao, Y.-Y., Synthesis, characterization and crystal structure of a novel 2D network structure based on hexacopper(II) substituted tungstoantimonate. *Inorg. Chimica Acta* **2009**, *362*, 3309-3313.

[8]. Yamase, T.; Fukaya, K.; Nojiri, H.; Ohshima, Y., Ferromagnetic Exchange Interactions for Cu_6^{12+} and Mn_6^{12+} Hexagons Sandwiched by Two B-α-$[XW_9O_{33}]^{9-}$ (X = AsIII and SbIII) Ligands in D3d-Symmetric Polyoxotungstates. *Inorg. Chem.* **2006**, *45*, 7698-7704.

[9]. Yamase, T.; Ishikawa, H.; Abe, H.; Fukaya, K.; Nojiri, H.; Takeuchi, H., Molecular Magnetism of M_6 Hexagon Ring in D_3d Symmetric $[(MCl)_6(XW_9O_{33})_2]^{12-}$ (M = Cu^{II} and Mn^{II}, X = Sb^{III} and As^{III}). *Inorg. Chem.* **2012**, *51*, 4606-4619.

[10]. Kortz, U.; Nellutla, S.; Stowe, A. C.; Dalal, N. S.; van Tol, J.; Bassil, B. S., Structure and Magnetism of the Tetra-Copper(II)-Substituted Heteropolyanion $[Cu_4K_2(H_2O)_8(\alpha\text{-}AsW_9O_{33})_2]^{8-}$. *Inorg. Chem.* **2004**, *43*, 144 -154.

[11]. Lv, H.; Gao, Y.; Guo, W.; Lauinger, S. M.; Chi, Y.; Bacsa, J.; Sullivan, K. P.; Wieliczko, M.; Musaev, D. G.; Hill, C. L., Cu-based Polyoxometalate Catalyst for Efficient Catalytic Hydrogen Evolution. *Inorg. Chem.* **2016**, *55*, 6750-6758.

[12]. Li, D.; Ma, X.; Wang, Q.; Ma, P.; Niu, J.; Wang, J., Copper-Containing Polyoxometalate-Based Metal–Organic Frameworks as Highly Efficient Heterogeneous Catalysts toward Selective Oxidation of Alkylbenzenes. *Inorg. Chem.* **2019**, *58*, 15832-15840.

[13]. Kortz, U.; Al-Kassem, N. K.; Savelieff, M. G.; Al Kadi, N. A.; Sadakane, M. Synthesis and Characterization of Copper-, Zinc-, Manganese-, and Cobalt-Substituted Dimeric Heteropolyanions, $[(\alpha\text{-}XW_9O_{33})_2M_3(H_2O)_3]^{n-}$ (n = 12, X = As^{III}, Sb^{III}, M = Cu^{2+}, Zn^{2+}; n = 10, X = Se^{IV}, Te^{IV}, M = Cu^{2+}) and $[(\alpha\text{-}AsW_9O_{33})_2WO(H_2O)M_2(H_2O)_2]^{10-}$ (M = Zn^{2+}, Mn^{2+}, Co^{2+}). *Inorg. Chem.* **2001**, *40*, 4742–4749.

[14]. Zhang, W.; Liu, S.; Feng, D.; Zhang, C.; Sun, P.; Ma, F., Two novel Krebs-type polyoxoanions $[CuI_2(WO_2)_2(\beta\text{-}XW_9O_{33})_2]^{12-}$ ($X=Sb^{III}$, Bi^{III}) resulting in 2D layer structures linked by copper(I) ions and copper(II) complex groups. *J. Mol. Struct.* **2009,** *936*, 194-198.

[15]. Roşu, C.; Rusu, M.; Casañ-Pastor, N.; Gómez-Garciac, C. J. Synthesis, Characterization and Electrochemistry of Cobalt(II) and Copper(II) Complexes of Bismutho(III)Polyoxotungstate Ligand Anion. *Syn. React. Inorg. Met.* **2000**, *30*, 369–377.

[16]. Pichon, C.; Mialane, P.; Dolbecq, A.; Marrot, J.; Rivière, E.; Keita, B.; Nadjo, L.; Sécheresse, F., Characterization and Electrochemical Properties of Molecular Icosanuclear and Bidimensional Hexanuclear Cu(II) Azido Polyoxometalates. *Inorg. Chem.* **2007**, *46* (13), 5292-5301.

[17]. Bao, Y.-Y.; Bi, L.-H.; Wu, L.-X.; Mal, S. S.; Kortz, U., Preparation and Characterization of Langmuir−Blodgett Films of Wheel-Shaped Cu-20 Tungstophosphate and DODA by Two Different Strategies. *Langmuir* **2009**, *25*, 13000-13006.

[18]. Mal, S. S.; Bassil, B. S.; Ibrahim, M.; Nellutla, S.; van Tol, J.; Dalal, N. S.; Fernández, J. A.; López, X.; Poblet, J. M.; Biboum, R. N.; Keita, B.; Kortz, U., Wheel-Shaped Cu_{20}-Tungstophosphate $[Cu_{20}X(OH)_{24}(H_2O)_{12}(P_8W_{48}O_{184})]^{25-}$ Ion (X = Cl, Br, I) and the Role of the Halide Guest. *Inorg. Chem.* **2009,** *48*, 11636-11645.

[19]. Bassil, B. S.; Haider, A.; Ibrahim, M.; Mougharbel, A. S.; Bhattacharya, S.; Christian, J. H.; Bindra, J. K.; Dalal, N. S.; Wang, M.; Zhang, G.; Keita, B.; Rutkowska, I. A.; Kulesza, P. J.; Kortz, U., 15-Copper(ii)-containing 36-tungsto-4-silicates(iv) $[Cu_{15}O_2(OH)_{10}X(A\text{-}\alpha\text{-}SiW_9O_{34})_4]^{25-}$ (X = Cl, Br): synthesis, structure, magnetic properties, and electrocatalytic CO_2 reduction. *Dalton Trans.* **2018,** *47*, 12439-12448.

[20]. Kato, C.; Nishihara, S.; Tsunashima, R.; Tatewaki, Y.; Okada, S.; Ren, X.-M.; Inoue, K.; Long, D.-L.; Cronin, L., Quick and selective synthesis of $Li_6[\alpha\text{-}P_2W_{18}O_{62}]\cdot 28H_2O$ soluble in various organic solvents. *Dalton Trans.* **2013,** *42*, 11363-11366.

Appendix 4(*i*). Details of bond distances and angles for compounds 1 and 2

*Bond distances (Å) and angles (°) for compound **1***

V(1)-O(2)	1.689(8)	V(4)-O(13)	1.634(8)
V(1)-O(4)	1.698(7)	V(4)-O(14)	1.926(7)
V(1)-O(1)	1.711(7)	V(4)-O(16)	1.945(7)
V(1)-O(3)	1.731(7)	V(4)-O(11)	1.963(8)
V(15)-O(46)	1.625(7)	V(4)-O(15)	2.050(7)
V(15)-O(8)	1.936(7)	V(3)-O(10)	1.630(8)
V(15)-O(34)	1.958(7)	V(3)-O(12)	1.952(8)
V(15)-O(9)	2.021(7)	V(3)-O(7)	1.962(7)
V(15)-O(32)	2.059(7)	V(3)-O(11)	2.000(7)
V(15)-O(4)	2.368(7)	V(3)-O(6)	2.029(7)
V(9)-O(30)	1.625(7)	V(3)-O(1)	2.413(8)
V(9)-O(25)	1.940(7)	V(19)-O(26)	1.651(8)
V(9)-O(31)	1.975(7)	V(19)-O(12)	1.903(8)
V(9)-O(21)	1.987(8)	V(19)-O(20)	1.936(8)
V(9)-O(32)	2.057(7)	V(19)-O(23)	2.058(7)
V(9)-O(4)	2.439(7)	V(19)-O(18)	2.073(8)
V(16)-O(45)	1.620(7)	V(19)-O(3)	2.198(8)
V(16)-O(44)	1.930(7)	V(14)-O(42)	1.670(9)
V(16)-O(35)	1.970(7)	V(14)-O(16)	1.866(7)
V(16)-O(34)	1.977(7)	V(14)-O(44)	1.903(8)
V(16)-O(43)	1.977(8)	V(14)-O(43)	1.936(8)
V(10)-O(33)	1.659(8)	V(14)-O(15)	2.111(8)
V(10)-O(34)	1.892(7)	V(7)-O(22)	1.641(8)
V(10)-O(31)	1.894(7)	V(7)-O(25)	1.873(7)
V(10)-O(35)	1.950(8)	V(7)-O(20)	1.886(7)
V(10)-O(32)	2.103(8)	V(7)-O(21)	1.960(8)
V(6)-O(19)	1.622(8)	V(7)-O(23)	2.129(8)
V(6)-O(20)	1.953(7)	V(13)-O(40)	1.625(8)
V(6)-O(21)	1.964(7)	V(13)-O(39)	1.928(8)
V(6)-O(7)	1.970(7)	V(13)-O(28)	1.953(8)
V(6)-O(9)	2.026(7)	V(13)-O(14)	1.970(8)
V(18)-O(47)	1.622(8)	V(13)-O(18)	2.071(8)
V(18)-O(8)	1.949(8)	V(2)-O(5)	1.632(9)
V(18)-O(44)	1.955(7)	V(2)-O(7)	1.870(7)
V(18)-O(6)	2.000(8)	V(2)-O(8)	1.902(7)
V(18)-O(15)	2.059(7)	V(2)-O(9)	2.024(8)
V(18)-O(1)	2.357(7)	V(2)-O(6)	2.026(8)
V(11)-O(41)	1.632(8)	V(12)-O(37)	1.647(9)
V(11)-O(16)	1.932(8)	V(12)-O(39)	1.873(8)
V(11)-O(39)	1.974(7)	V(12)-O(29)	1.884(8)
V(11)-O(43)	1.989(7)	V(12)-O(28)	1.970(8)
V(11)-O(38)	2.044(8)	V(12)-O(38)	2.106(8)
V(11)-O(2)	2.403(8)	V(5)-O(17)	1.634(9)
V(8)-O(27)	1.612(8)	V(5)-O(14)	1.856(8)
V(8)-O(29)	1.944(8)	V(5)-O(12)	1.895(8)
V(8)-O(28)	1.985(8)	V(5)-O(11)	1.960(7)
V(8)-O(25)	1.985(8)	V(5)-O(18)	2.129(8)
V(8)-O(23)	2.078(7)		
V(8)-O(3)	2.431(7)	O(2)-V(1)-O(4)	109.0(4)
V(17)-O(36)	1.620(8)	O(2)-V(1)-O(1)	109.4(4)
V(17)-O(31)	1.926(7)	O(4)-V(1)-O(1)	108.8(4)
V(17)-O(29)	1.966(8)	O(2)-V(1)-O(3)	108.9(4)
V(17)-O(35)	1.978(7)	O(4)-V(1)-O(3)	110.5(4)
V(17)-O(38)	2.082(8)	O(1)-V(1)-O(3)	110.2(4)
V(17)-O(2)	2.355(7)	O(46)-V(15)-O(8)	103.4(4)

O(46)-V(15)-O(34)	103.6(3)
O(8)-V(15)-O(34)	91.5(3)
O(46)-V(15)-O(9)	97.1(4)
O(8)-V(15)-O(9)	81.7(3)
O(34)-V(15)-O(9)	159.2(3)
O(46)-V(15)-O(32)	97.4(4)
O(8)-V(15)-O(32)	159.2(3)
O(34)-V(15)-O(32)	81.4(3)
O(9)-V(15)-O(32)	98.0(3)
O(46)-V(15)-O(4)	164.0(3)
O(8)-V(15)-O(4)	88.5(3)
O(34)-V(15)-O(4)	86.5(3)
O(9)-V(15)-O(4)	73.7(3)
O(32)-V(15)-O(4)	71.7(3)
O(30)-V(9)-O(25)	104.3(4)
O(30)-V(9)-O(31)	102.8(4)
O(25)-V(9)-O(31)	90.9(3)
O(30)-V(9)-O(21)	101.1(4)
O(25)-V(9)-O(21)	84.0(3)
O(31)-V(9)-O(21)	156.1(3)
O(30)-V(9)-O(32)	98.0(4)
O(25)-V(9)-O(32)	157.3(3)
O(31)-V(9)-O(32)	79.9(3)
O(21)-V(9)-O(32)	96.1(3)
O(30)-V(9)-O(4)	165.0(4)
O(25)-V(9)-O(4)	88.4(3)
O(31)-V(9)-O(4)	84.6(3)
O(21)-V(9)-O(4)	72.0(3)
O(32)-V(9)-O(4)	70.2(3)
O(45)-V(16)-O(44)	105.3(4)
O(45)-V(16)-O(35)	102.2(4)
O(44)-V(16)-O(35)	152.4(3)
O(45)-V(16)-O(34)	103.5(4)
O(44)-V(16)-O(34)	91.1(3)
O(35)-V(16)-O(34)	80.7(3)
O(45)-V(16)-O(43)	101.9(4)
O(44)-V(16)-O(43)	80.2(3)
O(35)-V(16)-O(43)	96.0(3)
O(34)-V(16)-O(43)	154.5(3)
O(33)-V(10)-O(34)	118.3(4)
O(33)-V(10)-O(31)	118.9(4)
O(34)-V(10)-O(31)	122.7(3)
O(33)-V(10)-O(35)	105.7(4)
O(34)-V(10)-O(35)	83.4(3)
O(31)-V(10)-O(35)	85.3(3)
O(33)-V(10)-O(32)	104.7(4)
O(34)-V(10)-O(32)	81.8(3)
O(31)-V(10)-O(32)	80.5(3)
O(35)-V(10)-O(32)	149.6(3)
O(19)-V(6)-O(20)	103.9(4)
O(19)-V(6)-O(21)	100.9(4)
O(20)-V(6)-O(21)	83.3(3)
O(19)-V(6)-O(7)	104.0(4)
O(20)-V(6)-O(7)	88.5(3)
O(21)-V(6)-O(7)	155.0(3)
O(19)-V(6)-O(9)	99.9(4)
O(20)-V(6)-O(9)	155.8(3)
O(21)-V(6)-O(9)	96.5(3)
O(7)-V(6)-O(9)	81.5(3)
O(47)-V(18)-O(8)	102.3(4)
O(47)-V(18)-O(44)	102.3(4)
O(8)-V(18)-O(44)	92.8(3)
O(47)-V(18)-O(6)	98.8(4)
O(8)-V(18)-O(6)	81.9(3)
O(44)-V(18)-O(6)	159.0(3)
O(47)-V(18)-O(15)	97.8(4)
O(8)-V(18)-O(15)	159.8(3)
O(44)-V(18)-O(15)	81.2(3)
O(6)-V(18)-O(15)	96.9(3)
O(47)-V(18)-O(1)	164.5(4)
O(8)-V(18)-O(1)	89.4(3)
O(44)-V(18)-O(1)	87.1(3)
O(6)-V(18)-O(1)	72.5(3)
O(15)-V(18)-O(1)	71.2(3)
O(41)-V(11)-O(16)	105.1(4)
O(41)-V(11)-O(39)	101.2(4)
O(16)-V(11)-O(39)	89.7(3)
O(41)-V(11)-O(43)	102.8(4)
O(16)-V(11)-O(43)	84.5(3)
O(39)-V(11)-O(43)	156.0(3)
O(41)-V(11)-O(38)	98.0(4)
O(16)-V(11)-O(38)	156.0(3)
O(39)-V(11)-O(38)	79.3(3)
O(43)-V(11)-O(38)	96.9(3)
O(41)-V(11)-O(2)	166.2(4)
O(16)-V(11)-O(2)	87.9(3)
O(39)-V(11)-O(2)	83.3(3)
O(43)-V(11)-O(2)	73.2(3)
O(38)-V(11)-O(2)	69.8(3)
O(27)-V(8)-O(29)	104.4(4)
O(27)-V(8)-O(28)	100.5(4)
O(29)-V(8)-O(28)	83.1(3)
O(27)-V(8)-O(25)	102.5(4)
O(29)-V(8)-O(25)	91.6(3)
O(28)-V(8)-O(25)	157.1(3)
O(27)-V(8)-O(23)	96.5(4)
O(29)-V(8)-O(23)	158.5(3)
O(28)-V(8)-O(23)	98.2(3)
O(25)-V(8)-O(23)	78.8(3)
O(27)-V(8)-O(3)	162.4(4)
O(29)-V(8)-O(3)	90.9(3)
O(28)-V(8)-O(3)	72.6(3)
O(25)-V(8)-O(3)	85.3(3)
O(23)-V(8)-O(3)	69.3(3)
O(36)-V(17)-O(31)	103.0(4)
O(36)-V(17)-O(29)	101.7(4)
O(31)-V(17)-O(29)	91.9(3)
O(36)-V(17)-O(35)	100.5(4)
O(31)-V(17)-O(35)	83.7(3)
O(29)-V(17)-O(35)	157.8(3)
O(36)-V(17)-O(38)	96.9(4)
O(31)-V(17)-O(38)	159.6(3)
O(29)-V(17)-O(38)	79.5(3)
O(35)-V(17)-O(38)	97.2(3)
O(36)-V(17)-O(2)	164.8(4)
O(31)-V(17)-O(2)	90.6(3)
O(29)-V(17)-O(2)	84.3(3)
O(35)-V(17)-O(2)	74.1(3)
O(38)-V(17)-O(2)	70.3(3)
O(13)-V(4)-O(14)	105.9(4)
O(13)-V(4)-O(16)	102.0(4)
O(14)-V(4)-O(16)	90.2(3)

O(13)-V(4)-O(11)	102.9(4)	O(25)-V(7)-O(20)	121.2(3)
O(14)-V(4)-O(11)	84.1(3)	O(22)-V(7)-O(21)	106.3(4)
O(16)-V(4)-O(11)	155.1(3)	O(25)-V(7)-O(21)	86.5(3)
O(13)-V(4)-O(15)	97.8(4)	O(20)-V(7)-O(21)	85.2(3)
O(14)-V(4)-O(15)	155.6(3)	O(22)-V(7)-O(23)	101.9(4)
O(16)-V(4)-O(15)	79.4(3)	O(25)-V(7)-O(23)	80.0(3)
O(11)-V(4)-O(15)	96.0(3)	O(20)-V(7)-O(23)	80.9(3)
O(10)-V(3)-O(12)	101.6(4)	O(21)-V(7)-O(23)	151.8(3)
O(10)-V(3)-O(7)	102.0(4)	O(40)-V(13)-O(39)	103.3(4)
O(12)-V(3)-O(7)	92.0(3)	O(40)-V(13)-O(28)	102.4(4)
O(10)-V(3)-O(11)	99.3(4)	O(39)-V(13)-O(28)	84.1(3)
O(12)-V(3)-O(11)	80.6(3)	O(40)-V(13)-O(14)	102.3(4)
O(7)-V(3)-O(11)	158.5(3)	O(39)-V(13)-O(14)	91.1(3)
O(10)-V(3)-O(6)	100.4(4)	O(28)-V(13)-O(14)	155.3(3)
O(12)-V(3)-O(6)	157.9(3)	O(40)-V(13)-O(18)	99.4(4)
O(7)-V(3)-O(6)	81.1(3)	O(39)-V(13)-O(18)	156.7(3)
O(11)-V(3)-O(6)	98.1(3)	O(28)-V(13)-O(18)	96.1(3)
O(10)-V(3)-O(1)	166.4(4)	O(14)-V(13)-O(18)	79.0(3)
O(12)-V(3)-O(1)	87.9(3)	O(5)-V(2)-O(7)	119.1(4)
O(7)-V(3)-O(1)	87.2(3)	O(5)-V(2)-O(8)	118.7(4)
O(11)-V(3)-O(1)	72.4(3)	O(7)-V(2)-O(8)	122.2(3)
O(6)-V(3)-O(1)	70.8(3)	O(5)-V(2)-O(9)	104.5(4)
O(26)-V(19)-O(12)	101.3(4)	O(7)-V(2)-O(9)	84.0(3)
O(26)-V(19)-O(20)	102.0(4)	O(8)-V(2)-O(9)	82.5(3)
O(12)-V(19)-O(20)	94.1(3)	O(5)-V(2)-O(6)	104.4(4)
O(26)-V(19)-O(23)	95.1(4)	O(7)-V(2)-O(6)	83.5(3)
O(12)-V(19)-O(23)	163.6(3)	O(8)-V(2)-O(6)	82.4(3)
O(20)-V(19)-O(23)	81.6(3)	O(9)-V(2)-O(6)	151.1(3)
O(26)-V(19)-O(18)	94.3(4)	O(37)-V(12)-O(39)	118.5(5)
O(12)-V(19)-O(18)	81.2(3)	O(37)-V(12)-O(29)	119.1(5)
O(20)-V(19)-O(18)	163.7(3)	O(39)-V(12)-O(29)	121.7(3)
O(23)-V(19)-O(18)	98.6(3)	O(37)-V(12)-O(28)	108.8(5)
O(26)-V(19)-O(3)	163.8(4)	O(39)-V(12)-O(28)	85.1(3)
O(12)-V(19)-O(3)	89.6(3)	O(29)-V(12)-O(28)	85.0(3)
O(20)-V(19)-O(3)	89.0(3)	O(37)-V(12)-O(38)	101.4(4)
O(23)-V(19)-O(3)	74.5(3)	O(39)-V(12)-O(38)	80.0(3)
O(18)-V(19)-O(3)	75.4(3)	O(29)-V(12)-O(38)	80.8(3)
O(42)-V(14)-O(16)	117.3(4)	O(28)-V(12)-O(38)	149.8(3)
O(42)-V(14)-O(44)	120.9(4)	O(17)-V(5)-O(14)	120.0(6)
O(16)-V(14)-O(44)	121.0(3)	O(17)-V(5)-O(12)	120.6(6)
O(42)-V(14)-O(43)	109.7(4)	O(14)-V(5)-O(12)	118.8(3)
O(16)-V(14)-O(43)	87.8(3)	O(17)-V(5)-O(11)	108.2(5)
O(44)-V(14)-O(43)	81.9(3)	O(14)-V(5)-O(11)	86.0(3)
O(42)-V(14)-O(15)	100.7(4)	O(12)-V(5)-O(11)	83.0(3)
O(16)-V(14)-O(15)	79.7(3)	O(17)-V(5)-O(18)	102.6(5)
O(44)-V(14)-O(15)	81.0(3)	O(14)-V(5)-O(18)	80.0(3)
O(43)-V(14)-O(15)	149.6(3)	O(12)-V(5)-O(18)	79.9(3)
O(22)-V(7)-O(25)	120.2(4)	O(11)-V(5)-O(18)	149.2(3)
O(22)-V(7)-O(20)	117.9(4)		

Symmetry transformations used to generate equivalent atoms: #1 x,-y+2,z+1/2 #2 x,-y+2,z-1/2 #3 x+1/2,y+1/2,z #4 x+1/2,-y+3/2,z-1/2 #5 x,-y+1,z-1/2 #6 x-1/2,-y+3/2,z-1/2 #7 x,-y+1,z+1/2 #8 x-1/2,y+1/2,z #9 x-1/2,-y+3/2,z+1/2 #10 x-1/2,y-1/2,z #11 x+1/2,-y+3/2,z+1/2 #12 x+1/2,y-1/2,z

*Bond distances (Å) and angles (°) for compound **2***

V(1)-O(1)	1.626(4)	V(1)-O(5)	1.943(4)
V(1)-O(2)	1.933(4)	V(1)-O(3)	1.960(4)
V(1)-O(4)	1.940(4)	V(3)-O(7)	1.614(4)

V(3)-O(8)	1.953(4)
V(3)-O(4)	1.956(4)
V(3)-O(17)#1	1.957(4)
V(3)-O(9)	1.958(4)
V(7)-O(18)	1.624(4)
V(7)-O(15)	1.940(4)
V(7)-O(2)#1	1.951(4)
V(7)-O(13)	1.951(4)
V(7)-O(19)	1.957(4)
V(9)-O(16)	1.624(4)
V(9)-O(17)	1.939(4)
V(9)-O(15)	1.945(4)
V(9)-O(14)	1.946(4)
V(9)-O(10)#1	1.955(4)
V(5)-O(21)	1.633(4)
V(5)-O(8)	1.920(4)
V(5)-O(5)	1.924(4)
V(5)-O(13)	1.954(4)
V(5)-O(19)	1.960(4)
V(6)-O(20)	1.613(4)
V(6)-O(3)#1	1.883(4)
V(6)-O(19)	1.893(4)
V(6)-O(5)	1.931(4)
V(6)-O(3)	1.952(4)
V(2)-O(6)	1.636(4)
V(2)-O(2)	1.917(4)
V(2)-O(15)#1	1.935(4)
V(2)-O(17)#1	1.940(4)
V(2)-O(4)	1.948(4)
V(4)-O(12)	1.626(4)
V(4)-O(14)	1.918(4)
V(4)-O(13)	1.941(4)
V(4)-O(9)	1.946(4)
V(4)-O(8)	1.948(4)
V(8)-O(11)	1.606(4)
V(8)-O(9)	1.875(4)
V(8)-O(10)	1.881(4)
V(8)-O(14)	1.912(4)
V(8)-O(10)#1	1.952(4)

O(1)-V(1)-O(2)	104.98(18)
O(1)-V(1)-O(4)	105.52(19)
O(2)-V(1)-O(4)	83.39(15)
O(1)-V(1)-O(5)	107.60(18)
O(2)-V(1)-O(5)	147.25(16)
O(4)-V(1)-O(5)	91.03(16)
O(1)-V(1)-O(3)	105.56(19)
O(2)-V(1)-O(3)	88.70(15)
O(4)-V(1)-O(3)	148.92(16)
O(5)-V(1)-O(3)	79.59(15)
O(7)-V(3)-O(8)	106.75(18)
O(7)-V(3)-O(4)	104.63(19)
O(8)-V(3)-O(4)	92.30(16)
O(7)-V(3)-O(17)#1	103.55(18)
O(8)-V(3)-O(17)#1	149.69(16)
O(4)-V(3)-O(17)#1	80.49(15)
O(7)-V(3)-O(9)	106.77(19)
O(8)-V(3)-O(9)	79.65(16)
O(4)-V(3)-O(9)	148.59(16)
O(17)#1-V(3)-O(9)	91.26(15)
O(18)-V(7)-O(15)	105.25(19)
O(18)-V(7)-O(2)#1	105.73(18)
O(15)-V(7)-O(2)#1	82.51(15)
O(18)-V(7)-O(13)	104.29(18)
O(15)-V(7)-O(13)	92.23(16)
O(2)#1-V(7)-O(13)	149.86(15)
O(18)-V(7)-O(19)	104.84(19)
O(15)-V(7)-O(19)	149.89(16)
O(2)#1-V(7)-O(19)	90.35(15)
O(13)-V(7)-O(19)	79.41(15)
O(16)-V(9)-O(17)	104.09(19)
O(16)-V(9)-O(15)	107.23(19)
O(17)-V(9)-O(15)	80.97(15)
O(16)-V(9)-O(14)	108.80(19)
O(17)-V(9)-O(14)	147.09(16)
O(15)-V(9)-O(14)	90.25(16)
O(16)-V(9)-O(10)#1	105.61(19)
O(17)-V(9)-O(10)#1	91.74(15)
O(15)-V(9)-O(10)#1	147.16(16)
O(14)-V(9)-O(10)#1	78.61(16)
O(21)-V(5)-O(8)	106.29(19)
O(21)-V(5)-O(5)	107.8(2)
O(8)-V(5)-O(5)	94.54(16)
O(21)-V(5)-O(13)	110.20(19)
O(8)-V(5)-O(13)	82.17(16)
O(5)-V(5)-O(13)	141.24(16)
O(21)-V(5)-O(19)	110.31(19)
O(8)-V(5)-O(19)	142.79(16)
O(5)-V(5)-O(19)	80.70(15)
O(13)-V(5)-O(19)	79.28(15)
O(20)-V(6)-O(3)#1	105.9(2)
O(20)-V(6)-O(19)	106.0(2)
O(3)#1-V(6)-O(19)	96.41(16)
O(20)-V(6)-O(5)	108.6(2)
O(3)#1-V(6)-O(5)	144.44(16)
O(19)-V(6)-O(5)	82.25(16)
O(20)-V(6)-O(3)	107.3(2)
O(3)#1-V(6)-O(3)	81.76(17)
O(19)-V(6)-O(3)	145.75(16)
O(5)-V(6)-O(3)	80.08(15)
O(6)-V(2)-O(2)	111.8(2)
O(6)-V(2)-O(15)#1	110.44(18)
O(2)-V(2)-O(15)#1	83.53(15)
O(6)-V(2)-O(17)#1	111.8(2)
O(2)-V(2)-O(17)#1	136.45(16)
O(15)#1-V(2)-O(17)#1	81.18(16)
O(6)-V(2)-O(4)	111.57(18)
O(2)-V(2)-O(4)	83.60(15)
O(15)#1-V(2)-O(4)	137.90(16)
O(17)#1-V(2)-O(4)	81.12(15)
O(12)-V(4)-O(14)	106.7(2)
O(12)-V(4)-O(13)	105.84(19)
O(14)-V(4)-O(13)	94.13(16)
O(12)-V(4)-O(9)	110.7(2)
O(14)-V(4)-O(9)	81.46(17)
O(13)-V(4)-O(9)	142.94(16)
O(12)-V(4)-O(8)	110.2(2)
O(14)-V(4)-O(8)	142.58(16)
O(13)-V(4)-O(8)	81.78(15)
O(9)-V(4)-O(8)	80.06(16)
O(11)-V(8)-O(9)	107.8(2)
O(11)-V(8)-O(10)	106.7(2)

O(9)-V(8)-O(10)	93.30(17)	O(10)-V(8)-O(10)#1	82.13(17)
O(11)-V(8)-O(14)	109.2(2)	O(14)-V(8)-O(10)#1	79.48(16)
O(9)-V(8)-O(14)	83.47(17)	O(30)-Na(3)-O(22)#1	89.5(2)
O(10)-V(8)-O(14)	143.20(17)	O(28)-Na(3)-O(6)#1	89.80(18)
O(11)-V(8)-O(10)#1	107.8(2)		
O(9)-V(8)-O(10)#1	143.92(17)		

Symmetry transformations used to generate equivalent atoms: #1 y,x,-z+1 #2 x-1,y,z #3 x-y,-y,-z+2/3 #4 x+1,y,z

Appendix 4(ii). Bond valance sum (BVS) calculations of compounds 1 and 2

Compound 1

Bond valence calculation. Numbers in brackets after atom symbols are at.no., r and c - see *O"Keeffe and Brese, J.A.C.S. 1991, 113, 3226*.

```
......V1O6

  V  (23, 1.21, 1.45)                        Rij   Dij   Vij
                     -O  ( 8,  .63, 3.15) 1.77  1.63  1.47
                     -O  ( 8,  .63, 3.15) 1.77  2.00   .54
                     -O  ( 8,  .63, 3.15) 1.77  1.96   .61
                     -O  ( 8,  .63, 3.15) 1.77  1.97   .59
                     -O  ( 8,  .63, 3.15) 1.77  2.02   .51
                     -O  ( 8,  .63, 3.15) 1.77  2.40   .18

  Bond valence sum for V   3.90

......V2O6

  V  (23, 1.21, 1.45)                        Rij   Dij   Vij
                     -O  ( 8,  .63, 3.15) 1.77  1.61  1.54
                     -O  ( 8,  .63, 3.15) 1.77  1.98   .57
                     -O  ( 8,  .63, 3.15) 1.77  2.06   .46
                     -O  ( 8,  .63, 3.15) 1.77  1.94   .64
                     -O  ( 8,  .63, 3.15) 1.77  1.94   .64
                     -O  ( 8,  .63, 3.15) 1.77  2.39   .19

  Bond valence sum for V   4.04

......V3O6

  V  (23, 1.21, 1.45)                        Rij   Dij   Vij
                     -O  ( 8,  .63, 3.15) 1.77  1.62  1.51
                     -O  ( 8,  .63, 3.15) 1.77  1.99   .55
                     -O  ( 8,  .63, 3.15) 1.77  2.06   .46
                     -O  ( 8,  .63, 3.15) 1.77  1.94   .64
                     -O  ( 8,  .63, 3.15) 1.77  1.93   .66
                     -O  ( 8,  .63, 3.15) 1.77  2.46   .16

  Bond valence sum for V   3.98

......V4O5
   V  (23, 1.21, 1.45)                        Rij   Dij   Vij
```

```
                      -O  ( 8,  .63, 3.15) 1.77  1.64  1.43
                      -O  ( 8,  .63, 3.15) 1.77  2.08   .43
                      -O  ( 8,  .63, 3.15) 1.77  1.86   .79
                      -O  ( 8,  .63, 3.15) 1.77  1.95   .62
                      -O  ( 8,  .63, 3.15) 1.77  1.90   .70

  Bond valence sum for V   3.98

......V5O6

  V  (23, 1.21, 1.45)                        Rij   Dij   Vij
                      -O  ( 8,  .63, 3.15) 1.77  1.63  1.48
                      -O  ( 8,  .63, 3.15) 1.77  1.93   .65
                      -O  ( 8,  .63, 3.15) 1.77  2.00   .55
                      -O  ( 8,  .63, 3.15) 1.77  2.05   .48
                      -O  ( 8,  .63, 3.15) 1.77  1.96   .61
                      -O  ( 8,  .63, 3.15) 1.77  2.45   .16

  Bond valence sum for V   3.92

......V6O6

  V  (23, 1.21, 1.45)                        Rij   Dij   Vij
                      -O  ( 8,  .63, 3.15) 1.77  1.63  1.46
                      -O  ( 8,  .63, 3.15) 1.77  2.06   .46
                      -O  ( 8,  .63, 3.15) 1.77  1.96   .60
                      -O  ( 8,  .63, 3.15) 1.77  1.93   .65
                      -O  ( 8,  .63, 3.15) 1.77  1.99   .56
                      -O  ( 8,  .63, 3.15) 1.77  2.33   .22

  Bond valence sum for V   3.96

......V7O5

  V  (23, 1.21, 1.45)                        Rij   Dij   Vij
                      -O  ( 8,  .63, 3.15) 1.77  1.62  1.51
                      -O  ( 8,  .63, 3.15) 1.77  2.00   .55
                      -O  ( 8,  .63, 3.15) 1.77  1.94   .64
                      -O  ( 8,  .63, 3.15) 1.77  1.99   .56
                      -O  ( 8,  .63, 3.15) 1.77  1.98   .57

  Bond valence sum for V   3.84

......V8O5

  V  (23, 1.21, 1.45)                        Rij   Dij   Vij
                      -O  ( 8,  .63, 3.15) 1.77  1.63  1.46
                      -O  ( 8,  .63, 3.15) 1.77  1.88   .75
                      -O  ( 8,  .63, 3.15) 1.77  2.00   .55
                      -O  ( 8,  .63, 3.15) 1.77  1.89   .72
                      -O  ( 8,  .63, 3.15) 1.77  2.08   .44

  Bond valence sum for V   3.92
 ......V9O6
```

```
  V  (23, 1.21, 1.45)                          Rij   Dij   Vij
                      -O  ( 8,  .63, 3.15) 1.77  1.63  1.49
                      -O  ( 8,  .63, 3.15) 1.77  1.96   .60
                      -O  ( 8,  .63, 3.15) 1.77  2.07   .45
                      -O  ( 8,  .63, 3.15) 1.77  1.94   .64
                      -O  ( 8,  .63, 3.15) 1.77  1.98   .57
                      -O  ( 8,  .63, 3.15) 1.77  2.45   .16

  Bond valence sum for V   3.91

......V10O6

  V  (23, 1.21, 1.45)                          Rij   Dij   Vij
                      -O  ( 8,  .63, 3.15) 1.77  1.62  1.50
                      -O  ( 8,  .63, 3.15) 1.77  1.95   .62
                      -O  ( 8,  .63, 3.15) 1.77  1.95   .62
                      -O  ( 8,  .63, 3.15) 1.77  2.06   .47
                      -O  ( 8,  .63, 3.15) 1.77  2.05   .47
                      -O  ( 8,  .63, 3.15) 1.77  2.33   .22

  Bond valence sum for V   3.90

......V11O5

  V  (23, 1.21, 1.45)                          Rij   Dij   Vij
                      -O  ( 8,  .63, 3.15) 1.77  1.61  1.54
                      -O  ( 8,  .63, 3.15) 1.77  1.96   .61
                      -O  ( 8,  .63, 3.15) 1.77  2.05   .48
                      -O  ( 8,  .63, 3.15) 1.77  1.96   .60
                      -O  ( 8,  .63, 3.15) 1.77  1.95   .62

  Bond valence sum for V   3.85

......V12O6

  V  (23, 1.21, 1.45)                          Rij   Dij   Vij
                      -O  ( 8,  .63, 3.15) 1.77  1.62  1.52
                      -O  ( 8,  .63, 3.15) 1.77  1.93   .65
                      -O  ( 8,  .63, 3.15) 1.77  1.99   .56
                      -O  ( 8,  .63, 3.15) 1.77  2.09   .43
                      -O  ( 8,  .63, 3.15) 1.77  1.98   .57
                      -O  ( 8,  .63, 3.15) 1.77  2.42   .17

  Bond valence sum for V   3.91

......V13O5

  V  (23, 1.21, 1.45)                          Rij   Dij   Vij
                      -O  ( 8,  .63, 3.15) 1.77  1.65  1.40
                      -O  ( 8,  .63, 3.15) 1.77  2.14   .37
                      -O  ( 8,  .63, 3.15) 1.77  1.89   .74
                      -O  ( 8,  .63, 3.15) 1.77  1.96   .61
                      -O  ( 8,  .63, 3.15) 1.77  1.89   .73
```

```
  Bond valence sum for V   3.85

......V14O6

  V  (23, 1.21, 1.45)                          Rij   Dij   Vij
                     -O  ( 8,  .63, 3.15) 1.77  1.67  1.33
                     -O  ( 8,  .63, 3.15) 1.77  1.91   .70
                     -O  ( 8,  .63, 3.15) 1.77  1.93   .65
                     -O  ( 8,  .63, 3.15) 1.77  2.05   .48
                     -O  ( 8,  .63, 3.15) 1.77  2.08   .43
                     -O  ( 8,  .63, 3.15) 1.77  2.19   .32

  Bond valence sum for V   3.92

......V15O5

  V  (23, 1.21, 1.45)                          Rij   Dij   Vij
                     -O  ( 8,  .63, 3.15) 1.77  1.62  1.54
                     -O  ( 8,  .63, 3.15) 1.77  1.96   .61
                     -O  ( 8,  .63, 3.15) 1.77  1.93   .66
                     -O  ( 8,  .63, 3.15) 1.77  1.96   .61
                     -O  ( 8,  .63, 3.15) 1.77  2.06   .46

  Bond valence sum for V   3.88

......V16O5

  V  (23, 1.21, 1.45)                          Rij   Dij   Vij
                     -O  ( 8,  .63, 3.15) 1.77  1.64  1.43
                     -O  ( 8,  .63, 3.15) 1.77  1.89   .73
                     -O  ( 8,  .63, 3.15) 1.77  2.02   .51
                     -O  ( 8,  .63, 3.15) 1.77  1.88   .74
                     -O  ( 8,  .63, 3.15) 1.77  2.12   .40

  Bond valence sum for V   3.81

......V17O5

  V  (23, 1.21, 1.45)                          Rij   Dij   Vij
                     -O  ( 8,  .63, 3.15) 1.77  1.65  1.39
                     -O  ( 8,  .63, 3.15) 1.77  2.10   .41
                     -O  ( 8,  .63, 3.15) 1.77  1.88   .75
                     -O  ( 8,  .63, 3.15) 1.77  1.88   .75
                     -O  ( 8,  .63, 3.15) 1.77  1.95   .61

  Bond valence sum for V   3.91

......V18O5

  V  (23, 1.21, 1.45)                          Rij   Dij   Vij
                     -O  ( 8,  .63, 3.15) 1.77  1.64  1.43
                     -O  ( 8,  .63, 3.15) 1.77  1.99   .56
                     -O  ( 8,  .63, 3.15) 1.77  1.88   .76
```

```
                    -O  ( 8,  .63, 3.15) 1.77  1.90   .71
                    -O  ( 8,  .63, 3.15) 1.77  2.11   .40

  Bond valence sum for V   3.87

......V19O4

  V  (23, 1.21, 1.45)                      Rij   Dij   Vij
                    -O  ( 8,  .63, 3.15) 1.77  1.70  1.21
                    -O  ( 8,  .63, 3.15) 1.77  1.70  1.22
                    -O  ( 8,  .63, 3.15) 1.77  1.73  1.13
                    -O  ( 8,  .63, 3.15) 1.77  1.72  1.16

  Bond valence sum for V   4.72
```

Compound 2

```
Bond valence calculation. Numbers in brackets after atom symbols are at.no., r and c
- see O"Keeffe and Brese, J.A.C.S. 1991, 113, 3226

......V1

  V  (23, 1.21, 1.45)                      Rij   Dij   Vij
                    -O  ( 8,  .63, 3.15) 1.77  1.96   .61
                    -O  ( 8,  .63, 3.15) 1.77  1.97   .59
                    -O  ( 8,  .63, 3.15) 1.77  1.95   .62
                    -O  ( 8,  .63, 3.15) 1.77  1.94   .63
                    -O  ( 8,  .63, 3.15) 1.77  1.63  1.49

  Bond valence sum for V   3.93

......V2

  V  (23, 1.21, 1.45)                      Rij   Dij   Vij
                    -O  ( 8,  .63, 3.15) 1.77  1.96   .61
                    -O  ( 8,  .63, 3.15) 1.77  1.97   .60
                    -O  ( 8,  .63, 3.15) 1.77  1.96   .61
                    -O  ( 8,  .63, 3.15) 1.77  1.96   .61
                    -O  ( 8,  .63, 3.15) 1.77  1.62  1.52

  Bond valence sum for V   3.94

......V3

  V  (23, 1.21, 1.45)                      Rij   Dij   Vij
                    -O  ( 8,  .63, 3.15) 1.77  1.94   .63
                    -O  ( 8,  .63, 3.15) 1.77  1.95   .61
                    -O  ( 8,  .63, 3.15) 1.77  1.95   .61
                    -O  ( 8,  .63, 3.15) 1.77  1.92   .67
                    -O  ( 8,  .63, 3.15) 1.77  1.63  1.48

  Bond valence sum for V   4.01

......V4
```

```
  V  (23, 1.21, 1.45)                          Rij   Dij   Vij
                      -O  ( 8,  .63, 3.15) 1.77  1.96   .61
                      -O  ( 8,  .63, 3.15) 1.77  1.90   .71
                      -O  ( 8,  .63, 3.15) 1.77  1.88   .75
                      -O  ( 8,  .63, 3.15) 1.77  1.94   .64
                      -O  ( 8,  .63, 3.15) 1.77  1.61  1.55

  Bond valence sum for V   4.26

......V5

  V  (23, 1.21, 1.45)                          Rij   Dij   Vij
                      -O  ( 8,  .63, 3.15) 1.77  1.96   .60
                      -O  ( 8,  .63, 3.15) 1.77  1.89   .72
                      -O  ( 8,  .63, 3.15) 1.77  1.92   .68
                      -O  ( 8,  .63, 3.15) 1.77  1.89   .73
                      -O  ( 8,  .63, 3.15) 1.77  1.60  1.58

  Bond valence sum for V   4.32

......V6

  V  (23, 1.21, 1.45)                          Rij   Dij   Vij
                      -O  ( 8,  .63, 3.15) 1.77  1.94   .64
                      -O  ( 8,  .63, 3.15) 1.77  1.96   .61
                      -O  ( 8,  .63, 3.15) 1.77  1.95   .62
                      -O  ( 8,  .63, 3.15) 1.77  1.95   .62
                      -O  ( 8,  .63, 3.15) 1.77  1.62  1.51

  Bond valence sum for V   3.99

......V7

  V  (23, 1.21, 1.45)                          Rij   Dij   Vij
                      -O  ( 8,  .63, 3.15) 1.77  1.93   .65
                      -O  ( 8,  .63, 3.15) 1.77  1.95   .62
                      -O  ( 8,  .63, 3.15) 1.77  1.95   .63
                      -O  ( 8,  .63, 3.15) 1.77  1.98   .58
                      -O  ( 8,  .63, 3.15) 1.77  1.62  1.51

  Bond valence sum for V   3.98

......V8

  V  (23, 1.21, 1.45)                          Rij   Dij   Vij
                      -O  ( 8,  .63, 3.15) 1.77  1.92   .67
                      -O  ( 8,  .63, 3.15) 1.77  1.97   .59
                      -O  ( 8,  .63, 3.15) 1.77  1.96   .60
                      -O  ( 8,  .63, 3.15) 1.77  1.92   .67
                      -O  ( 8,  .63, 3.15) 1.77  1.64  1.43

  Bond valence sum for V   3.96
 ......V9
```

```
V  (23, 1.21, 1.45)                          Rij    Dij    Vij
                    -O   ( 8,   .63, 3.15) 1.77   1.95    .63
                    -O   ( 8,   .63, 3.15) 1.77   1.92    .67
                    -O   ( 8,   .63, 3.15) 1.77   1.93    .65
                    -O   ( 8,   .63, 3.15) 1.77   1.94    .63
                    -O   ( 8,   .63, 3.15) 1.77   1.64   1.45

Bond valence sum for V   4.03
```

Appendix 4(iii). Elemental analysis reports

PBMDJFKBPCKEIH
KBPGJCJF
PMLFAPCEJJCJGD
IPFWGADF
PKCAFALEBHHGMB
CJFKGHBF

Issued to:
Dr.Sathish Kumar Kurapati
C/o Prof.Samar K Das, School of Chemistry,
University of Hyderabad, Hyderabad-500046.

Kind Attn.:Mr.Sateesh.M, 9908652965

Report No. :LLPL/18-19/001890
Issue Date : 08/06/2018
Customer Ref.: TRF

Ref.Date :31/05/2018

Sample Particulars : **NaV19O46**

Qty. Received : 1No Vial

Test Parameters : Vanadium as V,Sodium as Na

Date of Receipt of Sample : 31/05/2018
Date of completion of analysis : 08/06/2018

Date of Starting of Analysis : 07/06/2018
SAMPLE TESTED AS RECEIVED

TEST RESULTS

S.No.	Parameters	UOM	Results
1	Vanadium as V	% by mass	42.33
2	Sodium as Na	% by mass	7.20

Instrument Used: ICP-OES Varian 720-ES
NOTE : This report and results relate only to the sample / items tested.

Appendix Figure 4(a). Elemental analysis report of compound **1**.

PBMDJFKBPCKEIH
KBPGJCJF
PMLFAPCEJNCJGD
IDBKBIDF
PKCAFALEBHHGMB
LJJHHGBF

Issued to:
Dr.Sathish Kumar Kurapati
C/o Prof.Samar K Das, School of Chemistry,
University of Hyderabad, Hyderabad-500046.

Kind Attn.:Mr.Sateesh.M, 9908652965

Report No. :LLPL/18-19/001891
Issue Date : 08/06/2018
Customer Ref.: TRF

Ref.Date :31/05/2018

Sample Particular: **NaV18O42(Cl)**

Qty. Received : 1No Vial

Test Parameters : Vanadium as V,Sodium as Na,Chloride as Cl

Date of Receipt of Sample : 31/05/2018
Date of completion of analysis : 08/06/2018

Date of Starting of Analysis : 07/06/2018
SAMPLE TESTED AS RECEIVED

TEST RESULTS

S.No.	Parameters	UOM	Results
1	Vanadium as V	% by mass	42.52
2	Sodium as Na	% by mass	5.44
3	Chloride as Cl	% by mass	1.63

Instrument Used: ICP-OES Varian 720-ES & IS 3025 Part 32
NOTE : This report and results relate only to the sample / items tested.

Appendix Figure 4(b). Elemental analysis report of compound **2**

Appendix 5(i). Details of bond distances and angles for compounds 1 and 2

*Bond distances (Å) and angles (°) for compound **1***

V(2)-O(4)	1.6236(18)	O(5)#1-V(2)-V(1)	108.87(6)
V(2)-O(5)#1	1.9067(18)	O(3)-V(2)-V(1)	39.48(5)
V(2)-O(3)	1.9280(17)	O(5)-V(2)-V(1)	110.54(6)
V(2)-O(5)	1.9287(18)	O(8)#1-V(2)-V(1)	42.91(5)
V(2)-O(8)#1	1.9952(18)	V(3)-V(2)-V(1)	74.706(15)
V(2)-V(3)	2.9530(6)	V(3)#1-V(2)-V(1)	72.696(15)
V(2)-V(3)#1	2.9550(6)	O(6)-V(3)-O(7)	102.61(10)
V(2)-V(1)	3.0002(4)	O(6)-V(3)-O(3)	106.26(9)
V(3)-O(6)	1.6290(19)	O(7)-V(3)-O(3)	93.21(9)
V(3)-O(7)	1.8318(11)	O(6)-V(3)-O(8)	105.19(9)
V(3)-O(3)	1.9206(17)	O(7)-V(3)-O(8)	92.99(10)
V(3)-O(8)	1.9469(19)	O(3)-V(3)-O(8)	145.71(8)
V(3)-O(5)	1.9665(19)	O(6)-V(3)-O(5)	99.96(9)
V(1)-O(2)	1.637(3)	O(7)-V(3)-O(5)	157.43(9)
V(1)-O(3)#2	1.9464(17)	O(3)-V(3)-O(5)	80.01(7)
V(1)-O(3)	1.9465(17)	O(8)-V(3)-O(5)	81.44(7)
V(1)-O(8)#1	2.0527(18)	O(6)-V(3)-V(2)	104.14(7)
V(1)-O(8)#3	2.0527(18)	O(7)-V(3)-V(2)	131.05(8)
V(1)-O(1)	2.293(3)	O(3)-V(3)-V(2)	39.98(5)
O(1)-C(1)	1.275(3)	O(8)-V(3)-V(2)	117.96(6)
N(1)-N(1)#8	1.446(5)	O(5)-V(3)-V(2)	40.23(5)
O(4)-V(2)-O(5)#1	109.53(9)	O(6)-V(3)-V(2)#9	109.40(7)
O(4)-V(2)-O(3)	113.15(9)	O(7)-V(3)-V(2)#9	129.72(8)
O(5)#1-V(2)-O(3)	137.08(8)	O(3)-V(3)-V(2)#9	112.92(6)
O(4)-V(2)-O(5)	105.90(9)	O(8)-V(3)-V(2)#9	42.07(5)
O(5)#1-V(2)-O(5)	92.06(11)	O(5)-V(3)-V(2)#9	39.53(5)
O(3)-V(2)-O(5)	80.78(8)	V(2)-V(3)-V(2)#9	76.814(19)
O(4)-V(2)-O(8)#1	107.87(9)	O(2)-V(1)-O(3)#2	103.35(8)
O(5)#1-V(2)-O(8)#1	81.69(8)	O(2)-V(1)-O(3)	103.35(8)
O(3)-V(2)-O(8)#1	81.29(7)	O(3)#2-V(1)-O(3)	92.18(10)
O(5)-V(2)-O(8)#1	145.81(8)	O(2)-V(1)-O(8)#1	99.73(8)
O(4)-V(2)-V(3)	112.94(7)	O(3)#2-V(1)-O(8)#1	156.71(8)
O(5)#1-V(2)-V(3)	123.15(6)	O(3)-V(1)-O(8)#1	79.40(7)
O(3)-V(2)-V(3)	39.80(5)	O(2)-V(1)-O(8)#3	99.73(8)
O(5)-V(2)-V(3)	41.18(6)	O(3)#2-V(1)-O(8)#3	79.41(7)
O(8)#1-V(2)-V(3)	117.39(5)	O(3)-V(1)-O(8)#3	156.71(8)
O(4)-V(2)-V(3)#1	117.92(7)	O(8)#1-V(1)-O(8)#3	99.83(10)
O(5)#1-V(2)-V(3)#1	41.03(6)	O(2)-V(1)-O(1)	165.98(13)
O(3)-V(2)-V(3)#1	110.55(5)	O(3)#2-V(1)-O(1)	86.24(8)
O(5)-V(2)-V(3)#1	122.91(6)	O(3)-V(1)-O(1)	86.24(8)
O(8)#1-V(2)-V(3)#1	40.83(5)	O(8)#1-V(1)-O(1)	71.67(7)
V(3)-V(2)-V(3)#1	128.88(2)	O(8)#3-V(1)-O(1)	71.67(7)
O(4)-V(2)-V(1)	124.95(7)	V(3)#2-O(7)-V(3)	127.12(14)

V(3)-O(8)-V(2)#9	97.10(8)	V(2)#9-O(5)-V(2)	146.26(11)
V(3)-O(8)-V(1)#9	123.88(9)	V(2)#9-O(5)-V(3)	99.44(8)
V(2)#9-O(8)-V(1)#9	95.65(8)	V(2)-O(5)-V(3)	98.59(8)
C(1)-O(1)-V(1)	129.80(19)	O(1)#1-C(1)-O(1)	120.000(1)
V(3)-O(3)-V(2)	100.22(8)	O(1)#1-C(1)-O(1)#9	120.002(1)
V(3)-O(3)-V(1)	138.15(9)	O(1)-C(1)-O(1)#9	120.0
V(2)-O(3)-V(1)	101.49(8)		

Symmetry transformations used to generate equivalent atoms:
#1 -x+y+1,-x+2,z; #2 x-y+1,-y+2,z; #3 x,y,-z+1; #4 x-y+1,-y+2,-z+1; #5 y,x,z; #6 -y+2,x-y+1,z; #7 x,y+1,z; #8 -y+1,x-y+1,z; #9 -x+y,-x+1,z; #10 y,x,-z+1; #11 y,x,-z+2; #12 -y+1,x-y,z; #13 x-y,-y,-z+2; #14 x-y+1,-y+1,-z+2; #15 x,y-1,z; #16 -x+y+1,-x+1,z.

*Bond distances (Å) and angles (°) for compound **2***

O(8)-V(3)	1.611(13)	Na(3)-O(1)#15	2.291(14)
V(1)-O(1)	1.605(8)	Na(3)-O(10)#15	3.11(3)
V(1)-O(2)#1	1.916(3)	Na(3)-O(10)#14	3.11(3)
V(1)-O(2)	1.916(3)	O(1)-V(1)-O(2)#1	106.4(3)
V(1)-O(3)	1.951(5)	O(1)-V(1)-O(2)	106.4(3)
V(1)-O(3)#2	1.951(5)	O(2)#1-V(1)-O(2)	94.3(5)
V(3)-O(3)#2	1.976(5)	O(1)-V(1)-O(3)	109.0(3)
V(3)-O(3)#3	1.976(5)	O(2)#1-V(1)-O(3)	144.0(3)
V(3)-O(3)	1.976(5)	O(2)-V(1)-O(3)	82.1(3)
V(3)-O(3)#4	1.976(5)	O(1)-V(1)-O(3)#2	109.0(3)
V(2)-O(4)	1.621(8)	O(2)#1-V(1)-O(3)#2	82.1(3)
V(2)-O(5)	1.820(5)	O(2)-V(1)-O(3)#2	144.0(3)
V(2)-O(3)#5	1.915(5)	O(3)-V(1)-O(3)#2	80.3(3)
V(2)-O(3)	1.915(5)	O(8)-V(3)-O(3)#2	105.34(17)
V(2)-O(2)	2.009(9)	O(8)-V(3)-O(3)#3	105.34(17)
O(2)-V(1)#6	1.916(3)	O(3)#2-V(3)-O(3)#3	149.3(3)
O(2)-Na(2)	2.868(11)	O(8)-V(3)-O(3)	105.34(17)
O(1)-Na(3)#7	2.291(14)	O(3)#2-V(3)-O(3)	79.1(3)
Na(1)-O(9)#8	2.373(9)	O(3)#3-V(3)-O(3)	92.8(3)
Na(1)-O(9)	2.373(9)	O(8)-V(3)-O(3)#4	105.34(17)
Na(1)-O(9)#9	2.373(9)	O(3)#2-V(3)-O(3)#4	92.8(3)
Na(1)-O(6)#8	2.446(9)	O(3)#3-V(3)-O(3)#4	79.1(3)
Na(1)-O(6)	2.446(9)	O(3)-V(3)-O(3)#4	149.3(3)
Na(1)-O(6)#9	2.446(9)	O(4)-V(2)-O(5)	104.7(4)
O(5)-V(2)#10	1.820(5)	O(4)-V(2)-O(3)#5	109.47(16)
O(6)-Na(1)#3	2.446(9)	O(5)-V(2)-O(3)#5	91.16(18)
O(7)-Na(3)	2.34(2)	O(4)-V(2)-O(3)	109.47(16)
Na(2)-O(10)	2.90(5)	O(5)-V(2)-O(3)	91.16(18)
Na(2)-O(10)#11	2.90(5)	O(3)#5-V(2)-O(3)	139.0(3)
Na(2)-O(2)#11	2.868(11)	O(4)-V(2)-O(2)	99.6(4)
O(10)-Na(3)#7	3.11(3)	O(5)-V(2)-O(2)	155.7(4)
Na(3)-O(7)#13	2.34(2)	O(3)#5-V(2)-O(2)	80.67(18)
Na(3)-O(1)#14	2.291(14)	O(3)-V(2)-O(2)	80.67(18)

V(2)-O(3)-V(1)	99.6(2)	V(2)-O(5)-V(2)#10	132.4(6)
V(2)-O(3)-V(3)	137.7(3)	Na(1)#3-O(6)-Na(1)	80.8(4)
V(1)-O(3)-V(3)	99.9(2)	O(10)-Na(2)-O(10)#11	97.1(12)
V(1)#6-O(2)-V(1)	141.1(5)	O(10)-Na(2)-O(2)#11	107.1(2)
V(1)#6-O(2)-V(2)	97.6(3)	O(10)#11-Na(2)-O(2)#11	107.1(2)
V(1)-O(2)-V(2)	97.6(3)	O(10)-Na(2)-O(2)	107.1(2)
V(1)#6-O(2)-Na(2)	105.0(2)	O(10)#11-Na(2)-O(2)	107.1(2)
V(1)-O(2)-Na(2)	105.0(2)	O(2)#11-Na(2)-O(2)	127.4(7)
V(2)-O(2)-Na(2)	105.6(5)	Na(2)-O(10)-Na(3)#7	86.7(12)
V(1)-O(1)-Na(3)#7	168.8(6)	O(7)-Na(3)-O(7)#13	103.1(14)
O(9)#8-Na(1)-O(9)	94.6(4)	O(7)-Na(3)-O(1)#14	170.9(9)
O(9)#8-Na(1)-O(9)#9	94.6(4)	O(7)#13-Na(3)-O(1)#14	86.0(6)
O(9)-Na(1)-O(9)#9	94.6(4)	O(7)-Na(3)-O(1)#15	86.0(6)
O(9)#8-Na(1)-O(6)#8	90.5(3)	O(7)#13-Na(3)-O(1)#15	170.9(9)
O(9)-Na(1)-O(6)#8	171.4(4)	O(1)#14-Na(3)-O(1)#15	84.9(7)
O(9)#9-Na(1)-O(6)#8	91.8(3)	O(7)-Na(3)-O(10)#15	95.0(5)
O(9)#8-Na(1)-O(6)	91.8(3)	O(7)#13-Na(3)-O(10)#15	95.0(5)
O(9)-Na(1)-O(6)	90.5(3)	O(1)#14-Na(3)-O(10)#15	84.0(6)
O(9)#9-Na(1)-O(6)	171.4(4)	O(1)#15-Na(3)-O(10)#15	84.0(6)
O(6)#8-Na(1)-O(6)	82.5(3)	O(7)-Na(3)-O(10)#14	95.0(5)
O(9)#8-Na(1)-O(6)#9	171.4(4)	O(7)#13-Na(3)-O(10)#14	95.0(5)
O(9)-Na(1)-O(6)#9	91.8(3)	O(1)#14-Na(3)-O(10)#14	84.0(6)
O(9)#9-Na(1)-O(6)#9	90.5(3)	O(1)#15-Na(3)-O(10)#14	84.0(6)
O(6)#8-Na(1)-O(6)#9	82.5(3)	O(10)#15-Na(3)-O(10)#14	163.8(17)
O(6)-Na(1)-O(6)#9	82.5(3)		

Symmetry transformations used to generate equivalent atoms:
#1 -x+y+1,-x+2,z; #2 x-y+1,-y+2,z; #3 x,y,-z+1; #4 x-y+1,-y+2,-z+1; #5 y,x,z; #6 -y+2,x-y+1,z; #7 x,y+1,z; #8 -y+1,x-y+1,z; #9 -x+y,-x+1,z; #10 y,x,-z+1; #11 y,x,-z+2; #12 -y+1,x-y,z; #13 x-y,-y,-z+2; #14 x-y+1,-y+1,-z+2; #15 x,y-1,z; #16 -x+y+1,-x+1,z.

Appendix 5(ii). Elemental analysis reports

Issued to:
Prof. Samar K. Das
C/o Prof .Samar K.Das Lab -School of chemistry
University of Hyderabad - 019

Kind Attn.:M.sateesh

Report No. : LLPL/16-17/008631
Issue Date : 21/12/2016
Customer Ref. : TRF

Ref.Date : 17/12/2016

Sample Particulars : SKD13

Qty. Received : 260mg, Packed in Sealed bottle

Test Parameters : Vanadium as V,Sodium as Na

Date of Receipt of Sample : 19/12/2016
Date of completion of analysis : 21/12/2016

Date of Starting of Analysis : 21/12/2016
SAMPLE TESTED AS RECEIVED

TEST RESULTS

S.No.	Parameters	UOM	Results
1	Vanadium as V	% by mass	34.96
2	Sodium as Na	% by mass	6.58

Instrument Used: ICP-OES Varian 720-ES
NOTE : This report and results relate only to the sample / items tested.

Appendix Figure 5(a). Elemental analysis report of compound **1**.

Issued to:
Prof. Samar K. Das
C/o Prof .Samar K.Das Lab -School of chemistry
University of Hyderabad - 019

Kind Attn.:M.sateesh, +91 9908652965

Report No. : LLPL/17-18/008151
Issue Date : 10/02/2018
Customer Ref. : TRF

Ref.Date : 07/12/2017

Sample Particulars : V15(CO3)

Qty. Received : 150mg, Polythene Cover

Test Parameters : Bismuth as Bi

Date of Receipt of Sample : 06/02/2018
Date of completion of analysis : 10/02/2018

Date of Starting of Analysis : 10/02/2018
SAMPLE TESTED AS RECEIVED

TEST RESULTS

S.No.	Parameters	UOM	Results
1	Bismuth as Bi	ppm	<10.0

Instrument Used: ICP-OES Varian 720-ES
NOTE : This report and results relate only to the sample / items tested.

Appendix Figure 5(b). Elemental analysis report of bismuth for compound **1**.

Method filename: C:\Program Files\Thermo Finnigan\Eager 300 for EA1112\DATA\Sys_data_ex
Sample ID: V15CO3 (# 17)
Analysis type: UnkNown
Chromatogram filename: UNK-30012019-7.dat
Sample weight: 1.113

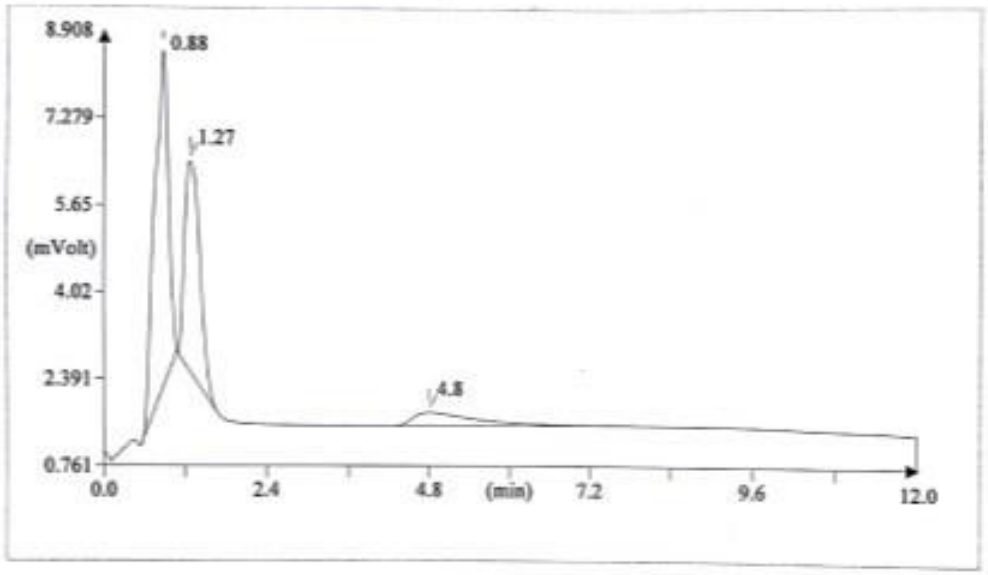

Element Name	Element %	Ret. Time
Nitrogen	3. 68	0. 88
Carbon	0. 56	1. 27
Hydrogen	3. 89	4. 80

Appendix Figure 5(c). CHN elemental analysis report of compound **1**.

PBMDJFKBOCKEIH
KBPGKBJF
PMJHAEAONNCJGD
ILHCJGNF
PKCAFEJGBHHGMB
FBCEAEBF

Issued to:
Prof .Samar K.Das
School of chemistry
University of Hyderabad - 046
Kind Attn.:M.sateesh

Report No. : LLPL/16-17/010661
Issue Date : 03/04/2017
Customer Ref.: TRF
Ref.Date : 21/02/2017

Sample Particulars : V15+HCl

Qty. Received : 30mg X1no Vial

Test Parameters : Vanadium as V,Sodium as Na,Chloride as Cl

Date of Receipt of Sample : 22/02/2017
Date of Starting of Analysis : 03/04/2017
Date of completion of analysis : 03/04/2017
SAMPLE TESTED AS RECEIVED

TEST RESULTS

S.No.	Parameters	UOM	Results
1	Vanadium as V	% by mass	40.40
2	Sodium as Na	% by mass	2.32
3	Chloride as Cl	% by mass	1.54

Instrument Used: ICP-OES Varian 720-ES & IS 3025 part 32
NOTE : This report and results relate only to the sample / items tested.

R.V. Rama Rao
Authorized Signatory

Page No. 1/1

Appendix Figure 5(d). Elemental (ICP-OES) analysis report of an amorphous compound.

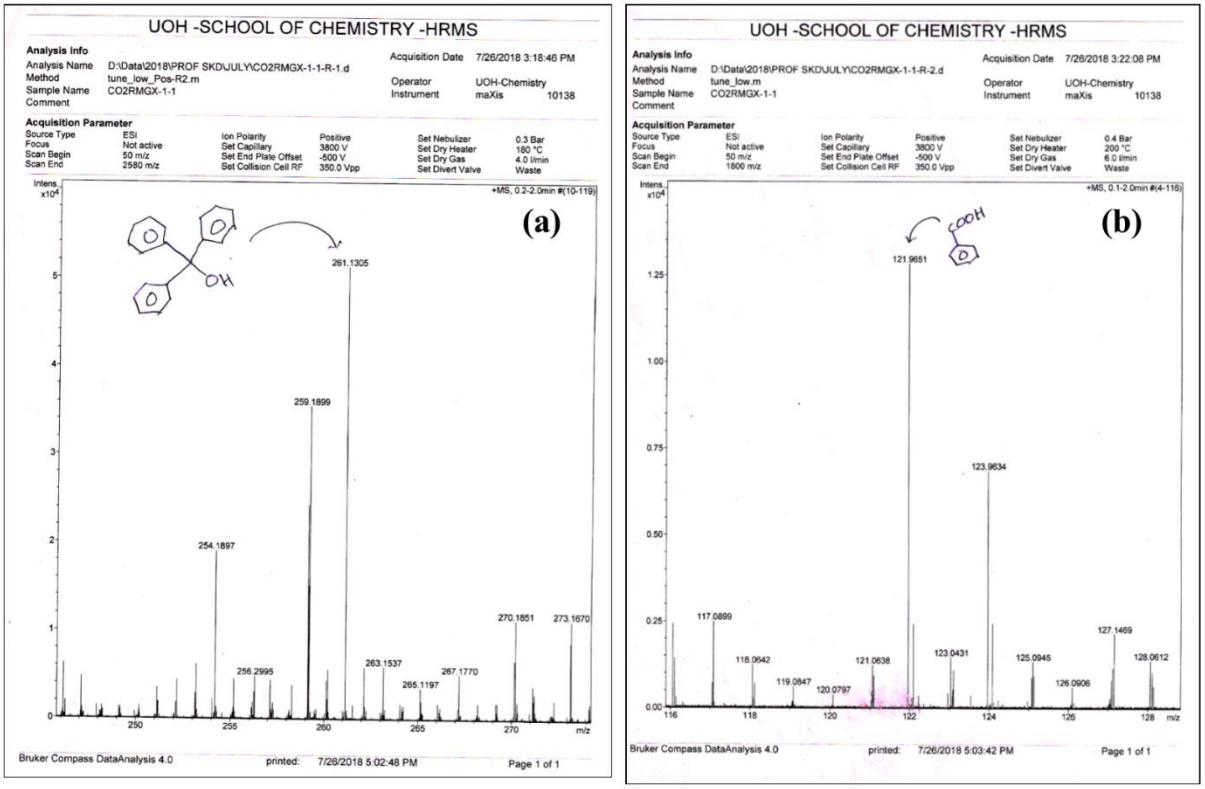

Appendix Figure 5(e). HR-MS analysis report of triphenyl methanol (left) and benzoic acid (right) resulted in a 1:1 mmol (compound **1**: PhMgBr reagent) ratio reaction.

Issued to:
Prof. Samar K. Das
C/o Prof .Samar K.Das Lab -School of chemistry
University of Hyderabad - 019

Kind Attn.:Mr.M.Sateesh

Report No. : LLPL/D/16-17/002209
Issue Date : 21/12/2016
Customer Ref. : TRF

Ref.Date : 30/11/2016

Sample Particulars : [V15(Cl)]

Qty. Received : 0.45gm ,Packed in Sealed bottle

Test Parameters : Vanadium as V,Sodium as Na,Chloride as Cl

Date of Receipt of Sample : 30/11/2016
Date of completion of analysis : 21/12/2016
Date of Starting of Analysis : 05/12/2016
SAMPLE TESTED AS RECEIVED

TEST RESULTS

S.No.	Parameters	UOM	Results
1	Vanadium as V	% by mass	35.53
2	Sodium as Na	% by mass	10.58
3	Chloride as Cl	% by mass	1.68

Instrument Used: ICP-OES Varian 720-ES & IS 3025 part 32
NOTE : This report and results relate only to the sample / items tested.

Appendix Figure 5(f). Elemental (ICP-OES) analysis report of compound **2**.

Appendix 5(iii). Bond valance sum (BVS) calculations of compounds 1 and 2

Compound 1

Bond valence calculation. Numbers in brackets after atom symbols are at.no., r and c - see *O"Keeffe and Brese, J.A.C.S. 1991, 113, 3226*.

```
V1
 V  (23, 1.21, 1.45)                          Rij   Dij   Vij
                      -O  ( 8,  .63, 3.15) 1.77  1.62  1.50
                      -O  ( 8,  .63, 3.15) 1.77  1.93   .65
                      -O  ( 8,  .63, 3.15) 1.77  1.93   .65
                      -O  ( 8,  .63, 3.15) 1.77  1.91   .70
                      -O  ( 8,  .63, 3.15) 1.77  2.00   .55

  Bond valence sum for V   4.05

V2
 V  (23, 1.21, 1.45)                          Rij   Dij   Vij
                      -O  ( 8,  .63, 3.15) 1.77  1.97   .59
                      -O  ( 8,  .63, 3.15) 1.77  1.95   .63
                      -O  ( 8,  .63, 3.15) 1.77  1.63  1.48
                      -O  ( 8,  .63, 3.15) 1.77  1.83   .85
                      -O  ( 8,  .63, 3.15) 1.77  1.92   .67

  Bond valence sum for V   4.22

V3
  V  (23, 1.21, 1.45)                          Rij   Dij   Vij
                      -O  ( 8,  .63, 3.15) 1.77  2.29   .25
                      -O  ( 8,  .63, 3.15) 1.77  1.64  1.42
                      -O  ( 8,  .63, 3.15) 1.77  1.94   .63
                      -O  ( 8,  .63, 3.15) 1.77  1.94   .63
                      -O  ( 8,  .63, 3.15) 1.77  2.05   .47

  Bond valence sum for V   3.40
```

Compound 2

```
V1
  V  (23, 1.21, 1.45)                          Rij   Dij   Vij
                      -O  ( 8,  .63, 3.15) 1.77  1.61  1.58
                      -O  ( 8,  .63, 3.15) 1.77  1.92   .68
                      -O  ( 8,  .63, 3.15) 1.77  1.95   .62
                      -O  ( 8,  .63, 3.15) 1.77  1.92   .68
                      -O  ( 8,  .63, 3.15) 1.77  1.95   .62

  Bond valence sum for V   4.18


V2
  V  (23, 1.21, 1.45)                          Rij   Dij   Vij
                      -O  ( 8,  .63, 3.15) 1.77  1.62  1.51
                      -O  ( 8,  .63, 3.15) 1.77  2.01   .53
                      -O  ( 8,  .63, 3.15) 1.77  1.82   .88
```

```
                      -O  ( 8,  .63, 3.15) 1.77  1.91   .68
                      -O  ( 8,  .63, 3.15) 1.77  1.91   .68

  Bond valence sum for V   4.28

V3
  V  (23, 1.21, 1.45)                          Rij   Dij   Vij
                      -O  ( 8,  .63, 3.15) 1.77  1.61  1.55
                      -O  ( 8,  .63, 3.15) 1.77  1.98   .58
                      -O  ( 8,  .63, 3.15) 1.77  1.98   .58
                      -O  ( 8,  .63, 3.15) 1.77  1.98   .58
                      -O  ( 8,  .63, 3.15) 1.77  1.98   .58

  Bond valence sum for V   3.87
```

List of Publications

1. **Carbonate Encapsulation from Dissolved Atmospheric CO_2 into a Polyoxovanadate Capsule.**

   Sateesh Mulkapuri, Sathish Kumar Kurapati and Samar K. Das ***Dalton Trans.,*** *2019*, *48*, 8773–8781.

2. **A Fully Reduced $\{V^{IV}_{18}O_{42}\}$ Host and VO_4^{3-}, Cl^- as Guest Anions: Synthesis, Characterization and Proton Conductivity.**

   Sateesh Mulkapuri, Sathish Kumar Kurapati, Subhabrata Mukhopadhyay and Samar K. Das ***New J. Chem.,*** **2019**, *43*, 17670—17679.

3. **W^{VI}–OH Functionality on Polyoxometalates for Hydrogen Evolution Reaction.**

   Sateesh Mulkapuri, Subhabrata Mukhopadhyay, Sathish Kumar Kurapati and Samar K. Das (***Communicated***).

4. **Barrel-shaped Polyoxometalates Exhibiting Electrocatalytic Hydrogen Evolution at Neutral pH.**

   Sateesh Mulkapuri, Sathish Kumar Kurapati, Marri Pradeep Kumar, Rajendar Nasani and Samar K. Das (***Ready Communicate***).

Poster and oral presentation

1. **Sateesh Mulkapuri**, Sathish Kumar Kurapati, **Samar K. Das.**

   A Fully Reduced Functional Polyoxovanadate Capsule: Aerial CO_2 Fixation, Its Exclusion in a Gas-Solid Reaction and efficient Proton Conduction.
   Poster presentation in **"MTIC–XVII"** held at CSIR-NCL, Pune and IISER–Pune, during 11-14 December, 2017.

2. **Sateesh Mulkapuri**, Sathish Kumar Kurapati, Subhabrata Mukhopadhyay and **Samar K. Das**.

   A Fully Reduced Functional Polyoxovanadate Capsule: Aerial CO_2 Capture, Its Exclusion in a Gas-Solid Reaction and Efficient Proton Conduction.
   Poster presentation in **"ICCCS-8"** held at School of Chemistry, University of Hyderabad, India, during 18-19 December, 2017.

3. **Sateesh Mulkapuri**, Sathish Kumar Kurapati, Subhabrata Mukhopadhyay and **Samar K. Das**.

   A Fully Reduced Functional Polyoxovanadate Capsule: Aerial CO_2 Fixation, Its Exclusion in a Gas-Solid Reaction and Efficient Proton Conduction.
   Poster presentation in "**CHEMFEST-2018"** held at University of Hyderabad, Hyderabad, during 9-10 March, 2018.

4. **Sateesh Mulkapuri**, Sathish Kumar Kurapati, Subhabrata Mukhopadhyay and **Samar K. Das**.
   Functional Polyoxometalates and Its Applications: Aerial CO_2 Fixation, Proton Conduction, Electrocatalytic Water Splitting.
   Oral and poster presentation in **"CHEMFEST-2019"** held at University of Hyderabad, Hyderabad, Hyderabad, during 22-23 February, 2019.

Functional Polyoxometalates for Clean Environment and Energy Applications

ORIGINALITY REPORT

29%	25%	26%	4%
SIMILARITY INDEX	INTERNET SOURCES	PUBLICATIONS	STUDENT PAPERS

PRIMARY SOURCES

1	pubs.rsc.org Internet Source	21%
2	Submitted to University of Hyderabad, Hyderabad Student Paper	1%
3	Sateesh Mulkapuri, Sathish Kumar Kurapati, Subhabrata Mukhopadhyay, Samar K. Das. " A fully reduced {VIV18O } host and VO , Cl as guest anions: synthesis, characterization and proton conductivity ", New Journal of Chemistry, 2019 Publication	1%
4	Declan L. Burke, Anthony P. O'Mullane, Vincent E. Lodge, Marcus B. Mooney. "Auto-inhibition of hydrogen gas evolution on gold in aqueous acid solution", Journal of Solid State Electrochemistry, 2001 Publication	<1%
5	Jing Zhu, Liangsheng Hu, Pengxiang Zhao,	

This is from our Publication
S.K.Das
22/09/2020

Prof. Samar K. Das
School of Chemistry
University of Hyderabad
Hyderabad-500 046., INDIA.
skdas@uohyd.ac.in

from our publication
S.K.Das
22/09/2020

Prof. Samar K. Das
School of Chemistry
University of Hyderabad
Hyderabad-500 046., INDIA.
skdas@uohyd.ac.in

	Lawrence Yoon Suk Lee, Kwok-Yin Wong. "Recent Advances in Electrocatalytic Hydrogen Evolution Using Nanoparticles", Chemical Reviews, 2019 Publication	<1%
6	Ina Loose, Elisabeth Droste, Michael Bösing, Heinrich Pohlmann et al. " Heteropolymetalate Clusters of the Subvalent Main Group Elements Bi and Sb ", Inorganic Chemistry, 1999 Publication	<1%
7	Chandani Singh, Subhabrata Mukhopadhyay, Samar K. Das. "Polyoxometalate-Supported Bis(2,2′-bipyridine)mono(aqua)nickel(II) Coordination Complex: an Efficient Electrocatalyst for Water Oxidation", Inorganic Chemistry, 2018 Publication	<1%
8	Subhabrata Mukhopadhyay, Olivia Basu, Aranya Kar, Samar K. Das. "Efficient Electrocatalytic Water Oxidation by Fe(salen)–MOF Composite: Effect of Modified Microenvironment", Inorganic Chemistry, 2019 Publication	<1%
9	mafiadoc.com Internet Source	<1%
10	Kwak, O.K.. "One-dimensional helical coordination polymers of cobalt(II) and iron(II)	<1%

	ions with 2,2'-bipyridyl-3,3'-dicarboxylate (BPDC^2^-)", Inorganica Chimica Acta, 20070401 Publication	
11	Lu Wang, Bai-Bin Zhou, Kai Yu, Zhan-Hua Su, Song Gao, Li-Li Chu, Jia-Ren Liu, Guo-Yu Yang. "Novel Antitumor Agent, Trilacunary Keggin-Type Tungstobismuthate, Inhibits Proliferation and Induces Apoptosis in Human Gastric Cancer SGC-7901 Cells", Inorganic Chemistry, 2013 Publication	<1%
12	chemistry-europe.onlinelibrary.wiley.com Internet Source	<1%
13	www.tandfonline.com Internet Source	<1%
14	link.springer.com Internet Source	<1%
15	Beñat Artetxe, Santiago Reinoso, Leire San Felices, Pablo Vitoria et al. "Functionalization of Krebs-Type Polyoxometalates with N,O-Chelating Ligands: A Systematic Study", Inorganic Chemistry, 2015 Publication	<1%
16	www.zora.uzh.ch Internet Source	<1%

17	raiith.iith.ac.in Internet Source	<1%
18	scholarworks.wm.edu Internet Source	<1%
19	pubs.acs.org Internet Source	<1%
20	Li-Na Xiao, Hao Zhang, Ting-Ting Zhang, Xiao Zhang, Xiao-Bing Cui. "Two new POMOF compounds constructed from polyoxoanions, metals and organic ligands", Journal of Solid State Chemistry, 2018 Publication	<1%
21	Tatsuya Shinagawa, Angel T. Garcia-Esparza, Kazuhiro Takanabe. "Insight on Tafel slopes from a microkinetic analysis of aqueous electrocatalysis for energy conversion", Scientific Reports, 2015 Publication	<1%
22	Atanu Dey, Vierandra Kumar, Anku Guha, Sumit Bawari, Shubhadeep Pal, Tharangattu N. Narayanan, Vadapalli Chandrasekhar. "A Tetranuclear Cobalt (II) phosphate Possessing a D4R Core: An Efficient Water Oxidation Catalyst", Dalton Transactions, 2020 Publication	<1%
23	www.freepatentsonline.com	

	Internet Source	<1%
24	T. Arumuganathan. "Two different zinc(II)-aqua complexes held up by a metal-oxide based support: Synthesis, crystal structure and catalytic activity of [HMTAH]2[{Zn(H2O)5}{Zn(H2O)4}{Mo7O24}]·2H2O (HMTAH = protonated hexamethylenetetramine)", Journal of Chemical Sciences, 01/2008 Publication	<1%
25	www.db-thueringen.de Internet Source	<1%
26	Suranjana Bose, Joyashish Debgupta, Rani M. Ramsundar, Samar K. Das. " Electrochemical Water Oxidation Catalyzed by an In Situ Generated α-Co(OH) Film on Zeolite-Y Surface ", Chemistry - A European Journal, 2017 Publication	<1%
27	baadalsg.inflibnet.ac.in Internet Source	<1%
28	www.frontiersin.org Internet Source	<1%
29	Submitted to University of Science and Technology Student Paper	<1%
	Xiaoxin Zou, Yu Zhang. "Noble metal-free	

30	hydrogen evolution catalysts for water splitting", Chemical Society Reviews, 2015 Publication	<1%
31	Paulami Manna, Samar K. Das. "Perceptive Approach in Assessing Rigidity versus Flexibility in the Construction of Diverse Metal–Organic Coordination Networks: Synthesis, Structure, and Magnetism", Crystal Growth & Design, 2015 Publication	<1%
32	scholarbank.nus.edu.sg Internet Source	<1%
33	Submitted to National Institute of Technology, Silchar Student Paper	<1%
34	edoc.ub.uni-muenchen.de Internet Source	<1%
35	Suresh Bommakanti, Samar K. Das. "A quantitative transmetalation with a metal organic framework compound in a solid–liquid interface reaction: synthesis, structure, kinetics, spectroscopy and electrochemistry", CrystEngComm, 2019 Publication	<1%
36	Kim D. von Allmen, Henrik Grundmann, Anthony Linden, Greta R. Patzke. " Synthesis and Characterization of 0D–3D Copper-Containing	<1%

Tungstobismuthates Obtained from the Lacunary Precursor Na [B-α-BiW O] ", Inorganic Chemistry, 2017
Publication

37 Qian Ren, Huile Jin, Xue Xu, Aili Liu, Jun Li, Jichang Wang, Shun Wang. "Hydrogen evolution reaction catalyzed by nickel/nickel phosphide nanospheres synthesized through electrochemical methods", Electrochimica Acta, 2018 <1%
Publication

38 A. Juliet Christina Mary, A. Chandra Bose. "Hydrothermal synthesis of Mn-doped ZnCo 2 O 4 electrode material for high-performance supercapacitor", Applied Surface Science, 2017 <1%
Publication

39 Amendra Fernando, K. L. Dimuthu M. Weerawardene, Natalia V. Karimova, Christine M. Aikens. "Quantum Mechanical Studies of Large Metal, Metal Oxide, and Metal Chalcogenide Nanoparticles and Clusters", Chemical Reviews, 2015 <1%
Publication

40 Atanu Dey, Vierandra Kumar, Shubhadeep Pal, Anku Guha, Sumit Bawari, Tharangattu N. Narayanan, Vadapalli Chandrasekhar. " A tetranuclear cobalt( ) phosphate possessing a <1%

	D4R core: an efficient water oxidation catalyst ", Dalton Transactions, 2020 Publication	
41	Caviglioli, G.. "Identification of degradation products of Ibuprofen arising from oxidative and thermal treatments", Journal of Pharmaceutical and Biomedical Analysis, 20021015 Publication	<1%
42	Submitted to Savitribai Phule Pune University Student Paper	<1%
43	repository.ias.ac.in Internet Source	<1%
44	Submitted to IIT Delhi Student Paper	<1%
45	onlinelibrary.wiley.com Internet Source	<1%
46	Paladugu Suresh, Chatla Naga Babu, Ganesan Prabusankar. "Semi-rigid imidazolium carboxylate controlled structural topologies in zwitterionic coordination networks", Polyhedron, 2015 Publication	<1%
47	Ding-Yi Fu, Simin Zhang, Zhiyu Qu, Xianghui Yu, Yuqing Wu, Lixin Wu. "Hybrid Assembly toward Enhanced Thermal Stability of Virus-like Particles and Antibacterial Activity of	<1%

	Polyoxometalates", ACS Applied Materials & Interfaces, 2018 Publication	
48	"Handbook of Heterogeneous Catalysis", Wiley, 1997 Publication	<1%
49	studentsrepo.um.edu.my Internet Source	<1%
50	Thomas McGlone, Carsten Streb, Martí Busquets-Fité, Jun Yan, David Gabb, De-Liang Long, Leroy Cronin. "Silver Linked Polyoxometalate Open Frameworks (Ag-POMOFs) for the Directed Fabrication of Silver Nanomaterials", Crystal Growth & Design, 2011 Publication	<1%
51	www.jiskha.com Internet Source	<1%
52	"Electrodeposition and Surface Finishing", Springer Science and Business Media LLC, 2014 Publication	<1%
53	journals.iucr.org Internet Source	<1%
54	Submitted to University College London Student Paper	<1%
	Submitted to iGroup	

55	Student Paper	<1%
56	Chenthattil Raril, Jamballi G. Manjunatha, Girish Tigari. "Low-cost voltammetric sensor based on an anionic surfactant modified carbon nanocomposite material for the rapid determination of curcumin in natural food supplement", Instrumentation Science & Technology, 2020 Publication	<1%
57	Tanmay Chatterjee, Monima Sarma, Samar K. Das. "Supramolecular Architectures from Ammonium-Crown Ether Inclusion Complexes in Polyoxometalate Association: Synthesis, Structure, and Spectroscopy", Crystal Growth & Design, 2010 Publication	<1%
58	scholarcommons.usf.edu Internet Source	<1%
59	Hong Liu, Chao Qin, Yong-Ge Wei, Lin Xu, Guang-Gang Gao, Feng-Yan Li, Xiao-Shu Qu. "Copper-Complex-Linked Polytungsto-Bismuthate (-Antimonite) Chain Containing Sandwich Cu(II) Ions Partially Modified with Imidazole Ligand", Inorganic Chemistry, 2008 Publication	<1%
	Submitted to Imperial College of Science,	

60	Technology and Medicine Student Paper	<1%
61	Prashanth W. Menezes, Arindam Indra, Chittaranjan Das, Carsten Walter et al. "Uncovering the Nature of Active Species of Nickel Phosphide Catalysts in High-Performance Electrochemical Overall Water Splitting", ACS Catalysis, 2016 Publication	<1%
62	"The Chemistry of the Actinide and Transactinide Elements", Springer Science and Business Media LLC, 2011 Publication	<1%
63	Subhabrata Mukhopadhyay, Joyashish Debgupta, Chandani Singh, Rudraditya Sarkar, Olivia Basu, Samar K. Das. "Designing UiO-66-Based Superprotonic Conductor with the Highest Metal–Organic Framework Based Proton Conductivity", ACS Applied Materials & Interfaces, 2019 Publication	<1%
64	cdn-pubs.acs.org Internet Source	<1%
65	Konrad Jobst. "Electrocatalytic Activity of Crystalline and Amorphous Nickel Model Alloys", Journal of Catalysis, 20020401 Publication	<1%

66	hdl.handle.net Internet Source	<1%
67	Submitted to Indian School of Mines Student Paper	<1%
68	"Encyclopedia of Applied Electrochemistry", Springer Nature, 2014 Publication	<1%
69	Shan-Shan TONG, Xue-Jing WANG, Qing-Chuan LI, Xiao-Jun HAN. "Progress on Electrocatalysts of Hydrogen Evolution Reaction Based on Carbon Fiber Materials", Chinese Journal of Analytical Chemistry, 2016 Publication	<1%
70	Faber, Matthew S., Mark A. Lukowski, Qi Ding, Nicholas Scott Kaiser, and Song Jin. "Earth-Abundant Metal Pyrites (FeS2, CoS2, NiS2, and Their Alloys) for Highly Efficient Hydrogen Evolution and Polysulfide Reduction Electrocatalysis", The Journal of Physical Chemistry C Publication	<1%
71	Submitted to Birla Institute of Technology and Science Pilani Student Paper	<1%
72	ir.canterbury.ac.nz Internet Source	<1%

73	Submitted to Auckland International College Student Paper	<1%
74	M Froehlich. "The Influence of the pH Value of the Electrolyte on the EMF Stability of the International Weston Cell", Metrologia, 1974 Publication	<1%
75	Samar Kumar Das, Subhabrata Mukhopadhyay, Olivia Basu. "ZIF-8 MOF Encapsulated Co-porphyrin, an Efficient Electrocatalyst for Water Oxidation in a Wide pH Range: Works Better at Neutral pH", ChemCatChem, 2020 Publication	<1%
76	Supriya Sabbani, Samar K. Das. " Reversible solid to solid transformation in a crystalline state gas–solid reaction under ambient conditions: Fe–N(pyridine) bond formation at the expense of Fe–OH bond breaking and vice versa ", CrystEngComm, 2015 Publication	<1%
77	Bo You, Nan Jiang, Meili Sheng, Margaret Winona Bhushan, Yujie Sun. " Hierarchically Porous Urchin-Like Ni P Superstructures Supported on Nickel Foam as Efficient Bifunctional Electrocatalysts for Overall Water Splitting ", ACS Catalysis, 2015 Publication	<1%

Exclude quotes	On	Exclude matches	< 14 words
Exclude bibliography	On		

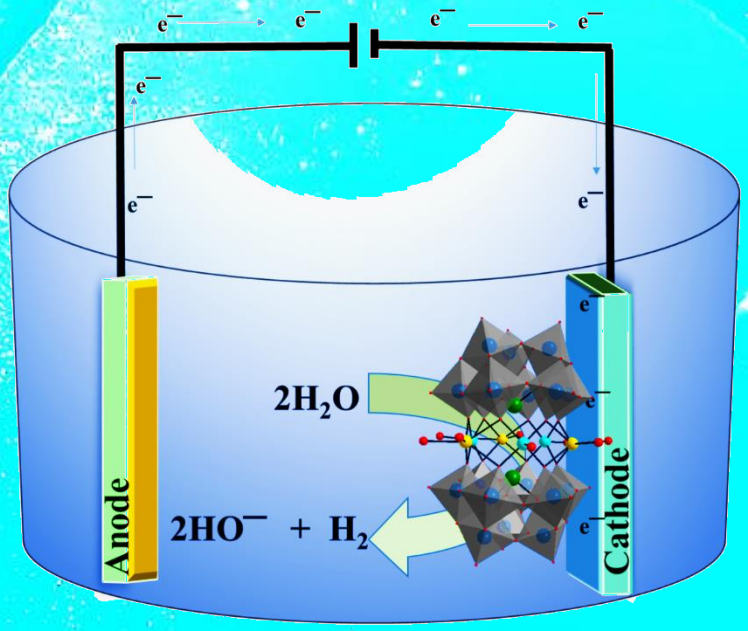

Catalytic Hydrogen Evolution

School of Chemistry, University of Hyderabad (IoE), Hyderabad-500 046, India